Functional Analysis of the Fat Mass and Obesity Associated (*Fto*) Gene and Protein

A Thesis submitted to the University of Oxford for

the degree of Doctor of Philosophy

Lukasz Stasiak

Department of Physiology, Anatomy and Genetics

Linacre College

Hilary 2015

Functional Analysis of the Fat Mass and Obesity Associated (*Fto*) Gene and Protein

A Thesis submitted to the University of Oxford for the degree of Doctor of Philosophy

Lukasz Stasiak, Linacre College, Hilary 2015

Abstract

Genome wide association studies have shown that common variants in the human fat mass and obesity-associated (*FTO*) gene predispose to obesity and increased fat mass. Mice globally lacking *Fto* are lean, while mice globally overexpressing *Fto* have increased body weight due to increased fat mass. FTO protein was shown to localise to the nucleus and demethylate ssDNA and ssRNA. However, the mechanisms by which FTO mediates its effects on body phenotype remain unknown.

In this thesis, I found that native FTO can be detected in both the nucleus and the cytoplasm during interphase, and that nuclear FTO was exported through the nuclear membrane during early prophase of the mitotic cell division. I developed co-immunoprecipitation (Co-IP) protocol to pull-down native FTO and identified a large number of new candidate binding partners (CBPs). Computational analysis predicted a role for FTO, and many CBPs, in RNA post-transcriptional modification and processing. I confirmed that the E3 ubiquitin-protein ligase TRIM21 interacts with FTO in multiple mouse tissues and binds FTO through its SPRY domain. Importantly, TRIM21 ubiquitinated FTO which did not lead to its degradation. FTO partially co-localised with TRIM21 and the decapping enzyme DCP2 in mRNA processing bodies (p-bodies). Overexpression of TRIM21 led to the accumulation of FTO outside the nucleus, but was reversed when both proteins were overexpressed. Additionally, I created a muscle specific *Fto* knock-out mouse model and found that lack of FTO in muscle did not result in the body composition phenotype reported in global *Fto* knock-out mice.

Taken together, FTO can function in both the cytoplasm and the nucleus, where it interacts with TRIM21 which ubiquitinates FTO and potentiates its cytoplasmic localisation. Moreover, function of FTO in muscle does not mediate the obesity phenotype in mice.

To Mum

Acknowledgments

I would like to express my sincere gratitude to Professor Dame Frances Ashcroft and Professor Roger Cox, for giving me the amazing opportunity to work on this project. I am very thankful for their patience, support and understanding, especially during the difficult times in my first year of working on the project. Thank you for allowing me to construct my own ideas and take the ownership the project.

I wish to thank Dr Holger Kramer for his guidance and advice on mass spectrometry, co-immunoprecipitation techniques and many others. I would like to especially thank Jeremy Sanderson for sharing his scientific knowledge of bioimaging, and Dr Chris Esapa for his priceless advice on proteomics. Many thanks to Dr Gregor Sachse for his advice on cloning, Sheena Lee for teaching me pathway analysis, and Philippe Dixon for explaining statistics. I would also like to thank the Mary Lyon Centre staff, in particular Dr Sara Wells, Lucie Vizor, Lisa Ireson, Tamzin Osborne and Dr Lydia Teboul, for supporting my animal work. Moreover, I would like to thank Elizabeth Darley and the entire histology team for carrying out essential staining.

I would like to thank all the members of the Ashcroft group and the Cox group I had the pleasure to work with. Thank you for creating a fun and stimulating work environment, and for your friendships. I would especially like to thank Dr Melissa Brereton for helping me master my immunocytochemistry skills, and allowing me to see what others did not. Thank you for all the great time we had working together, for the unforgettable dinners and parties at Linacre, and for teaching me how to speak proper English (and Mancunian). Moreover, I would like to thank Dr Myrte Merkestein for her insightful advice (on literary everything) whenever I needed it, and for help with animal experiments. Thank you for being a great "FTO partner in crime" and making hours of tissue dissection fun.

I also thank all my friends and family for believing in me and supporting me. Finally, I thank Panos Bardas for creating a perfect place to live and work, and taking care of me while writing this thesis in Greece. Thank you for your love, patience, and understanding.

Declaration

The work in this thesis is my own, with the following exceptions. Dr Holger Kramer conducted all the Liquid Chromatography - Tandem Mass Spectrometry runs for the data presented in Chapter 4 and 5. Mr Daniel Andrew provided valuable technical assistance by genotyping all the mice that were used in Chapters 6. Harvest of adult tissue and processing for LacZ Staining was performed by Histology Team at Harwell MRC.

Contents

Abbreviations

2OG	2-Oxoglutarate
4E-BP1	Eukaryotic Translation Initiation Factor 4E-Binding Protein 1
α-MSH	α-Melanocyte-Stimulation Hormone
aa	Amino Acid
AARS	Aminoacyl-tRNA Synthetase
AAV	Adeno-Associated Virus
acetyl-CoA	Acetyl Coenzyme A
ADP	Adenosine-5'-Diphosphate
AGRP	Agouti-Related Protein
AKT	RAC-Alpha Serine/Threonine-Protein Kinase
AlkB	Alpha-Ketoglutarate-Dependent Dioxygenase
ALKBH	Alpha-Ketoglutarate-Dependent Dioxygenase Homolog
AMP	Adenosine-5'-Monophosphate
AMPK	AMP-kinase
ANOVA	Analysis of Variance
ARC	Arcuate Nucleus of the Hypothalamus
ASP	Acylation-Stimulating Protein
ATP	Adenosine-5'-Triphosphate
AUC	Area Under the Curve
BAT	Brown Adipose Tissue
BLAST	Basic Local Alignment Search Tool
BMC	Bone Mineral Content
BMD	Bone Mineral Density
BMI	Body Mass Index
BSA	Bovine Serum Albumin
C/EBP	CCAAT/Enhancer Binding Protein
CART	Cocaine and Amphetamine Related Transcript
CBP	Candidate Binding Partner
CC	Coiled-Coil
CDKN1B	Cyclin-Dependent Protein Kinase Inhibitor 1B
CDS	Coding Sequences
CLIP-Seq	Cross-Linking Immunoprecipitation Sequencing
CMV	Cytomegalovirus
CNS	Central Nervous System
Co-IP	Co-Immunoprecipitation
Cre	Cre Recombinase
CTD	C-Terminal Domain
CUTL1	Cut-Like Homeobox 1
CY-2	Cyanine Dye 2
D2R	Dopamine Receptor 2
DA	Dopaminergic
DAPI	4',6-Diamidino-2-Phenylindole
DAT	Dopamine Transporter
DCP2	Decapping Enzyme 2

DDX41	Probable ATP-dependent RNA Helicase
DEXA	Dual-Energy X-ray Absorptiometry
DIC	Differential Interference Contrast
DM	Depleted Material
DMH	Dorsomedial Nuclei of Hypothalamus
DPBS	Dulbecco's Phosphate-Buffered Saline
DTT	Dithiothreitol
DUB	De-Ubiquitinating Enzyme
E	Embrionic Day
E.coli	Escherichia Coli
E1	Ubiquitin-Activating E1
E2	Ubiquitin-Conjugating E2
E3	Ubiquitin-Protein Ligase E3
Echo-MRI	Echo-Magnetic Resonance Imaging
EDTA	Ethylenediaminetetraacetic Acid
eEF2	Eukaryotic Elongation Factor 2
eIF4E	Eukaryotic Translation Initiation Factor 4E
ER	Endoplasmic Reticulum
ERAD	Endoplasmic Reticulum Associated Degradation
ES cells	Embryonic Stem Cells
F	Phenylalanine
FBS	Fetal Bovine Serum
Fc	Constant Region of IgG
FIH1	Factor Inhibiting HIF-1
FLIP	Fluorescence Loss in Photo Bleaching
Ft	Fused-Toe
FTO	Fat Mas and Obesity Associated
GABA	Gamma-Aminobutyric Acid
GAPDH	Glyceraldehyde-3-Phosphate Dehydrogenase
GFP	Green Fluorescent Protein
GIRK	G Protein–Coupled Inwardly-Rectifying Potassium Channel
GWAS	Genome-Wide Association Studies
HA	Hemagglutinin
HEK293	Human Embryonic Kidney 293 Cell Line
HEPA1-6	Hepatoma Cell Line
HFD	High Fat Diet
HIF	Hypoxia-Inducible Factor
HNRNPA1	Heterogeneous Nuclear Ribonucleoprotein A1
HRP	Horseradish Peroxidase
HSC 70	70 kDa Heat Shock Protein
HSG	Human Salivary Gland
I	Isoleucine
IB	Immunoblotting
IgG	Immunoglobulin G
IKK	Inhibitor of Kappa B Kinase
IL	Interleukin

ILPs	Insulin-Like Peptides
IM	Input Material
INFα	Type 1 Interferon
INS-1	Rat Insulinoma Cell Line-1
IP	Intraperitoneal
IPA	Ingenuity Pathway Analysis
IPGTT	Intraperitoneal Glucose Tolerance Test
IR	Insulin Receptor
IRF	Interferon Regulatory Factors
IRX3	Iroquois Homeobox 3
JNK	C-Jun N-terminal Kinase
K	Lysine
KO	Knock-Out
LacZ	β-Galactosidase Gene
LB	Luria Bertani
LC-MS/MS	Liquid Chromatography–Tandem Mass Spectrometry
LDS	Lithium Dodecyl Sulfate
LEPR	Long-Form Leptin Receptors
LH	Lateral Nuclei
LHA	Lateral Hypothalamic Area
LN	Liquid Nitrogen
LPL	Lipoprotein Lipase
LWB	Last Wash Buffer
LZ	Leucine Zipper
M	Molar
m^1A	1-Methyladenosine
m^1G	1-Methylguanine
m^3C	3-Methylcytosine
m^3T	3-Methylthymine
m^6A	6-Methyloadenosine
Mck	Muscle Creatine Kinase Gene
MCR	Melanocortin Receptors
MEFs	Mouse Embryonic Fibroblasts
Meox2	Mesenchyme Homeobox 2
METTL3	m^6A Methyltransferase
MRS	Methionyl-tRNA Synthetase
MS	Mass Spectroscopy
MSC	Multi-tRNA Synthetase Complex
mTOR	Mammalian Target of Rapamycin
mTORC	Mammalian Target of Rapamycin Complex
NEMO	NF-Kappa-B Essential Modulator
NES	Nuclear Export Signal
NF-κB	Nuclear Factor Kappa B
NLS	Nuclear Localisation Signal
NO	Nitric Oxide

NRY	Neuropeptide Y Receptor
NTD	N-Terminal Domain
NTS	Nucleus of the Solitary Tract
NUP	Nuclear Pore Complex Protein
Ob	Obese
OCT-1	Octamer-Binding Protein 1
p-bodies	Processing Bodies
PBS	Phosphate-Buffered Saline
PCR	Polymerase Chain Reaction
PET	Positron Emission Tomography
PFA	Paraformaldehyde
PGK	Human Phosphoglycerate Kinase 1
PHD	Prolyl Hydroxylase Domain-Containing Proteins
PI3K	Phosphatidylinositol 3-Kinase
PMSF	Phenylmethanesulfonylfluoride
POMC	Pro-Opiomelanocortin
PPI	Protein-Protein Interaction
Prx1	Paired-Related Homeobox 1 Gene
PTM	Post-Translational Modification
PVN	Paraventricular Nuclei
Q	Glutamine
qPCR	Quantitative PCR
QTL	Quantitative Trait Loci
R	Arginine
RANBP17	Ran-Binding Protein 17
RIPA	Radioimmunoprecipitation Assay Buffer
RMR	Resting Metabolism Rate
ROS	Reactive Oxygen Species
RPGRIP1L	Retinitis Pigmentosa GTPase Regulator-Interacting Protein 1-Like
S6K1	40S Sibosomal S6kinase-1
SDS-PAGE	Sodium Dodecyl Sulfate Polyacrylamide Gel Electrophoresis
SEM	Standard Error of the Mean
SFA	Subcutaneous Fat Area
Sim1	Single-Minded Homology 1Gene
SNP	Single Nucleotide Polymorphism
SNS	Sympathetic Nervous System
SPSS	Statistical Package for the Social Science
SRSF	Serine/Arginine-Rich Splicing Enhancer
SSA1	Sjögren Ayndrome Type A
ssDNA	Single Stranded DNA
ssRNA	Single Stranded RNA
STAT3	Signal Transducer and Activator of Transcription 3
T	Tetracycline
T2D	Type 2 Diabetes
TG	Triacylglycerols
TL	Transmitted Light

TNF	Tumor Necrosis Factor
TOR	Target of Rapamycin
TRIM	Tripartite Motif
TSS	Transcription Start Site
U	Uridine
UB	Ubiquitin
Ubc	Ubiquitin C Gene
UBE	Ubiquitin-Conjugating Enzyme
UBEH	Human Ubiquitin-Conjugating Enzyme
UCP1	Uncoupling Protein 1
UN	Uninduced
UPR	Unfolded Protein Response
UTR	Untranslated region
VCP	Valosin-Containing Protein
VFA	Visceral Fat Area
VLDPs	Very Low Density Lipoproteins
VMN	Ventromedial Nuclei of the Hypothalamus
VTA	Ventral Tegmental Area
WAT	White Adipose Tissue
WC	Waist Circumference
WHR	Waist-Hip Ratio
XPO	Exportin
XRN1	5'-3' Exoribonuclease 1
YFP	Yellow Fluorescent Protein
YTHDF2	YTH Domain-Containing Family Protein 2

1 Introduction

1.1 Obesity

There is currently an escalating global epidemic of obesity ('WHO | Obesity' 2015). In 2005, it was estimated that around 1.3 billion individuals (33.0% of the world's adult population) were overweight or obese and it was predicted that the number will reach 3.3 billion people (57.8% of the world's adult population) by 2030 (Kelly et al. 2008). Over 50% of people in WHO European Region are overweight or obese, and over 20% are obese ('WHO Europe Obesity' 2015). Currently, 65% of the global population are living in countries where more people die of obesity than starvation ('WHO | Obesity' 2015). This epidemic is not confined to adults - in 2012, nearly 7% of children under 5 years of age worldwide (around 44 millions) were overweight or obese ('WHO Global Database on Child Growth and Malnutrition' 2015).

Overweight and obese adults are most commonly classified according to body mass index (BMI), calculated by dividing the weight of the individual in kilograms by the square of individual's height in metres (kg/m^2) ('WHO | Obesity' 2015). Patients with a BMI ≥ 25 kg/m^2 are considered overweight while patients with a BMI ≥ 30 kg/m^2 are considered obese.

Importantly, obesity increases the risk of developing multiple diseases, including type 2 diabetes (T2D), osteoarthritis, hypertension, cardiovascular diseases and even cancer

(Guilbert 2003). Overweight and obese children are more likely to become obese adults, and excessive weight can lead to adverse metabolic effects on blood pressure, insulin levels, and the respiratory system, and cause psychological problems, disabilities, and even premature death ('World Health Statistics 2014').

1.1.1 Energy Homeostasis and Obesity

Obesity is a disorder of energy balance between energy intake, energy expenditure and energy stored (Hill, Wyatt, and Peters 2012). When energy intake exceeds energy expenditure, obesity is the result. (Trayhurn 2005; Hill, Wyatt, and Peters 2012; Jou 2014). The surplus of energy can occur either due to an excess of food intake (especially energy-dense foods with high fat and sugar content) or a lack of physical activity ('WHO | Obesity' 2015). The positive energy deposits are stored mostly as triacylglycerol in white adipose tissue (WAT) (Hill and Commerford 1996).

Under most circumstances, energy homeostasis in the human body is maintained in balance (Hall 2010, chap. 71). The balance is achieved by a complex physiological system that involves feedback loops of afferent and efferent signals that inform about the energy stored and energy needed or spent. The signals are exchanged between the peripheral tissues (liver, pancreas, adipose tissue, muscle, and gut) and central nervous system (CNS). (Sandoval, Cota, and Seeley 2008; Hill, Wyatt, and Peters 2012). The components of the energy balance system act upon changes in each other to neutralise effects of short energy excess or deficiency, thus preventing swings of body weight from day to day. Also, due to all the connections between the components of the energy balance system, obesity cannot be

reduced by focusing only on one site of the energy balance equation (e. g. only on reducing energy intake, or only on increasing energy expenditure) (Hill, Wyatt, and Peters 2012).

1.1.2 Nutrient Sensing and Regulation of Cellular Metabolism

At the cellular level, metabolic pathways are regulated by sensing of extracellular and intracellular nutrients as well as their metabolites (Krejčí 2012). While AMP-activated protein kinase (AMPK) modulates cellular metabolism by sensing the cellular energy levels, other pathways have evolved to monitor the cellular nutrients and metabolites levels (Yuan, Xiong, and Guan 2013). Amino acid sensing is crucial for cell growth and synthesis of new protein, but also for synthesis of glucose, nucleic acid and ATP.

At the core of the cellular nutrient sensing and control of the cell growth is serine/threonine kinase target of rapamycin (TOR) (Hietakangas and Cohen 2009). Mammalian TOR (mTOR) is a member of two distinctive protein complexes mTORC1 and mTORC2, both include other specific binding partners, Raptor and Rictor, respectively. mTORC1 senses intracellular amino acid availability at the lysosome level and plays a crucial role in the modulation of the protein synthesis through regulation of the translation initiation and elongation (Hietakangas and Cohen 2009).

When amino acids are opulent, mTORC1 stimulates protein synthesis through phosphorylation of eukaryotic translation initiation factor 4E (eIF4E)-binding protein 1 (4E-BP1). This results in the dissociation of 4E-BP1 form eIF4E, and recruitment of translation initiation factor eIF4G to the 5′ cap of a specific mRNA (Ma and Blenis 2009).

Additionally, mTORC1 promotes elongation of protein synthesis through 40S ribosomal S6kinase-1 (S6K1) mediated indirect regulation of eukaryotic elongation factor 2 (eEF2) (Hay and Sonenberg 2004).

1.1.3 Nutritional Excess, Cellular Stress and Inflammation

Normal patterns of the metabolic pathways and the cell functions are diet and nutrient dependent, thus prolonged excess of nutrition and insulin/growth factor in some cells may result in metabolic abnormality and cellular stress (Wellen and Thompson 2010; Hotamisligil 2006).

Nutrient excess can cause endoplasmic reticulum (ER) stress (Wellen and Thompson 2010; Hamanaka and Chandel 2010). The endoplasmic reticulum is a subcellular network of interconnected membranes where protein translation, folding, maturation, storage as well as selection of misfolded and unfolded protein for proteasomal degradation takes place (Alberts et al. 2002, chap. 12). ER stress due to nutrient excess activates the unfolded protein response (UPR) which results in attenuation of protein translation, up-regulation of chaperone protein production and degradation of misfolded proteins, as well as cell cycle arrest (Hamanaka and Chandel 2010; Bernales, Papa, and Walter 2006).

Excess of cellular nutrients and their metabolites also results in abnormally high levels of reactive oxygen species (ROS) produced by mitochondria through the electron transport system. Pathologically high levels of ROS can lead to damage to DNA and DNA repair enzymes, activation of hypoxia-inducible factor (HIF), promotion of growth signalling, and

eventually to damage to cellular components, cancer development and cell death (Veal, Day, and Morgan 2007; Trachootham, Alexandre, and Huang 2009; Hamanaka and Chandel 2010; Wellen and Thompson 2010). Moreover, high levels of ROS result in stimulation of inflammatory pathways through activation of NF-kB, inhibitor of kappa B kinase (IKK) and c-Jun N-terminal kinase (JNK) (Sen and Packer 1996; Kamata et al. 2005; Gloire, Legrand-Poels, and Piette 2006). In fact, a chronic inflammatory response is now recognised as a feature of the metabolic disorders caused by nutrition excess including obesity and T2D (Hotamisligil 2006; Wellen and Hotamisligil 2005).

1.2 Genetics and Obesity

1.2.1 Adoption and Twin Studies

Adoption and twin studies have provided convincing evidence that obesity and being overweight are heritable (Clement and Sorensen 2007, 19–27).

In 1986 Stunkard et al. reported the results of a study of human fatness in 540 adult Danish adoptees, including information about their biologic and adoptive parents (A. J. Stunkard et al. 1986). There was a strong relationship between both the BMI and body weight of adopted children and their biological parents, while no relationship was found with their foster parents. The authors concluded that the body weight of adopted children was determined by genes, not by environment. Similarly, the BMI of monozygotic twins was nearly the same, regardless of whether they were raised together (intrapair correlation coefficient of BMI was 0.74 and 0.66 for men and women respectively) or apart (intrapair

correlation coefficient of BMI was 0.70 and 0.66 for men and women respectively) (Stunkard et al. 1990). Moreover, long-term overfeeding of 12 pairs of identical male twins led to similar effects on body weight, fat mass and fat mass distribution in each twin. This further suggested that genetic factors are important in the regulation of energy balance (Bouchard et al. 1990). Numerous subsequent twin and adoption studies have been performed and recently all the data were grouped, reanalysed and published in a number of reviews (Silventoinen et al. 2010; Nan et al. 2012). The results clearly show that genetic factors have a major impact on BMI of subjects regardless the age, while environmental factors play substantial role in mid-childhood, but their importance weakens with age.

1.2.2 Monogenic Obesity

Obesity can result from a mutation in a single gene (monogenic obesity). This was demonstrated first using *ob/ob* mice, which are characterised by extreme obesity, reduced energy expenditure, hyperphagia, hyperinsulinemia and glucose intolerance (Ingalls, Dickie, and Snell 1950). This phenotype was later discovered to be caused by a mutation (at position 105) in the gene coding leptin (Zhang et al. 1994), a satiety hormone secreted by adipocytes (Lancha, Frühbeck, and Gómez-Ambrosi 2012). The mutation creates an early stop codon and leads to truncation of the protein and undetectable levels of leptin. Several human patients with leptin mutations have also been identified (Strobel et al. 1998; Montague et al. 1997). Mutations in the melanocortin 4 receptor gene (MC4R), however account for the most common forms of monogenic obesity in humans (Farooqi et al. 2003). Over 130 mutations have been identified in *MC4R:* these include both heterozygous and homozygous mutations, which result in partial or total lack of receptor activity (Vaisse et al. 2000; Hinney et al. 2006; Fan and Tao 2009). They are found in approximately 1% of obese adults and in 2–6% of obese children (Vrbikova and Hainer 2009). Homozygous

disruption of *Mc4r* gene in mice led to decrease in energy expenditure, hyperphagia and obesity, while heterozygous disruption led to intermediate effects (Huszar et al. 1997). Restoration of MC4R in specifically in *Sim1* expressing neurons reduced food intake and body weight, although the energy expenditure remained low (Balthasar et al. 2005). Monogenic obesity however is extremely infrequent, and thus cannot explain the global increase in obesity prevalence.

1.2.3 Polygenic Obesity

In most individuals, multiple genes contribute to obesity. These have little effect separately but cooperatively can cause polygenic obesity (Hinney, Vogel, and Hebebrand 2010). The individual effect on body weight of each risk alleles can be as little as 100g, and mean effect size on BMI around 0.03-0.5 kg/m^2 (Hinney, Vogel, and Hebebrand 2010). Thus, polygenic risk factors can only be studied using large sample sizes and sophisticated statistical analyses. Some previously known monogenic obesity genes, such as leptin, have also been found to contain sequence variants predisposing to polygenic obesity (Li et al. 1999).

1.2.4 Genome-Wide Association Studies (GWAS)

Several gene variants predisposing to obesity have been identified by the candidate gene analysis based on the prior knowledge of disease phenotype, pharmacological findings, or animal models (Rankinen et al. 2006). However, most progress in the search for genetic variants associated with obesity has been made by genome-wide association studies (GWAS). These involve high-throughput genotyping of genetic variations in the individual nucleotides (single nucleotide polymorphism, SNP) within the entire DNA material

(genome) of tens of thousands of individuals (Manolio 2010). In most common experimental set-up, a particular SNP (and its location region within the genome) is considered to be associated with a specific disease if the frequency of the SNP occurrence is greater in a group of people with that disease than in a group of controls. The validation of the candidate SNP and its location must be carried out by replication of the study in multiple populations and by meta-analysis (Manolio 2010). Commonly, associations with $P < 5.0 \times 10^{-8}$ are considered valid (Wang, Jia, and Hu 2014).

1.2.5 GWAS and Obesity

Four large GWAS meta-analyses, each larger than the previous one, identified (as of August 2014) more than 73 obesity-associated loci with $p < 5.0 \times 10^{-8}$, of which 59 were in European and 14 in non-European populations (Wang, Jia, and Hu 2014). Among the identified loci, 42 were BMI traits, 3 were body fat percentage traits, 26 were waist circumference (WC) or waist-hip ratio (WHR) traits, and 2 were for subcutaneous fat area (SFA) and visceral fat area (VFA) traits. Most of the loci identified and the original publications associated with specific loci are presented in **Figure 1**.

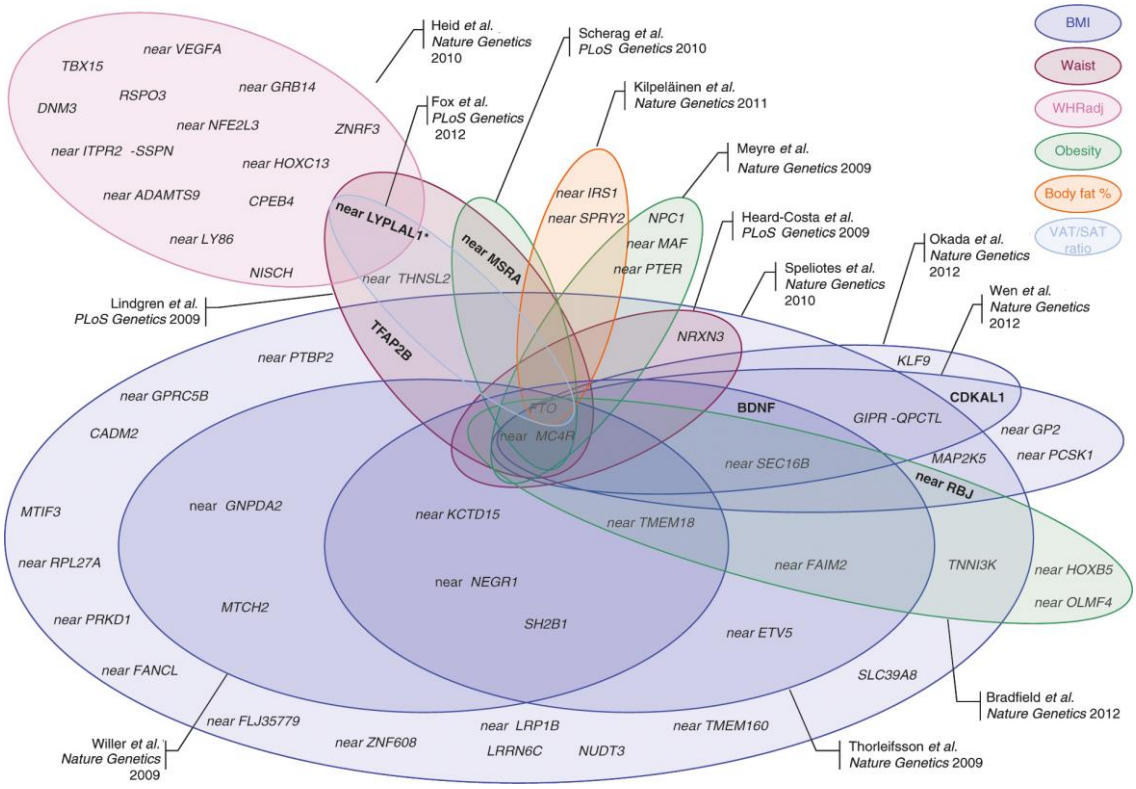

Figure 1. Obesity-susceptibility loci discovered through GWAS. Each Venn diagram represents the loci from one paper, (Willer et al. 2009; Thorleifsson et al. 2009; Speliotes et al. 2010; Kilpeläinen, Zillikens, et al. 2011; Lindgren et al. 2009; Heard-Costa et al. 2009; Scherag et al. 2010; Heid et al. 2010; Fox et al. 2012; Hinney et al. 2007; Okada et al. 2012; Wen et al. 2012; Bradfield et al. 2012) except for papers that discovered only one locus i.e. FTO (Frayling et al. 2007; Scuteri et al. 2007; Hinney et al. 2007) and the near-MC4R loci (Loos et al. 2008; Chambers et al. 2008) for which no Venn diagram was drawn. Loci discovered after 2012 are not depicted. Each trait category is coloured with according to the legend. Taken from (Lu and Loos 2013).

1.2.6 GWAS and *FTO* Gene

The first obesity related loci identified by GWAS was in the first intron of the fat mass and obesity associated (*FTO*) gene on chromosome 16 (Frayling et al. 2007; Scuteri et al. 2007). Frayling et al. compared autosomal SNPs in 1924 U.K. type 2 diabetes (T2D) patients with 2938 U.K. healthy controls, and identified a cluster of SNPs in intron one of *FTO* (Frayling et al. 2007). The initial association of the at-risk SNP rs9939609 (A allele variant) and T2D was abolished after adjusting for BMI. Further analysis confirmed the linkage of this rs9939609 A allele with increased BMI. It manifests from the age of 7 onwards, with each

copy of the at-risk allele increasing BMI by ~0.4 kg/m^2, and increasing the odds of developing obesity by 1.2 fold (Frayling et al. 2007). Moreover, the increased body weight resulted specifically from increased fat mass. A copy of the rs9939609 A allele is found in ~ 63 % of adult European population, while those carrying two copies (homozygous) account for 16 % (Dina et al. 2007; Frayling et al. 2007). Homozygous individuals weight on average 3 kg more and have a 1.67 higher risk of developing obesity than individuals without the risk allele (Frayling et al. 2007). Even though it may seem that the effect of *FTO* locus is small, and it accounts only for 0.34 % of the inter-individual variation in BMI (Speliotes et al. 2010), it still has the largest known effect size on BMI from all known SNPs ever identified **Figure 2** (Lu and Loos 2013).

Since its discovery, the association of *FTO* with obesity has been widely replicated in multiple GWA studies and populations ('Catalog of Published Genome-Wide Association Studies' 2015). Numerous SNPs related to different trait categories have been identified (**Figure 2**, **Table 1**). These are mainly associated with higher BMI, fat mass or lean mass, but variations in whole body fat distribution as determined by the magnetic resonance imaging have also been identified (Haupt et al. 2008). Interestingly, the association of the *FTO* risk allele with obesity has been associated with increased energy intake in some studies [as reported for the rs9939609 SNP (Cecil et al. 2008; Speakman 2010; Timpson et al. 2008; Tanofsky-Kraff et al. 2009), but not in others (Hakanen et al. 2009; Do et al. 2008; Tanofsky-Kraff et al. 2009)]. No association between *FTO* risk alleles and energy expenditure or physical activity has been found (Jonsson et al. 2009; Berentzen et al. 2008), although physical activity was reported to reduce the effects of *FTO* SNP polymorphisms (Kilpeläinen et al. 2011; Rampersaud et al. 2008; Andreasen et al. 2008).

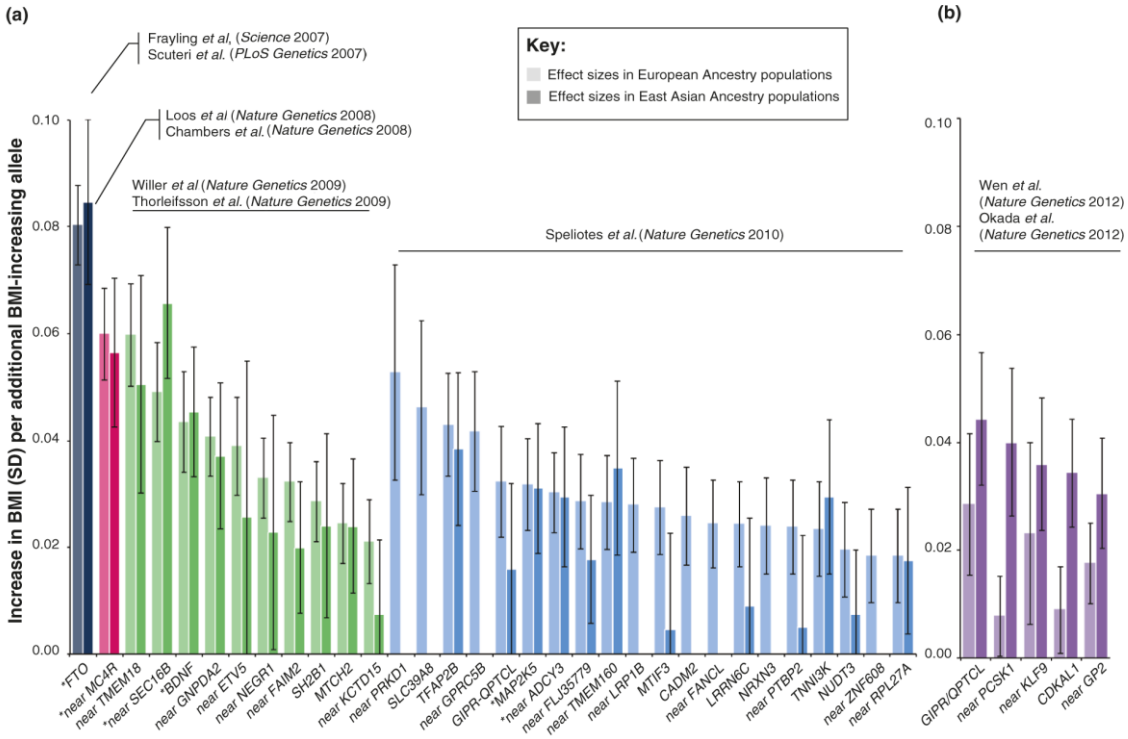

Figure 2. Effect sizes for the 32 BMI-associated SNPs identified in European and Asian ancestry populations. Effect sizes for **(a)** the 32 BMI-associated SNPs identified in European ancestry populations and **(b)** the five BMI-associated SNPs identified in East Asian ancestry populations. The lighter shaded bars represent the effect sizes [and 95% confidence interval (CI)] in European ancestry populations (Speliotes et al. 2010) [in both (a) and (b)], the darker shaded bars represent the effect sizes (and 95% CI) in East Asian ancestry populations (Okada et al. 2012; Wen et al. 2012). Data were obtained and adapted from (Wen et al. 2012). Asterisks indicate SNPs that reached genome-wide significance in GWAS meta-analyses of East Asian ancestry populations (Wen et al. 2012). SD, standard deviation. Taken from (Lu and Loos 2013).

FTO risk alleles have also been associated with T2D (**Table 1**, (Zeggini et al. 2007; Scott et al. 2007; Zeggini et al. 2008), cardiovascular disease and myocardial infarction (Lappalainen et al. 2011), polycystic ovary syndrome (Attaoua et al. 2008; Barber et al. 2008; Kowalska et al. 2009; Yan et al. 2009), osteoarthritis (Loughlin et al. 2012), cognitive decline, an increased risk of Alzheimers Disease and reduced brain volume in the elderly (Ho et al. 2010; Reitz et al. 2012; Bressler et al. 2013). Associations between *FTO* genotype and melanoma, breast cancer (Gaudet et al. 2010; Kaklamani et al. 2011; Iles et al. 2013) and even increased all-cause mortality (Zimmermann et al. 2009) have also been reported.

The majority of obesity related SNPs were identified in intron one of FTO, although a few were found in intron two (Zhang et al. 2010; Hassanein et al. 2010; Bollepalli et al. 2010), intron three (Tönjes et al. 2010) and intron eight (Adeyemo et al. 2010). The location of the cluster of SNPs in the first intron of FTO at chr16q12.2, in proximity to the start of FTO transcription, may suggest that they serve a regulatory role, possibly influencing FTO expression (Wang, Jia, and Hu 2014).

Table 1. *FTO* GWAS. Studies which identified SNP risk alleles in *FTO* gene from the oldest to the newest. Only studies which assessed a minimum of 100,000 SNPs are included. Based on the "FTO" search results from the ('Catalog of Published Genome-Wide Association Studies' 2015).

Reference	Date	Disease/Trait	Population	Strongest SNP-Risk Allele	p-Value	Intron
(Frayling et al. 2007)	12/04/2007	Body mass index	European ancestry	rs9939609-A	2E-20	Intron 1
(Scott et al. 2007)	26/04/2007	Type 2 diabetes	European ancestry	rs8050136-A	1E-12	Intron 1
(Zeggini et al. 2007)	26/04/2007	Type 2 diabetes	European ancestry	rs8050136-A	7E-14	Intron 1
(Burton et al. 2007)	07/06/2007	Type 2 diabetes	European ancestry	rs9939609-A	2E-7	Intron 1
(Scuteri et al. 2007)	20/07/2007	Obesity-related traits	Sardinian ancestry	rs9930506-A	9E-7	Intron 1
(Scuteri et al. 2007)	20/07/2007	Obesity-related traits	Sardinian ancestry	rs9930506-A	3E-8	Intron 1
(Scuteri et al. 2007)	20/07/2007	Obesity-related traits	Sardinian ancestry	rs9930506-A	9E-7	Intron 1
(Hinney et al. 2007)	26/12/2007	Obesity (early onset extreme)	European ancestry	rs1121980-T	1E-7	Intron 1
(Zeggini et al. 2008)	30/03/2008	Type 2 diabetes	European ancestry	rs8050136-A	7E-6	Intron 1
(Loos et al. 2008)	04/05/2008	Body mass index	European ancestry	rs1121980-?	4E-8	Intron 1
(Timpson et al. 2008)	03/12/2008	Type 2 diabetes	European ancestry	rs8050136-?	2E-17	Intron 1
(Thorleifsson et al. 2009)	14/12/2008	Body mass index	European, African American ancestry	rs6499640-A	4E-13	Intron 1
(Thorleifsson et al. 2009)	14/12/2008	Body mass index	European, African American ancestry	rs8050136-A	1E-47	Intron 1
(Thorleifsson et al. 2009)	14/12/2008	Weight	European, African American ancestry	rs6499640-A	6E-14	Intron 1
(Thorleifsson et al. 2009)	14/12/2008	Weight	European, African American ancestry	rs8050136-A	5E-36	Intron 1
(Willer et al. 2009)	14/12/2008	Body mass index	European ancestry	rs9939609-A	4E-51	Intron 1
(Meyre et al. 2009)	18/01/2009	Obesity	European ancestry	rs1421085-C	1E-28	Intron 1

Reference	Date	Disease/Trait	Population	Strongest SNP-Risk Allele	p-Value	Intron
(Cho et al. 2009)	26/04/2009	Biomedical quantitative traits	Korean ancestry	rs9939609-A	2E-7	Intron 1
(Cotsapas et al. 2009)	24/06/2009	Obesity (extreme)	European ancestry	rs9941349-T	6E-12	Intron 1
(Heard-Costa et al. 2009)	26/06/2009	Waist circumference	European ancestry	rs1558902-?	5E-19	Intron 1
(Scherag et al. 2010)	22/04/2010	Obesity (early onset extreme)	European ancestry	rs1558902-A	5E-19	Intron 1
(Voight et al. 2010)	27/06/2010	Type 2 diabetes	European ancestry	rs11642841-A	3E-8	Intron 1
(Speliotes et al. 2010)	10/10/2010	Body mass index	European ancestry	rs1558902-A	5E-120	Intron 1
(Wan et al. 2011)	29/10/2010	Body mass in chronic obstructive pulmonary disease	European ancestry	rs8050136-A	4E-8	Intron 1
(Elks et al. 2010)	21/11/2010	Menarche (age at onset)	European, Old Order Amish, Erasmus Rucphen ancestry	rs9939609-A	3E-8	Intron 1
(Dorajoo et al. 2012)	19/04/2011	Obesity	Chinese Malay, Asian Indian ancestry	rs1558902-T	1E-7	Intron 1
(Wang et al. 2011)	28/04/2011	Obesity	European ancestry	rs17817449-?	2E-12	Intron 1
(Kilpeläinen et al. 2011)	26/06/2011	Adiposity	European Indian Asian ancestry	rs8050136-C	3E-26	Intron 1
(Okada et al. 2012)	19/02/2012	Body mass index	Japanese ancestry	rs12149832-A	5E-22	Intron 1
(Kristiansson et al. 2012)	07/03/2012	Metabolic syndrome	European ancestry	rs9940128-A	2E-9	Intron 1
(Fox et al. 2012)	10/05/2012	Subcutaneous adipose tissue	European ancestry	rs9922619-T	6E-8	Intron 1
(Fox et al. 2012)	10/05/2012	Subcutaneous adipose tissue	European ancestry	rs1421084-A	3E-6	Intron 1
(Perry et al. 2012)	31/05/2012	Type 2 diabetes	European ancestry	rs9939609-A	1E-20	Intron 1
(Prescott et al. 2012)	04/06/2012	Sex hormone-binding globulin levels	European ancestry	rs12596210-C	9E-6	Intron 8

Reference	Date	Disease/Trait	Population	Strongest SNP-Risk Allele	p-Value	Intron
(Loughlin et al. 2012)	02/07/2012	Osteoarthritis	European ancestry	rs8044769-C	4E-6	Intron 1
(Yang et al. 2012)	12/09/2012	Body mass index	European ancestry	rs7202116-G	2E-10	Intron 1
(Tabassum et al. 2013, 21)	03/12/2012	Type 2 diabetes	Indo-European ancestry	rs8050136-A	6E-6	Intron 1
(Iles et al. 2013)	03/03/2013	Melanoma	European ancestry	rs16953002-A	4E-12	Intron 8
(Berndt et al. 2013)	07/04/2013	Body mass index	European ancestry	rs11075990-G	2E-51	Intron 1
(Berndt et al. 2013)	07/04/2013	Obesity	European ancestry	rs8043757-T	5E-110	Intron 1
(Berndt et al. 2013)	07/04/2013	Obesity	European ancestry	rs7185735-G	1E-79	Intron 1
(Berndt et al. 2013)	07/04/2013	Obesity	European ancestry	rs1421085-C	6E-39	Intron 1
(Berndt et al. 2013)	07/04/2013	Obesity	European ancestry	rs1558902-A	2E-81	Intron 1
(Wheeler et al. 2013)	07/04/2013	Obesity (early onset extreme)	European ancestry	rs1421085-C	3E-28	Intron 1
(Monda et al. 2013)	14/04/2013	Body mass index	African American, Nigerian ancestry	rs17817964-T	1E-10	Intron 1
(Tanaka et al. 2013)	01/05/2013	Dietary macronutrient intake	European ancestry	rs1421085-C	1E-9	Intron 1
(Graff et al. 2013)	12/05/2013	Body mass index	European ancestry	rs9940128-A	4E-23	Intron 1
(Willer et al. 2013)	06/10/2013	HDL cholesterol	European ancestry	rs1121980-A	7E-9	Intron 1
(Willer et al. 2013)	06/10/2013	Triglycerides	European ancestry	rs1121980-A	3E-8	Intron 1
(Pei et al. 2014)	08/10/2013	Body mass index	European, African American, Hispanic, Han Chinese ancestry	rs62033400-G	2E-14	Intron 1
(Namjou et al. 2013)	03/12/2013	Body mass index	European ancestry	rs8050136-A	1E-7	Intron 1
(Mahajan et al. 2014)	09/02/2014	Type 2 diabetes	European East Asian, South Asian,	rs9936385-C	1E-12	Intron 1

Reference	Date	Disease/Trait	Population	Strongest SNP-Risk Allele	p-Value	Intron
			Mexican ancestry			
(Wen et al. 2014)	26/05/2014	Body mass index	East Asian, South East ancestry	rs1558902-A	7E-27	Intron 1

1.3 Fat Mass and Obesity Associated Gene and Protein

The genome wide association studies between *FTO* SNPs and phenotypes, although widely replicated, were unable to provide insight into the cause of the observed phenotypic variations. When the first SNP was discovered by Frayling, *FTO* was described as "a gene of unknown function in an unknown pathway" (Frayling et al. 2007). Moreover, little was known about the *FTO* gene product and none of the SNPs reported were expected to result in change in the FTO function.

1.3.1 *FTO* knowledge before GWAS

The *Fto* gene was first identified when studying the fused-toe (Ft) mouse (van der Hoeven et al. 1994), which as a result of transgenic insertional mutagenesis, lacked 1.6 Mb of genomic DNA on chromosome 8 (Peters, Ausmeier, and Rüther 1999; Thomas Peters et al. 2002). The missing DNA included the Iroquois B cluster (*Irx3*, *Irx5*, and *Irx6*) and three unknown genes called *Ft1* (now called *Aktip*), *Ftm* (now called *Rpgrip1l)* and *Fto*. Mice heterozygous for the Ft deletion survived, but displayed syndactyly of the forelimbs and thymic hyperplasia, while homozygous *Ft/Ft* embryos died during gestation exhibiting severe malformations of craniofacial structures (van der Hoeven et al. 1994). No body weight or adiposity phenotype has been reported in these mice.

Positional cloning of *Fto* and PCR revealed that full-length cDNA encoded a putative 58-kDa protein with no homology to any previously known proteins or motifs (Peters, Ausmeier, and Rüther 1999). The DNA sequence encoding FTO spans more than 400 kb and contains

9 exons and 8 introns. In mice the gene is located on chromosome 8 and in humans on chromosome 16 (**Figure 3**) ('Ensembl Genome Browser' 2015). In both human and mouse genomes, the transcriptional start of the gene *RPGRIP1L* is ~3.4 kb upstream of *FTO*, followed by *AKTIP*, *RBL2*, and *CHD9*. Downstream of *FTO,* the sequences of *IRX3*, *IRX5* and *IRX6* are found. Interestingly, the transcriptional sites of *Fto* and *Rpgrip1l* are co-regulated (although *Rpgrip1l* codes for the opposite DNA strand), and in human genome are in close proximity to SNPs allele strongly associated with adiposity (Stratigopoulos et al. 2008). Thus it was suggested that the SNPs are associated with both *Fto* and *Rpgrip1l* expression, or even only with *Rpgrip1l* expression.

There is limited evidence suggesting a role of *Rpgrip1l* in the regulation of body weight phenotype, but numerous studies support role for this gene in the development of ciliopathies and Joubert Syndrome type B (Delous et al. 2007; Chen et al. 2015). Expression of *Rpgrip1l* in the hypothalamus, a brain region involved in the regulation of food intake and energy homeostasis, is ~6 fold lower than that of *Fto* (Stratigopoulos et al. 2008). Moreover, in mice with reduced body weight, adipose mass and adipocyte size due to *Fto* knock-out, *Rpgrip1l* expression was unchanged, suggesting that the body phenotype was not associated with regulation of *Rpgrip1l* (Fischer et al. 2009). No change in *Rpgrip1l* expression was also reported in *Fto* overexpression mouse tissue. Homozygous mice lacking *Rpgrip1l* died around birth, and showed microphthalmia, preaxial polydactyly in fore and hind limbs, craniofacial deformations and disturbed left-right asymmetry, although they did not have fused toes like Ft mice (Vierkotten et al. 2007). This suggests that *Rpgrip1l* may not be as important for obesity as FTO.

Recently, Smemo et al. proposed a new role for regions marked by the SNPs in the first intron of *FTO* suggesting that they act as long-range enhancers of the *IRX3* promoter,

regulating expression of *IRX3 rather than FTO* (Smemo et al. 2014). Mice in which *Irx3* was globally knocked out exhibited up to 30% loss of body weight, mostly due to a decrease in fat mass, and increase in metabolic rate and browning of WAT. However, these data present some uncertainties. First, the obesity-associated SNPs were shown to have multiple interactions across the region including both *Fto* and *Irx3* genes. Second, interactions between the obesity-associated SNPs and *Fto* promoter were identified in mouse embryos. The lack of these interactions in adult mouse brain as well as presence of numerous long-range interactions with a promoter of *Irx3* was presented in support of the group's hypothesis. However, Smemo's phenotyping data shows that loss of *Irx3* had no effect on embryonic lethality, which was observed in mice lacking *Fto* (Fischer et al. 2009). Perhaps if *Fto* gene expression plays a role mostly during embryonic development, the lack of interaction between the SNPs and the *Fto* promotor in adult mice is not surprising. Lastly, expression quantitative trait locus (QTL) analysis suggested a link between SNPs and *Irx3* expression (but not *Fto* expression) in human cerebellum, which is not recognised as a brain region involved in food intake and energy homeostasis.

Figure 3. Position of *FTO* gene and surrounding sequences in the mouse and human genome. Mb, Megabase; p, petite arm; q, long arm. Image adapted from ('Ensembl Genome Browser' 2015).

1.3.2 FTO Expression

FTO is ubiquitously expressed throughout embryonic development (detected from E8.5) and in both adult mice and humans (Peters, Ausmeier, and Rüther 1999; Gerken et al. 2007; 'EMBL-EBI Expression Atlast' 2014). In the brain, *FTO* mRNA levels are particularly high within the hippocampus and hypothalamic nuclei (ARC, VMN, and PVN), regions critical for regulating energy balance (Gerken et al. 2007). The hypothalamic expression of FTO suggests a potential role in the control of food intake and whole body metabolism. However, nutritional regulation of brain *Fto*/FTO expression in rodents is somewhat controversial as some authors have reported that fasting lead to up-regulation (Fredriksson et al. 2008; Olszewski et al. 2009; Vujovic et al. 2013), whereas others have shown down-regulation

(Gerken et al. 2007; Stratigopoulos et al. 2008; Wang et al. 2011) or no effect (Gao et al. 2010; McTaggart et al. 2011; Olszewski et al. 2011). These contrasting findings may result from differences in the fasting sensitivity of rodents and the range of fasting durations used in these studies. Expression of *Fto* increased in the arcuate nucleus of the hypothalamus (ARC) (a region involved in the regulation of food intake and energy homeostasis) of rats after 10 weeks exposure to a high fat diet (Tung et al. 2010), whereas cold exposure reduced hypothalamic *Fto* in mice (Stratigopoulos et al. 2008). Taken together, these findings suggest a role for FTO in energy homeostasis, by an unknown mechanism.

Transcription of *FTO* (as well as *RPGRIP1L*) in human fibroblasts was found to be regulated by the DNA binding protein Cut-like homeobox 1 (CUTL1), and siRNA knockdown of *CUTL1* led to a 90% decrease in *FTO* levels (and 65% in *RPGRIP1L* levels) (Stratigopoulos et al. 2008). Interestingly, the CUTL1 binding site was found to be associated with SNP rs8050136 (linked to variations in body weight), and CUTL1 had higher preference for the risk A-variant, than C-variant. Moreover, Berulava and Horsthemke showed that in nuclear RNA isolated from the blood of individuals heterozygous for SNP rs9939609, the expression levels of the allelic *FTO* transcripts containing the A (at-risk) allele were more abundant than transcripts containing the T allele (Berulava and Horsthemke 2010). Additionally, Karra and colleagues reported that in peripheral blood samples *FTO* transcript levels were higher in rs9939609 AA homozygous subjects than in TT subjects, suggesting that high levels of *FTO* may predispose to obesity (Karra et al. 2013). Analysis of *FTO* mRNA levels in subcutaneous adipose tissue in rs9939609 AA and TT homozygous subjects showed no difference between genotype groups, however adipose tissue levels of *FTO* mRNA were higher in obese than lean subjects (Wåhlén, Sjölin, and Hoffstedt 2008). In skeletal muscle, *FTO* mRNA levels were unaffected by the genotype, although positively associated with glucose oxidation rates, and expression of genes involved in oxidative phosphorylation.

They were negatively associated to fat (Grunnet et al. 2009). Recently, higher *FTO* mRNA expression levels were found in peripheral blood samples of patients with T2D (Shen et al. 2015).

At the cellular level, FTO and *Fto* mRNA expression in mouse and human cells were shown to be down-regulated by glucose and essential amino acid deprivation (Cheung et al. 2012). An increased rate of mRNA degradation suggested a mechanism at the transcriptional level. Moreover, conditional expression of *Fto* in INS-1 rat cells revealed that FTO is rapidly degraded (4-6 hours) in a ubiquitin and proteasome dependent manner (Russell and Morgan 2011).

Additionally, Wang at el reported that in cells isolated from mouse arcuate nucleus of the hypothalamus (ARC), FTO expression was down-regulated by leptin via signal transducer and activator of transcription 3 (STAT3) pathway (Wang et al. 2011). However, in neonatal rat cardiomyocytes FTO expression was up-regulated by leptin via activation of JAK2/STAT3 (Gan et al. 2013). Expression of the CUTL1 transcriptional factor was also up-regulated, suggesting its regulatory control.

1.3.3 *FTO* Sequence Homology and Catalytic Activity

Bioinformatics analysis revealed that homologs of *FTO* are present within vertebrates (from fish to mammals) and marine algae (from unicellular photosynthetic picoplankton to multicellular seaweed), but absent in invertebrates, fungi, and other green plants (Fredriksson et al. 2008; Robbens et al. 2008; Sanchez-Pulido and Andrade-Navarro 2007;

Gerken et al. 2007). Sequence analysis further revealed that FTO contains features of the Fe (II) and 2-oxoglutarate (2OG) oxygenases, and shows highest homology to the *Escherichia coli* (*E. coli*) enzyme AlkB, and its human homologs (ALKBHs) (Sanchez-Pulido and Andrade-Navarro 2007; Gerken et al. 2007). *In vitro* studies confirmed that FTO can catalyse the turnover of [1-^{14}C]-2OG into [^{14}C]-carbon dioxide when stimulated by ascorbate and $FeSO_4$ (Gerken et al. 2007).

The 2-Oxoglutarate (2OG) dependent oxygenases are ubiquitously expressed. They are highly conserved enzymes that employ non-heme Fe (II) as a cofactor and 2-oxoglutarate (2OG) and oxygen as co-substrates to catalyse oxidation of diverse substrates. They release succinate and carbon dioxide as by-products (Schofield and Zhang 1999; Hewitson et al. 2005; Rose et al. 2011). There are more than sixty predicted human 2OG oxygenases, which catalyse a diverse range of biochemically and physiologically important reactions, including hydroxylation and demethylation of protein and nucleic acids (Loenarz and Schofield 2011).

The AlkB family of Fe (II) and 2OG oxygenases is a family of enzymes involved in oxidative nucleic acid demethylation (Lu et al. 2014). Bacterial AlkB was the first family member identified and is capable of carrying out oxidative demethylation of N1-methyladenosine (m^1A) and N3-methylcytosine (m^3C) in bacterial nucleic acids in order to protect them from alkylation-induced toxicity (Kataoka and Sekiguchi 1985; Kondo et al. 1986; Chen, Carroll, and Samson 1994) and reverse DNA damage (Falnes, Johansen, and Seeberg 2002; Trewick et al. 2002). AlkB is highly conserved and to date 9 human homologues have been identified (ALKBH 1-8 and FTO). The known functions and substrates of AlkB family members are included in **Table 2**.

Table 2. The functions of the FTO homologues. m^1A, 1-methyladenine; m^3C, 3-methylcytosine; m^1G, 1-methylguanine; m^3T, 3-methylthymine; ethanoA, 1,N6-ethenoadenine; ethenoC 3,N4-ethenocytosine; mcm^5U, 5-methoxycarbonylmethyluridine; (S)-$mchm^5U$, (S)-6-methyoxycarbonylhydroxymethyluridine.

Family Member	Activity	Biomolecule Substrate	Mouse model	Reference
E.coli AlkB	Demethylation of m^1A, m^3C, m^3T m^1G with lower activity, dealkylation of ethanoA, ethenoC	dsDNA, ssDNA, RNA,	Not applicable	(Trewick et al. 2002; Falnes, Johansen, and Seeberg 2002; Ougland et al. 2004; Delaney and Essigmann 2004; Delaney et al. 2005; Frick et al. 2007)
ALKBH1	Demethylation of m^3C (low activity), DNA lyase activity at abasic sites (without the need for Fe(II) and 2OG), histone demethylation	ssDNA/RNA (mitochondrial), histone H2A	KO: delayed fetal growth and low birth weight. Also sex-ratio distortion, reduced survival, incompletely penetrant eye, neural tube, skeleton and craniofacial defects and spermatogenic defects	(Westbye et al. 2008; Ougland et al. 2012; Mueller, Meek, and Hausinger 2010; Duncan et al. 2002; Nordstrand et al. 2010)
ALKBH2	Demethylation of m^1A, m^3C, dealkylation of ethanoA, ethenoC, DNA lyase activity	dsDNA	KO: normal phenotype, progressive accumulation of m^1A in their genomic DNA caused by impaired DNA repair	(Aas et al. 2003; Duncan et al. 2002; Ringvoll et al. 2008; Fu and Samson 2012; Calvo et al. 2012)
ALKBH3	Demethylation of m^1A, m^3C, DNA lyase activity	ssDNA, RNA,	KO: normal phenotype	(Ougland et al. 2004; Aas et al. 2003; Duncan et al. 2002; Calvo et al. 2012)
ALKBH4	Protein biding, demethylation of monomethylated site of actin	Proteins associated with chromatin and /or involved in transcription, actin	KO: lethality prior to weaning	(Li et al. 2013; Bjørnstad et al. 2012)
ALKBH5	Demethylation of m^6A	RNA	KO: males show reduces fertility	(Zheng et al. 2013)
ALKBH6	unknown function	Probably nucleic acids	-	(Kurowski et al. 2003)

ALKBH7	Protein binding, short chain fatty acid oxidation, programmed necrosis induced by alkylation and oxidation	unknown	KO: increased body weight and body fat	(Solberg et al. 2013; Fu, Jordan, and Samson 2013)
ALKBH8	Hypermodification of tRNA leading to biogenesis of mcm^5U and (S)-$mchm^5U$ at tRNA wobble positions	t-RNA	KO: normal phenotype	(van den Born et al. 2011; Songe-Møller et al. 2010; Y. Fu et al. 2010; D. Fu et al. 2010)

1.3.4 FTO Structure and Substrate Specificity

After classifying FTO as a Fe (II) and 2OG oxygenase, Gerken et al. screened a panel of substrates and found that FTO demethylated 1-methyladenine (m^1A), 3-methylcytosine (m^3C) and 3-methylthymine (m^3T) in ssDNA, with the preference for m^3T (Gerken et al. 2007). Succinate, formaldehyde, and carbon dioxide were produced as by-products. Activity towards m^3T in ssDNA was later confirmed by Jia et al. who also reported that of FTO demethylated 3-methyluracil (m^3U) in ssRNA, with even greater efficiency than m^3T in ssDNA (Jia et al. 2008). No detectable activity towards dsDNA or dsRNA was found. Importantly, the naturally existing mutation of Arg96His in human FTO resulted in loss of demethylase activity (Meyre et al. 2010).

Crystallography studies revealed crucial information about the structure of FTO and substrate specificity (**Figure 4**) (Han et al. 2010). The preference of FTO towards m^3U and m^3T over m^1A and m^3C was reported, suggesting RNA rather than DNA as a major substrate (Han et al. 2010). FTO has two well-defined domains; the N-terminal domain (NTD aa 32-326) and the C-terminal domain (CTD aa 327-498). The catalytic core is located in the NTD within a jelly roll motif composed of 4 double strand β-helix pairs (β5-β12) and displays high structural similarity to bacterial AlkB. However, an extra loop (L1) linking β5-β6 was identified, which was predicted to prevent the catalytic core from binding to the DNA duplex. This suggests an affinity for ssDNA and ssRNA, just as ALKBH1 and ALKBH3. The CTD consists mainly of α-helices, with α7, α8 and 10 forming a three helix-bundle and represents a new fold as no other structure shows significant homology. Extensive interaction of CTD with NTD is believed to be important for protein conformation stability and catalytic activity.

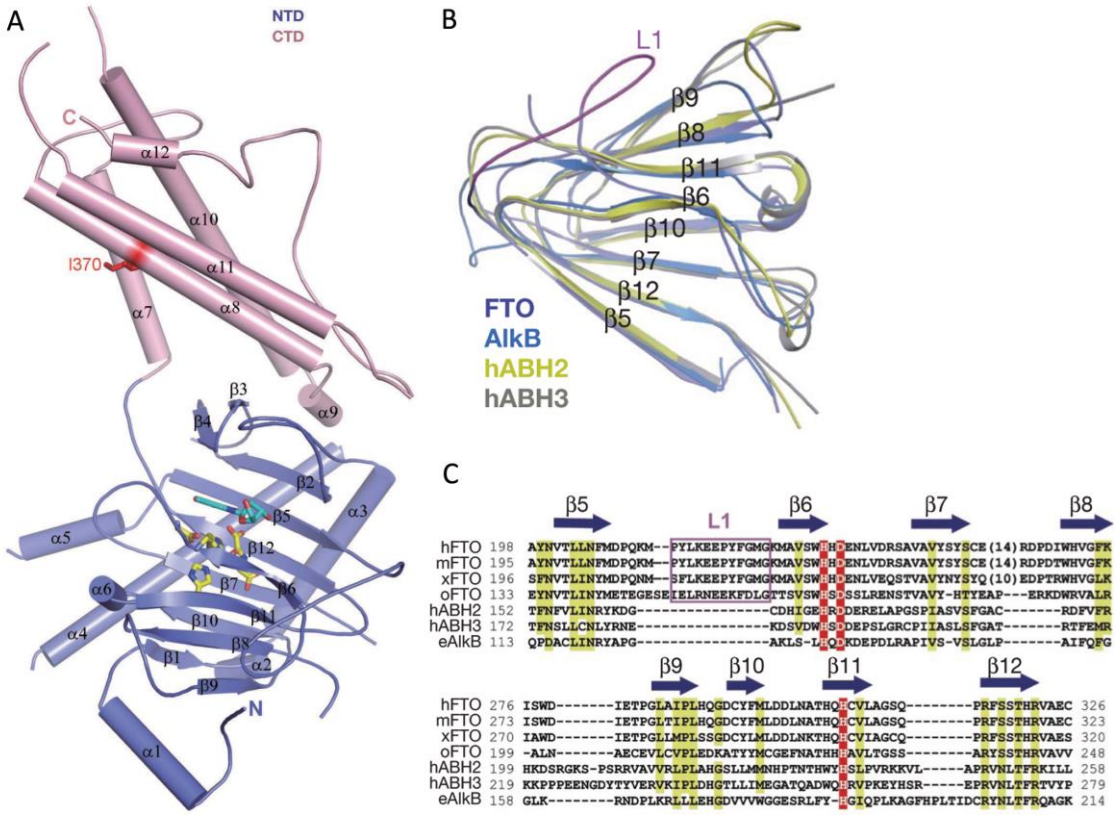

Figure 4 The structural characteristics of a human FTO. A, Cartoon of FTO crystal structure with N-terminal domain in slate and C-terminal domain in pink. The α-helices are shown as cinders and β-sheets are presented as arrows. Fe^{2+} (grey sphere), its coordinating residues (yellow stick) and m^3T (cyan stick) are shown. Residue Ile 370 (red stick) corresponds to Ile 367 of mouse FTO. **B**, Superposition of the FTO, AlkB, ALKBH2 and ALKBH3 central jelly-roll motif. L1 (loop 1) is shown in pink. **C**, Sequence alignment of FTO and AlkB family members within the jelly-roll motif. e, *E.coli*; h, *Homo sapiens*; m, *Mus musculus*; o, *Ostreococcus lucimarinus*; x, *Xenopus laevis*. Taken from (Han et al. 2010).

Following the discovery that FTO prefers single stranded nucleic acids, Jia et al. showed that FTO preferentially demethylated 6-methyloadenosine (m^6A) in ssDNA and ssRNA *in vitro* (**Figure 5**), and that activity was abolished in catalytically inactive FTO mutants (Jia et al. 2011). Moreover, overexpression of FTO in human cells decreased the level of m^6A in total mRNA, while FTO knockdown resulted in the opposite (Jia et al. 2011; Meyer et al. 2012). Since m^6A is not found in genomic DNA of higher eukaryotes (Jia, Fu, and He 2013) these data suggested that m^6A in mRNA is a major FTO substrate. However, when Berulava at el. compared brain RNA from *Fto* knock-out mice and wild type mice, no change in m^6A methylation levels were identified. Instead loss of FTO increased the ratio of m^3U/U and

decreases ratio of pseudouridine/U (Berulava et al. 2012). Also, no change in m^{6}A methylation levels were found in total RNA isolated from MEFs carrying two additional copies of *Fto* (Merkestein et al. 2014). This was likely because total RNA consists mostly of ribosomal RNA not mRNA (where m^{6}A is most prevalent) (Jia et al. 2011). However, Merkestein et al. also report a lack of difference in m^{6}A levels in total mRNA in FTO overexpressing MEFs, which suggests that FTO affects only a small number of specific mRNAs (Merkestein et al. 2014).

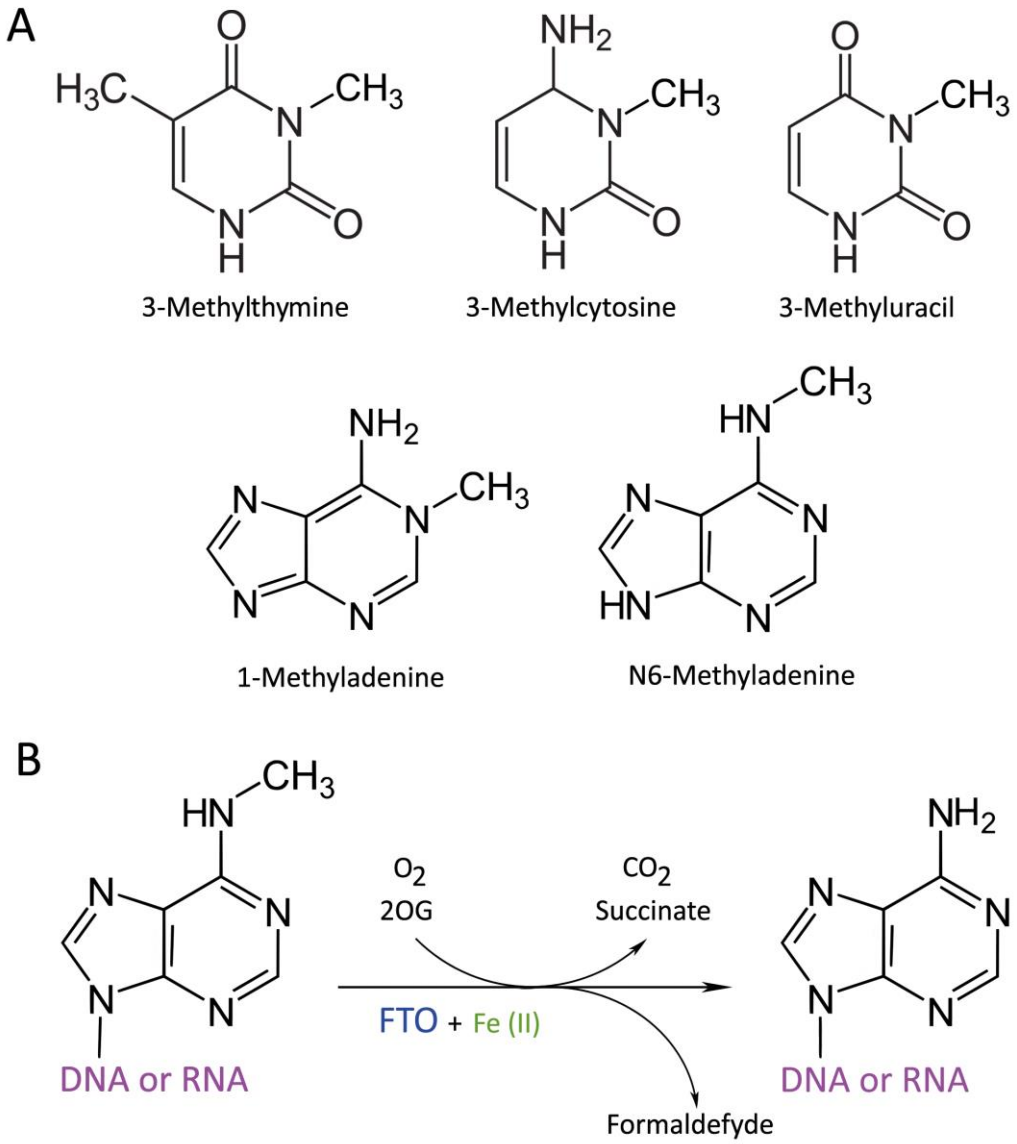

Figure 5. The catalytic activity of FTO. A, Substrates found to be demethylated by FTO. **B,** Schematic representation of FTO catalysed oxidative demethylation reaction of most favourable FTO substrate, N6-methyladenine.

1.3.5 The Role of FTO in Humans

The first clinical data reporting the role of FTO in humans came from the study of a large Palestinian Arab consanguineous family in which 9 members were identified with an arginine to glutamine mutation at amino acid 316 (R316Q) (Boissel et al. 2009). The arginine at residue 316 is involved in 2-oxoglutarate coordination and is absolutely conserved across FTO orthologs and other members of the ALKB family (Gerken et al. 2007; Boissel et al. 2009; Han et al. 2010). The R316Q mutation results in FTO catalytic inactivation and a severe phenotype in homozygous patients, including early lethality, postnatal growth retardation, microcephaly, facial dimorphism, psychomotor delay, and in some individuals cardiac abnormalities, brain malformations, genital defects and cleft palate (Boissel et al. 2009). This phenotype is similar to that of the Ft mutant mouse (Peters, Ausmeier, and Rüther 1999; Peters et al. 2002) and provides further evidence that FTO plays a fundamental role in normal development in humans.

Heterozygous FTO mutations were also found, including another loss-of-function R322Q mutation and an R96H mutation, which led to reduction of catalytic activity (Meyre et al. 2010). However, these mutations were identified in both obese and lean patients, indicating that loss of one functional copy of FTO is compatible with either lean or obese phenotype.

Duplication of *FTO* was reported in an obese female patient with a partial trisomy for the long arm of the chromosome 16, who also suffered from mental retardation, asymmetry of the breasts and multiple developmental disorders (van den Berg et al. 2010). Increased *FTO* copy number was confirmed by qPCR, although no evidence of increased expression on protein level was found in immortalised lymphocytes from the patient, which could be due

to maternal imprinting of the maternally derived chromosome 16 (van den Berg et al. 2010).

1.3.6 Mouse Models of FTO

To help further understand the influence of FTO on body weight, body composition and energy homeostasis, several animal models have been developed (summarised in **Table 3**).

A homozygous global *Fto* knock-out mice (*Fto*$^{-/-}$), generated by gene trap, showed increased postnatal mortality, postnatal growth retardation, and significant reduction of body weight, fat mass and lean mass despite relative hyperphagic (Fischer et al. 2009). The authors suggested that the reduction of adipose tissue resulted from increased energy expenditure, although this idea has been challenged due to lack of statistic power and appropriate statistical normalisation method (Speakman 2010; Fischer et al. 2010). Heterozygous *Fto*$^{+/-}$ mice did not share the above-mentioned phenotype, but both *Fto*$^{-/-}$ and *Fto*$^{+/-}$ mice were protected from obesity when fed a high fat diet (HFD) (Fischer et al. 2009).

The global *Fto* germline knock-out mice reported by McMurray and colleagues showed a similar phenotype to the gene-trap *Fto*$^{-/-}$ mice, having high perinatal lethality, reduction in body length, fat mass, and lean mass. However, they displayed no difference in energy expenditure when multiple linear regression normalisation was used (McMurray et al. 2013). Mice with *Fto* conditionally knocked out in all tissues also exhibited postnatal growth retardation and lower body weight, but in contrast to other *Fto* knock-out models, did not show a reduction in fat mass (Gao et al. 2010). However, there was a trend of fat

mass content increase (fat mass/total tissue mass %). Moreover, these mice were susceptible to diet-induced-obesity and showed increased energy intake and energy expenditure.

Perhaps a model more relevant to the *FTO* polymorphism phenotype described in humans was reported by Church and colleagues. Mice with decreased FTO expression and reduced catalytic activity due to the homozygous dominant point mutation I367F (*Fto*^{I367F}) had reduced body weight and fat mass, but did not show perinatal lethality or any developmental growth abnormalities (Church et al. 2009). These mice were protected from obesity when fed a HFD and the lean phenotype was explained by increased energy expenditure. Similarly, global conditional knock-out of *Fto* in adult mice (from week 6) resulted in lower body weight and lean mass, but did not cause any developmental growth abnormalities and food intake and energy expenditure were not affected (McMurray et al. 2013). This suggests an important role of FTO in the control of lean mass, independently of food intake. Surprisingly, fat mass was almost doubled in 20-week old mice.

Global overexpression of FTO in mice (*Fto*-3 and *Fto*-4) resulted in a gene copy dependent increase in body weight due to an increase in fat mass (Church et al. 2010). The phenotype was explained by increased food intake on both a standard diet and a HFD. These data indicate a direct role of FTO in the regulation of energy intake and metabolism in mice. Furthermore, since the expression levels of the *FTO* at-risk rs9939609 (A-allele) transcripts were found to be higher in the obese subjects (Berulava and Horsthemke 2010; Karra et al. 2013) the FTO overexpression mice may help explain the predisposition to obesity in human individuals with the at-risk rs9939609 A-allele (Frayling et al. 2007).

Since the FTO levels are high in brain, particularly within the hippocampus and hypothalamic nuclei (Gerken et al. 2007), the role of brain FTO in energy homeostasis was also assessed. Mice with *Fto* conditionally knocked out in the brain showed a phenotype similar to the global conditional knock-out mice described by Gao, suggesting crucial roles for neuronal FTO in postnatal growth (Gao et al. 2010). However, the *Nestin*-CRE used to knock-out Fto in the brain has a body weight and growth retarded phenotype (Harno, Cottrell, and White 2013), and no *Nestin*-CRE control was used in the study (Gao et al. 2010). Loss of *Fto* in the mediobasal hypothalamus of adult mice [achieved by injections of an adeno-associated virus (AAV)] resulted in only a small reduction of body weight (due to small decrease in food intake) and no effect on body composition and energy expenditure was reported (McMurray et al. 2013). This suggests that FTO may also act in brain regions other than the hypothalamus. On the other hand, down-regulation of FTO expression in the arcuate nucleus (ARC) in adult mice using AAV increased food intake while up-regulation caused the opposite, suggesting a role of ARC FTO in energy homeostasis (Tung et al. 2010).

Overall, the animal studies demonstrate that manipulation of FTO expression has a direct effect on body weight, body composition and energy regulation, and that down-regulation of FTO levels results in loss of body weight while up-regulation leads to increased body weight. However, the mechanisms underlying these body composition effects are still unclear. Hence it is difficult to conclude what is the precise role of FTO in energy homeostasis and metabolism. A more detailed analysis of the role of FTO in peripheral tissues, especially adipose tissue and muscle, may contribute to better understanding of FTO role in obesity phenotype.

Table 3. Summary of *Fto* mouse models. Abbreviations: ↓, decrease; ↑, increase; BW, body weight; HFD, high fat diet; SD, standard diet; W, week, RER, respiratory exchange ratio; FFA, free fatty acids; HDL, high density lipoprotein; LDL, low density lipoprotein; ER. Adapted from (Fawcett and Barroso 2010).

Trait	Mouse Model					
	***Fto*$^{-/-}$ mouse** (Fischer et al. 2009)	***Fto*^{I367F} mouse** (Church et al. 2009)	**Conditional *Fto*$^{-/-}$ mouse** (Gao et al. 2010)	**Brain *Fto*$^{-/-}$ mouse** (Gao et al. 2010)	**Adult *Fto*$^{-/-}$ mouse** (McMurray et al. 2013)	***Fto*-3 / *Fto*-4 mouse** (Church et al. 2010)
Pre- and post-natal body weight	No prenatal effect. After birth: ↓ BW, fat mas, lean mass (fat mass more pronounced); ↓ weight gain on HFD	No prenatal effect. After birth: males show maturity-onset ↓ BW due to ↓ fat mass; ↓ weight gain on HFD	No prenatal effect. After birth: ↓ BW and lean mass; ↑ fat mass, fat content (fat mass /total tissue mass %) in males	No prenatal effect. After birth: ↓ BW and lean mass; ↑ fat content (fat mass /total tissue mass %)	No prenatal effect. After induction: ↓ BW, lean mass; ↑ fat mass	No prenatal effect. After birth: Copy number dependent ↑ in BW due to ↑ fat mass; ↑ BW gain and fat mass of HFD
Post-natal death	↑ frequency	None	↑ frequency (50%)	Not reported	Some	None
Growth retardation	Yes, from postnatal day 2	None	Yes, immediate	Yes, immediate	None	None
Development	None	None	None	None	None	None
Adipose tissue mass and adipokines	↓ in adipose tissue mass; ↓ leptin; ↑ adiponectin	↓ in adipose tissue mass; ↑ leptin per unit of body fat; No difference in adiponectin	No difference in adipose tissue mass; ↑ percent fat	No difference in adipose tissue mass; ↑ percent fat	↑ adipose tissue mass	Copy number dependent ↑ in adipose tissue; ↑ adipocyte size on HFD; ↓ leptin in *Fto-4* mice on SD and HFD at

						W8, but disappeared at W20
FTO expression and function	Abolished expression in all tissues	Reduced expression, reduced catalytic activity in all tissues	Abolished expression in all tissues	Abolished expression in the brain	Abolished expression from W6 in all tissues	Overexpression (one and two additional copies)
Sex differences	↓ body length, more pronounced in males; ↓ body length at W20 in *Fto*$^{+/-}$ females, not males	At W12, only males showed ↓ BW	↑f at mass fat content (fat mass /total tissue mass %) in males	↑ fat content (fat mass /total tissue mass %) more pronounced in females	Not reported	BW ↑ more pronounced in females; ↑ adipocyte size at W20 on SD in females; ↑ lean mass in females *Fto*-4 on SD
Energy intake	↑ energy intake relative to lean mass	None	↑ energy intake relative to lean mass	↑ energy intake relative to lean mass	None	↑ energy intake on both SD and even more pronounced HFD
Energy expenditure	↑ energy expenditure	↑ energy expenditure	↓ O_2 consumption and CO_2 production rate; ↑ metabolic rate	↓ O_2 consumption and CO_2 production rate; ↑ metabolic rate	None, but ↓ CO_2 output and RER	↑ energy expenditure in *Fto-4* mice on SD
Physical activity	↓ physical activity	None	None	Not Reported	Not reported	None
Glucose tolerance and insulin sensitivity	Mild improvement in insulin sensitivity (probably as a consequence of leanness)	None	Not reported	Not reported	Not reported	Reduction in glucose tolerance in *Fto-4* mice on HFD

Lipids	Not reported	↑ triglycerides and high-density lipoprotein (HDL) cholesterol	Not reported	Not reported	Not Reported	↑ triglycerides, FFA, HDL, cholesterol; ↓ LDL cholesterol
Other gene expression	*Npy* mRNA induction Blunted, *Pomc* mRNA repression exaggerated in fasted *Fto*$^{-/-}$ mice	Altered expression of genes involved in inflammation, fatty acid catabolism and synthesis, carbohydrate metabolism and the ER stress response; *Npy* expression was lower in fed mutant mice	None	None	None	None

1.3.7 FTO Cellular Location

Initial studies reported that FTO was located within the nucleus, did not co-localise with mitochondria (Gerken et al. 2007; Church et al. 2009; Fischer et al. 2009) and contained a nuclear localisation signal (NLS) (Meyre et al. 2010). Further analysis showed a varying pattern and intensity of FTO staining in nucleoplasm in different cell lines (Berulava et al. 2012). These authors also reported a weak FTO signal in the nucleoli, but when FTO expression was induced, intensity of this signal was unchanged. Moreover, chromatin staining on the included images do not allow clear identification of the nucleoli, thus the presence of FTO in these subnuclear compartments remains unclear. Partial co-localisation to the nuclear speckles (but not paraspeckles) and an association of FTO with nuclear pre-mRNA splicing components has been reported (Jia et al. 2011; Berulava et al. 2012). However, there is growing evidence suggesting that FTO is also found in other cellular compartments. Immunofluorescent analysis of the rat brain sections dissected after 48h fasting showed increased cytoplasmic expression of FTO in neurons of the lateral hypothalamic area (LHA), PVN and VMN, but not in ARC, cortex and hippocampal neurons (Vujovic et al. 2013). Subcellular fractionation revealed that FTO was detected in both nuclear and cytoplasmic fractions in *Fto* overexpression mouse embryonic fibroblasts (MEFs), mouse pancreatic β-cells and hypothalamic N46 cells (Gulati et al. 2013). Recently, live cell imaging coupled with fluorescence loss in photobleaching (FLIP) of GFP-FTO expressing COS7 cells suggested that FTO can shuttle between the cytoplasm and the nucleus, possibly through interaction with exportin 2 (XPO2) (Gulati et al. 2014). Moreover, FTO lacking its N-terminal domain did not show a predominant nuclear location. Overall, these results provide some support for multiple locations of FTO action, although closer examination of molecular and cellular events triggering its varying presence in subnuclear locations and transport of FTO to the specific cell compartment is needed.

1.3.8 Other Potential Roles of FTO

Although activity of FTO as a Fe (II) and 2OG dependent oxygenase has been reported by numerous studies (1.3.3 and 1.3.4), the molecular and cellular functions of FTO still remain elusive. The possibility that FTO acts as a sensor of intracellular metabolism by detecting 2-oxoglutarate (2OG) (an intermediate product of citric acid cycle) is unlikely, since the 2OG concentration at which the FTO catalytic reaction rate reached half of its maximum value (Km) was lower than the normal intracellular 2OG concentration (Ma et al. 2012). Thus, if FTO was to act as a cellular 2OG sensor, it would be saturated all the time.

A role of FTO in amino acid sensing has been proposed as *Fto* mRNA/ FTO levels were reported to be reversibly down-regulated by non-essential amino acid deprivation (Cheung et al. 2012). Also, $Fto^{-/-}$ MEFs showed a decreased survival rate when deprived of total amino acids compared to $Fto^{+/+}$ MEFs (Gulati et al. 2013). Moreover, a link between FTO and the cell growth and translation was suggested by a decreased growth rate, reduced mRNA translation and increased autophagy in $Fto^{-/-}$ MEFs (Gulati et al. 2013). Gulati et al. also showed that FTO interacts with several aminoacyl-tRNA synthetases (AARSs) and that lack of FTO affects the formation and/or stability of the multi-tRNA synthetase complex (MSC). Finally, this group also suggested that FTO facilitates the response to amino acid depravation through the activation of the mTORC1 signalling pathway and that FTO demethylase activity is required for that response (Gulati et al. 2013).

Several other cellular functions of FTO have been proposed. Wu et al. suggested that FTO is a transcription coactivator and increases binding of the CCAAT/enhancer binding proteins

(C/EBPs), although FTO did not bind to methylated oligonucleotide (Wu et al. 2010). Moreover, the same effect was found for the unmethylated gene as well as when the gene was modified with 5-methylcytosine (a previously unknown FTO substrate). A role for FTO in dopaminergic control via dopamine receptor 2 and 3 (D2R and D3R) has also been suggested (Hess et al. 2013). Global and specific midbrain dopaminergic (DA) neurons *Fto* knock-out mice ($Fto^{\Delta DAT}$) showed reduced activation of the G protein–coupled inwardly-rectifying potassium (GIRK) channel conductance when cocaine and quinpirole were applied. The phenotype of $Fto^{\Delta DAT}$ mice resembled mice with D2R inactivated specifically in DAT positive neurons, although energy homeostasis was unaltered (Hess et al. 2013). Lack of FTO was also reported to cause growth retardation and developmental defects in zebrafish and to affect the Wnt signalling pathway both *in vivo* and *in vitro* (Osborn et al. 2014). The canonical (beta-Catenin dependent) branch of the Wnt pathway was down-regulated while the non-canonical pathway was up-regulated. Moreover, lack of FTO was associated with tissue specific defects in development and in the formation of cilia in zebrafish and mice (Osborn et al. 2014).

Several reports have provided more insight into the role of FTO in the development of obesity. Karra and colleagues reported that individuals with the rs9939609 risk (AA) allele had reduced post-meal suppression of hunger and suppression of circulating levels of acyl-ghrelin, an orexigenic peptide hormone released from the gastrointestinal tract (Karra et al. 2013). Moreover, the neuronal activity in brain regions associated with reward and homeostasis was different between rs9939609 AA and TT subjects in response to food images, regardless if subjects has been fasted or fed. This suggest an association between FTO, ghrelin and eating behaviour which may explain the obesity phenotype of AA rs9939609 subjects.

1.3.9 Role of FTO in RNA Metabolism and Processing

Initial identification of FTO as an ALKB ssDNA demethylase that localised to the nucleus suggested a potential role in maintenance and repair of lesions in nuclear DNA, similarly to the *E. coli* enzyme AlkB and human ALKBH2 and ALKBH3 (Gerken et al. 2007). However, the higher activity of FTO towards m^3U in ssRNA over m^3T in ssDNA, and the increased prevalence of m^3U in *Fto* knock-out mice implied a potential regulatory role at the rRNA level (where m^3U modification is the most prevalent) (Jia et al. 2008; Han et al. 2010; Berulava et al. 2012; Kowalak et al. 1993). Finally, the discovery by Jia et al. that FTO is the first known m^6A demethylase, and that m^6A methylation in RNA is reversible, shifted attention to a role for FTO in mRNA epigenetics, RNA metabolism and processing (Jia et al. 2011; Jia, Fu, and He 2013).

Methylation at N^6-adenosine is the most prevalent modification in eukaryotic mRNA (but is not detectable in genomic DNA of higher eukaryotes), is formed before splicing and does not affect the coding capability of transcripts (Jia, Fu, and He 2013). Recently, m^6A-sequencing (m^6A-seq) revealed the positions of m^6A within the human and mouse transcriptome (Dominissini et al. 2012). Putative m^6A sites were highly conserved in humans and mice and were enriched in the proximity of the 3' untranslated region (UTR) (close to the stop codon but very rarely exactly at the stop codon), in long internal exons and coding sequences (CDS) and to lesser extent at the transcription start site (TSS) and 5'UTR. Some of the signal from the TSS was thought to come from the 5'-cap structure. Loss of m^6A methyltransferase (METTL3) in HepG2 cells resulted in significant changes in gene expression and splicing patterns as well as increased apoptosis via the p53 pathway (Dominissini et al. 2012).

Meyer and colleagues confirmed m^{6}A modification occurs at the 3'UTR of mRNAs (near stop codons) and reported much lower levels in the 5'UTR (Meyer et al. 2012). Moreover, the group identified motifs within mRNA that are enriched with m^{6}A. Interestingly, m^{6}A was not associated with poly(A) signals and splice junctions, and it was found unlikely to influence binding of the splicing factors, although an association with miRNA was identified. Finally, Meyer at el. reported that m^{6}A can be subjected to tissue and cell specific regulation and m^{6}A levels increase throughout brain development (Meyer et al. 2012).

The role of m^{6}A in the regulation of RNA splicing was further demonstrated by Zhao and colleagues who showed that m^{6}A was more prevalent in multi-isoform genes than single-isoform genes (Zhao et al. 2014). Moreover m^{6}A overrepresentation overlapped with 5′ and 3′ exonic sequences flanking splice sites and with exonic binding clusters recognised by serine/arginine-rich (SR) splicing enhancer SRSF1 and SRSF2.

There is increasing evidence to support the biological importance of FTO-dependent m^{6}A demethylase activity. Partial co-localisation of FTO with the methylation and splicing machinery in nuclear speckles suggests a role for FTO in nuclear pre-mRNA splicing and mRNA nuclear export (Jia et al. 2011; Berulava et al. 2012). Analysis of m^{6}A levels in mRNA isolated from midbrain and striatum of *Fto* knock-out mice showed increased methylation at N^6-adenosine of over 1,500 mRNA, indicating that FTO demethylation is selective (Hess et al. 2013). Moreover, these transcripts were associated with cell signalling and synaptic transmission suggesting FTO demethylation is involved in neuronal signalling. Interestingly, a small increase in expression of these mRNAs was observed but the protein expression was reduced (Hess et al. 2013). A study on ghrelin, a peptide hormone released

in the gastrointestinal track that increases appetite, showed that FTO overexpression in MGN3-1 and HEK293T cells reduced m^{6}A levels in ghrelin mRNA and up-regulated ghrelin mRNA and peptide levels (Karra et al. 2013). Similarly, ghrelin mRNA was isolated from peripheral blood cells of individuals with rs9939609 risk (AA) allele. Also, lower m^{6}A levels were found in total RNA from whole blood of T2D patients, which correlated with increased levels of *FTO* mRNA (Shen et al. 2015).

A recent study by Zhao and colleagues suggested that altered levels of m^{6}A, due to FTO-dependent demethylation, plays an important role in adipogenesis (Zhao et al. 2014). Knockdown of *FTO* in 3T3-L1 pre-adipocytes significantly impaired differentiation, and this was fully restored by catalytically active FTO. Moreover expression levels of FTO decreased during differentiation of 3T3-L1 pre-adipocytes and global m^{6}A levels increased, while METTL3 levels were unaltered. Depletion of FTO led to the increased presence of m^{6}A at exonic sequences flanking constitutive and alternative splice sites, and increased binding of the serine/arginine-rich splicing enhancer SRSF2. This resulted in increased inclusion of alternative exons and decreased exon skipping of several transcripts including Runt-related transcription factor 1 (*RUNX1T1)* which regulates preadipocyte differentiation (Zhao et al. 2014).

In summary, these findings suggest that FTO-dependent m^{6}A demethylation plays an important role in gene regulation by affecting pre-mRNA splicing and RNA processing. However, the recent discovery of the YTH-family proteins that selectively bind to m^{6}A and transport mRNA to cytoplasmic sites of mRNA decay (e.g. P-bodies) suggests that reversible methylation of N^6-adenosine affects the translation and lifetime of mRNA (Meyer et al. 2012; Dominissini et al. 2012; Wang et al. 2014; Fu et al. 2014).

2 Materials and Methods

This chapter lists general materials and methods common to the thesis. Information about the techniques and materials used in chapter specific experiments are included in the methods sections of relevant chapters.

2.1 Animal Husbandry and Metabolic Phenotyping

All animal studies were carried out in accordance with the 1986 UK Animals (Scientific Procedures) Act and under the guidance issued by the Medical Research Council: Responsibility in the Use of Animals in Medical Research (July 1993) and Home Project Licence Nos. 30/2642.

2.1.1 Animal Care

Mice were kept in accordance with UK Home Office welfare guidelines and project license restrictions under controlled light (12 hours light and 12 hours dark cycle), temperature (21 °C ± 2 °C) and humidity (55 % ± 10 %) conditions. They had free access to water (25 ppm chlorine) and were fed *ad libitum* (unless otherwise stated) on a commercial diet (SDS Rat and Mouse No.3 Breeding diet RM3, Dietex International) containing 11.5 kcal % fat, 23.93 kcal % protein and 61.57 kcal % carbohydrate. Phenotyping tests were designed according to the European Phenotyping Resource for Standardised Screens from EUMORPHIA (EMPReSS) and performed as described in standard operating procedures (SOPs) available at http://empress.har.mrc.ac.uk.

2.1.2 Generation of Mice

Mice with *Fto* exon 3 flanked with LoxP sites were previously generated by Chris Church at MRC Harwell (McMurray et al. 2013). The targeted *Fto* locus was designed to contain a LoxP sites flanking exon 3 and a neomycin (Neo) selection cassette under control of a strong *PGK* promoter, flanked by FRT recombination sites. The Neo selection cassette enabled selection of positive 129 ES cell clones. Successfully transfected ES cell clones were then injected into C57BL/6J blastocysts (at Transgenesis and Gene Targeting Unit, MRC Harwell) and chimeras were bred to C57BL/6J mice and offspring and tested for germline transmission. PGK-Neo was removed by crossing LoxP-Exon3-FRT-PGKNeo-FRT-LoxP mice to a line congenic to C57BL/6J expressing improved thermostable FLPe recombinase (Rodríguez et al. 2000) under the control of the β-actin promoter, generating the *Fto* conditional allele FTO-KO-FLOX-B6 ($Fto^{+/Flox}$). FLPe recombinase was removed by further crossing to C57BL/6J mice.

Mice in which *Fto* was selectively knocked out in muscle were generated using the Cre-lox approach. Crossing FTO-KO-FLOX-B6 mice with mice harbouring the Cre-recombinase gene under the control of the mouse muscle creatine kinase promoter (*Mck*-Cre) would result in excision of *Fto* exon 3 in cardiac and muscle cells and frameshift mutation which would further result in the termination of translation. *Mck*-Cre were kindly provided by J.Brüning (Institute of Genetics, Cologne, Germany).

Additionally *Mck*-Cre mice were crossed with the reporter line R26R-LACZ ($Gt(ROSA)26Sor^{tm1Sor}$) which has a *β-galactosidase* gene preceded by a LoxP-flanked transcriptional termination sequence. This resulted in excision of the transcriptional

termination sequence in cells expressing Cre under the *Mck* promoter and expression of *β-galactosidase* under the *LacZ* promoter.

2.1.3 Genotyping of Generated Mice

Mice were weaned and ear clipped approximately at 2-3 weeks of age. Genomic DNA was isolated from the ear tissue using the DNA Extract All Reagents Kit (Applied Biosystems, 4403319) and the genotypes of individual mice were assessed by two assays:

a) Amplicon Genotyping Assay for determining presence or absence of the Cre sequence using the High Resolution Melting (HRM) system LightScanner (Idaho Technology). PCR was performed in the presence of the double stranded DNA binding dye LCGreen (Idaho Technology). After PCR, samples were heated on the LightScanner and the fluorescence emitted by bound LCGreen was monitored. Depending on the pattern, peaks were grouped together and a Cre genotype was determined by presence of a peak at 87 ^{o}C. The housekeeping gene *SLC40A1* was used as a control.

Primer	**Sequence**
CRE Froward	5'-GCGGTCTGGCAGTAAAAACTATC-3'
CRE Reversed	5'-GTGAAACAGCATTGCTGTCACTT-3'
SLC40A1 Froward	5'-TGTAACTTCCTCTGTGTC-3'
SLC40A1 Reversed	5'-CTGAAGTCTTTCATGATAACTGCATT-3'

PCR Step	Temperature	Time
Initial Denaturation	95 °C	2 minutes
32 cycles of		
Denaturation	95 °C	30 seconds
Annealing	60 °C	30 seconds
Extension	72 °C	30 seconds
Hybridisation		
Denaturation	95 °C	30 seconds
	25 °C	30 seconds
	15 °C	30 seconds

b) PCR in order to detect presence or absence of the FRT-LoxP site inserted after exon 3 of the FTO gene followed by gel electrophoresis (3-4 % agarose gel, 100 V). A band at 254 bp indicated the presence of the floxed exon and a band at 104 bp indicated the presence of the wild type exon.

Primer	Sequence
FLPeDEL Forward	5'-GCATGCTCGATGGCAGTGTG-3'
FLPeDEL Reversed	5'-GTGAGACCGGCCAGGAAAGGAA-3'

PCR Component	20 µl Reaction	Final Concentration
Phu buffer (5 X)	4 µl	1 X
10 mM dNTPs	0.4 µl	200 µM
10 µM Forward Primer	1 µl	0.5 µM
10 µM Reverse Primer	1 µl	0.5 µM
Template DNA 50-250 ng	5 µl	variable
Phusion DNA Polymerase	0.2 µl	0.4 units/20 µl PCR
Nuclease-Free Water	to 20 µl	

PCR Step	Temperature	Time
Initial Denaturation	98 °C	30 seconds
35 cycles of		
Denaturation	98 °C	8 seconds
Annealing	65 °C	20 seconds
Extension	72 °C	30 seconds
Final		
Final Extension	72 °C	10 minutes
Hold	4-10 °C	

2.1.4 Adult Tissue Collection

A lethal dose of anaesthesia (Euthatal (200 mg/ml) 50:50 solution in physiological saline, Merial Animal Health Ltd.) was administered intraperitoneally (IP) and mouse tissue (brain, tongue, heart, diaphragm, liver, pancreas, kidneys, white adipose tissue (WAT), brown adipose tissue (BAT), skeletal muscle and abdominal muscle) were collected and snap frozen in liquid nitrogen using 2 ml cryotubes (Nunc, Thermo Fischer Scientific) and stored in -80 ^{o}C.

2.1.5 Terminal Blood Collection

A lethal dose of anaesthesia was administered intraperitoneally and a terminal blood sample was collected from the orbital sinus. A disposable capillary (10 µl, Hirschmann Labotgerate) was inserted at a 45° angle into the corner of the eye underneath the eyeball puncturing the sinus. Blood was collected into Lithium-Heparin plasma tubes (Li 1000A Standard, KABE Labortechnik).

2.1.6 Intraperitoneal Glucose Tolerance Test (IPGTT)

Mice were fasted overnight (16 hours) before the experiment to establish a baseline glucose level "T0" (time 0). After weighing, local anaesthesia (EMLA Cream, lidocaine 2.5 % and prilocaine 2.5 %, AstraZeneca) was applied on each mouse tail and before each bleeding animals were kept in a hot box (Thermacage MK3, Datesand Ltd.) for 10-15 minutes. Blood samples were collected from the tail vein using Lithium-Heparin microvette tubes (CB300LH, Sarstedt). Subsequently, mice were injected IP with glucose (2 g glucose/kg body weight, solution 20 % glucose in 0.9 % NaCl) and blood samples were collected after 60 minutes and 120 minutes after glucose injection. Fasted blood samples were taken from the tail vein as described above.

2.1.7 Plasma Analysis

Red blood cells and plasma were separated by centrifugation of blood samples at 3000 rpm (800 x g) for 10 minutes at RT using a Biofuge Pico microcentrifuge (Thermo Fisher Scientific). The plasma was collected and stored at -20 ^{o}C. Plasma glucose was measured using a Glucose Analyser GM9 (Analox), following the manufacturer's protocol.

2.1.8 Body Composition Measurements

Mice were weighed weekly using electronic scales calibrated to 0.01 g. Fat mass and lean tissue mass was measured without any anaesthesia using Body Composition Analyzer EchoMRI-130™ (EchoMRI,) with horizontal gantry. Bone mineral content and density were

measured in mice at the age of 20 weeks using the Dual-energy X-ray Absorptiometry (DEXA) analyser (DEXA, PIXImus). Quality control was performed on the day of the measurement using phantoms delivered by the manufacturer. Animals received a lethal dose of anaesthesia (2.1.4) by IP injection, and body length (from nose to anus) was measured with 0.1 cm accuracy using a ruler. Unconscious mice were placed on a tray to perform a scan. The analysis of the data comprised a whole body analysis excluding the head area.

2.1.9 Food and Water Consumption, Urine and Faeces Output Measurements

Mice were housed individually in metabolic Techniplast cages (Buggeggiate) enclosed in a Scantainer Ventilated Cabinet (Scarnub Technology). They had free access to water and were fed *ad libitum* on a commercial diet (2.1.1). Food and water consumption were measured by weighing food and water placed in the cage at the beginning of the experiment and 24 hours later. Urine and faeces were collected and weighed. The difference in individual mouse body weight before and after the experiment was also registered.

2.1.10 Grip Strength Test

The maximal strength of combined forelimbs and hind limbs was measured with a Grip Strength Meter apparatus (Bioseb). Mice were held by the base of the tail between the thumb and the forefinger. Once both front paws and hind paws had gripped the grid, mice were pulled steadily and horizontally to the grid until it has been released. Each measurement was repeated three times.

2.1.11 Harvest of Adult Tissue and Processing for *LacZ* Staining

A lethal dose of anaesthesia (2.1.4) was administered intraperitoneally (IP) and the animal was placed on the perfusion tray. Once the withdrawal and corneal reflexes disappeared, the heart left ventricle was carefully pushed onto the cannula and the mouse was perfused with 4 % paraformaldehyde (PFA) pH 8.0 at the flow rate of 2.83 ml/minute until rigidity and colour change were observed (average time 10-15 minutes). Multiple organs were dissected out and fixed in 4 % PFA for 30 minutes on ice followed by three 20 minutes washes in a large volume of PBS pH 8.0 at 4 °C. Staining was performed at 4 °C with gentle agitation for 48 hours using 2.5 % X-Gal (Life Technologies Ltd.) in dimethylformamide (DMF). After two washes with PBS pH 8.0 (30 minutes each) the specimens were again incubated in 4 % PFA pH 8.0 overnight (12- 16 hours) at 4 °C with gentle agitation and then rinsed with PBS pH 8.0. Specimens were cleared with 50 % glycerol overnight (12-16 hours) at 4 °C with gentle agitation followed by clearing and storage in 70 % glycerol in the dark at 4 °C. Specimens were left in 70 % glycerol for a minimum for 24 hours prior to data being recorded.

Table 4. *LacZ* staining solution composition

Compound	Concentration
Magnesium Chloride	2 mM
IGEPAL	0.02 %
Potassium Ferrocyanide	5 mM
Potassium Ferricyanide	5 mM
Sodium Deoxycholate	0.01 %
X-Gal in DMF	1 mg/ml
Made in cold PBS pH 8.0	

2.1.12 Statistical Analysis

Statistical analysis of the data were performed using SPSS Statistics (IBM) version 21. The data was separated by sex and results are expressed as mean ± standard error of the mean (SEM). Data was first graphically examined for presence of outliers (as assessed by inspection of a boxplot for values greater than 1.5 box-lengths from the edge of the box) and extreme outliers (as assessed by inspection of a boxplot for values greater than 3 box-lengths from the edge of the box). The Shapiro-Wilk Test of Normality was performed to assess if the data is normally distributed (normality assumption is met when $p>0.05$). The homogeneity of variances was assessed by Levene's Test of Homogeneity of Variance (assumption is met when $p>0.05$). When the homogeneity of variances was met, the comparison of the means of genotype groups was performed using one way analysis of variance (ANOVA) followed by post hoc Bonferroni multiple comparison testing between all genotype groups. When the homogeneity of variances was violated the comparison of the means of genotype groups was assessed using Welch's ANOVA followed by Games-Howell post-hoc test. Significance was assigned to results that occurred with less than 5 % probability, $p<0.05$. Time-course data was analysed using the mixed ANOVA model followed by Bonferroni's post hoc tests to compare individual means from genotype groups. The significance levels between genotype groups are indicated by asterisks in each figure above the bars: *$p\leq0.05$; **$p\leq0.01$; ***$p\leq0.001$.

2.2 DNA Methods

2.2.1 DNA Separation by Gel Electrophoresis

The DNA fragments were resolved by gel electrophoresis using 1-2 % agarose gels (w/v) in TAE (Tris-acetate; 40 mM Tris acetate and 1 mM EDTA) buffer supplemented with 10000x GelRed Nucleic Acid Gel Stain (41003-T, Biotium). DNA was mixed with 6x Blue/Orange Loading Dye (G190A, Promega) and DNA fragments were separated for 30 minutes at 100 V in TAE buffer. Resolved DNA was visualised with UV light and a DNA standard ladder Gene Ruler 1 kb (SM0313, Thermo Scientific) was used to assess the length of the DNA fragments.

2.2.2 Purification of DNA Fragments from the Agarose Gel

The DNA fragments of interest separated by the gel electrophoresis were visualised in the agarose gel under UV light using Dual-Intensity Transilluminator (Genetic Research Instrumentation Ltd.). Fragments were excised using a clean scalpel, weighed and placed in the microcentrifuging tube. DNA was purified using the GeneJET Gel Extraction Kit (K0691, Thermo Scientific) following the manufacturer's protocol.

2.2.3 Bacterial Transformation

The DH5α™ competent cells (18265-017, Invitrogen) were thawed on ice and 50 µl were used for each transformation. Cells were gently mixed with 1-5 µl (1-10 ng) of DNA and incubated on ice for 30 minutes followed by a 20-second heat shock in 42 °C water bath without shaking. After an additional 2-minute incubation on ice, cells were spread on pre-warmed selective LB broth agar plates and incubated at 37 °C overnight (12-16 hours) in a static incubator.

2.2.4 Plasmid DNA Isolation and Purification from Bacterial Culture

Single colonies of transformed bacteria cells were used to inoculate liquid LB broth media supplemented with a specific antibiotic. Bacteria were cultured overnight (12-16 hours) in a shaking incubator (200-250 rpm) at 37 °C and harvested by the centrifugation. Depending on the scale of preparation and the protocol used, cells were pelleted from 5 ml cultures at 6800 g for 2 minutes at room temperature, or from 50 ml cultures at 3000 g for 60 minutes at 4 °C. Plasmid DNA was isolated following the manufacturer's protocol using the GeneJET Plasmid Miniprep Kit (K0503, Thermo Scientific) for the 5 ml culture, or the HiSpeed Plasmid Midi Kit (12663, Qiagen) for the 50 ml culture.

2.2.5 Determination of Nucleic Acid Concentrations

Concentration of purified plasmid DNA was assessed using a Nanodrop 10000 spectrophotometer (Thermo Scientific). A buffer used for nucleic acid purification was applied first as a blank, followed with 1 µl of nucleic acid solution. Concentration of nucleic acid solution was determined based on the absorbance with wavelength at 260 nm. The

ratio 260/280 nm was used to assess nucleic acid purity. A ratio ~ 1.8 was accepted for "pure" DNA.

2.2.6 Polymerase Chain Reaction (PCR)

Primers were purchased from Sigma-Aldrich. Nuclease free water was used to dilute all primers and reaction components. Reactions were carried out using a 2720 Thermal Cycler (Applied Biosystems) and was performed using Q5 Hot Start High-Fidelity DNA Polymerase (M0493L, New England Biolabs Ltd.) according to the following protocol:

PCR Component	**20 µl Reaction**	**Final Concentration**
Q5 Reaction Buffer (5 X)	10 µl	1 X
10 mM dNTPs	1 µl	200 µM
10 µM Forward Primer	2.5 µl	0.5 µM
10 µM Reverse Primer	2.5 µl	0.5 µM
Template DNA	1 ng	20 pg/µl
Q5 Hot Start High-Fidelity DNA Polymerase	1 µl	0.02 U/µl
Nuclease-Free Water	to 50 µl	

PCR Step	**Temperature**	**Time**
Initial Denaturation	98 °C	30 seconds
35 cycles of		
Denaturation	98 °C	10 seconds
Annealing	55 °C	25 seconds
Extension	72 °C	30 seconds
Final		
Final Extension	72 °C	2 minutes
Hold	4-10 °C	

2.2.7 DNA Sequence Analysis

Purified plasmid DNA and products of PCR reactions were sequenced using the Sanger sequencing services provided by Source Bioscience (Oxford, U.K.). Samples were diluted to 100 ng/µl and placed in separate tubes (5 µl per reaction). Standard sequencing primers were provided by the sequencing services. Custom designed primers were sent with a sample at 3.2 pmol/µl. DNA sequences were analysed using Basic Local Alignment Search Tool (BLAST) software available on-line. A plasmid editor software (ApE, v2.0.47) was used to visualise plasmids, perform virtual double digest and design primers for cloning experiments.

2.3 Cell Biology Methods

2.3.1 Cell Culture

All procedures were performed under sterile conditions in a Class II vertical laminar-flow biological cabinet. The cultures were incubated in a humidified atmosphere (5-7 % carbon dioxide) at 37 ^{o}C. Cell culture media and reagents were purchased from Gibco, Life Technologies unless specified. Cells were routinely cultured in 25 cm^2 and 75 cm^2 culture flasks (Sigma-Aldrich).

HEPA1-6 [hepatoma cells derived from BW7756 tumour in a C57L mouse (Darlington et al., 1980)] (ATTC, CRL-1830) were cultured in DMEM, High Glucose, GlutaMAX™, Pyruvate (31966-047) 1 X Penicillin/Streptomycin (15070-063), and 10 % fetal bovine serum (FBS)

(10500-064). Cells were cultured until ~ 90% confluent and subcultivated three times weekly at a 1:5 ratio.

HEK 293 [Human Embryonic Kidney 293 cells (Graham FL, et al.) Gentaur Ltd] were cultured in DMEM (Sigma, D6546) supplemented with 20 ml of 200 mM L-glutamine (Sigma, G7513), 10 % FBS (10500-064) and 1 X Non-Essential Amino Acids (Sigma, M7145). Cells were cultured until ~ 90 % confluent and subcultivated three times weekly at a 1:5 ratio.

INS-1 (Rat Insulinoma Cell line-1) conditionally expressing FTO were kindly provided by Dr Mark Russel (Russell and Morgan 2011). Cell were cultured in RPMI 1640 GlutaMAX™ (Life Technologies, 61870-044) supplemented with 10% FBS, 2 mM L-glutamine, 100 units/ml penicillin, 100 µg/ml streptomycin, 50 µM 2-mercaptoethanol. Cells were cultured until ~ 90 % confluent and subcultivated three times weekly at a 1:5 ratio.

Cells were incubated until the desired confluency, washed with Dulbecco's phosphate-buffered saline (DPBS) (14190-094, calcium and magnesium free) and detached from the surface of the flask by incubating with 1 ml of trypsin solution (TripLE Select, 12563011) for 5 minutes at 37 ^{o}C, or by scraping with a Cell Scraper (BD Falcon) in the presence of 1 ml of DPBS. The cell suspension was diluted with 5 ml of media to inactivate the trypsin and centrifuged at 1200 rpm for 2 minutes. Pelleted cells were suspended in the appropriate media and split in a 1:5 ratio.

2.3.2 Mammalian Cell Transfections

Transfections were carried out using TransIT-LT1 Transfection Reagent (MIR 2305, Mirus) following the manufacturer's protocol for adherent cells. Cells were split the day before transfections and incubated as described in 2.3.1 until 50-70 % confluent. Transfection complexes were formulated in Opti-MEM medium (31985-047, Life technologies) using DNA stock range from 1-3 µg/µl and a DNA to reagent ratio of 1:3 (µg:µl). Cells were incubated with the transfection complexes under normal growth conditions for 48-72 hours.

2.3.3 Immunocytochemistry Analysis

Cells were cultured on a round, cover glass (ø18 mm, thickness No. 1.5, VWR) in a 12 well plate (150628, Nunc, Thermo Scientific) with a seeding density of approximately 0.1 x 10^6 cells/well. Cells were washed in PBS and fixed in 4 % paraformaldehyde for 15 minutes at room temperature. After 3 washes (5 minutes each) with PBS, specimens were blocked for 1 hour in Blocking Buffer containing; 5 % (v/v) normal serum from the secondary antibody host species, 0.3 % Triton X-100, in PBS for 60 minutes. Blocking Buffer was removed and cells were incubated with primary antibody diluted in Antibody Dilution Buffer (ADB; 1 % BSA, 0.3 % Triton X-100 in PBS) for 2 hours at room temperature or overnight at 4 ^{o}C. After 3 washes with PBS, specimens were incubated for 2 hours at room temperature with a fluorophore conjugated secondary antibody diluted in ADB. Specimens were washed 3 times with PBS and stained with DAPI (1:100000 dilution) for 10 minutes, then washed again 3 times with PBS and mounted with the media (Prolong Gold Antifade Reagent, P36934, Life technologies). Alternatively, staining with DAPI was replaced by using

mounting media containing DAPI (Prolong Gold Antifade Reagent with DAPI, P36935, Life technologies).

2.3.4 Confocal Laser Microscopy

Immunofluorescence of cells was studied using an LSM 710 NLO Confocal/Multi-photon Microscope (Zeiss, Jena) on an upright Axio-Examiner Z1 stand, equipped with objectives: Plan-apochromat 10x/NA 0.45; Plan-apochromat 20x/NA 0.80; Plan-Neofluar semi-apochromat 40x/NA 1.3 (oil) and Plan-apochromat 63x/NA 1.4 (oil). The microscope was used in single-photon (confocal) mode using the following lasers: near-UV Diode 405-30 (405 nm); Argon-gas (458, 488, 514 nm), Diode-Pumped Solid State 561-10 (561 nm) and HeNe-gas 633 (633 nm). The images were acquired using sequential channels to prevent bleed-through of signal and captured with proprietary photo-multiplier tubes and processed using ZEN 2010 version 6,0,0,485 software (Zeiss, Jena). Pinhole size for each channel was set up to 1 AU. Images were acquired with Frame Scan mode and image size varied from 512-1024 pixels square. Multidimensional acquisition was carried out using Z-stack and Regions function. Further analysis was carried out using Image J version 1.46r (Wayne Rasband, National Institutes of Health).

2.4 Protein Methods

2.4.1 Protein Extraction from Tissue

A ceramic mortar and pestle were pre-chilled with liquid nitrogen (LN) and frozen tissue fragments (~ 0.3 g) were added to the mortar. Tissue was broken into small pieces with the pestle and covered with LN. After LN evaporated, 750 µl of RIPA buffer containing 10 µl/ml protease inhibitor cocktail proteCEASE-50 EDTA-free (786-326G, Biosciences), was added causing the mixture of tissue and buffer to freeze. The mixture was ground with a pestle until it reached the consistency of an ice cream. After, 750 µl of RIPA buffer was added and grinding continued until a clear and colourless mixture was achieved. The mixture was collected into an Eppendorf tube and incubated on ice with 2 µl of 250 units/µl Benzonase Nuclease (E1014-25KU, Sigma-Aldrich) for 20 minutes. Cellular debris were removed by centrifugation at 12 000 rpm (Eppendorf Centrifuge 5417R, F-45-30-11 rotor) for 20 minutes at 4 ^{o}C. The supernatant was collected and stored at -80 ^{o}C until use.

2.4.2 Protein Extraction from Cell Culture

Cell culture dishes were placed on ice and washed with ice-cold PBS. Cells were scraped in the presence of ice-cold RIPA buffer supplemented with 10 µl/ml protease inhibitor cocktail proteCEASE-50 EDTA-free (786-326G, Biosciences). Depending on the size of the cell culture dish, 1 ml per 10^7 cells/ 150 cm^2 flask, or 0.5 ml per $5x10^6$ cells/ 75 cm^2 of RIPA buffer was used. Cells were lysed at 4 ^{o}C for 1 hour maintaining constant agitation. Cellular debris were removed by centrifugation at 12 000 rpm (Eppendorf Centrifuge 5417R, F-45-

30-11 rotor) for 20 minutes at 4 °C. The supernatant was collected and stored at -80 °C until use.

2.4.3 Determination of Protein Concentration

The protein concentration was measured with a commercially available DC Protein Assay (Bio-Rad) following the Microplate Assay Protocol. This is a colorimetric assay in which the colour is developed primarily due to the presence of tyrosine and tryptophan. Twenty microliters of lysates were added to each well and mixed with 25 µl of reagent A' and 200 µl of reagent B. After a 15 minutes incubation at room temperature, the absorbance was read at 750 nm on a Spectra MR spectrometer (DYNEX Technologies). Protein lysates were read against a known bovine serum albumin (BSA) standard curve (serial dilution of 2000, 1500, 1000, 750, 500, 250, 125, 25, and 0 µg/ml).

2.4.4 SDS-PAGE and Immunoblotting Analysis

The SDS-PAGE and immunoblotting were carried out using XCell SureLock™ Mini-Cell with XCell II™ Blot Module (EI0002, Invitrogen). Protein samples (50 µg unless stated otherwise) were prepared with NuPage LDS Sample Buffer (NP0008, Invitrogen), supplemented with NuPAGE® Sample Reducing Agent (NP0009, Invitrogen) and denatured by heating for 10 minutes at 90 °C. Next, samples alongside a Spectra Multicolor Broad Range Protein Ladder (26623, Pierce) were separated on NuPAGE® 4-12 % Bis Tris Gel with 1 X Rapid SDS Run Buffer (NXB50425, RunBlue) for 40 minutes at 200 V constant. Proteins were then transferred from a gel to an Immobilon-P Transfer Membrane (IPVH00010, Millipore,) with 1 X Tris-Glycine buffer supplemented with 20 % (v/v) of methanol for 2 hours at 30 V. The

membrane was blocked overnight at 4 °C with 5 % skimmed milk powder (70166-500G, Sigma Aldrich) in TBST and then incubated for 2 hours with the primary antibodies diluted in 5 % skimmed milk in TBST. Alternatively, the incubation was carried out overnight at 4 °C. Next, the membrane was washed three times for 5 minutes in TBST and incubated for 1 hour with a horseradish peroxidise (HRP) conjugated secondary antibodies diluted in 5 % skimmed milk. After 3 washes with TBST, proteins were revealed by Amersham ECL Western blotting detection reagent (RPN2109, GE Healthcare) using Xograph Film Processor and Hyperfilm ECL autoradiography film (Amersham, GE Healthcare).

2.4.5 In-Gel Digestion of Proteins Separated by SDS-PAGE

All the procedures were carried out at room temperature, unless indicated otherwise. After SDS-PAGE, the gel was stained for 2 hours with Instant Blue (ISB1LUK, Expedeon) and gel pieces containing the protein of interest were cut out, placed in an Eppendorf tube and washed overnight with 200 µl of wash solution (50 % methanol, 5 % acetic acid in water). The following day, wash solution was replaced and the gel pieces were incubated for additional 3 hours. Next, the gel pieces were incubated for 5 minutes with 200 µl acetonitrile and dried in a Savant SpeedVac SPD 101B (Thermo Scientific). Then, the protein was reduced with 30 µl of 10 mM DTT for 30 minutes, and subsequently alkylated with 30 µl of 100 mM iodoacetamide for 30 minutes (for ubiquitination analysis, protein was alkylated with chloroaceramide). After another incubation with acetonitrile, the gel pieces were dried, rehydrated for 10 minutes in 200 µl of 100 mM ammonium bicarbonate and then incubated with acetonitrile and dried. Afterwards, the gel pieces were rehydrated with 30 µl of trypsin (20 ng/µl in ice cold, 50 mM ammonium bicarbonate) for 10 minutes. Next, the excess of trypsin was removed, 5 µl of 50 mM ammonium bicarbonate was added and the digestion of the protein in the gel pieces was carried out overnight at 37 °C. The next

day, the digested protein was extracted by three subsequent 10 minutes incubations with: 60 µl of 50 mM ammonium bicarbonate, 60 µl of Extraction Buffer I (50 % methanol, 5 % acetic acid in water) and 60 µl of Extraction Buffer II (85 % methanol, 5 % acetic acid in water). All supernatants were combined and the volume was reduced to < 20 µl by evaporation in a SpeedVac. Next, the volume of digest was adjusted to ~20 µl with 5 % acetonitrile and 0.1 % formic acid in water. Finally, samples were sonicated for 15 minutes in an Ultrasonic bath (Ultrawave Ltd.), centrifuged for 20 minutes at 4 ^{o}C at 13200 rpm and transferred to the new tubes.

2.4.6 Liquid Chromatography–Tandem Mass Spectrometry (LC-MS/MS)

For the analysis of in-gel digested protein material, liquid chromatography was performed using an Ultimate 3000 nano-HPLC system (Dionex) comprising a WPS-3000 micro auto sampler, a FLM-3000 flow manager and column compartment, a UVD-3000 UV detector, an LPG-3600 dual-gradient micro-pump, and an SRD-3600 solvent rack controlled by Hystar (Bruker Daltonics) and DCMS link 2.0 software. Samples were concentrated on a trapping column Dionex (Sunnyvale), 300 µm i.d., 0.1 cm) at a flow rate of 20 µl/min. For the separation with a C18 Pepmap column (75 µm i.d., 15 cm, Dionex), a flow rate of 250 nl/min was used as generated by a cap-flow splitter cartridge (1/1000). Peptides were eluted by the application of a 30 minutes multi-step gradient using solvents A (98 % H2O, 2 % acetonitrile, 0.1 % formic acid) and B (80 % acetonitrile, 20 % water, 0.1 % formic acid):

Composition (% solvent B)	**Run time (min)**
2-10	0-3

Composition (% solvent B)	Run time (min)
10-25	3-18
25-50	18-30
50-90	30-30.2

The liquid chromatography was interfaced directly with a 3D high capacity ion trap mass spectrometer (amaZon; Bruker Daltonics) utilizing 10 µm i.d. distal coated SilicaTips (New Objective) and nano-ESI mode. SPS parameter settings on the ion trap were tuned for a target mass of 850 m/z, compound stability 100 % and a smart ICC target of 250,000. MS/MS analysis was initiated on a contact closure signal triggered by HyStar software (version 3.2). Up to five precursor ions were selected per cycle with active exclusion (0.5 min) in collision-induced dissociation (CID) mode. CID fragmentation was achieved using helium gas and a 30 %–200 % collision energy sweep with amplitude 1.0 (ions are ejected from the trap as soon as they fragment).

2.4.7 LC-MS/MS Data Processing and Database Searching

Raw LC-MS/MS data were processed and Mascot compatible files were created using DataAnalysis 4.0 software (Bruker Daltonics). Database searches were performed using the Mascot algorithm (version 2.4) and the UniProt_SwissProt database with *Mus musculus* or mammalian taxonomy restriction. The following parameters were applied: 2+, 3+ and 4+ ions, peptide mass tolerance 0.3 Da, 13C = 2, fragment mass tolerance 0.6 Da, number of missed cleavages: two, instrument type: ESI-TRAP, fixed modifications: Carbamidomethylation (Cys), variable modifications: Oxidation (Met). Additionally variable modification of GlyGly (K) was chosen when studying protein ubiquitination. The ions score significance threshold was chosen to be 0.05.

2.4.8 Dynabeads M210 Epoxy and Antibody Coupling

Prior to the coupling, the antibody stock was centrifuged at 16000 g for 10 minutes at 4 °C to remove any precipitation. The coupling reaction was carried out using a Dynabeads Antibody Coupling Kit (14311D, Invitrogen) following the antibody coupling protocol. In the reaction, 7.5 mg of Dynabeads M210 Epoxy and 52.5 µg of each antibody were used. The final concentration of the antibody-coupled beads was adjusted to 10 mg of antibody coupled beads/ml.

2.4.9 Cryolysis of Cultured Mammalian Cells

Cells were cultured in Nuclon Dishes (Thermo Scientific, 166508) to 90 % confluence, washed in PBS, scraped and centrifuged for 10 minutes at 500 g, 4 °C. Then, the cell pellet was washed twice with 50 ml of ice cold 20 mM HEPES (pH 7.4), supplemented with 1 mM phenylmethanesulfonylfluoride (PMSF), and centrifuged for 10 min at 500 g, 4 °C. The cells were centrifuged again for 10 minutes at 500g, 4 °C and the remaining buffer was removed. Next, the cell pellet was weighed, transferred to a syringe without a needle and pressed into liquid nitrogen (LN) immediately freezing into “noodles”. After the LN was removed the tube containing the cell noodles was left opened at -80 °C to evaporate remaining LN. Next, the cell noodles were lysed by manual cryogrinding using a mortar and pestle immersed in LN. All equipment, tools and tubes used in this procedure were chilled in LN prior to the lysis. Finally, the cell powder was transferred to a 50 ml falcon tube and stored at -80 °C until use.

2.4.10 Co-Immunoprecipitation Using Dynabeads Epoxy and Cryolysis

Co-Immunoprecipitation was performed using Dynabeads® Co-Immunoprecipitation Kit (143-21D, Invitrogen,). For co-immunoprecipitation that would be analysed by Coomassie staining and mass spectrometry, at least 3.5 g of the cell powder was weighed, allowed to thaw to an ice-cream consistency and resuspended by vortexing (30 seconds) in Extraction Buffer (1 x IP buffer with varying NaCl concentrations and presence of $MgCl_2$, DTT and DNase) at a 1:9 ratio of cell powder to Extraction Buffer. Then, the lysate was centrifuged at 2600 g for 5 minutes at 4 ^{o}C and the supernatant was immediately used for co-immunoprecipitation. In parallel, 7.5 mg of the antibody-coupled beads were washed with 900 µl of Extraction Buffer. Washed beads were resuspended in the cell lysate and incubated on a rotator for 60 minutes at 4 ^{o}C. Next, the beads were separated on a magnetic rack and the depleted material was collected. Subsequently, the beads were washed 3 times with 900 µl of Extraction Buffer, followed by a 5 minutes wash with 900 µl of Last Wash Buffer supplemented with 0.02 % Tween 20. Optionally, additional three washes with Last Wash Buffer without Tween 20 were applied. Co-immunoprecipitated protein was eluted from the beads in two serial elutions with High PH Elution Buffer (HPH EB; 0.5 M NH_4OH, 0.5 mM EDTA). In each elution, 500 µl of HPH EB was incubated at room temperature for 10 min with rotation. Eluents were combined and dried overnight using SpeedVac. The lyophilised protein was solubilised in 100 µl of SDS-PAGE Sample Loading Buffer and stored at 4 ^{o}C. In each experiment, control Co-IP was performed in parallel using rabbit anti-GFP (A-11122, Invitrogen) antibody-coupled beads.

For co-immunoprecipitation that would be analysed by immunoblotting at least 0.5 g of the cell powder was used and 1.5 mg of the antibody-coupled beads. The samples were processed as described above, although 200 µl of Extraction Buffer and 200 µl of Last Wash

Buffer (with and without Tween 20) were used for washing. Additionally, precipitated protein were eluted from the beads with 60 µl of Elution Buffer (included by the manufacturer). Eluents were used for immunoblotting analysis without concentration in SpeedVac.

3 Study of FTO Subcellular Localisation

3.1 Introduction

Most of the proteins in a cell are synthesized on the ribosomes in the cytosol and must be transported to a specific subcellular compartment in order to fulfill their biological role (Alberts et al. 2002, p.149). Thus, to fully understand a function of a specific protein, it is essential to know the compartments to which the protein is localised, and understand how the protein is moved from the cytoplasm to its final subcellular destination.

Initial studies showed exclusive nuclear localisation of FTO protein (Gerken et al. 2007; Church et al. 2009; Fischer et al. 2009). This was consistent with the proposed role of FTO in Fe(II)- and 2OG-dependent demethylation of 3-methylthymine in single-stranded DNA and 3-methyluracil in single-stranded RNA (Gerken et al. 2007; Jia et al. 2008). The presence of a putative nuclear localisation signal (NLS) in the FTO sequence (Peters, Ausmeier, and Rüther 1999; Meyer et al. 2012), further strengthened the association of FTO function with the nucleus.

Subsequent *in vitro* and *in vivo* studies have focussed attention on the activity of FTO towards N6-methyladenosine (m^6A) in ssRNA, and suggested partial FTO localisation to nuclear speckles and an association with nuclear pre-mRNA splicing components (Jia et al. 2011). Initially poorly understood, methylation of the N6 position of adenosine in now known to be the most widespread modification of eukaryotic mRNA, and m^6A demethylation by FTO is thought to affect aspects of mRNA metabolism and processing

including nuclear export and subcellular localisation, translation, stability and degradation (Meyer et al. 2012; Jia, Fu, and He 2013; Meyer and Jaffrey 2014; Zhao et al. 2014).

However, the current model of mRNA metabolism and processing involves cycling of mRNA between different subcellular compartments, many of which are located outside of the nucleus, in the cytoplasm (e.g. stress granule, translation initiation complex, processing-bodies), (Parker and Song 2004; Meyer, Temme, and Wahle 2004; Parker and Sheth 2007). Moreover, the recently demonstrated recruitment of m^6A-modified mRNA to processing bodies (p-bodies) for decay (Wang et al. 2014) further focuses attention on events taking place in the cytosol. This raises the question of whether FTO can also act on cytosolic mRNA and regulate cytosolic mRNA processing. However, this idea is in conflict with the nuclear FTO localisation previously reported.

Therefore, I studied the subcellular localisation of FTO to help to understand the functional role of FTO within the cell.

The specific aims included:

1) Computational prediction of FTO subcellular localisation.
2) Analysis of cellular fractions to localise FTO protein.
3) Investigating the localisation of FTO during the cell cycle.

3.2 Methods

3.2.1 Computational Analysis of FTO Amino Acid Sequence

The reference amino acid sequence of FTO in FASTA format was used in these analyses. Prediction analyses were performed using WoLF PSORT ('WoLF PSORT' 2014), an extended version of PORTII (Horton et al. 2007). Based on the localisation features within the FTO sequence and the amino acid composition, the software created numerical localisation features, which were then converted to weighted k-nearest neighbor classifier. This classifier was used for the prediction analysis. Importantly, this system does not depend on BLAST protein sequence homology. A one line prediction summary was given by the software and included the top three predicted subcellular localisations and their scores. Additionally, the software produced a detailed list of analysis outcomes for each of the important localisation features as well as a list of known protein with the most similar localisation features to FTO.

Prediction of subcellular localisation was also performed using CELLO v2.5 ('CELLO: Subcellular Localisation Predictive System' 2014; Yu et al. 2006; Yu, Lin, and Hwang 2004). CELLO used a two-level support vector machine (SVM) system to generate probable FTO localisation: the first level created a set of classifiers based on the feature vectors generated from the amino acid sequence. The second level, which consists of a jury system, produced the output probability distribution of decisions for possible localisations. This system also does not depend on BLAST protein sequence homology.

Searching for the nuclear localisation signal (NLS) specific to the importin α-β pathway was performed by the NLS Mapper ('NLS Mapper' 2014; Kosugi et al. 2009). The reference data set included four profiles of NLSs, generated by extensive amino acid replacement analysis of each of four NLS classes (class 1/2, class 3, class 4, and bipartite). The final NLS score generated by the software was based on the contribution of every amino acid residue at every position within a specific NLS class to the final NLS activity. No cut-off for the NLS score was used in the analysis.

The NetNES 1.1 Server ('NetNES 1.1 Server' 2014), was used to search for possible leucine-rich nuclear export signals NESs specific to exportin 1 (XPO1), mediator of the nuclear export (Cour et al. 2004). The software utilised the Artificial Neural Network (ANN) as well as the Hidden Malkov Models (HMM) in the analysis to generate final NES score for each residue of FTO sequence. The residues with the NES score higher than 0.5 were considered valid for the prediction.

3.2.2 Nuclear Extraction at the Interface of Two Sucrose Solutions

All the procedures were performed at 4 ^{o}C and the solutions contained 1 mM PMSF. Mouse liver HEPA1-6 cells were trypsinised, washed with PBS and centrifuged at 1400 rpm for 4 minutes. The cell pellet was resuspended in 5 volumes of hypo-osmotic medium (10 mM Tris, 10 mM Na_2HPO_4, pH 8) and homogenised with a homogeniser (0.076-0.126 mm, Jencons), (25 strokes). Next, 2 volumes of nuclear isolation medium NIM (0.25 M sucrose, 2.5 mM KCl, 5mM $MgCl_2$, 10 mM Tris, pH 7.4) were added and the mixture was centrifuged at 800 g for 10 minutes. The supernatant, consisting of the cytoplasmic fraction, was collected and the pellet was resuspended in 8 ml of NIM and mixed thoroughly with 16 ml

of sucrose dense buffer (SDB, 2.3 M sucrose, 25 mM KCl, 5 mM Tris, pH 7.4). The mixture was carefully deposited on top of 8 ml of SDB and centrifuged at 100000 g for one hour in SW 32 Ti Swinging-Bucket Rotor (Beckman Coulter). Purified nuclei floating at the interface of two sucrose solutions were carefully removed and resuspended in Resuspension Buffer (200 mM Hepes, 250 mM sucrose, 1 mM $MgCl_2$, pH 8.5). After 30 minutes of centrifugation at 1400 rpm, the nuclear pellet was resuspended in Non-denaturing Buffer (137 mM NaCl, 1 % NP-40, 2 mM EDTA, 20 mM Tris HCl, pH 8) and nuclei were examined under the microscope. Next, nuclei were lysed by five, 5 seconds cycles in sonicator bath followed by 1 hour incubation with constant agitation. The nuclear extract was centrifuged at 14000 rpm for 10 minutes to remove nuclear debris.

3.2.3 Ultracentrifugation through a Dense Sucrose Cushion

All the procedures were performed at 4 ^{o}C and the solutions contained 1 mM PMSF. Mouse liver HEPA1-6 cells were washed in PBS and scraped in the presence of 9 volumes of Homogenisation Buffer (0.25 M sucrose, 5 mM $MgCl_2$, 10 mM Tris-HCl, pH 7.4). The cells were homogenised with 10 vigorous stokes using a homogeniser (0.076-0.126 mm, Jencons) and centrifuged at 600 g for 10 minutes. The supernatant consisting of the cytoplasmic fraction was collected, the crude nuclear pellet containing membranes and mitochondria was resuspended in half of the original volume of homogenisation buffer and centrifuged again at 600 g for 10 minutes and the supernatant was collected. The obtained crude nuclear pellet was resuspended in 9 volumes of Ultracentrifuging Medium (2.2 M sucrose, 1 mM $MgCl_2$, 10 mM Tris-HCl, pH 7.4) and further homogenised with 5 vigorous stokes using the homogeniser. The suspension of nuclei was then centrifuged at 80000 g for 80 min in SW 32 Ti Swinging-Bucket Rotor (Beckman Coulter) and the supernatant carefully removed. The nuclear pellet was resuspended in 0.5 ml of Non-denaturing Buffer

and isolated nuclei were examined under the microscope. Next, the nuclei were lysed by 3 hour incubation on a shaker followed by five, 5 seconds cycles in a sonicator bath. The nuclear extract was centrifuged at 14000 rpm for 10 min to remove nuclear debris.

3.2.4 Immunoblotting Analysis

Immunoblotting was performed as described in 2.4.4 using the antibodies listed in **Table 5**.

Table 5. Antibodies used for immunoblotting analysis in the experiments described in Chapter 3. Antibodies were used in pairs (e.g. A1 with B1, A2 with B2).

Label	Name	Dilution	Source	Cat. Number
A1	rabbit anti-FTO	1:500	raised in-house	
B1	anti-rabbit-HRP	1:2500	GE Healthcare	NA934
A2	rabbit anti-GAPDH	1:800	Santa Cruz	Sc-25778
B2	anti-rabbit-HRP	1:10000	GE Healthcare	NA934
A3	rabbit anti-OCT-1	1:100	Santa Cruz	Sc-232
B3	anti-rabbit-HRP	1:8000	GE Healthcare	NA934
A4	mouse anti-FTO6-1	1:2500	MAb Technologies	Fto06-1
B4	anti-mouse-HRP	1:2500	GE Healthcare	NA931

3.2.5 Immunocytochemistry Analysis

Cells were subjected to the immunocytochemistry analysis according to the protocol described in 2.3.3. Combinations of antibodies used in the experiments described in Chapter 3 are listed in **Table 6**.

Table 6. Antibodies used in the immunocytochemistry analysis in Chapter 3. Antibodies were used in pairs (e.g. A1 with B1, A2 with B2).

Label	Name	Dilution	Source	Cat. Number
A1	rabbit anti-FTO	1:100	raised in-house	
B1	anti-rabbit Alexa-488	1:400	Life Technologies	A-11034
A2	mouse anti-LAMIN A/C	1:35	Cell Signalling	4777
B2	anti-mouse Alexa 680	1:100	Life Technologies	A-21057

3.3 Results

3.3.1 Computational Prediction of the Subcellular Localisation of FTO

Computational analysis of a specific protein sequence can provide important information about the possible distribution of a protein within subcellular compartments and predict the mechanisms of protein trafficking between the compartments. Thus it can help understand the function of the protein within the cell and therefore I analyzed the mouse FTO amino acid sequence (**Figure 6**).

```
        10         20         30         40         50         60
MKRVQTAEER EREAKKLRLL EELEDTWLPY LTPKDDEFYQ QWQLKYPKLV FREAGSIPEE

        70         80         90        100        110        120
LHKEVPEAFL TLHKHGCLFR DVVRIQGKDV LTPVSRILIG DPGCTYKYLN TRLFTVPWPV

       130        140        150        160        170        180
KGCTVKYTEA EIAAACQTFL KLNDYLQVET IQALEELAVR EKANEDAVPL CMAEFPRAGV

       190        200        210        220        230        240
GPSCDDEVDL  SRAAYNVTL LNFMDPQKMP YLKEEPYFGM GKMAVSWHHD ENLVDRSAVA

       250        260        270        280        290        300
VYSYSCEGSE DESEDESSFE GRDPDTWHVG FKISWDIETP GLTIPLHQGD CYFMLDDLNA

       310        320        330        340        350        360
THQHCVLAGS QPRFSSTHRV AECSTGTLDY ILERCQLALQ NVLNDSDDGD VSL SFDPAV

       370        380        390        400        410        420
LKQGEEIHNE VEFEWLRQFW FQGNRYKLCT DWWCEPMTHL EGLWKKMESM TNAVLREVKR

       430        440        450        460        470        480
EGLPVEQRSE ILSAILVPLT VRQNLRKEWH ARCQSRVVRT LPVQQKPDCR PYWE DDPSM

       490        500
PLPFDLTDVV SELRGQLLEA RS
```

Figure 6. Amino acid sequence of mouse FTO in one letter code. Numbers represent the amino acid location within the protein sequence.

First, I used WoLF PSORT ('WoLF PSORT' 2014), a recently updated version of PSORT II, which performs an extensive amino acid sequence analysis and prediction of eukaryotic proteins (Horton et al. 2007). The results of the analysis of the mouse FTO sequence are summarized in **Table 7** and the full results are included in the Appendix 3.1.

The one line summary of the results provided by the software revealed a nearly identical score for cytoplasmic localisation alone (score 15.5) and for both cytoplasmic and nuclear localisation (score 15). The third score was for the nuclear localisation alone (13.5) although it is similar to the previous scores. The scores represent the approximate number of nearest neighbors to the studied protein found in the software database, which localise to specific subcellular compartments adjusted for the possibility of multiple localisations. The sequence alignment analysis of important localisation features provided a list of 32 neighboring proteins that have localisation sequences most similar to that of FTO (**Table Appendix 1**). The protein with the most similar localisation features and a percentage of amino acid sequence identify of ~14 %, was human NF-kappa-B essential modulator (NEMO, also known as IKK-γ), (**Figure 7**), which is known to be localised to both the cytoplasm and the nucleus, and whose nuclear export is promoted by monoubiquitination on Lys-277 and Lys-309 (Huang et al. 2003). Comparison of Normalised Feature Values between FTO and NEMO (data not shown) indicated that the different lysine content of the protein (FTO-53 lysines; NEMO-74 lysines) could result in the pattern of localisation differing between FTO and NEMO. Further analysis did not identify any signalling motifs. Additionally, no motifs were found that suggested FTO was sorted through the vesicular pathway, or retained in the endoplasmic reticulum (ER), peroxisomes or Golgi.

Table 7. Summary of the mouse FTO protein sequence analysis using WoLF PSORT.

Analysis	Evaluation (method specific)	Answer
Signal peptide prediction	-4.40	Not sorted through the vesicular pathway
Predicted number of transmembrane segments	0	Not a transmembrane protein
Recognition of mitochondrial targeting signals	-5.39	Not a mitochondrial protein
Recognition of classical type nuclear localisation signal	Pat4:0 Pat7:0	Not a nuclear protein
Recognition of bipartite type nuclear localisation signal	11.6%	Both nuclear and cytoplasmic protein
Detection of ER retention motif in the C-terminus	0	Not retained in ER
Detection of ER membrane retention signals	0	Not retained in ER membrane
Detection of peroxisomal targeting signal in the C-terminus	0	Not localised to peroxisomes
Detection of possible vacuolar targeting motif	0	Not a vacuolar protein
Detection of actinin-type actin-binding motif (type 1 and type 2)	0	Not a cytoskeletal protein
Detection of N-myristoylation pattern	0	Not N-myristoylated/palmitylated
Detection of farnesylation/ geranylgeranylation motif	0	Not farnesylated/geranylgeranylated
Detection of transport motif from cell surface to Golgi	0	Not transported to Golgi

Figure 7. Sequence alignment of mouse FTO with NF-kappa-B essential modulator (NEMO). Numbers represent amino acid location within the protein sequence. Starts represent residues identical in both sequences. Alignment was performed using ClustalW2 ('ClustalW2, Multiple Sequence Alignment, EMBL-EBI' 2015).

Finally, nuclear localisation signal (NLS) analysis did not identify any monopartite types of NLS (from SV40 large T antigen) in mouse FTO, although it did detect a bipartite type of NLS (from nucleoplasmin of Xenopus) with the amino acid sequence KRVQTAEEREREAKKLR (aa 2-19). The basic residue content of the identified bipartite NLS was 11.6%. A protein is considered by WoLF to have a higher probability of being localised to the nucleus than cytoplasm if the basic residue content is higher than 20%. The bipartite NLS identified by WoLF corresponds to the putative NLS in human FTO reported by Meyre et al (KRTPTAEEREREAKKLRL, aa 2-19), (Meyre et al. 2010), although the basic residue content does not suggest a high probability of nuclear localisation - rather it implies both cytoplasmic and nuclear localisation.

Next, for comparison, I performed a simple analysis of possible mouse FTO subcellular localisations using another prediction software package called CELLO v2.5 ('CELLO' 2014; Yu et al. 2006; Yu, Lin, and Hwang 2004). The analysis predicted the cytoplasm as the most probable FTO localisation site (**Table 8**). Interestingly, CELLO analysis of human FTO (**Table Appendix 2**) revealed that the N-terminal peptide composition suggested a nuclear localisation, rather than a cytoplasmic localisation as predicted for mouse FTO. Additionally, the overall prediction score obtained for nuclear localisation was higher for human FTO (1.353) than mouse FTO (0.996). This may be due to differences in amino acid sequences in the N-terminal domain of human and mouse FTO (**Figure Appendix 1**).

Table 8. Analysis report of mouse FTO sequence performed by CELLO v2.5.

Analysis	LOCALISATION	RELIABILITY
Amino Acid Composition	Cytoplasmic	0.608
N- terminal peptide Composition	Cytoplasmic	0.614
Partitioned sequence Composition	Cytoplasmic	0.694
Physico-chemical Composition	Cytoplasmic	0.704
Neighbouring sequence Composition	Cytoplasmic	0.757
CELLO Prediction:	LOCALISATION	SCORE
1	Cytoplasmic	3.378
2	Nuclear	0.996
3	Extracellular	0.155
4	Mitochondrial	0.134
5	ER	0.114
6	Peroxisomal	0.065
7	Golgi	0.065
8	Chloroplast	0.044
9	PlasmaMembrane	0.018
10	Lysosomal	0.016
11	Cytoskeletal	0.009
12	Vacuole	0.007

Overall, the results of computational analysis by WoLF and CELEO predicted that FTO could be localised to both the cytoplasm and the nucleus. This raises the question of whether FTO might shuttle between the nucleus and the cytoplasm. Because nucleocytoplasmic shuttling is controlled by the nuclear localisation signal (NLS) and the nuclear export signal (NES), I next performed a separate detection analysis on the mouse FTO amino acid sequence to search for possible NLS and NES signals.

To analyse the NLS of FTO in more detail, I used the NLS Mapper ('NLS Mapper' 2014), which predicts NLSs recognised by the importin α-β pathway (Kosugi et al. 2009). The analysis output ranked the activity of detected monopartite and bipartite NLSs on a scale from 1- 10, with the top score (10) indicating the highest probability of the NLS resulting in exclusively nuclear localisation, and the lowest score (1) indicating the highest probability of exclusively cytoplasmic localisation (**Figure 8**). One monopartite NLS was found (REREAKKLRLLEE -marked in green) at aa 10-22: however the score (6) predicted localisation to both cytoplasm and nucleus (**Figure 8 A, B**). Additionally, 16 bipartite NLSs were identified (marked in red). One of these, that was highly similar to the NLS identified by WoLF (KRVQTAEEREREAKKLRL), was ranked by NLS Mapper as 10, indicating the highest probability of an exclusively nuclear localisation (**Figure 8 A, B**). This signal can be considered as a true NLS.

A

```
MKRVQTAEEREREAKKLRLLEELEDTWLPYLTPKDDEFYQQWQLKYPKLV     50
FREAGSIPEELHKEVPEAFLTLHKHGCLFRDVVRIQGKDVLTPVSRILIG     100
DPGCTYKYLNTRLFTVPWPVKGCTVKYTEAEIAAACQTFLKLNDYLQVET     150
IQALEELAVREKANEDAVPLCMAEFPRAGVGPSCDDEVDLKSRAAYNVTL     200
LNFMDPQKMPYLKEEPYFGMGKMAVSWHHDENLVDRSAVAVYSYSCEGSE     250
DESEDESSFEGRDPDTWHVGFKISWDIETPGLTIPLHQGDCYFMLDDLNA     300
THQHCVLAGSQPRFSSTHRVAECSTGTLDYILERCQLALQNVLNDSDDGD     350
VSLKSFDPAVLKQGEEIHNEVEFEWLRQFWFQGNRYKLCTDWWCEPMTHL     400
EGLWKKMESMTNAVLREVKREGLPVEQRSEILSAILVPLTVRQNLRKEWH     450
ARCQSRVVRTLPVQQKPDCRPYWEKDDPSMPLPFDLTDVVSELRGQLLEA     500
RS                                                      502
```

B

Predicted monopartite NLS		
Pos.	Sequence	Score
10	REREAKKLRLLEE	6
Predicted bipartite NLS		
Pos.	Sequence	Score
2	KRVQTAEEREREAKKLRL	10
10	REREAKKLRLLEELEDTWLPYLTPKDDEFYQQW	2.5
45	KYPKLVFREAGSIPEELHKEVPEAFLTLH	2
48	KLVFREAGSIPEELHKEVPEAFLTLHKHGCL	3.4
71	TLHKHGCLFRDVVRIQGKDVLTPVSRILI	2.4
71	TLHKHGCLFRDVVRIQGKDVLTPVSRILIGD	3.3
80	RDVVRIQGKDVLTPVSRILIGDPGCTYKYLNTRLFT	2.1
350	DVSLKSFDPAVLKQGEEIHNEVEFEWLRQFW	2.8
357	DPAVLKQGEEIHNEVEFEWLRQFWFQGNRYKL	2.6
377	RQFWFQGNRYKLCTDWWCEPMTHLEGLWKKME	2.7
377	RQFWFQGNRYKLCTDWWCEPMTHLEGLWKKMESMT	2.2
384	NRYKLCTDWWCEPMTHLEGLWKKME	3
384	NRYKLCTDWWCEPMTHLEGLWKKMESMTNA	2.2
416	REVKREGLPVEQRSEILSAILVPLTVRQN	2.1
416	REVKREGLPVEQRSEILSAILVPLTVRQNL	3.5
442	RQNLRKEWHARCQSRVVRTLPVQQKPDCRPYWE	2.2

C

Scores	10	9	8	7	6	5	4	3	2	1
Type	N	N>>Nc	N>Nc	Nc	Nc>NC	Nc<NC	NC	NC>C	NC<C	C

Figure 8. NLSs identified by detection analysis using NLS Mapper. A; Amino acid sequence of mouse FTO in one letter code with NLSs identified by NLS Mapper marked in green and red. Numbers represent amino acid location within the protein sequence. **B**; Predicted mono and bipartite NLSs. Pos – starting amino acid position of specific NLS. **C**; Score representation of subcellular localisation. N, exclusively nuclear; Nc, partially nuclear; NC, localised into both the nucleus and the cytoplasm in a similar extent; C, exclusively cytoplasmic.

To detect NES sequences I used NetNES 1.1 Server ('NetNES 1.1 Server' 2014), which searched for possible leucine-rich NESs that are recognised by exportin 1 (XPO1), an evolutionary conserved receptor mediating nuclear export (la Cour et al. 2004), (**Figure 9**). The graphical representation of NES scores (red) obtained in the analysis for each of the FTO residues showed that lysine 339 had an NES score higher than threshold (NES score 0.516, threshold 0.5). However, no other residues around lysine 339 had an NES score that passed threshold. This means that the software did not identify any leucine-rich NES that could be recognised by the XPO1.

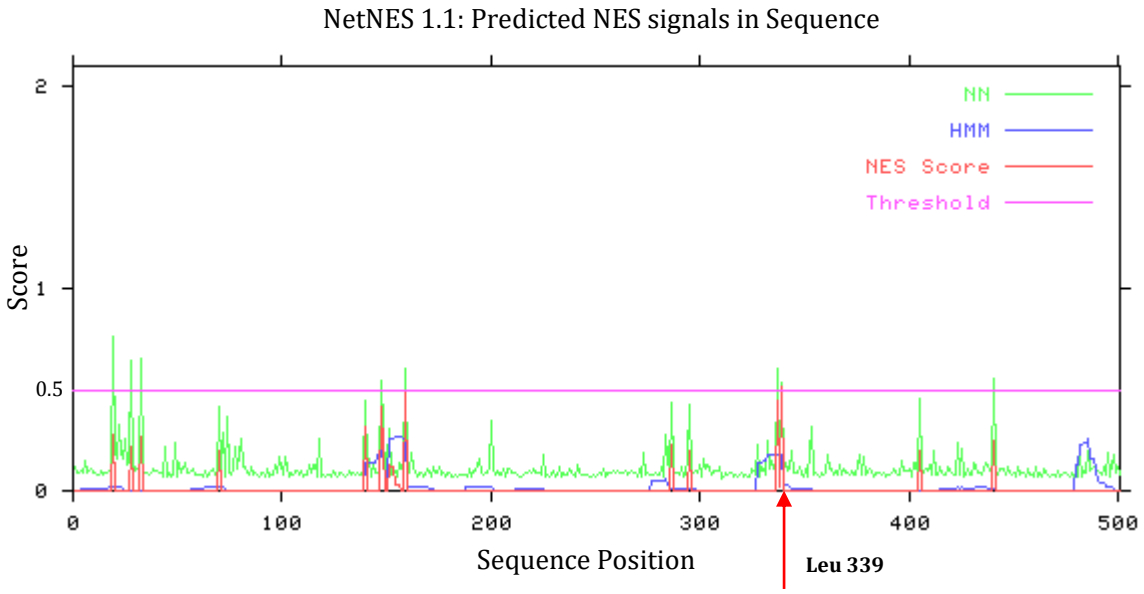

Figure 9. Output of the NES detection analysis for mouse FTO using NetNES 1.1. Graphical plot of the NES score values given by the software for each residue of FTO. The software calculated the NES scores using Artificial Neural Network (NN) scores and Hidden Markov Model (HMM) scores which are also presented in green and blue respectively. Only NES scores higher than threshold (0.5) are considered in the NES prediction.

In summary, the computational analysis of the mouse FTO amino acid sequence predicted a possible FTO localisation to both the cytoplasm and the nucleus. Furthermore, a bipartite NLS was identified predicting that FTO could be imported to the nucleus by the importin α-β pathway. However, no NES recognised by XPO1 was detected. This implies that if FTO was

to be exported from the nucleus, there is a low probability it would happen through direct interaction with XPO1, perhaps by interaction with another helper protein which has an NES in the amino acid sequence.

Overall, these results contrast with earlier experimental data showing exclusive nuclear localisation of FTO (Gerken et al. 2007; Church et al. 2009; Fischer et al. 2009). These data indicate that cytoplasmic localisation of FTO is theoretically possible, but this has yet to be experimentally demonstrated. Thus, I decided to experimentally investigate the distribution of FTO in the cytoplasm and the nucleus.

3.3.2 FTO Was Detected in the Cytoplasmic Fraction Isolated by Ultracentrifugation

To test the hypothesis that FTO can be localised to both the cytoplasm and the nucleus I isolated subcellular fractions of HEPA1-6 liver cells and compared the amount of FTO protein in the cytoplasmic and the nuclear fractions. I used two different fractionation protocols based on ultracentrifugation. In both protocols, cells were broken by liquid sheering using a homogeniser. Since EDTA can make the nuclei fragile and cause DNA leakage (Graham and Rickwood 1997), it was not included in nuclear isolation medium. Instead, $MgCl_2$ was included to improve nuclear integrity and the ultracentrifugation medium contained ~2 M sucrose to minimalize leaching of nuclear proteins.

Testing FTO nuclear localisation: Nuclear extraction at the interface of two sucrose solutions – hypo-osmotic method.

In the first protocol, I used a hypo-osmotic medium to stress the cells osmotically before homogenisation. Next, nuclei were isolated by ultracentrifugation using extraction at the interface of two sucrose solutions (3.2.2). The isolated cytoplasmic and nuclear fraction, as well as the resuspension buffer used to wash the isolated nuclei prior to lysis, were analysed by SDS-PAGE and immunoblotting (2.4.4). Total cell lysate was used as a positive control. Glyceraldehyde-3-phosphate dehydrogenase (GAPDH) and octamer-binding protein 1 (OCT-1) were chosen as markers for the cytoplasmic and the nuclear fraction respectively. The presence of FTO was detected using an in-house rabbit anti-FTO antibody, while the presence of GAPDH and OCT-1 was detected using commercially available rabbit anti-GAPDH and rabbit anti-OCT antibody (3.2.4).

The immunoblotting results of nuclear isolation at the interface of two sucrose solutions (**Figure 10, Figure Appendix 2**) showed a band indicating that GAPDH (a cytoplasmic marker) was present in all subcellular fractions, the resuspension buffer and the total cell lysate, while the nuclear marker OCT-1 was found in the nuclear fraction and the total cell lysate. When probed with an anti-FTO antibody, two distinct bands were observed in the nuclear fraction (~55 kDa and ~62 kDa) and one band (of 58 kDa) in the cytoplasmic fraction and total cell lysate. No FTO band was detected in the nuclei resuspension buffer.

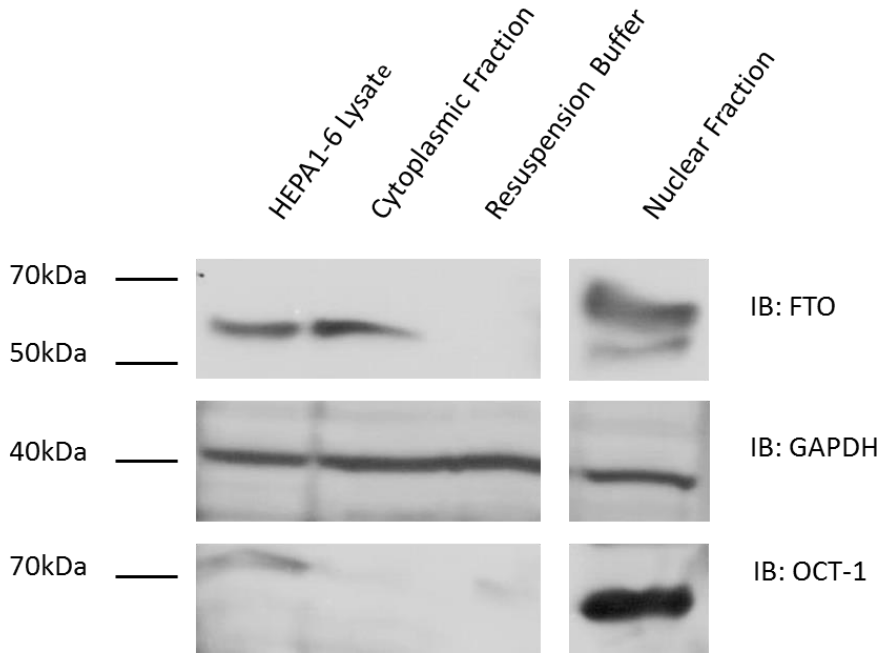

Figure 10. Immunoblotting analysis of subcellular fractions obtained by the nuclear extraction at the interface of two sucrose solutions. The protein concentration of each of the fractions was assessed by a colorimetric assay (2.4.3) and 50 µg of each samples was loaded in each well. IB, Immunoblotting using specific antibody- in house raised rabbit anti-FTO, rabbit anti-GAPDH, rabbit anti-OCT1 (3.2.4).

The results indicate that the majority of FTO was present in the isolated nuclei but some was also present in the cytoplasmic fraction. The presence of a strong OCT-1 band in the nuclear fraction and the absence of the band in the cytoplasmic fraction suggests that the experiment resulted in the successful isolation of intact nuclei. Moreover, the presence of GAPDH in the nuclear fraction suggests that the nuclei were purified with the outer nuclear membrane, which is continuous with the endoplasmic reticulum. The contamination of cytoplasmic markers is commonly found in the nuclear fractions (Graham and Rickwood 1997) unless the nuclear membranes are removed by detergent or a modified protocol is used.

Testing FTO nuclear localisation: Ultracentrifugation through a dense sucrose cushion– isotonic method.

In order to avoid cytoplasmic contamination of nuclear fractions, I next applied a modified protocol based on ultracentrifugation through a dense sucrose cushion (3.2.3). Briefly, cells were homogenised in isotonic medium containing 0.25 M sucrose which should cause the rough and smooth ER to vesiculate (Graham and Rickwood 1997). Since nuclei are very delicate in this medium, the number of strokes of the homogeniser was reduced from 25 to 10. Two simple differential pelleting steps gave a crude nuclear pellet and a supernatant containing the contaminating membranes and mitochondria. In order to further remove the membrane contamination, the crude nuclear pellet was subjected to an additional five strokes in a homogeniser and then ultracentrifugation through a dense sucrose cushion. Only pure nuclei without outer membranes should pellet at the bottom of the ultracentrifugation tube. Collected fractions were analysed by SDS-PAGE and immunoblotting (**Figure 11**).

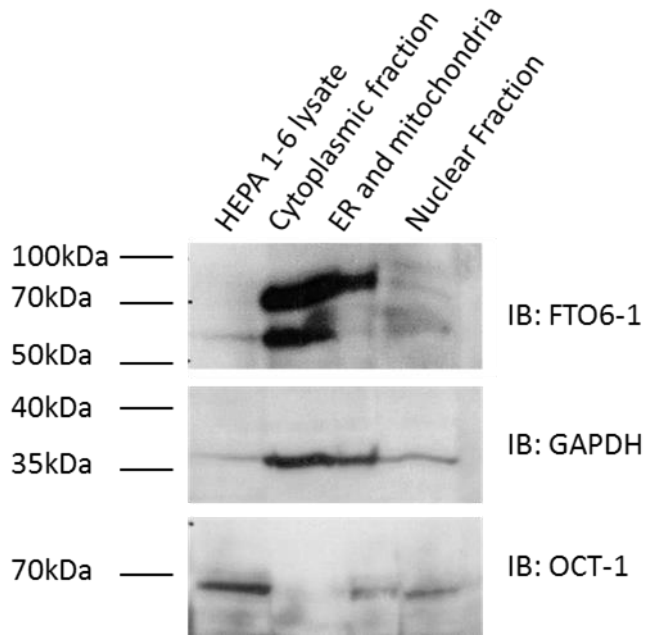

Figure 11. Immunoblotting analysis of subcellular fractions obtained by ultracentrifugation through a dense sucrose cushion. Protein concentration of each of the fraction was assessed by colorimetric assay (Methods 2.5.3) and 40 µg of each sample was loaded in each well. IB, Immunoblotting using specific antibodies - commercial mouse anti-FTO6-1, rabbit anti-GAPDH and rabbit anti-OCT1 (3.2.4).

Immunoblotting of the fractions collected after two differential pelleting steps and ultracentrifugation through a dense sucrose cushion showed that OCT-1 was present in the total lysate as well as the nuclear fraction and the rough endoplasmic reticulum (ER)/mitochondrial fractions. GAPDH was concentrated in the cytoplasmic and ER/mitochondrial fractions, although a weak band was also visible in the nuclear fraction. When the membrane was probed with anti-FTO antibody, weak bands of similar intensity were detected in the total cell lysate and the nuclear fraction. Moreover, higher molecular weight FTO bands were also visible in the nuclear fraction. Interestingly, concentrated FTO was detected in the cytoplasmic and ER/mitochondrial fractions, and appeared as two strong bands in the former and as a single band of higher molecular weight in the latter.

These data suggest that this protocol resulted in decreased membrane contamination of the nuclear fraction and caused concentration of GAPDH in the cytoplasm and ER fractions. Additionally the protocol resulted in concentration of FTO in both cytoplasmic and ER fractions, which was not observed in the fractions obtained from nuclei extraction at the interface of two sucrose solutions. This implies that the removal of the outer nuclear membrane might have affected FTO subcellular compartmentation.

Overall, the results of both the fractionation experiments further support the hypothesis that FTO is located in both the cytoplasm and the nucleus, and suggest that the outer nuclear membrane/ER may a play role in FTO trafficking.

3.3.3 Immunocytochemistry Demonstrates that FTO Is Distributed Throughout the Nucleoplasm and the Cytoplasm

The results of the subcellular fractionation experiments suggest partial FTO localisation in the cytoplasm. However, it can be argued that these results represent an artificial state in which the integrity of the cell has been compromised and the distribution of molecules may have been altered. Thus, I next aimed to study FTO subcellular localisation using immunocytochemistry.

Mouse HEPA1-6 liver cells grown on cover slips were subjected to indirect immunocytochemistry analysis as described in 2.3.3. To visualise FTO, cells were probed with an in-house rabbit anti-FTO primary antibody and a secondary anti-rabbit Alexa488 antibody. Two different anti-FTO antibody dilutions were used: high dilution (D1 - 1:400)

and low dilution (D2 – 1:100). The nuclei were counterstained with DAPI. Immunofluorescence was studied using an LSM 710 NLO Confocal/Multi-photon Microscope (2.3.4).

The images acquired using the blue (DAPI), green (FTO) and TL (transmitted light) channels, as well as merging of all channels are shown in **Figure 12**. Images of cells probed with high dilution of the primary antibody (1:400) revealed the presence of FTO in the nucleus (**Figure 12 A**). In certain places, FTO seemed to be more abundant than other, producing a 'speckled' appearance. When a lower dilution of the primary antibody was used the intensity of the nuclear FTO signal became stronger (**Figure 12 A**). More interestingly, a closer examination of the higher magnification images revealed a weak signal, with a dot-like pattern, outside the nucleus (**Figure 12 B**). This cytoplasmic signal was observed in nearly all cells studied.

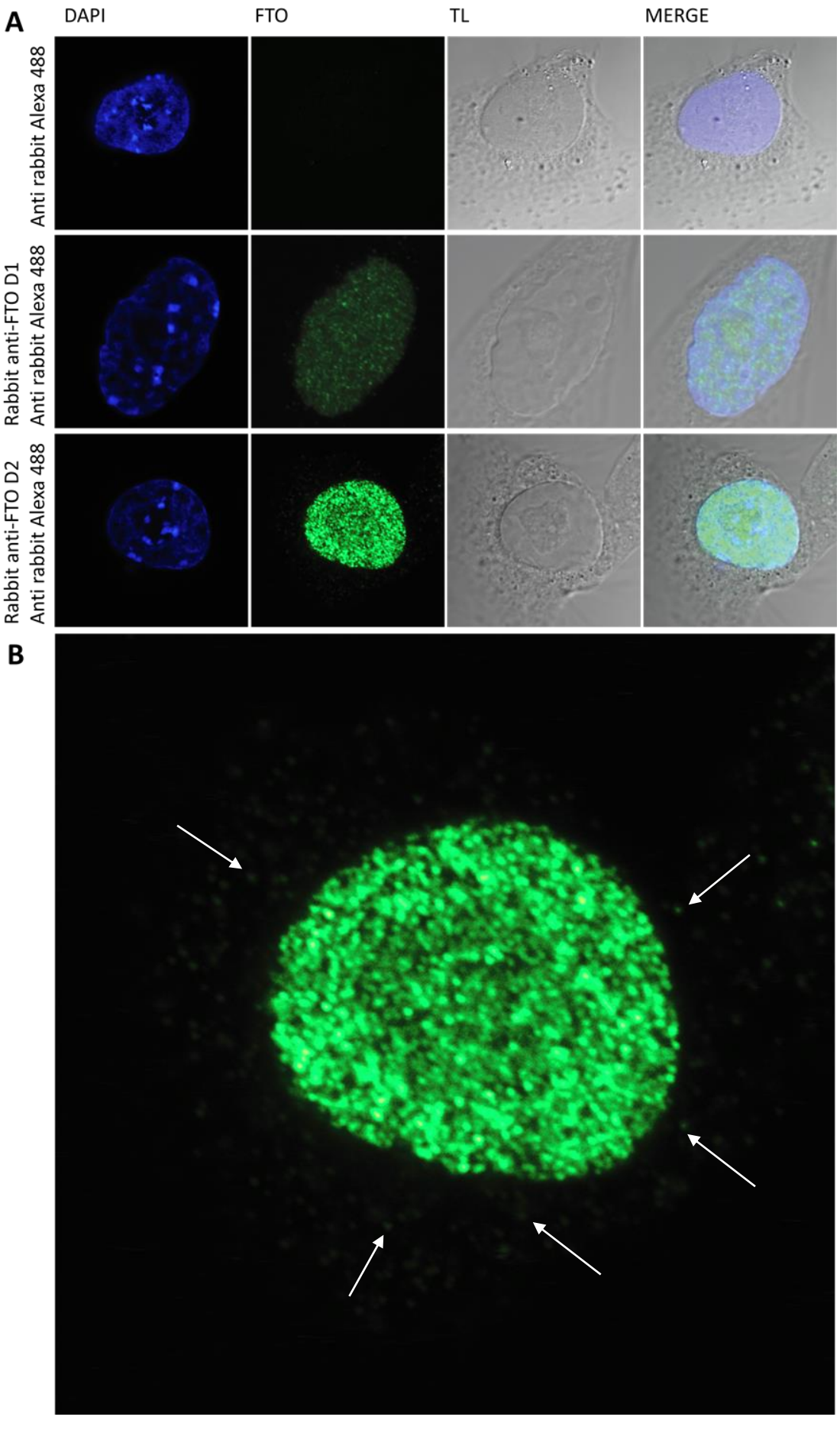
A
DAPI
FTO
TL
MERGE
Anti rabbit Alexa 488
Rabbit anti-FTO D1
Anti rabbit Alexa 488
Rabbit anti-FTO D2
Anti rabbit Alexa 488
B

Figure 12. Confocal fluorescence images of HEPA1-6 cells subjected to indirect immunocytochemistry. Cells were fixed and incubated overnight with anti-FTO rabbit antibody followed by 2h incubation with Alexa 488 goat anti-rabbit antibody (green). Nuclei were counterstained with DAPI (blue). **A**; Three channel (BLUE and GREEN and Transparent TL) representation of experimental samples and merge. **B**; Zoom of GREEN channel of sample treated with the anti-FTO antibody D2 and Alexa 488 antibody. TL- transmitted light channel, D1 and D2- dilution one and two of anti-FTO antibody (1:400 and 1:100 respectively).White arrows indicate location of some of the cytoplasmic FTO.

When the fluorescence brightness, contrast and gamma of the green channel (FTO) was adjusted in the display settings (in parallel with the negative control images) the FTO cytoplasmic signal became even more apparent in the cells probed with the 1:100 dilution of the antibody (**Figure 13**). Multiple images taken at different focal planes within the cell (Z-stack) starting from the top of the cell towards the bottom revealed that FTO is distributed throughout the nucleoplasm and the cytoplasm in a speckle-like pattern with the majority of the FTO localised to the nucleus.

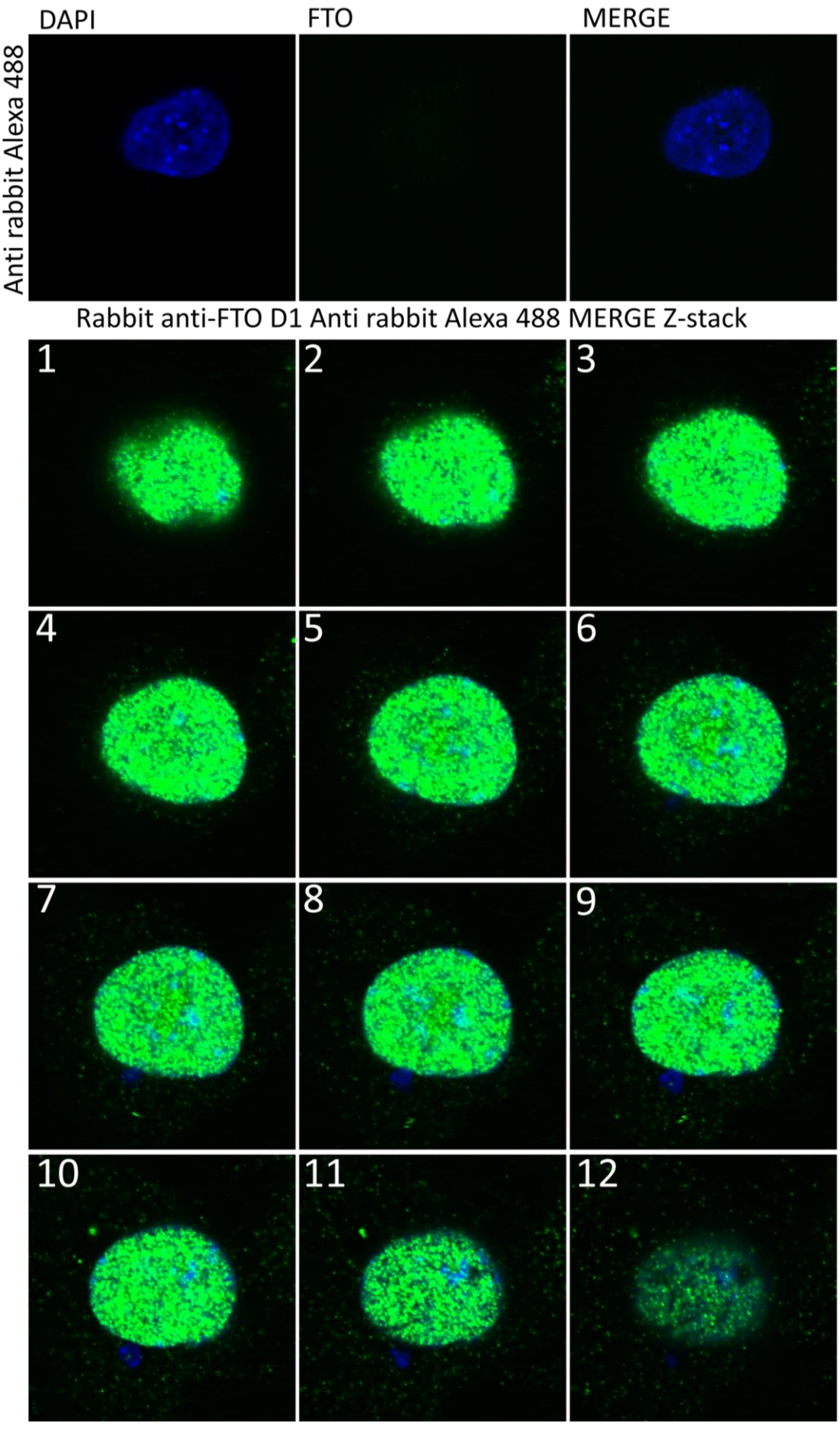
DAPI
FTO
MERGE
Anti rabbit Alexa 488
Rabbit anti-FTO D1 Anti rabbit Alexa 488 MERGE Z-stack
1
2
3
4
5
6
7
8
9
10
11
12

Figure 13. Confocal fluorescence Z-stack images of HEPA1-6 cells with adjusted signal intensity. Cells were subjected to indirect immunocytochemistry using D2 (1:100) dilution of the anti-FTO antibody. Top panel: two channel (BLUE and GREEN) representation of the negative control and the merge. Lower panel: 12 blue and a green channel merge images of Z-stack from top of the cell (1) towards the bottom (12). The intensity of the signal in the green channel was adjusted in parallel with the negative control.

Overall, the results of the immunocytochemistry analysis are in line with the results of the computational prediction analysis and the cellular fractionation experiments, and show that the majority of FTO is localised to the nucleus although small amounts are also present outside of the nucleus. These results suggest multiple cellular locations of FTO action and expands the range of potential molecules or potential cellular networks that FTO could be acting on.

3.3.4 Nuclear FTO Localisation Changes during Cell Interphase

I next used immunocytochemistry and investigated the nuclear localisation of FTO in fixed cells during various stages of the interphase. Since the size and the number of the nucleoli can be used as an indicator of the metabolic state of the cell, with single large nucleoli present in actively growing cells focused on protein synthesis (Cooper 2000), I searched for the cells at various stages of the nucleolar fusion.

The confocal images acquired after immunocytochemistry staining using anti-FTO antibody showed cells at four different stages of the nucleolar fusion (**Figure 14**). The results revealed that at the first stage (probably telophase) when the chromatin was in a semi-dispersed state, and no nucleoli were observed, FTO was present throughout the nucleoplasm in a dot-like pattern as previously described in 3.3.3. However, FTO seemed to be more abundant in the places where DAPI staining was weak (euchromatin) and less abundant in the strong DAPI staining areas (heterochromatin) (**Figure 14 Stage I**). These differences are even more apparent in the cell with greater variations of the chromatin condensation (**Figure 14 Stage II**). Additionally, FTO immunofluorescence was less pronounced in places of spherical chromatin concentrations, visible as strong DAPI stained

spheres. Moreover, FTO was less abundant in small multiple nucleoli formed within this nucleus. The images of cells which progressed further throughout the interphase and had bigger multiple nucleoli (**Figure 14 Stage III**) and finally one large fused nucleolus (**Figure 14 Stage IV**) showed dramatic reduction of FTO signal in the nucleolus as well as places of heterochromatin localised to strong DAPI foci within the nucleus and to the periphery of the nucleus.

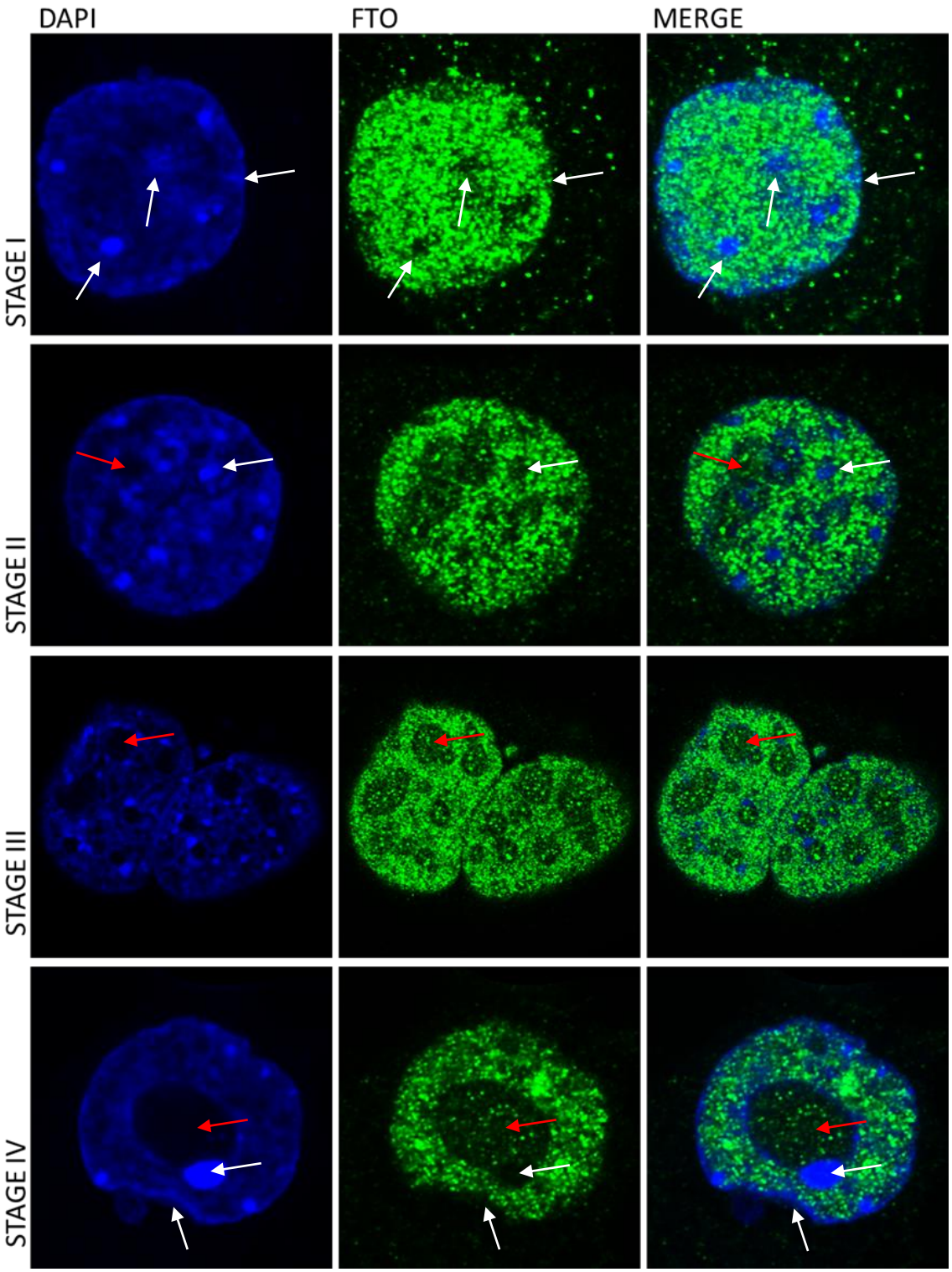

Figure 14. Confocal fluorescence images of HEPA1-6 cells at various stages of the nucleolar fusion. Two channel (BLUE and GREEN) representation of experimental samples and merge. Cells were fixed and incubated with the anti-FTO rabbit antibody followed by incubation with Alexa 488 goat anti-rabbit antibody (green). Nuclei were counterstained with DAPI (blue). White arrows indicate location of chromatin condensations and red arrows indicate nucleoli.

Overall, these results suggest that FTO is not equally distributed thought the nucleoplasm and its localisation changes during various stages of the interphase. Increased FTO abundance in euchromatin as opposed to heterochromatin, condensed chromatin spheres or nucleoli may further suggest a role of FTO within less condensed chromatin and involvement in the mechanism subsequent or parallel to transcription.

3.3.5 Nuclear FTO Is Exported to the Cytoplasm through the Nuclear Membrane at the Beginning of the Cell Division

I next studied FTO subcellular localisation during mitotic cell division. HEPA1-6 cells were subjected to immunocytochemistry (2.3.3) using anti-FTO antibody, and images of cells at various stages of the cell cycle were acquired using florescent confocal microscope (2.3.4).

The images of cell at P1 (interphase) showed the nuclear and cytoplasmic localisation pattern of FTO previously described, with the majority of the signal in the nucleus (**Figure 15 P1**). Images of a cell with chromatin condensed into chromosomes, but still having rounded nuclear shape (P2, probably prophase) showed the majority of FTO localised to the cytoplasm and lack of co-localisation of FTO with condensed chromatin (**Figure 15 P2**). Images of cells during later stages of the mitotic cell division showed that when chromatin further condensed into more distinct chromosomes (P3, probably promethaphase), chromosomes lined up (P4, methaphase), moved to the opposite ends of the cell (P5, anaphase) and finally unwound to chromatin (P5, probably telophase and cytokinesis), FTO did not co-localise with condensed chromatin and was localised in a dot-like pattern throughout the entire cell. Lastly, images of two growing sister cells after the mitotic

division revealed that the majority of FTO was once more localised to the nucleus with a weaker signal detectable in the cytoplasm (**Figure 15 P7**).

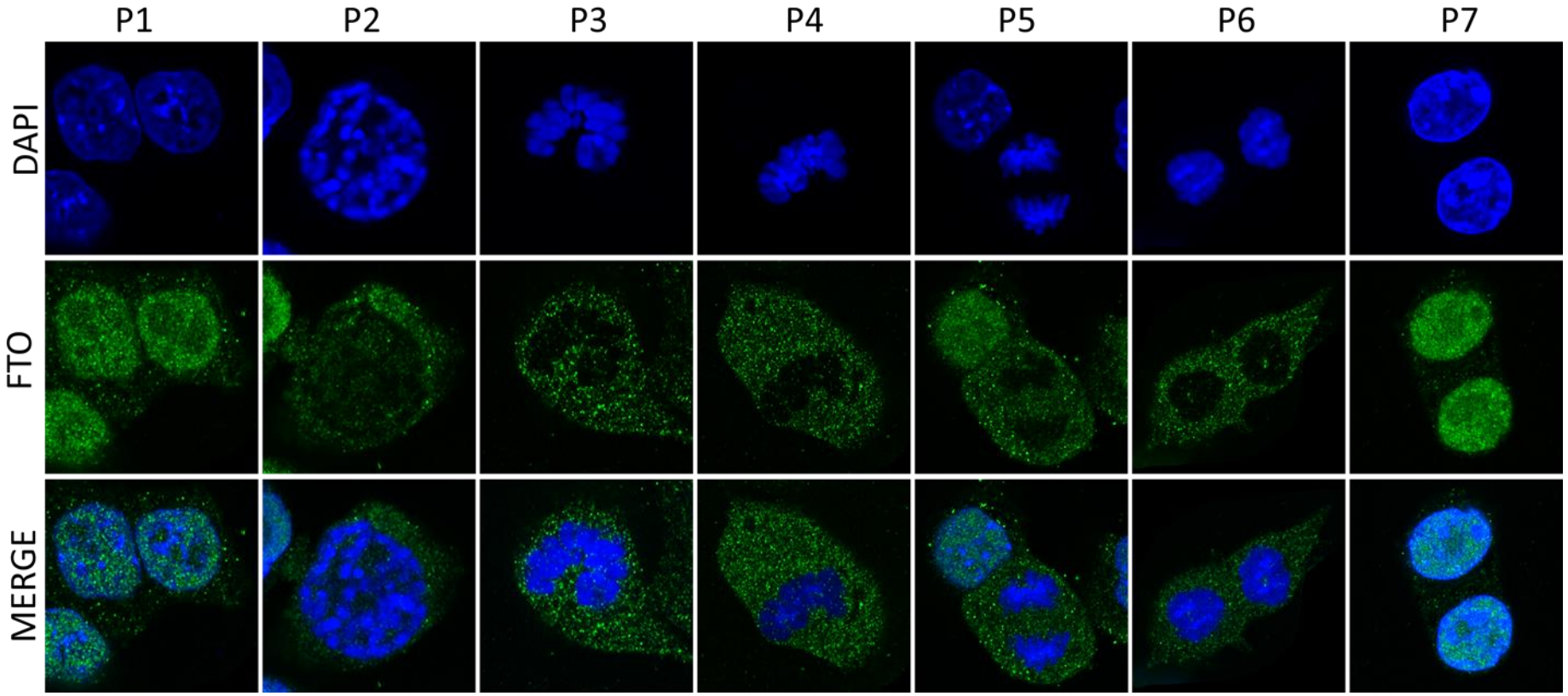

Figure 15. Confocal fluorescence images of HEPA1-6 cells at various stages of the cell division. Two channel (BLUE and GREEN) representation of experimental samples and merge. Cells were fixed and incubated with the anti-FTO rabbit antibody followed by incubation with the Alexa 488 goat anti-rabbit antibody (green). The nuclei were counterstained with DAPI (blue). These cells were imaged in a single experiment, although similar phenotypes were observed also in other experiments where cells were stained for FTO and DAPI.

These results show that FTO does not co-localise with packed chromatin and chromosomes, and suggest that FTO is not involved in protection of chromosome integrity during cell division. More importantly, the data suggest that FTO localisation can change dramatically upon chromatin condensation and instead of being localised mainly to the nucleus, FTO moves to the cytoplasm. However, the question remains whether the change in FTO localisation is triggered by active export of FTO through the nuclear membrane or increased cytoplasmic FTO is a secondary effect of nuclear membrane break down? To answer this question, I performed further immunocytochemistry analysis including staining for the nuclear membrane using the mouse anti-lamin A/C antibody, which recognise lamin A and C, proteins found in the nucleoplasmic side of the inner nuclear membrane (McKeon, Kirschner, and Caput 1986).

The results of immunocytochemistry and confocal fluorescent imaging showed FTO localisation (green) and the nuclear membrane marker lamin A/C (in red) during various stages of the HEPA1-6 cell division (**Figure 16**). The images of the cells at P1 (interphase) showed the majority of the FTO present in the nucleus surrounded by the nuclear membrane (**Figure 16 P1**). However, the images of the cell at the very beginning of the cell division when the chromatin started to condense (P2-beginning of the prophase) showed that FTO was distributed equally throughout the cell, but the nuclear membrane was still present (**Figure 16 P2, P2 ZOOM**). Images of the cells during later stages of the mitotic cell division when the chromatin further condensed into more distinct chromosomes (**Figure 16 P3**), moved to the opposite ends of the cell (**Figure 16 P4**) and finally unwind to chromatin (**Figure 16 P5**), showed similar to P2 localisation of FTO, although the nuclear membrane was no longer visible.

These results suggest that FTO can be actively exported from the nucleus to the cytoplasm though the nuclear membrane at the beginning of the prophase, when chromatin begins to condense into the chromosomes, and after the cell division, when the nuclear membrane is rebuilt and chromosomes unwind, FTO is transported back to the nucleus. This further suggests that FTO is not involved in processes related to chromatin condensation and chromosome integrity during cell division.

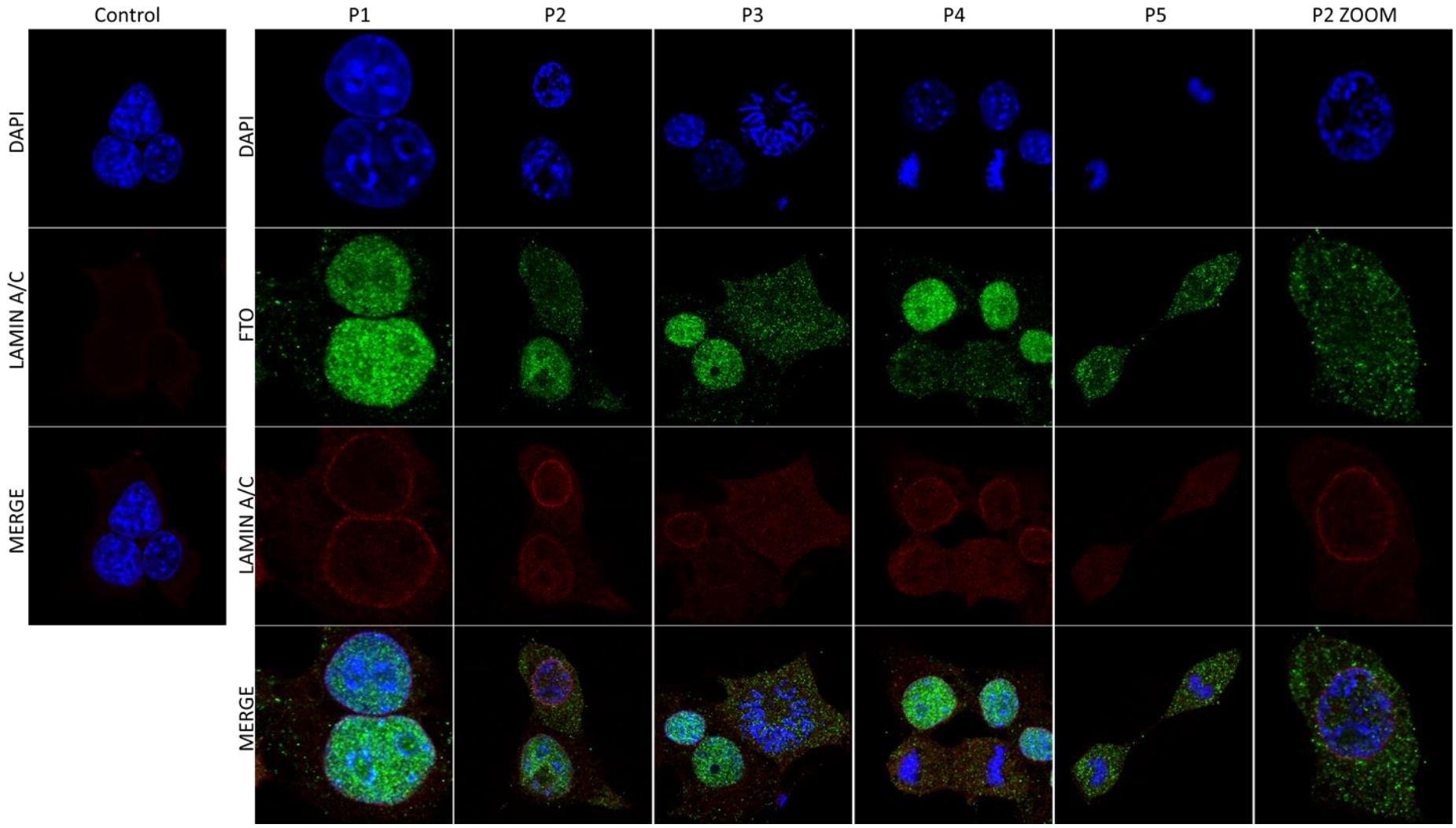
Control
P1
P2
P3
P4
P5
P2 ZOOM
DAPI
LAMIN A/C
MERGE
DAPI
FTO
LAMIN A/C
MERGE

Figure 16. Confocal fluorescence images of nuclear membrane at various stages of the cell cycle. Three channel (BLUE, GREEN and RED) representation of experimental samples and merge. HEPA1-6 cells were incubated with rabbit anti-FTO antibody and mouse anti-lamin A/C followed by incubation with Alexa 488 anti-rabbit antibody (green) and Alexa 680 anti-mouse (red) respectively. Nuclei were counterstained with DAPI (blue).

3.4 Discussion

3.4.1 Summary

The aim of this study was to examine the cellular distribution of FTO and to test the hypothesis that FTO was found localised outside of the nucleus. By employing computational analysis, subcellular fractionation techniques and immunofluorescence imaging I found evidence indicating that FTO can be found in the cytoplasm and the nucleus, and that the cytoplasmic and nuclear localisation pattern changed during cell growth and the cell cycle. Moreover, the preferential nuclear localisation of FTO was abolished during early prophase, suggesting that FTO can be actively exported through the nuclear membrane.

3.4.2 FTO Can Be Found in the Nucleus and the Cytoplasm

It was initially suggested that FTO was exclusively found in the nucleus. The homology of FTO with *E. coli* AlkB and other nuclear human ALKB proteins, the presence of a predicted nuclear localisation signal (NLS) in FTO, and the proposed role of FTO in nucleic acid repair as well as immunofluorescence data which showed FTO located in the nucleus, supported the idea of FTO being a strictly nuclear protein (Gerken et al. 2007; Church et al. 2009; Fischer et al. 2009; 2010; Berulava et al. 2012). However, the immunofluorescence experiments reported usually involved a YFP-tagged murine FTO, that was overexpressed in non-murine cell line (Gerken et al. 2007; Church et al. 2009). This may have affected the localisation of FTO due to post-translational modifications (PTMs) of the tag or by swamping the cell with overexpressed protein (Noselli and Perrimon 2000; Berggård,

Linse, and James 2007). Also, the strong nuclear staining, especially relative to the weak cytoplasmic staining I observed, may have contributed to the conclusion that FTO was confined to the nucleus (Jia et al. 2011a; Berulava et al. 2012). Moreover, low magnification of the imaged cells might have impeded the detection of the cytoplasmic signal. (Gerken et al. 2007; Fischer et al. 2009; Church et al. 2009).

I applied computational analysis to predict possible subcellular locations of mouse FTO based on the amino acid sequence. WoLF found FTO localisation to cytoplasm and nucleus equally possible, and CELLO's report suggested the cytoplasm as the prime location. These *in silico* predictions were next validated *in vitro* by two subcellular fractionation experiments which showed an FTO signal in the cytoplasmic and the nuclear fractions. Finally, immunocytochemistry revealed that during interphase the majority of FTO was in the nucleus, but a weak signal was also detected in the cytoplasm.

A number of localisation prediction programmes are available ('Psort' 2015) and, may produce different results depending on the algorithms being used. I chose to use several widely used programmes, namely WoLF, CELLO, NLS Mapper and NetNES 1.1 Server. Predictions by WoLF and CELLO contradicted the previously published experimental data (Gerken et al. 2007; Church et al. 2009; Jia et al. 2011; Berulava et al. 2012).

Identification of NF-kappa-B essential modulator (NEMO) by WoLF as a protein with the most similar localisation features to FTO may suggest that localisation of FTO also can be regulated by post-translational modification (e.g. phosphorylation, ubiquitination).

A strong bipartite NLS was identified by NLS Mapper (which also corresponds to NLS identified by WoLF). This NLS had previously been described (Peters, Ausmeier, and Rüther 1999; Meyre et al. 2010), although no link between FTO and importin α-β pathway was made in these publications. Importins transfer cargo proteins into the nucleus by binding to their NLS, hence masking of the NLS can prevent nuclear transport (Cook et al. 2007). The presence of a NLS may in fact be crucial for FTO nuclear import, as FTO lacking an N-terminal domain (including the NLS) does not exhibit preferential nuclear localisation (Gulati et al. 2014). Given the association with the importin α-β pathway it would be interesting to look at whether deletion of the NLS (or its modification) would affect nuclear import of FTO. If so, examination of m^6A levels in mRNA, or of the mechanism of adipogenesis, could provide insights into the cellular compartment where FTO functions.

No leucine-rich nuclear export signal (NES) for exportin 1 (XPO1) has been identified in FTO, suggesting a different mechanism for FTO nuclear export. Interestingly, exportin 2 (XPO2), another export mediating protein has been reported to interact with FTO and proposed to be a plausible mediator of FTO nucleocytoplasmic trafficking (Gulati et al. 2014). These findings do not contradict the results of my NetNES analysis since substrate specificity of specific exportins is known to be different (Güttler and Görlich 2011). In fact, XPO1 has a broad spectrum of substrates due to a promiscuous binding site, while XPO2 seems to only bind to imporin-α and facilitate its transport back to the cytoplasm for another round of nuclear import (Güttler and Görlich 2011). Moreover, Gulati et al. suggest that XPO2 binds to the N-terminal domain of FTO, although they showed that N-terminal FTO was nearly always nuclear while the C-terminal FTO had increased cytoplasmic localisation. Additional immunofluorescent co-localisation or functional studies would provide more insight into the character of XPO2 and FTO interaction.

My identification of native FTO in both cytoplasmic and nuclear fractions (obtained by cellular fractionations) provided experimental support for the computational predictions. Since these experiments were performed, similar findings were reported in the literature and showed FTO to be present in both the cytoplasmic and the nuclear fractions obtained after cellular fractionation of MEFs overexpressing FTO (Gulati et al. 2013).

It must be recognised that in all fractionation experiments, the cell environment is changed drastically upon cell homogenisation and may cause the redistribution of cellular macromolecules resulting in the presence of nuclear proteins in cytoplasmic fractions (de Recondo and Abadiedebat 1976; Preller and Wilson 1992). However, since no FTO was identified in the resuspension buffer in which the purified intact nuclei were washed after the nuclear extraction at the interface of two sucrose solutions, it suggests that FTO did not leak out of nucleus in this experiment. Moreover, lack of OCT-1 in the cytoplasmic fraction excludes the possibility of nuclei breakage during the homogenisation. Hence, we can conclude that the FTO signal in the cytoplasmic fraction represents FTO located outside of the nucleus.

However, the removal of ER most probably increased cytoplasmic FTO concentration. The ER is continuous with the outer nuclear membrane, and outer and inner nuclear membranes are joined by the nuclear pores which facilitate active transport of macromolecules through the nuclear envelope (Cooper 2000, chap. 8). Thus, the removal of ER and the outer nuclear membrane might have destroyed the nuclear pores, resulting in nonspecific FTO export. Interestingly, OCT-1, a transcription factor that binds to DNA and regulates the transcription of variety of genes (Jaffe et al. 1995; Roberts, Segil, and Heintz 1991), was not detected in the cytoplasmic fraction, perhaps indicating that the affinity of FTO to the permanently nuclear components (e.g. DNA, histones) is different than OCT-1,

hence FTO could be detected in both cytoplasm and nucleus. The presence of multiple FTO bands in the nuclear, cytoplasmic, and ER/mitochondria fractions is somewhat unexpected. Since FTO routineously co-purifies with DNA (unpublished observation by Dr. Wei Shen Aik), it seems likely that concentrated DNA in the nuclear fraction affected FTO protein separation on the gel (**Figure 10, 11**). The cause of presence of multiple FTO bands in cytoplasmic, ER and mitochondria fractions (**Figure 11**) is difficult to explain. If FTO is subjected to post-translational modification specifically in cytoplasm or ER (e.g. ubiquitination), perhaps concentration of cytoplasmic and ER proteins after fractionation led to increased rate of FTO modification than normally observed in the diluted cell lysate.

Detection of FTO by immunofluorescence in the cytoplasm of HEPA1-6 cells appeared at the time of study to be the first evidence of cytoplasmic FTO in the cell and contrasted with all previously published results. Since then, at least two immunofluorescence evidence of cytoplasmic FTO have been reported (Gulati et al. 2014; Vujovic et al. 2013). Vujovic et al. observed increased FTO expression and mostly cytoplasmic FTO localisation in lateral hypothalamic area (LHA), PVN and VMN neurons of 48 h-fasted rats. Gulati et al. detected cytoplasmic GFP-FTO in overexpressing live COS7. Immunocytochemistry evidence of cytoplasmic FTO is in line also with another study by Gulati et al. and supports the suggested possibility of FTO to regulate mRNA translation and interact with aminoacyl-tRNA synthetases (Gulati et al. 2013).

3.4.3 Nuclear FTO Distribution Changes during the Interphase

The speckled pattern of FTO nuclear localisation was in line with previously reported studies (Jia et al. 2011; Berulava et al. 2012; Vujovic et al. 2013). However, detail examination of the nuclei of cells at various stages of interphase revealed that FTO abundance is subjected to subnuclear compartmentation. FTO was less concentrated in regions of heterochromatin, nucleoli and nuclear bodies.

During interphase, nuclear components (especially chromatin) are distributed in different regions of the nucleus where they perform specific functions. These subnuclear compartments include chromatin organisation territories and subnuclear bodies (Trinkle-Mulcahy and Lamond 2008). FTO was less abundant in the nuclear periphery in regions of highly condensed heterochromatin, where no or very little gene transcription takes place. However, in regions located more towards the centre of the nucleus where less dense and transcriptionally active euchromatin is located, FTO was more concentrated. These observations are in line with the currently proposed role for FTO in mRNA processing and RNA splicing as both of these processes take place in euchromatin territories (Trinkle-Mulcahy and Lamond 2008). Euchromatin shares space with nucleoli which are the centres of rRNA gene transcription, rRNA processing as well as ribosome biogenesis and export (Padeken and Heun 2014). A clear reduction of FTO in multiple small nucleoli as well as the large central nucleolus may suggest it is unlikely that FTO plays a crucial role in rRNA processing and ribosome biogenesis. This is in line with the previously observed variable staining of FTO in the nucleoplasm of HeLa, HEK293, 293 T-Rex and MCF-7cells (Berulava et al. 2012). Interestingly, in the same study, the presence of FTO in nucleoli was reported. However, the FTO signal seemed much weaker in the nucleoli than in the nucleoplasm. Moreover, Berulava reported that overexpression of FTO did not lead to increased localisation in the nucleoli.

3.4.4 FTO Distribution Changes during the Cell Cycle

The subcellular location of FTO during various stages of the cell cycle has never been reported before. This study showed that FTO localisation was dramatically changed during early prophase. Despite the presence of the nuclear envelope, FTO was no longer primarily nuclear: instead, it was equally distributed through the cell. This implies that FTO can be actively exported from the nucleus to the cytoplasm though the nuclear membrane.

The weak co-localisation of FTO with chromosomes was in line with the low abundancy of FTO in condensed chromatin previously observed in the nuclei during interphase. Transport of FTO outside of the nucleus precisely at time of chromosome condensation in early prophase further supports an association of FTO with relaxed chromatin and suggests that FTO is unlikely to play a role in chromatin packing or supporting chromosome integrity during cell division.

Increased FTO abundance outside of the nucleus during early prophase is previously unknown phenomenon and indicates that FTO can move in and out of the nucleus. Shuttling of FTO between cytoplasm and nucleus has also been recently reported by Gulati et al. (Gulati et al. 2014) although to a lesser extent and during interphase in living cells. In my study, the phase of the cell cycle when FTO was exported out of the nucleus was identified by observation of the nuclear membrane and chromosome condensation. Disintegration of nuclear membranes and the nuclear lamina marks the end of prophase (Cooper 2000, chap. 8; Padeken and Heun 2014). At this point, lamins A and C dissociate to the cytoplasm. Immunocytochemistry staining showed that when FTO was already exported from the nucleus, lamins A and C were still associated with the nuclear envelope, marking this time

as early prophase. Another way to pin down the exact moment of the cell cycle in which FTO leaves the nucleus would be to follow expression of specific cyclin-dependent kinases (e.g. M-Cdk that triggers the G2/M checkpoint and events of early mitosis).

3.4.5 Future Plans

Whether FTO acts in the nucleus or in the cytoplasm, it must at some point of its life cycle be transported though the nuclear envelope. I would like to further investigate the mechanisms of FTO nuclear import and export. It would be interesting to examine whether a truncated variant of FTO lacking NLS would still show nuclear localisation. Moreover, if FTO is imported to the nucleus by the classical (importin α-β) pathway, then heat stress should also affect its nuclear localisation (Kodiha et al. 2008).

Regarding FTO export, it would be interesting to experimentally validate whether XPO2 plays a role, as suggested by Gulati (Gulati et al. 2014). Moreover it would be interesting to assess the effects of altering FTO localisation on mRNA translation (Gulati et al. 2013) and m^6A demethylation of mRNA (Hess et al. 2013).

Regarding FTO translocation during early prophase, it would be interesting to investigate what triggers this dramatic change. Is it that FTO is not required in the nucleus (because gene transcription is terminated at this time) or because it plays an important role in the cytoplasm at that stage (e.g. by retention or degradation of mRNA)? This could be examined by investigating whether the nuclear export of FTO is associated with total mRNA export perhaps by in-situ hybridisation and immunofluorescent staining of RNA.

3.4.6 Conclusions

In my experiments I found that FTO can be localised to both the nucleus and the cytoplasm and further, that the localisation pattern changes during interphase and mitotic cell division. Moreover, FTO can be actively exported from the nucleus through the intact nuclear envelope. Evidence of multiple subcellular location sites of FTO may lead to the discovery of new functions.

4 Identification of Proteins That Interact With FTO

4.1 Introduction

All biological mechanisms within the cell are controlled by proteins. Some proteins can function independently, but the majority require another protein partner or partners to fulfil their role (Berggård, Linse, and James 2007). Identification of protein-protein interactions (PPI) can be essential for understanding the molecular function of FTO and identifying its role in biological networks within the cell.

A large number of physical, biophysical, biochemical and genetic techniques are now available, allowing PPI to be studied *in vivo* and *in vitro*. Nevertheless, co-immunoprecipitation (Co-IP) is still one of the best methods, offering the advantages of both effectiveness and simplicity (Phizicky and Fields 1995; Berggård, Linse, and James 2007; Rao et al. 2014). Typically, a cell lysate is prepared and antibodies against the target protein are added. The antigen and its interacting partner are precipitated and any contamination is removed by series of washes. The immunoprecipitated antigen with its interacting partners are eluted and studied using standard molecular biology techniques (Bonifacino and Dell'Angelica 2001, chap. 7, 9).

Although the Co-IP procedure is uncomplicated, performing a Co-IP which results in the successful identification of an authentic binding partner can be challenging. However, it is possible if the following criteria are considered.

The protein of interest (the antigen for the antibody) should be ubiquitously expressed in the cell population or the tissue studied (Bonifacino and Dell'Angelica 2001). The precipitation of native proteins is preferable as it prevents complications resulting from the introduction of artificial tag sequences and ensures the physiological sub-localisation of the protein and its correct post-translational modifications (PTMs). Preserving protein-protein interactions throughout the entire Co-IP procedure is crucial, but may prove difficult due to the mechanical and chemical stress involved in the cell lysis and washing steps. For example, since these conditions are far from a true cellular environment, low-affinity, or transient, protein-protein interactions may be lost. Since each protein complex is different, there are no guidelines on how to extract the protein correctly, or the washing buffer composition, and these conditions have to be optimised. The high quality and specificity of the antibodies used in Co-IP is critical for the success of the experiment. It is essential to establish that the antibodies can bind to the antigen under the conditions of the Co-IP experiment, and to test if the antibody is specific and does not recognise the co-precipitated protein.

The final step of each Co-IP is identification of the PPI. The identification of the interacting partners by mass spectrometry offers the advantage of high-throughput and is also a hypothesis-independent method. However, the high sensitivity of the modern MS techniques also results in a large number of contaminants being identified in each Co-IP experiment. Thus, independent confirmation of the protein-protein interaction by reverse Co-IP using an antibody specific to the novel candidate binding partner (CBP) is required.

Computational, structural and kinetic studies revealed that FTO is a member of the Fe(II)- and 2-oxoglutarate-dependent dioxygenase superfamily, has affinity towards single stranded DNA/RNA, and catalyses oxidative demethylation of m^3T in ssDNA and m^3U in

ssRNA, but mostly m^6A in ssRNA (Sanchez-Pulido and Andrade-Navarro 2007.; Gerken et al. 2007; Jia et al. 2008; Han et al. 2010; Jia et al. 2011). However, the biological significance of these discoveries may only become evident when we understand the interaction of FTO with other proteins and its place in the cellular proteome. According to Phizicky and Fields (Phizicky and Fields 1995), a protein partner binding to FTO could have the following effects:

(**i**) alter the kinetic properties of FTO, by causing conformational or allosteric changes;

(**ii**) facilitate substrate channelling between domains;

(**iii**) construct a new binding site for small effector molecules;

(**iv**) inactivate or destroy FTO;

(**v**) alter the specificity of FTO for its substrate, or enable binding of new substrates that are not bound by either of the partners alone;

(**vi**) serve a regulatory role in upstream or down-stream events;

(**vii**) change the subcellular localisation of FTO, thereby affecting its functional roles.

Therefore I hypothesised that knowledge of the proteins that interact with FTO would help to answer the question of what is the precise role of FTO is within the cell and its effect on obesity. Thus, I aimed to identify proteins that interact with FTO using co-immunoprecipitation.

The specific aims of this chapter were to:

1) Determine how efficiently native FTO protein can be immunoprecipitated by the available antibodies prior to attempting Co-IP.
2) Optimise the immunoprecipitation protocol to isolate native FTO and its interacting partners.
3) Identify FTO interacting partners purified by Co-IP.
4) Validate the interaction of FTO with candidate partners.

4.2 Methods

4.2.1 Agarose Protein G Immunoprecipitation with Antibodies in the Solution

All steps were performed on ice or at 4 °C unless specified. The cell or tissue lysates were mixed with 5-10 µl of the specific antibody in an Eppendorf tube and incubated for the desired time period (normally 12-14 hours) with gentle rotation. Next, 100 µl of the Recombinant Protein G Agarose beads (Life Technologies, 15920-010) was equilibrated in 500 µl of the Binding Buffer (0.01 M Sodium phosphate, pH 7.0, 0.15 M NaCl) and separated by centrifugation in a Corning® Costar® Spin-X® centrifuge tube filters (Sigma-Aldrich, ACLS8162-96EA) at 1000 rpm for 2 minutes. Then, the equilibrated Recombinant Protein G Agarose beads were added to the lysate-antibody mixture, and the lysate-antibody-bead mixture was incubated for 1-4 hours with gentle rotation. The beads were then separated out by centrifugation at 1000 rpm for 2 minutes. After three washes with the Wash Buffer, the proteins were eluted from the beads by 10 minutes incubation at 70 °C with 1 X with the NuPage LDS Sample Buffer (Invitrogen, NP0008), supplemented with the NuPAGE® Sample Reducing Agent (Invitrogen, NP0009).

Antibodies used in the immunoprecipitation experiment

rabbit anti-FTO	in-house raised	NA
rat anti-HA	Roche	11867423001

Wash Buffer Components

TRIS; adjust to pH 7.4	10 mM
EDTA	1 mM
EGTA; pH 8.0	1 mM
NaCl	150 mM
Triton X-100	1 %
Sodium Ortho-vanadate	0.2 mM
Protease inhibitor cocktail	1 X

Stored up to 6 months at 4 °C.

Protease inhibitors (Prote CASE-50 EDTA free, G Biosciences, 786-326) were added to the buffer immediately before use.

4.2.2 Dynabeads® Protein G Indirect and Direct Immunoprecipitation

Immunoprecipitation using either the indirect or the direct method (see Results) was performed using Magnetic Dynabeads® Protein G (Invitrogen, 100-03D), (50 µl per sample) and the Non-denaturing Buffer.

Non-denaturing Buffer

TRIS HCl ; adjust to pH 8	20 mM
EDTA	2 mM
NaCl	137 mM
NP-40	1 %
Protease inhibitor cocktail	1 X

Stored up to 6 months at 4 °C.

Protease inhibitors (Prote CASE-50 EDTA free, G Biosciences, 786-326) were added to the buffer immediately before use.

Indirect Immunoprecipitation

The cell lysate was mixed with 10 µl of the antibodies and incubated for 1 hour with rotation at room temperature. Meanwhile, 50 µl of the beads were separated on a magnetic rack and washed with 200 µl of the Non-denaturating Buffer. Washed beads were then incubated with the cell lysate and antibody mixture for 30 min with rotation at room temperature. The supernatant was removed, the antibody-coupled beads were washed three times with 200 µl of PBS with 0.02% Tween and transferred into a fresh Eppendorf tube. After the final wash, the proteins were eluted from the beads with 40 µl of the NuPage LDS Sample Buffer (Invitrogen, NP0008), supplemented with the NuPAGE® Sample Reducing Agent (Invitrogen, NP0009) for 10 minutes at 90 ^{o}C. The eluates, washes and depleted materials were stored at – 20 ^{o}C.

Direct Immunoprecipitation

The beads (50 µl) were transferred into an Eppendorf tube and separated on a magnetic rack. After resuspension in 200 µl of the Non-denaturating Buffer, 10 µl of the antibodies were added and the mixture was incubated for 10 minutes with rotation at room temperature. The antibody-coupled beads were separated on a magnetic rack and washed with 200 µl of PBS supplemented with 0.02% Tween. After wash, the antibody-coupled beads were mixed with the cell lysate and incubated for 1 hour with rotation at room temperature. The supernatant was removed, the antibody-coupled beads were washed three times with 200 µl of PBS with 0.02% Tween and transferred into a fresh Eppendorf tube. After the final wash, proteins were eluted from the beads with 40 µl of the NuPage

LDS Sample Buffer supplemented with the NuPAGE® Sample Reducing Agent for 10 minutes at 90 °C. The eluates, washes and depleted materials were stored at – 20 °C.

Antibodies used in the immunoprecipitation experiment

rabbit anti-FTO	in-house raised	NA
mouse anti-FTO	MAb Technologies	Fto06-1

4.2.3 Ingenuity Pathways Analysis

Data were analysed using Ingenuity® Pathway Analysis ('IPA®, QIAGEN Redwood City' 2014). A CVS data file was uploaded which contained a list of protein IDs expressed in the UniProt/SwissProt accession system, without any MS characteristics (number of peptides identified or protein score), thus each protein had the same weight on the outcome of the analysis. The Ingenuity Knowledge Database (gene + endogenous chemicals) was used as a reference set for the analysis. Only the direct and indirect relationships that were experimentally observed, were accepted in the networks generation process. A limit of 35 molecules per network, and 25 networks per analysis was set up. The analysis was performed using all available data sources, all tissues and cell lines, all species and all mutations known. Each function or network identified in the analysis was given a *p*-value calculated by the IPA software using the right-tailed Fisher Exact Test. The *p*-value was calculated by IPA based on the number of proteins from the FTO pull-down that fall into a specific category and the total number of proteins known to be associated with this category. Thus one function/network might have a higher *p*-value than another, even if the former included fewer molecules from the pull-down than the latter. The *p*-value calculated

expresses the likelihood of the link between the given set of proteins and a particular function or a network being identified by random chance. The smaller the *p*-value, the more significant the association. Thresholds of $p<0.05$ was used identify statistically significant functions networks.

4.2.4 Immunoblotting Analysis

Immunoblotting was performed as described in 2.4.4 using the antibodies listed in **Table 9**.

Table 9. Antibodies used for immunoblotting analysis in the experiments described in Chapter 4. Antibodies were used in pairs (e.g. A1 with B1, A2 with B2).

Label	Name	Dilution	Source	Cat. Number
A1	rabbit anti-FTO	1:1000	raised in-house	
B1	anti-rabbit-HRP	1:2500	GE Healthcare	NA934
A2	rat anti-HA	1:2500	Roche	11867423001
B2	anti-rat-HRP	1:1000	GE Healthcare	NA935
A3	mouse anti-FTO	1:1000	MAb Technologies	Fto06-1
B3	anti-mouse-HRP	1:2500	GE Healthcare	NA931
A4	rabbit anti-TRIM21	1:1000	Abcam	91423
B4	anti-rabbit-HRP	1:1000	GE Healthcare	NA934

4.3 Results

4.3.1 Assessment of the Specificity and Immunoprecipitation Capacity of the Rabbit Anti-FTO Antibody

To test the capacity of our in-house raised polyclonal rabbit anti-FTO antibody to immunoblot native mouse FTO as well as exogenous FTO, untransfected and transfected HEPA1-6 cells and skeletal muscle tissue dissected from a C57BL/6J mouse were lysed using RIPA buffer (2.4.2 and 2.4.1). Protein concentration was assessed using a colorimetric assay (2.4.3). Commercially available monoclonal rat anti-HA antibody was used to detect exogenous FTO in control cells transfected with pcDNA plasmid encoding mouse HA-FTO (2.3.2). The immunoblotting analysis of 40 µg of lysate was performed as described in 2.4.4.

The analysis revealed bands representing FTO in both of the HEPA1-6 cell lysates and in the muscle lysate (**Figure 17 A**). Due to protein overexpression, the FTO band in HA-FTO transfected cells was stronger than the band representing endogenous FTO in cells transfected with empty vector. The rat anti-HA antibody detected an HA-FTO band only in the lysate of cells expressing HA-FTO. This demonstrated that both antibodies worked well with immunoblotting.

Next, I aimed to immunoprecipitate native FTO using rabbit anti-FTO antibody. The rat anti-HA antibody (confirmed to be suitable for Co-IP by the manufacturer) was used in parallel to immunoprecipitate HA-FTO from HEPA1-6 cells expressing HA-FTO. The immunoprecipitation was performed as described in 4.2.1. Briefly, 250 µg of each lysate and

5 µl of each antibody were used for IP. Lysates were diluted in Wash Buffer and incubated with antibodies at 4 °C for 14 hours. Then, 100 µl of Recombinant Protein G Agarose was added for a further 4 hours. After washing, the eluted proteins were separated by electrophoresis and visualised by immunoblotting.

Immunoblotting analysis showed enrichment of FTO in the FTO eluate compared to the depleted material (i.e. the lysate after the IP) in all three experimental samples when our in-house anti-FTO antibody was used (**Figure 17 B**). When IP was performed with the anti-HA antibody, enrichment of HA-FTO was observed only in the eluate from the lysate obtained from HA-FTO transfected cells. Beads that were not conjugated with antibody did not precipitate FTO, confirming that the FTO found in the FTO eluate was specifically precipitated by the antibody (**Figure 17 C**). Finally, a band of molecular weight similar to FTO was detected in a sample containing ~ 1 µg of in-house anti-FTO antibody when the membrane was probed with the same anti-FTO antibody and secondary anti-rabbit-HRP (**Figure 17 D**). These results showed that the heavy chain of the rabbit anti-FTO antibody can be detected with the secondary anti-rabbit HRP when the primary antibody is present in the sample in a large amount. This suggested that the primary antibody used for IP may obscure the IP results. One way to solve this problem would be to use a different antibody in the immunoblotting analysis of the IP samples, or a different IP protocol in which the antibody would not be present in the eluate.

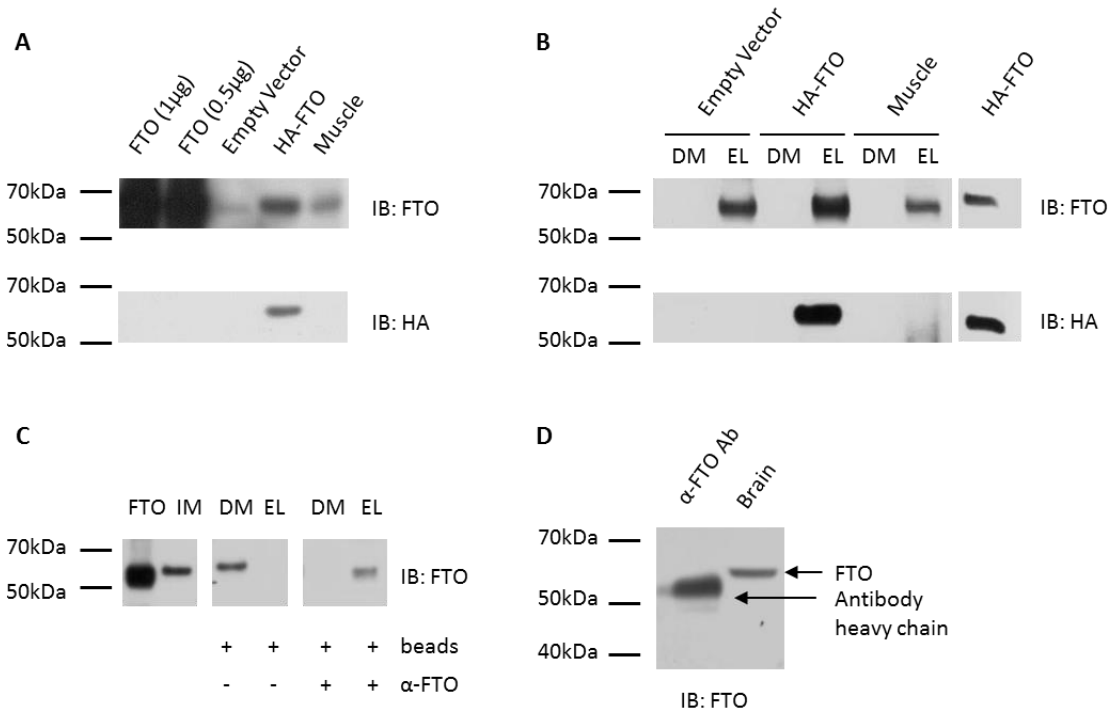

Figure 17. Immunoblotting and immunoprecipitation of mouse FTO and mouse HA-FTO. **A**; Immunoblotting analysis of HEPA1-6 cell lysate, pcDNA-HA-FTO transfected HEPA1-6 cell lysate and C57BL/6J mouse muscle lysate using rabbit anti-FTO (top panel) and rat anti-HA antibody (bottom panel). **B**; Lysates were subjected to immunoprecipitation with either rabbit anti-FTO or rat anti-HA antibody and analysed as described in A. **C**; HEPA1-6 lysate was used to immunoprecipitate FTO using beads with rabbit anti-FTO antibody or empty (unbound) beads. IM, input material; DM, depleted material; EL, eluate. **D**; Immunoblotting analysis of a sample containing ~1 µg of in-house anti-FTO antibody analysed as described in A.

Nevertheless, the presence of single, sharp bands on the immunoblots of the IP samples, and the reduction of FTO in the depleted material (DM), which was visible only when the IP was performed using antibody-bound beads, clearly shows that the rabbit anti-FTO antibody successfully immunoprecipitated native FTO from cell and tissue lysates. Also, anti-HA antibody precipitated HA tagged FTO. Thus, both of the antibodies are suitable for further immunoprecipitation studies. However, to avoid the issues resulting from overexpressing tagged protein, I decided to use the anti-FTO antibody in the future co-immunoprecipitation studies and study the PPI of native FTO protein.

4.3.2 The Comparison of Direct and Indirect Immunoprecipitation using Monoclonal and Polyclonal Antibodies

The experiment described in 4.3.1 involved indirect capture of FTO by free antibodies floating in the solution. Immobilization of the antibodies on the beads took place after the recognition of FTO by the antibodies. However, the alternative direct route (**Figure 18**) when antibodies are first immobilized on the beads and then the antibody-coupled beads are added to the cell lysate can sometimes be more effective, especially when the antigen is present in large quantities. Also, direct IP requires less antibody. As the outcome of the indirect and direct IP protocols cannot be predicted, I tested if alteration of the IP protocol would have an effect on FTO pull-down.

Additionally, I compared the effect of monoclonal and polyclonal antibodies on the success of FTO pull-down. Monoclonal antibodies may show better specificity, but polyclonal antibodies can be more efficient. I used our in-house polyclonal rabbit anti-FTO antibody and a commercial monoclonal mouse anti-FTO (MAb Technologies, Fto06-1).

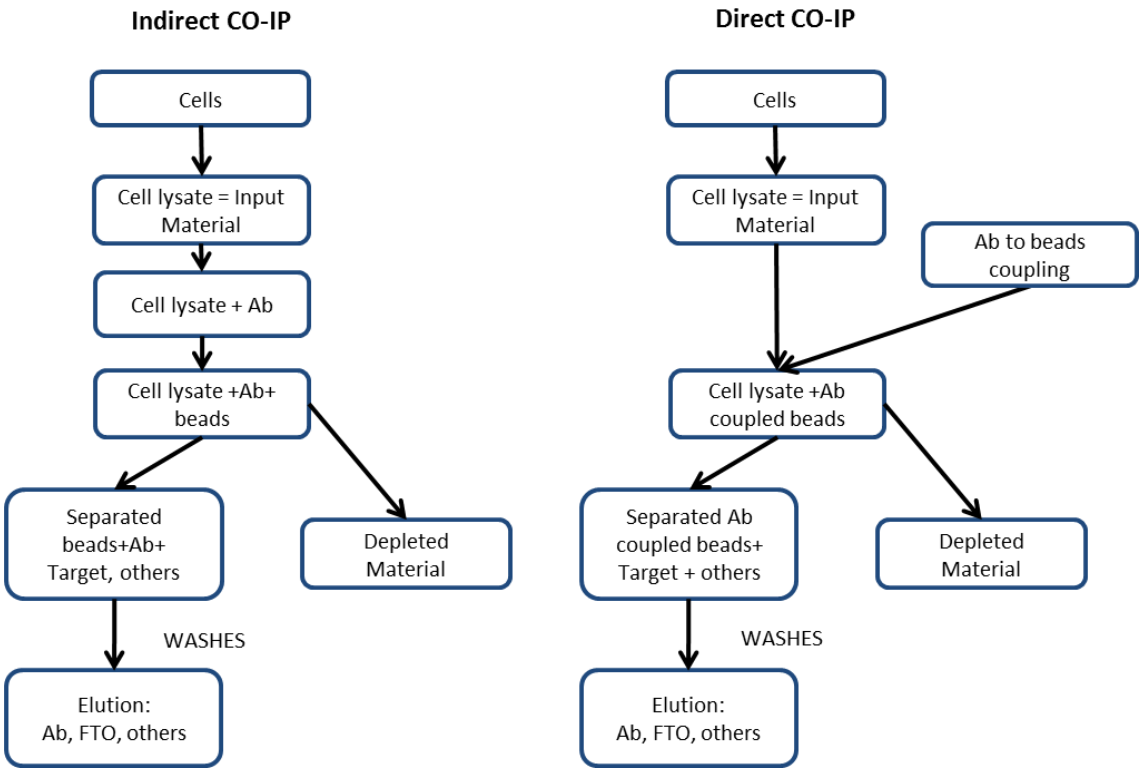

Figure 18. Indirect and direct immunoprecipitation.

Evaluation of the best methods of performing the IP, and comparison of the two types of antibodies was performed in parallel, in one experiment (4.2.2). The results of indirect and direct IP are shown in **Figure 19**. The presence of FTO in the samples from the IP using the polyclonal rabbit anti-FTO antibody was visualised with the *monoclonal* mouse anti-FTO antibody. Likewise, the presence of FTO in the samples from the IP using the monoclonal mouse anti-FTO antibody was visualised with the *polyclonal* rabbit anti-FTO antibody.

The results show that native FTO was successfully immunoprecipitated with the polyclonal rabbit anti-FTO antibody using both indirect and direct protocols (**Figure 19 A**, **C**). Distinct FTO bands, of similar intensity, were observed in the input material (IM) and the eluent, and FTO was no longer detectable in the depleted material (DM). Moreover, there were no

noticeable differences in FTO pull-down efficiency between indirect and direct IP. Similar observations were made for indirect and direct IP performed using the monoclonal mouse anti-FTO antibody (**Figure 19 B**, **D**). However, in this case an FTO band was still present in the depleted material and the intensity of the FTO band in the eluent was lower than in either the input or the depleted material.

These results indicate that both monoclonal and polyclonal antibodies can be used for IP, but the polyclonal antibody appears to be more efficient and produce a higher yield. Since commercial monoclonal antibodies are provided as ascites of unknown concentration (supplemented with glycerol), it is difficult to assess (other than empirically) the required amount of the antibody for IP. The glycerol present in the antibody solution might also impede antibody coupling to the beads. Overall, the polyclonal rabbit anti-FTO antibody seemed to be a better candidate for IP experiments. However, the monoclonal mouse anti-FTO could be used for immunoblotting.

Additionally, the comparison of indirect and direct IP protocols suggested that the outcome of each of the protocol is similar and the methods can be used interchangeably if necessary. The direct IP approach would be more suitable for MS analysis as antibody co-elution and sample contamination can be prevented by covalently coupling the antibody to the beads.

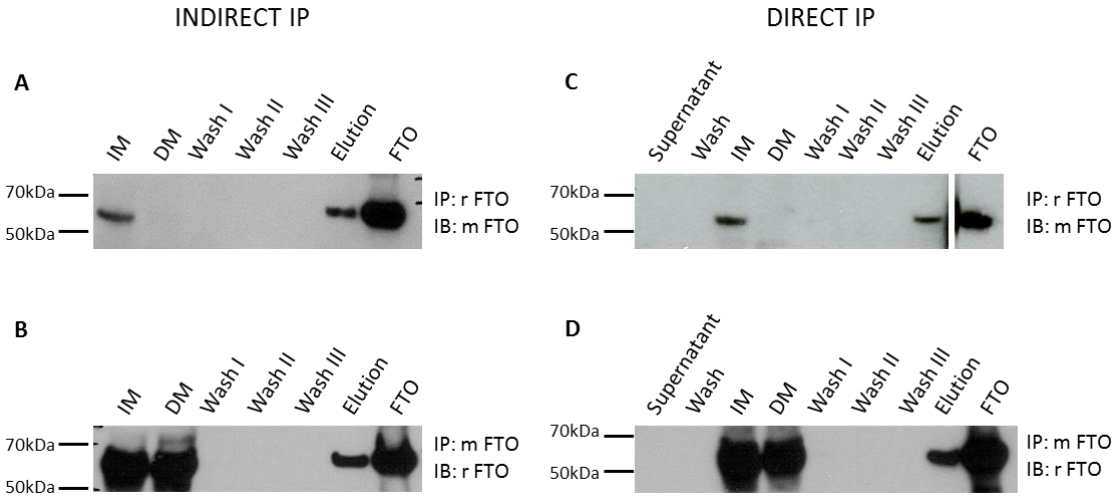

Figure 19. Immunoprecipitation of native FTO by monoclonal and polyclonal antibody using indirect and direct protocol. HEPA1-6 cells were lysed and immunoprecipitation was performed simultaneously for both antibodies. **A**, **C**; Immunoprecipitation was performed with polyclonal rabbit anti-FTO and immunoblotting was performed using monoclonal mouse anti-FTO. **B**, **D**; Immunoprecipitation was performed with monoclonal mouse anti-FTO and immunoblotting was performed with polyclonal rabbit anti-FTO. IM, input material; DM, depleted material; m FTO, monoclonal mouse anti-FTO; r FTO, polyclonal rabbit anti-FTO.

4.3.3 Analysis of Immunoprecipitated Proteins by Mass Spectrometry

Having established effective IP conditions for FTO pull-down, I next searched for proteins that co-immunoprecipitate with FTO, using mass spectrometry (MS). To assess the amount of FTO necessary for MS detection, I analysed eluents from various Co-IP experiments, using increasing amounts of starting protein extract (**Figure 20**). Proteins were separated by electrophoresis and the presence of FTO in the eluate was confirmed by immunoblotting (data not shown). Bands visualised with Coomassie stain were cut out and subjected to in-gel trypsin digestion (2.4.5). Extracted peptides were analysed using Liquid Chromatography–Tandem Mass Spectrometry (LC-MS/MS), (2.4.6) and database searches were performed using the Mascot and the UniProt/SwissProt (2.4.7).

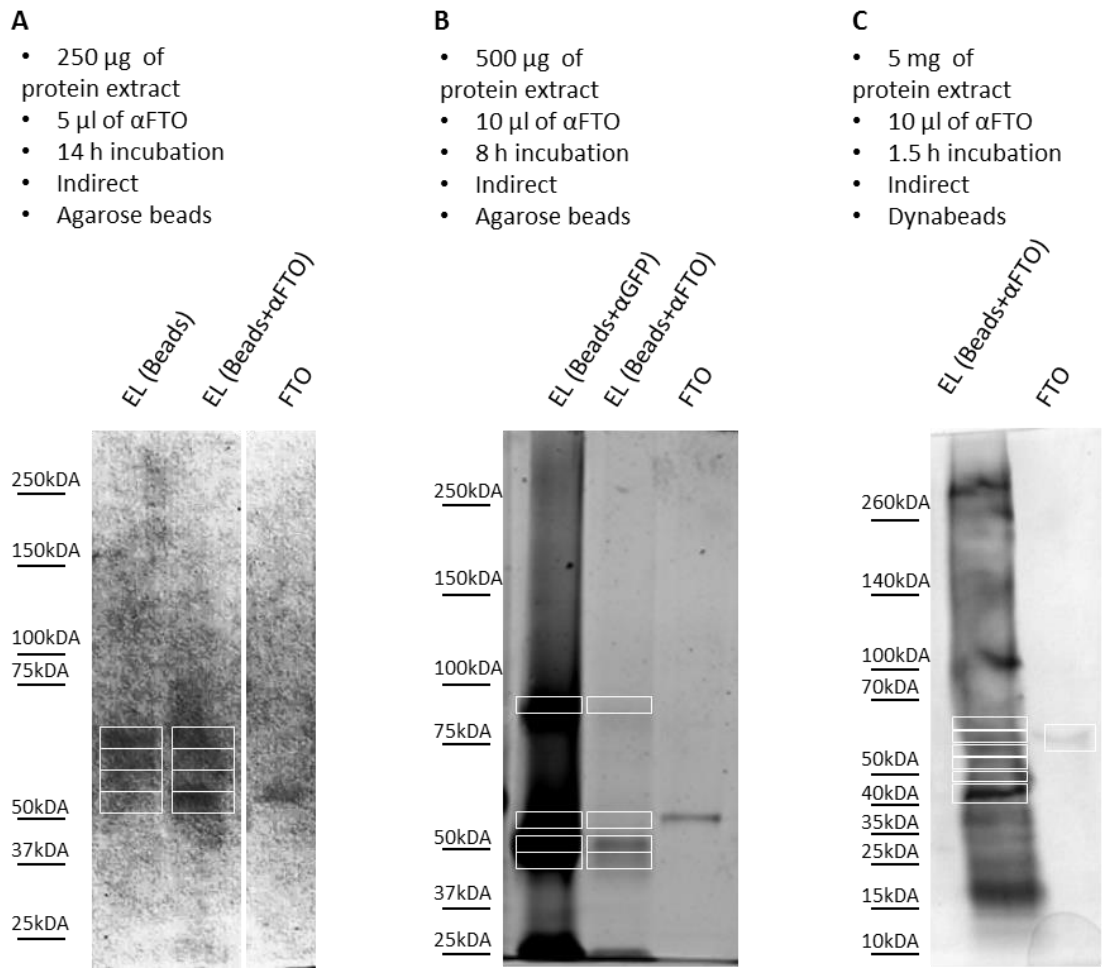

Figure 20. Coomassie stained gels of protein immunoprecipitated by the rabbit anti-FTO antibody. Immunoprecipitation was performed using increasing amounts of protein extract from HEPA1-6 cells, increasing amount of antibody and decreased incubation time (indicated above the panels). White boxes indicate bands subjected to further analysis by MS. αFTO - rabbit anti-FTO antibody.

The proteins detected by MS are listed in the **Table Appendix 3**. Surprisingly, the analysis did not result in the identification of FTO in any of the bands excised from the elution lines, although I confirmed the presence of FTO in the FTO control lane (**Figure 20 C**). Furthermore, a high abundance of keratin, tubulin, actin, ribosomal proteins (commonly known contaminants) but also trypsin and the antibody were detected.

These results indicate that the amount of immunoprecipitated FTO identified by immunoblotting was insufficient to be detected by MS. It is possible that the high abundance of common contaminants, as well as the antibodies, masked small amounts of FTO present in the bands excised from the elution lines. Therefore, in order to identify native FTO and its interacting partners by MS, I aimed to increase the amounts of the protein extract subjected to immunoprecipitation. In addition, the extraction conditions were further optimised to facilitate better protein solubilisation and preservation of protein-protein interactions. Finally, I aimed to reduce sample contamination and antibody co-elution, by introducing more stringent washes and covalently conjugating the antibodies to the beads.

4.3.4 Identification of Novel Candidate Binding Partners of FTO by Cryolysis and Direct Co-Immunoprecipitation with Antibody-Coupled Beads

In order to detect native FTO with its binding partners by MS, I increased the starting material significantly, to at least 3.5 grams of a cell pellet. To achieve this amount of the material, HEPA1-6 cells were grown in giant Nuclon Cell Culture Dishes (Thermo Scientific, 166508) of 500 cm^2 growth area.

To prevent contamination of the pull-down samples with the co-eluted antibodies, I used the direct IP approach and covalently conjugated the antibodies to the beads (2.4.8). The Dynabeads® Antibody Coupling Kit was used with the Dynabeads® M-270 Epoxy beads. The coupling reaction, using glycidyl ether (epoxy) and the antibody, resulted in the irreversible, covalent bond between the beads and the antibody (see **Figure 21**). The rabbit

anti-FTO antibody-coupled beads were stored for months without leakage of the antibody or loss of antibody specificity (as tested by protein electrophoresis and immunoblotting, data not shown).

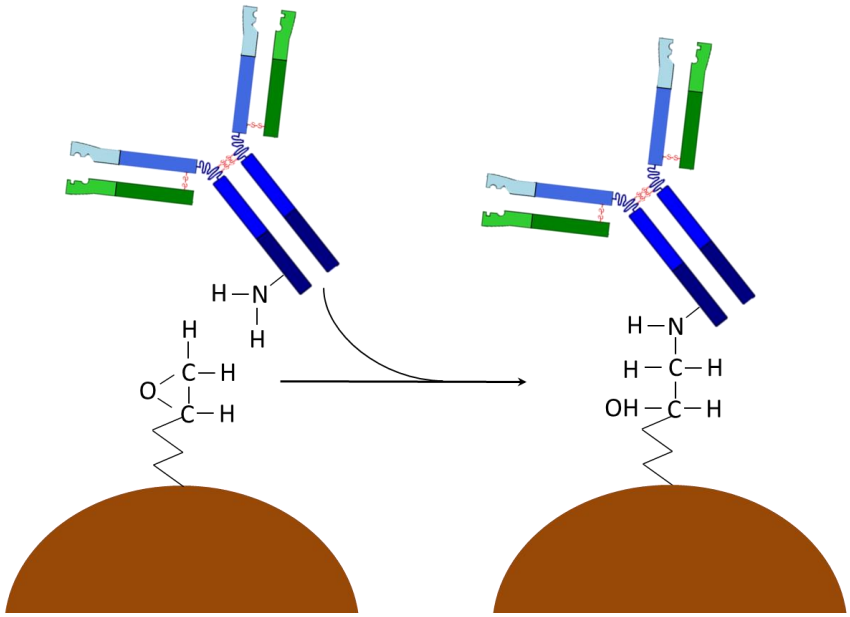

Figure 21. Antibody coupling to magnetic Dynabeads® M-270 Epoxy beads. A covalent bond forms between the amino or sulfhydryl groups of the antibody and the glycidyl ether group of the beads. Adapted from the Dynabeads® M-270 Epoxy Manual, Life Technologies.

I further modified the cell destruction protocol. Instead of detergent lysis, which was used in the IP experiments previously described, I now used cryolysis of the cell pellet in the presence of the liquid nitrogen, in order to preserve protein-protein interactions. (2.4.9). The cell powder obtained could be stored (if necessary) at -80 ^{o}C for several months without affecting protein complexes.

To reduce non-specific binding and ensure low-affinity interacting partners are included in the IP eluents, I reduced the incubation time of the antibody-coupled beads with the protein

extract to 1 hour at 4 °C, and increased the number of washes (up to 7 washes) with buffers of various stringency.

Finally, to ensure reproducible results, I used the co-immunoprecipitation buffer system provided by Dynabeads® Co-Immunoprecipitation Kit. The basic IP Buffer consisted of buffering salts (pH 7.4), 110 mM Potassium Acetate to facilitate dissociation of proteins from DNA, and 0.5% Triton X-100 to ensure sufficient solubilisation of the proteins in their native conformation, without affecting the protein complexes. Additionally, the Last Wash Buffer consisting of buffering salts (pH 7.5) was also included in the kit.

Since different salt concentrations and the presence/absence of certain buffer additives may affect the stability of protein complexes and the success of the Co-IP experiment, I tested three buffer compositions to establish the effect of buffer stringency, presence of additives, and additional washes on the success of identification of the interacting partners of FTO by MS.

The different stringency of the IP buffers was achieved by varying NaCl concentrations and adding $MgCl_2$, DTT and DNase (**Table 10**). Since the significance of ions in formation of the complex of FTO with its binding partners is unknown, and the depletion of ions could potentially affect the interaction, EDTA was avoided. Washing conditions were also slightly modified (**Table 11**). To maintain reproducible conditions, a 1:9 ratio of the sample to the IP Buffer was used in each Co-IP experiment (2.4.10). Dynabeads® M-270 Epoxy beads conjugated to the rabbit anti-GFP antibody were used as a negative control in all Co-IP experiments.

Table 10. Components of different co-immunoprecipitation buffers.

Component	Condition A Low Stringency Buffer	Condition B Mild Stringency Buffer	Condition C High Stringency Buffer
Extraction buffer	1 x IP buffer	1 x IP buffer	1 x IP buffer
NaCl	100 mM	150 mM	200 mM
Protease Inhibitors (EDTA free)	1 mM	1 mM	1 mM
$MgCl_2$	-	2 mM	2 mM
DTT	-	1 mM	1 mM
DNase	-	1ul/1ml of lysate	1ul/1ml of lysate

Table 11. Washing conditions after co-immunoprecipitation.

	Condition A Low Stringency Buffer	Condition B Mild Stringency Buffer	Condition C High Stringency Buffer
Washes	Wash I,II,III Last Wash Buffer +0.02%Tween	Wash I,II,III Last Wash Buffer +0.02%Tween Last Wash Buffer I, II, III	Wash I,II,III Last Wash Buffer +0.02%Tween Last Wash Buffer I, II, III

The immunoblotting analysis (**Figure 22 A**, **C**, **E**) showed that in all three Co-IP experiments FTO was enriched in the eluates obtained using the rabbit anti-FTO antibodies but not in the eluates obtained using the rabbit anti-GFP antibody. This demonstrates the specificity of the pull-down. SDS-PAGE analysis of the samples collected from Co-IP Condition A (**Figure 22 B**) revealed a large number of eluted proteins of similar intensity in both the GFP and FTO antibody lanes. This suggests that the stringency of the buffer A was too low. Mass spectrometry analysis of the bands excised from these lanes did not result in the identification of FTO.

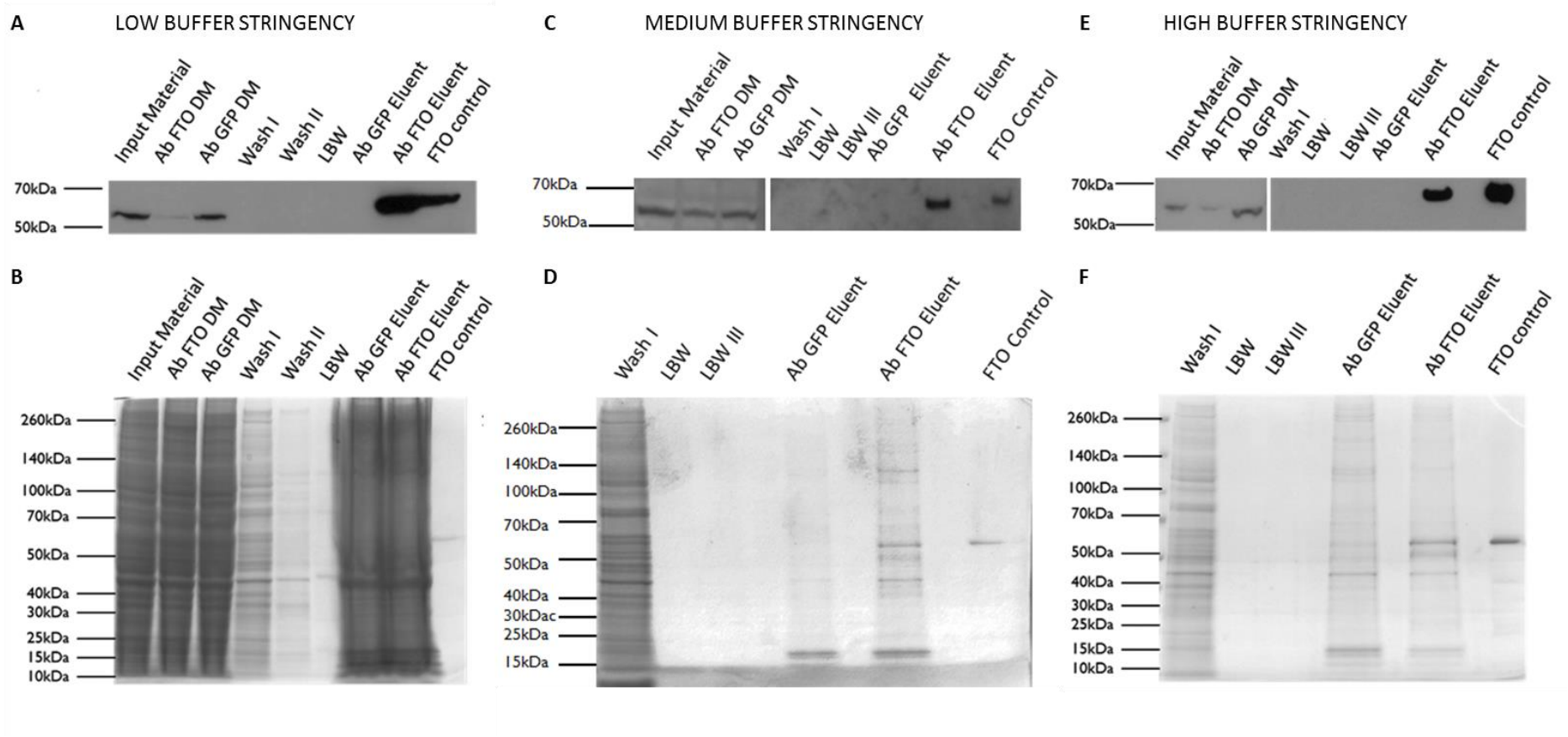

Figure 22. Co-Immunoprecipitation of FTO using cryolysis and antibody coupled to Dynabeads® M-270 Epoxy. Immunoblotting and SDS-PAGE analysis of samples collected during the co-IP experiment using Low Stringency Buffer conditions (**A**, **B**), Mild Stringency Buffer conditions (**C**, **D**) and High Stringency Buffer conditions (**E**, **F**). Immunoblotting analyses were done using mouse anti-Fto06-1 antibody (1:1000) and secondary anti-mouse antibody (1:2500).

In contrast, when the GFP and FTO eluates from Co-IP Condition B and C were examined (**Figure 22 D**, **F**), a number of distinct bands were observed. Interestingly, in each of the FTO pull-downs there were strong bands with a molecular weight corresponding to the FTO control band. These strong bands were not present in the GFP pull-down obtained using conditions B and C. MS analysis of the peptides obtained from the gel pieces which corresponded to FTO in molecular weight, confirmed that these bands represent immunoprecipitated native FTO (**Figure 23**). No FTO was detected in the gel pieces from the GFP eluate lanes in conditions B and C.

Further, Mascot analysis of all gel pieces excised from the entire GFP and FTO elution lanes resulted in identification of ~ 160 protein hits, unique for the FTO pull-down in each of the conditions B and C (**Table Appendix 4**). Between two conditions, 8 identical proteins were identified (including FTO) and 15 homologous proteins. Interestingly, MS analysis of the condition B and C pull-downs revealed that the E3 ubiquitin-protein ligase TRIM21 co-purified with FTO. Moreover, FTO and TRIM21 had one of the highest protein scores, significant protein matches, and significant protein sequences identified in the FTO unique protein lists from conditions B and C.

Overall, these results indicate that the Co-IP system consisting of cryolysis of the cell pellet in liquid nitrogen, and the direct co-immunoprecipitation method using magnetic Dynabeads® coupled to the rabbit anti-FTO antibody, allowed effective isolation and MS identification of native FTO with its candidate interacting partners. Furthermore, the results of the SDS-PAGE analysis and the MS analysis suggest that the Mild and High Stringency Buffers provided better extracting and washing conditions than the Low Stringency Buffer. Introduction of additional washes in conditions B and C also contributed to the reduction of common contaminants and a cleaner FTO pull-down. Most importantly,

the identification of TRIM21 in two separate FTO pull down experiments strongly suggests that TRIM21 in a novel candidate binding partner of FTO.

FTO identified in Condition B using Medium Stringency Buffer

Protein sequence coverage: 51%

1	MKR**VQTAEER**	EREAKKLRLL	EELEDTWLPY	LTPK**DDEFYQ**	**QWQLK**YPKLV
51	FR**EAGSIPEE**	**LHKEVPEAFL**	**TLHKHGCLFR**	DVVRIQGK**DV**	**LTPVSRILIG**
101	**DPGCTYKYLN**	**TRLFTVPWPV**	**K**GCTVK**YTEA**	**EIAAACQTFL**	**K**LNDYLQVET
151	IQALEELAVR	**EKANEDAVPL**	**CMAEFPRAGV**	**GPSCDDEVDL**	**K**SR**AAYNVTL**
201	**LNFMDPQKMP**	**YLKEEPYFGM**	**GK**MAVSWHHD	ENLVDRSAVA	VYSYSCEGSE
251	DESEDESSFE	GR**DPDTWHVG**	**FK**ISWDIETP	GLTIPLHQGD	CYFMLDDLNA
301	THQHCVLAGS	QPRFSSTHR**V**	**AECSTGTLDY**	**ILER**CQLALQ	NVLNDSDDGD
351	VSLK**SFDPAV**	**LK**QGEEIHNE	VEFEWLR**QFW**	**FQGNR**YKLCT	DWWCEPMTHL
401	EGLWK**KMESM**	**TNAVLREVKR**	**EGLPVEQRSE**	**ILSAILVPLT**	**VR**QNLRKEWH
451	ARCQSRVVRT	LPVQQKPDCR	PYWEK**DDPSM**	**PLPFDLTDVV**	**SELRGQLLEA**
501	**R**S				

FTO identified in Condition C using High Stringency Buffer

Protein sequence coverage: 49%

1	MKRVQTAEER	EREAKKLRLL	EELEDTWLPY	LTPK**DDEFYQ**	**QWQLK**YPKLV
51	FR**EAGSIPEE**	**LHK**EVPEAFL	TLHK**HGCLFR**	**DVVRIQGKDV**	**LTPVSRILIG**
101	**DPGCTYK**YLN	TR**LFTVPWPV**	**K**GCTVK**YTEA**	**EIAAACQTFL**	**K**LNDYLQVET
151	IQALEELAVR	**EKANEDAVPL**	**CMAEFPRAGV**	**GPSCDDEVDL**	**KSRAAYNVTL**
201	**LNFMDPQKMP**	**YLK**EEPYFGM	GKMAVSWHHD	ENLVDRSAVA	VYSYSCEGSE
251	DESEDESSFE	GR**DPDTWHVG**	**FK**ISWDIETP	GLTIPLHQGD	CYFMLDDLNA
301	THQHCVLAGS	QPRFSSTHR**V**	**AECSTGTLDY**	**ILERCQLALQ**	**NVLNDSDDGD**
351	**VSLK**SFDPAV	LK**QGEEIHNE**	**VEFEWLRQFW**	**FQGNR**YKLCT	DWWCEPMTHL
401	EGLWK**KMESM**	**TNAVLREVK**R	EGLPVEQR**SE**	**ILSAILVPLT**	**VR**QNLRKEWH
451	ARCQSRVVRT	LPVQQKPDCR	PYWEK**DDPSM**	**PLPFDLTDVV**	**SELR**GQLLEA
501	RS				

Figure 23. Sequence coverage of identified FTO as detected by MS. Gel pieces dissected from FTO elution lanes were subjected to in-gel digestion and the peptides were identified by MS. Data were analysed by Mascot as described in 2.4.7. Matched peptides are shown in bold red.

4.3.5 Functions and Network Analysis of FTO Unique Pull-Down Hits

To identify potential networks and molecular mechanisms that FTO and its interacting partners may be involved in, the unique proteins identified in the FTO pull-down (Condition B) were further subjected to the networks and functions analyses, through the use of Ingenuity Pathway Analysis (IPA, QIAGEN), (4.2.3).

The molecular and cellular functions analysis revealed 29 statistically significant functions (**Figure 24**). The top seven functions are summarised in the **Table 12** and include (in a descending order): RNA Post-Transcriptional Modification, Cellular Function and Maintenance, Gene Expression, Cellular Growth and Proliferation, Amino Acid Metabolism, DNA Recombination, Replication and Repair, and Small Molecule Biochemistry. Interestingly, IPA identified the processing of RNA as the function with the most significant association (p=5.14E-12) and 18 molecules from the FTO pull-down are known to show this function (**Table 13**).

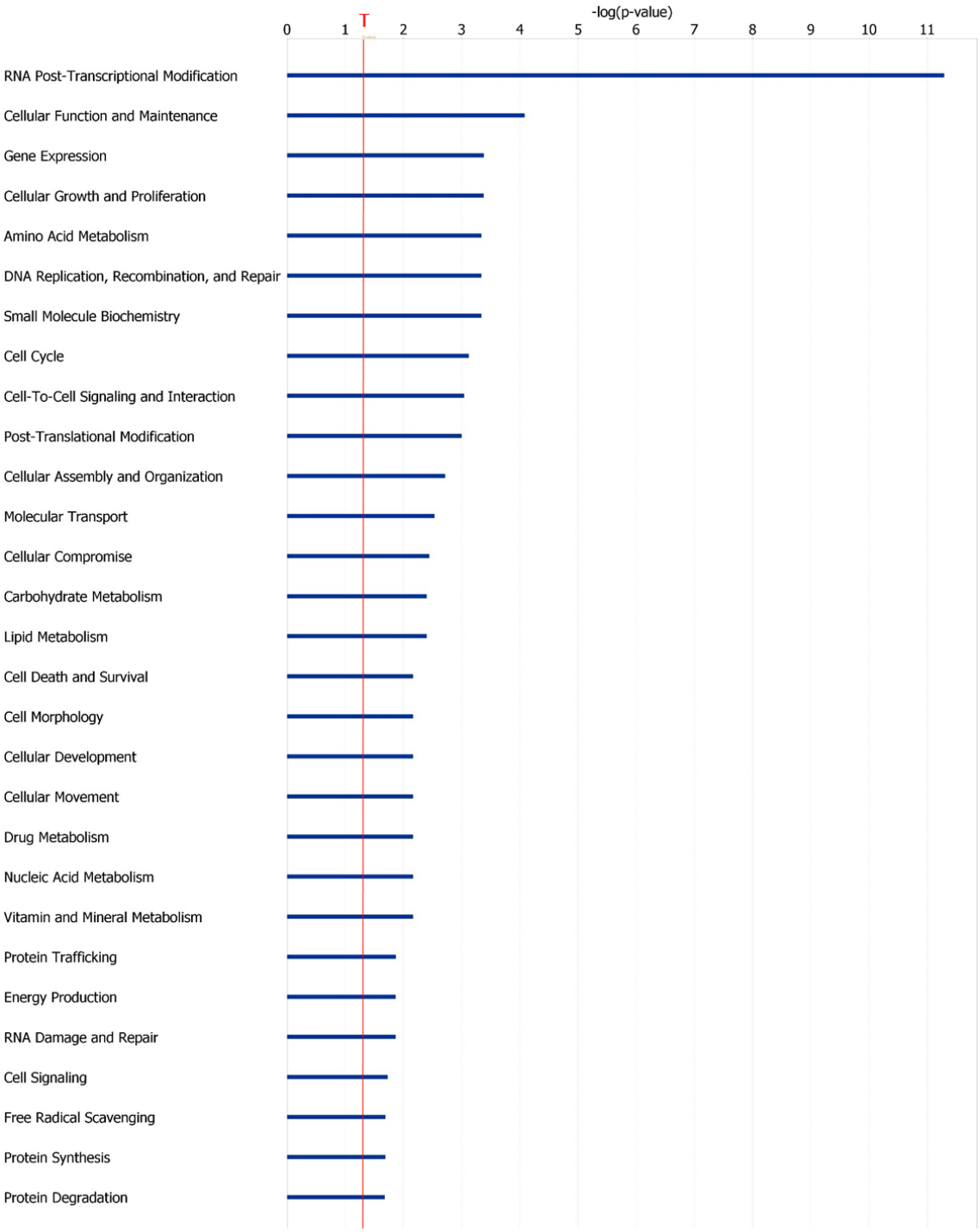

Figure 24. Molecular and cellular functions identified based on the proteins co-precipitated with FTO. The unique proteins in the FTO pull-down (Condition B) were categorised in the functional groups based on the current scientific knowledge using IPA. *p*-values were calculated by the software using he Fisher's exact test. T- threshold ($p<0.05$).

Table 12. Top Molecular and Cellular Functions identified by IPA. Functional groups which included FTO as one of the molecules are labelled with a "(FTO)".

ID	Name	p-value	# Molecules
1	RNA Post-Transcriptional Modification (FTO)	5.14E-12 – 2.70E-02	21
2	Cellular Function and Maintenance (FTO)	8.24E-05 – 3.04E-02	33
3	Gene Expression	4.15E-04 – 1.36E-02	40
4	Cellular Growth and Proliferation (FTO)	4.16E-04 – 2.70E-02	55
5	Amino Acid Metabolism	4.57E-04 – 2.70E-02	5
6	DNA Recombination, Replication and Repair	4.57E-04 – 1.36E-02	16
7	Small Molecule Biochemistry (FTO)	4.57E-04 – 3.34E-02	17

Table 13. Functions in the RNA Post-Transcriptional Modification category.

Function	p-value	Molecules	# Molecules
Processing of RNA	5.14E-12	HNRNPA1,HNRNPF,HNRNPH1, HNRNPU,NOP56,PHRF1,PRPF19, RBMX,RBMXL1,RPL35A,RPS19, RPS28,SAFB,SNRPF,SRSF2,SRSF7, SSB,TARDBP	18
Splicing of RNA	6.08E-08	HNRNPA1,HNRNPF,HNRNPH1, PRPF19,RBMX, RBMXL1,SNRPF,SRSF2,SRSF7, TARDBP	10
Processing of mRNA	1.66E-05	HNRNPA1,PHRF1,PRPF19,RBMX, RBMXL1,SAFB,SRSF2,SRSF7	8
Splicing of mRNA	3.56E-05	HNRNPA1,PRPF19,RBMX,RBMXL1, SRSF2,SRSF7	6
Processing of rRNA	3.49E-04	NOP56,RPL35A,RPS19,RPS28	4
Annealing of RNA	4.57E-04	HNRNPC,HNRNPU	2
Alternative splicing of mRNA	6.43E-04	HNRNPA1,RBMX,RBMXL1	3
Selection of splice site	3.44E-03	RBMX,RBMXL1	2
Binding of tRNA-Val	6.83E-03	SSB	1
Unwinding of siRNA	6.83E-03	DDX58	1
Splicing of primary transcript RNA	8.12E-03	HNRNPF,HNRNPH1	2
Maturation of tRNA	1.36E-02	SSB	1
Repair of RNA	1.36E-02	FTO	1
Splicing of hnRNA	2.70E-02	TARDBP	1

Next, I used IPA to investigate networks that are comprised of the proteins identified in the FTO pull down (4.2.3). The network of proteins involved in Cellular Function and Maintenance, Cardiac Enlargement, Organ Morphology received the highest score (69) and contained 30 molecules, including FTO (**Table 14, Figure Appendix 3**). Interestingly, networks with second and third highest scores were involved in RNA Post-Transcriptional Modification. Network 3 (**Figure Appendix 4**) with score 34 contained 18 of the proteins pulled down by FTO, including TRIM21. No network included both FTO and TRIM21, however this is understandable as IPA provides only information about known, previously demonstrated interactions.

Table 14 Top Networks identified by IPA.

ID	Function of the Network	Score	# Molecules
1	Cellular Function and Maintenance, Cardiac Enlargement, Organ Morphology	69	31
2	RNA Post-Transcriptional Modification, Amino-Acid Metabolism, Small Molecule Biochemistry	60	18
3	RNA Post-Translational Modification, Post-Translational Modification, Hereditary Disorder	34	19
4	Cardiovascular Disease, Hereditary Disorder, Cellular Function and Maintenance	26	15
5	Cell Death and Survival, Cell Cycle, Embryonic Development	26	15
6	Lipid Metabolism, Molecular Transport, Small Molecule Biochemistry	24	14

Overall, these results are consistent with the increasing evidence that FTO functions in m^6A demethylation (described in Chapter 1) and provide an insight into candidate molecular mechanisms and networks that FTO and its binding partners may be involved in. Identification of RNA post-translational modification as the top function and one of the top networks provides a starting point for further investigations.

4.3.6 TRIM21 is a Novel Binding Partner of FTO and the Interaction Can Be Found in Mice and Humans

Using Co-IP of native FTO and MS analysis of the co-immunoprecipitated proteins I have identified E3 protein ligase TRIM21 as a candidate binding partner of FTO. To test if TRIM21 is a real interacting partner of FTO, I first validated the MS results by immunoblotting (**Figure 25 A**). The immunoblotting analysis of GFP and FTO pull-downs (Conditions B) using rabbit anti-TRIM21 antibody revealed the presence of TRIM21 in the FTO eluate, but not in the GFP eluate. Interestingly, the band representing TRIM21 in the FTO eluate had higher molecular weight than the control band. This may be a result of post-transcriptional modifications (PTMs) occurring during the Co-IP or in concentrated eluate sample.

Next, to validate the interaction of TRIM21 with FTO, I performed reversed Co-IP of native TRIM21 using magnetic Dynabeads® coupled to the rabbit anti-TRIM21 antibody (2.4.8, 2.4.9 and 2.4.10) and condition B buffers and washing protocol. Beads conjugated to the rabbit anti-GFP antibody were used as a control. The immunoblotting analysis using rabbit anti-TRIM21 antibody showed that native TRIM21 was successfully precipitated from the HEPA1-6 cells and that TRIM21 was present in the TRIM21 eluate, but not in the GFP eluate (**Figure 25 B**). Similarly to the previous experiment on the FTO eluate, the TRIM21 band in the TRIM21 eluate had a higher molecular weight than the TRIM21 bands in the input material or the depleted material. This was observed each time the experiment was repeated (3 times). Importantly, immunoblotting analysis of the same pull down samples using the rabbit anti-FTO antibody revealed enrichment of FTO in the TRIM21 eluate, but not in the GFP eluate (**Figure 25 C**).

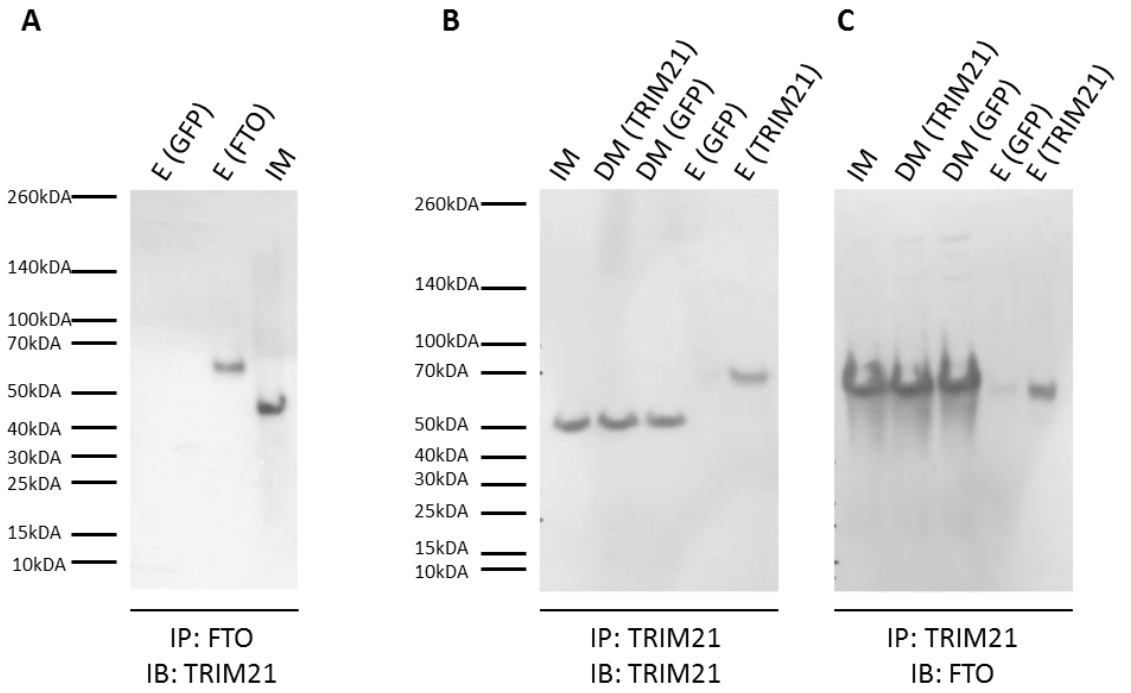

Figure 25. Immunoblotting analysis of FTO Co-IP and reversed TRIM21 Co-IP. A; GFP and FTO eluates from the FTO Co-IP (Condition B) were analysed using rabbit anti-TRIM21 antibody. **B, C**; Reversed Co-IP was performed with polyclonal rabbit anti-TRIM21 antibody. GFP and FTO eluates were analysed using the rabbit anti-TRIM21 antibody (**B**), and the rabbit anti-FTO antibody (**D**); IM, input material; DM, depleted material; E, elution; IP, immunoprecipitation: IB, immunoblotting.

Lastly, I have investigated if the TRIM21 and FTO interaction is cell type specific or also occurs in other mouse and human cells (**Figure 26**). Tissues were dissected from 20-week old C57BL/6J male mice (2.1.4) and as a negative control, the heart was dissected from 20-week old male mice in which FTO was genetically deleted specifically in muscle (muscle-specific FTO-KO mice). To study the TRIM21 and FTO interaction in human cells, HEK293 cells were grown in T175 flasks and cryolysed. Tissue and cell powder after cryolysis were subjected to Co-IP using the magnetic Dynabeads® coupled to the rabbit anti-FTO antibody (2.4.9 and 2.4.10).

The results of the immunoblotting analysis of the FTO eluates from the mouse tissues and the human cells using the rabbit anti-FTO antibody showed that FTO was successfully

immunoprecipitated from the human HEK293 cells and all the tissues studied except the pancreas (**Figure 26 A**). However, an FTO band of low molecular weight was detected in the pancreas sample lane. This band most probably represents FTO degraded by pancreatic proteases prior to, or during, the Co-IP experiment. As expected, no FTO was pulled down from the muscle-specific FTO-KO heart tissue. More importantly, the immunoblotting analysis using the rabbit anti-TRIM21 antibody showed that TRIM21 was co-precipitated in all the samples containing precipitated FTO (**Figure 26 B**). No TRIM21 was detected in FTO pull-down from FTO-KO heart tissue.

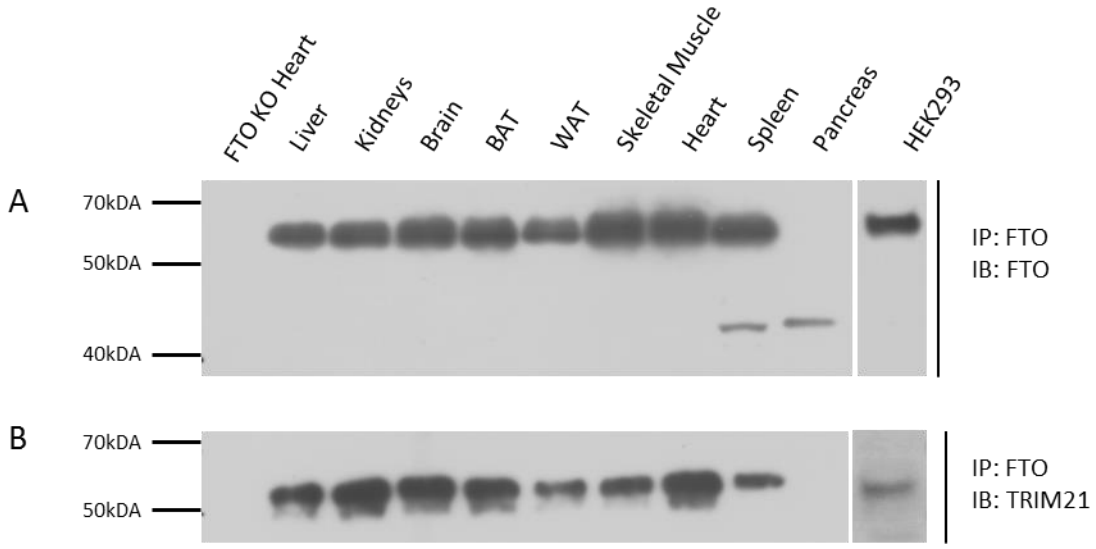

Figure 26. Immunoblotting analysis of FTO Co-IP from mouse tissue and human cells. Mouse tissues and human HEK293 cells were subjected to Co-IP using the magnetic Dynabeads® coupled to the rabbit anti-FTO antibody. **A**; GFP and FTO eluates from the FTO Co-IP (Condition B) were analysed using rabbit anti-TRIM21 antibody. FTO eluates were analysed using the rabbit anti-FTO antibodies (**A**), and the rabbit anti-TRIM21 antibody (**B**); IP, immunoprecipitation: IB, immunoblotting.

Overall these results indicate that TRIM21 and FTO are real binding partners and that the interaction occurs in many different mouse tissues as well as human cells. Finally, the lack of TRIM21 in the FTO pull down from the FTO-KO heart tissue confirms the specificity of the interaction and excludes the possibility of TRIM21 binding non-specifically to the antibody or the beads during Co-IP.

4.4 Discussion

4.4.1 Summary

A cellular role of FTO has yet to be clearly demonstrated. Thus, I searched for proteins that interact with FTO to gain more insight into the function of FTO. No proteins that interact with FTO were known at the start of this thesis [although some have been identified subsequently (Gulati et al. 2013; Gulati et al. 2014)]. After extensive protocol optimisation I isolated native mouse FTO and identified a number of candidate binding partners (CBPs) by mass spectrometry (MS). Analysis of FTO CBPs revealed RNA Post-transcriptional Modification as a top molecular and cellular function, and 18 molecules from this category are involved in processing of RNA. Networks involved in RNA Post-transcriptional Modification were also reported as the second and third top network identified by the IPA software. Moreover, the E3 ubiquitin-protein ligase TRIM21 was co-immunoprecipitated in two independently replicated experiments. Reverse Co-IP, using an anti-TRIM21 antibody, confirmed the specificity of the FTO-TRIM21 interaction. Finally, I showed that the interaction occurs in various mouse tissues as well as in human cells.

4.4.2 Optimisation of a Co-IP Protocol for Studying Protein Binding Partners of Native FTO

Initially, I considered performing IP on isolated nuclei, however based on the evidence that FTO can be found in the cytoplasm (Chapter 3), I decided to immunoprecipitate FTO from whole cell lysates. I chose to use endogenous FTO rather than overexpressing FTO in cultured cells for the following reasons. First, overexpressed protein may swamp the

normally fine-tuned signalling pathways, making the overexpressed protein unable to bind to its partners or skewing its preferential localisation (Noselli and Perrimon 2000). Moreover, the tagged protein may be subjected to a post-translational modifications (PTMs), such as phosphorylation, which may increase or decrease its affinity for interacting partners (Berggård, Linse, and James 2007).

A polyclonal rabbit anti-FTO antibody was raised in-house, thus its ability to immunoprecipitate FTO had first to be assessed. FTO was depleted from the lysate only when the antibody was used, which indicated that the antibody successfully pulled-down FTO. The detection of a band of a similar molecular weight to FTO in the sample containing~1 μg of rabbit anti-FTO antibody does not undermine the IP ability of the antibody. However, it demonstrated that caution must be taken when choosing the elution technique or IP protocol. Contamination of eluents with antibody is common and occurs when the antigen-antibody-beads complexes are treated with reducing elution buffers (e.g. sample buffer at high temperatures as used in this experiment). Perhaps, detection reagents (e.g. CleanBlot HRP Detection Reagent, Thermo Scientific) that recognise only native antibody could be used to avoid detection of reduced antibody on the membrane.

Our polyclonal anti-FTO antibody was more efficient at IP than the commercial monoclonal antibody, as assessed by comparison of the amount of FTO remaining in the depleted material. A likely explanation may be that our polyclonal antibody was raised against the whole FTO molecule, and thus might recognise FTO even if some epitopes were modified or hidden due to interaction with binding partners. The affinity of the monoclonal antibody may have been weak, and some of the antigen and its interacting partners may have been lost during the IP incubation and washes (Bonifacino and Dell'Angelica 2001). An alternative explanation of the differences in FTO antibody pull-down efficiency might be

that due to the unknown concentration of the monoclonal antibody, less of the antibody was used than the polyclonal antibody. Lastly, differences in band intensity observed in the IP immunoblots performed with monoclonal versus polyclonal antibodies could result from differences in antibody performance during immunoblotting, not from variability in the protein amounts.

Immunoprecipitated FTO from 250 μg, 500μg and 5mg of cell lysate was not detected by MS (although it was detected in the immunoblot). The most likely explanation is that the amount of starting material was not enough to identify pulled-down FTO and its binding partners. Immunoblotting analysis are known to be very sensitive, and depending on quality of antibodies and chemiluminescence reagents can detect just a few hundred molecules ('UK Proteomics Core Facility' 2014). In contrast, mass spectrometry (MS) techniques require about 1 billion molecules. An alternative explanation may be that proteins of similar molecular weight to FTO (e.g. IgG heavy chain) that were more abundant in the pull-down masked FTO.

4.4.3 Identification of FTO Binding Partners by MS

Based on the evidence from the optimisation process, I have determined the final conditions that resulted in purification and identification by MS of native FTO and its binding partners. I believe that the success of the final protocol was based on several factors.

First, large amounts of cell starting material ensured a high abundancy of native FTO. Second, shorter incubations should have reduced non-specific binding. Third, rapid harvest

and freezing of the cells in liquid nitrogen followed by cryogrinding should have provided sufficient sample homogenisation while preserving large and labile complexes. Cryogrinding with mortar and pestle was time consuming and might have caused inconsistencies in sample processing as well as contamination (collagen from human skin was identified by MS) (Burden 2012). Thus, an automated cryogrinder could be an alternative option, especially for high-throughput experiments.

In the final protocol, I used anti-FTO antibody conjugated to the magnetic beads. This improved further MS analyses of FTO and its partners, although it might have led to a reduction of antibody sensitivity, especially when working with a monoclonal antibody ('Antibody Labelling and Immobilization Sites' 2015). However, our antibody did not show any signs of reduced activity or stability (as assessed by repeated IPs and gel electrophoresis of suspension buffer) even after 6 months of storage at 4 ^{o}C (data not shown). Furthermore, my selection of magnetic beads with hydrophilic, low background binding surface might have further reduced background contamination and certainly improved ease of handling ('Dynabeads® Co-Immunoprecipitation Kit' 2014).

I believe that my extraction and IP conditions as well as optimisation of the buffer components were essential for successful IP and MS analysis. Since stock buffers were purchased from Invitrogen, it is difficult to discuss the effect of each buffering salt components, as they are not disclosed. Regardless of that, the results of buffer additives optimisation suggest that NaCl ≥ 150 mM, $MgCl_2$ 2 mM, DTT 1 mM, and additional DNase might have been crucial for extraction and Co-IP of native FTO. While it is reasonable to propose that additional washes reduced nonspecific binding, careful examination of the Last Wash Buffer (LWB) lanes on the SDS-PAGE gels shows that in conditions B and C the lanes show no visible contamination. However, this is not the case in condition A. Thus, the

stringency of the buffer and the additives may be key factors contributing to reduction of nonspecific contamination and efficient FTO extraction. Since FTO employs non-heme Fe (II) as a cofactor and other ions may be crucial components of FTO complexes, EDTA was avoided in all buffers. However, as no experiments were performed in this study where EDTA was included in the buffer, I cannot comment on the role of ions in FTO pull-down.

Mass Spectroscopy analysis and Mascot database searching identified native FTO (with ~ 50% sequence coverage) and around 270 unique proteins were detected between stringency conditions B (moderate) and C (high). In this study, unique FTO protein hits were identified by comparing all protein hits in anti-FTO pull-down to proteins detected in parallel anti-GFP pull-down. Both antibodies were raised in rabbit. Antibodies raised in the same species are commonly used as negative controls (Bonifacino and Dell'Angelica 2001, chap. 9). Ideally, the same antibody isotype should be used; however, as our anti-FTO antibody was raised in-house, it consists of a mixture of all rabbit antibody isotypes. Perhaps another way of addressing Co-IP control would be to use knock-out and wild-type MEFs or mouse tissue.

4.4.4 Candidate Binding Partners (CBPs) of FTO

The extensive protocol optimisation and MS analysis led to isolation of native mouse FTO and identification of a large number of candidate binding partners (CBPs) of FTO. Identification of and validation of TRIM21 is discussed in 4.4.6.

The small number of identical proteins observed to bind to FTO using conditions B and C FTO is not uncommon. Only 3 % of proteins were reported to be identified by more than one method (von Mering et al. 2002; Tord Berggård 2007). This can be explained by

variability and inconsistency of experimental protocol, the high rate of nonspecific contamination and/or limitation in purification of certain type of protein complexes. For these reasons, proteins identified by Gulati's studies may not be detected in this study, especially since Gulati et al. used tagged FTO in the initial MS analysis, EDTA and overnight incubation, all which I avoided. Nevertheless, I detected methionyl-tRNA synthetase (MRS) in condition C and exporin-2 (XPO2) in condition B pull-downs, both recently reported as FTO binding partners (Gulati et al. 2013; Gulati et al. 2014). However, both hits had very low significant protein matches. Although none of the other aminoacyl-tRNA synthetases reported by Gulati et al. were detected in this study, identification of MRS supports the suggested role of FTO in mRNA translation and link with amino acid sensing (Gulati et al. 2013).

The role of XPO2 in FTO nuclear export is still unknown and has yet to be clearly demonstrated. Since XPO2 binds only importin α in the presence of RanGTP in the nucleus and exports it to the cytoplasm (Kutay et al. 1997; Cook et al. 2007; Güttler and Görlich 2011), perhaps the presence of XPO2 in FTO pull-downs supports the prediction that FTO nuclear import may be mediated through importin α-β pathway (discussed in Chapter 3, 3.3.1). Interestingly, at least three other proteins involved in nucleocytoplasmic transport were identified in this study in FTO pull-downs including Ran-binding protein 17 (RANBP17), nuclear pore complex protein 85 and 88 (NUP85, NUP88), which could be interesting targets for future FTO nuclear export studies.

4.4.5 FTO and Its CBPs May Be Involved in RNA Post-Transcriptional Modification

Identification of RNA Post-Transcriptional Modification as the most significant functional category, as well as second and third top networks, strongly supports the link between m^6A demethylase activity of FTO and the currently proposed roles of m^6A modification in RNA metabolism and processing (discussed in Chapter 1, 1.4.9). Processing of RNA was the top function identified and comprised of 18 molecules from FTO pull-down including heterogeneous nuclear ribonucleoproteins (hnRNPs) and other RNA binding proteins. This strongly suggest FTO has a role in events that pre-mRNAs undergo before becoming translationally active mRNAs. Processing of pre-mRNA and mRNA in the nucleus is facilitated by complexes of over 20 hnRNPs, with several containing nuclear export signal (NES), eventually transporting RNAs to the cytoplasm (Cooper 2000, chap. 8; Kim et al. 2000). HNRNPA1, a protein that shuttles between the nucleus and cytoplasm transporting RNA and localises to messenger RNA ribonucleoprotein (mRNP) granules in the cytoplasm (Guil, Long, and Cáceres 2006), was co-immunoprecipitated with FTO. Another hnRNP detected, HNRNPU, is also associated with cytoplasmic mRNP granules and untranslated mRNA (Weidensdorfer et al. 2009). Given the dual FTO cellular localisation, these CBPs may interact with nuclear or cytoplasmic FTO or facilitate export through direct interaction or export of mRNA with bound FTO.

Splicing of RNA was the second top function within RNA Post-Transcriptional Modification category, which is consistent with the reported role of FTO in alternative splicing (Zhao et al. 2014), its location in nuclear speckles, and its association with nuclear pre-mRNA splicing components (Jia et al. 2011; Berulava et al. 2012). At least ten molecules from my FTO pull-down are involved in RNA splicing, including SRSF2, which is reported to have increased binding to m^6A when FTO is depleted (Zhao et al. 2014). The numerous functions predicted by the software analysis that are related to rRNA, tRNA and hnRNA suggest that FTO binding partners and its networks may target a variety of RNAs.

The link to Cellular Function and Maintenance is in line with the association of FTO with ciliogenesis and Wnt signalling (Osborn et al. 2012). Interestingly, several CBPs of FTO were associated by IPA with movement of organelles, maintenance of the cell and organisation of the nucleus, which could be relevant to FTO changes in cellular localisation during the cell cycle (Chapter 3). The predicted association with Gene Expression is in line with the suggested role of m^6A modification in mRNA (Dominissini et al. 2012) and increased mRNA levels due to overrepresentation of m^6A in set of mRNAs resulting from FTO knock-out (Hess et al. 2013). This association further strengthens the link between FTO and RNA processing. The association with Cell Growth and Proliferation supports reported decrease in growth rate and reduced mRNA translation in *Fto*$^{-/-}$ MEFs (Gulati et al. 2013; Merkestein et al. 2015) and can further be linked with suggested role of FTO in amino acid sensing and link with mTORC1 pathway (Gulati et al. 2013). Interestingly TRIM21 was also associated with this function due to its role in regulation of proliferation and cell death of mouse B lymphoma cells (Espinosa et al. 2006). Identification of Amino Acid Metabolism may suggest link between FTO and amino acid synthesis through association with succinate, an intermediate product of citric acid cycle.

Top networks identified by IPA were in line with the functions mentioned above and further support an association of FTO with cellular maintenance and RNA processing. FTO was included in Network 1 due to indirect relationship with RAC-alpha serine/threonine-protein kinase (AKT) (phosphorylation of AKT was changed in cultured fibroblasts isolated from *Fto* KO mice), (Osborn et al. 2014). Interestingly TRIM21 was included in Network 3, also involved in RNA processing. Overall, the networks identified by IPA spanned the cytoplasm and the nucleus further supporting the possibility of multiple compartments of FTO action and can be helpful while designing future experiment to confirm specific

protein-protein interaction. Agreeably, the computational predictions of MS data cannot substitute experimental confirmation of individual FTO interaction and its function, however the analysis allowed me to systematize vast amount of information related to CBPs of FTO, validate the relevance of performed Co-IP and gave me directions for future experiments. Moreover, the predicted networks may be helpful when choosing CBPs of FTO for validation and further studies.

4.4.6 TRIM21 Binds to FTO in Various Mouse Tissues and Human Cells

Two independent Co-IP experiments identified TRIM21 as a candidate binding partner of FTO. Reversed Co-IP of native TRIM21 revealed that FTO can be pulled-down by TRIM21. This demonstrated that FTO and TRIM21 do indeed interact.

The higher molecular weight of the TRIM21 band in the eluents compared to the general lysate or the depleted material in both Co-IPs was unexpected, but was observed each time the experiments were repeated. One possible explanation might be that due to sample concentration after Co-IP, different salt concentration in the lysates and eluents affected the protein's mobility on the gel. However, this is unlikely because the location of FTO in the same sample was unaffected. The higher molecular weight band TRIM21 band might represent a post-translationally modified protein that was enriched in the sample, perhaps due to preferential pull-down. However, the shift in TRIM21 molecular weight was observed in both anti-TRIM21 and anti-FTO pull-down, and it is unlikely that two different antibodies would preferentially pull-down TRIM21 with the same PTMs. The most probable explanation for the shift in the molecular weight of the TRIM21 band is that it is related to the E3 ubiquitin-protein ligase activity and autoubiquitination capability of TRIM21

(Espinosa et al. 2006). Perhaps the increased concentration of TRIM21 and bound E2 and E1 enzymes of ubiquitination system on the beads during the pull-down increased the probability of autoubiquitination of TRIM21, resulting in a higher molecular weight.

Confirmation that TRIM21 and FTO interact in a number of different mouse tissues indicates that the FTO-TRIM21 interaction occurs in mice and is not tissue-specific. The conserved character of the FTO-TRIM21 interaction may suggest that binding of these proteins is crucial for the function or life cycle of each protein. Moreover, the proteins seem to be forming a stable complex as TRIM21 was pulled-down with FTO even after 12 hours Co-IP incubation (data not shown). The lack of TRIM21 in the anti-FTO pull-down from *FTO* knock-out heart confirmed that TRIM21 does not bind non-specifically to the anti-FTO antibody. Moreover, the lack of co-precipitated TRIM21 from pancreas may suggest that TRIM21 does not bind to truncated FTO.

4.4.7 Future Plans

Although I have successfully immunoprecipitated native FTO and identified ~250 unique CBPs, it would be interesting to further modify the Co-IP conditions and continue the search for FTO binding partners. Because PTMs can affect protein-protein interactions, I would like to examine FTO interactions in presence of inhibitors of phosphorylating/ dephosphorylating or ubiquitinating/ deubiquitinating enzymes. Moreover, I would like to search for labile and weak FTO interactions using chemical cross-linking (Tang and Bruce 2009).

I would also like to use Co-IP to study FTO binding to RNA. First, I would like to examine the effect of RNA degradation on ability of FTO to co-precipitate identified CBPs (especially all

RNA binding proteins) and validate if RNA is necessary for TRIM21-FTO interaction. Because FTO can demethylate RNAs, I would also like to modify my Co-IP protocol to preserve RNA and FTO interactions (e.g. UV light crosslinking) and co-immunoprecipitate FTO with bound RNA. A similar approach (CLIP-Seq) has been already applied to study the distribution of m^6A modification in RNA (Meyer et al. 2012) and its changes upon *Fto* knock-out (Zhao et al. 2014). CLIP-Seq using anti-FTO antibody would provide direct information about the variety of RNA and cellular processes regulated by FTO.

Moreover, since effects of FTO in specific tissues on the body mass phenotype are yet unknown, I would like to repeat the FTO Co-IP from a variety of different mouse tissues and subject pull-downs to MS analysis to study tissue-specific interactions. Pathway and function analysis of unique FTO CBPs could indicate which cellular functions are associated with FTO in each tissue type. This might help to determine which tissues are involved in the effects of FTO on body mass, and identify key tissues for future mouse studies.

4.4.8 Conclusions

I have developed a Co-IP protocol to investigate protein binding partners of native FTO. Using mass spectrometry, I have identified ~ 270 unique candidate binding partners of FTO. Moreover, I have demonstrated that E3 protein ubiquitin ligase TRIM21 is a novel, conserved binding partner of FTO.

5 Characterisation of TRIM21 and FTO Interaction

5.1 Introduction

Using co-immunoprecipitation of native FTO isolated from mouse HEPA1-6 liver cells, I identified TRIM21 as a novel interacting partner of mouse and human FTO. TRIM21 is also known as the 52 kDa ribonucleoprotein autoantigen RO52 or Sjögren syndrome type A antigen (SSA1), but here I will refer to it simply as TRIM21.

In humans, the *TRIM21* gene lies on chromosome 11 in the HLA region 11p15 (Reymond et al. 2001). It is expressed throughout the body, with variable mRNA expression levels; the lowest levels are found in pancreas (relative level 1), cerebral cortex (3) testis (3), heart (4), and highest levels in lungs (19), lymph node (19) and spleen (22)('EMBL-EBI Expression Atlast' 2014). At the protein level TRIM21 was detected at medium/high levels in all cell lines studied ('The Human Protein Atlas' 2014).

Structural studies suggest diverse molecular and cellular functions for TRIM21. First, Chan et al. described a putative zinc finger domain in the N-terminal domain of TRIM21 (residues 20 - 59), and a leucine zipper domain in the middle region (residues 213 - 238) of the protein suggesting a role in DNA and/or RNA binding (Chan et al. 1991). Indeed, this hypothesis was confirmed by Frank and colleagues, who revealed that human TRIM21 binds to human double-stranded DNA, but not to single-stranded DNA, in a sequence-specific manner (Frank, McCubbin, and Heldermon 1995; Frank 1999). Later, TRIM21 was classified as a member of the tripartite motif family (TRIM) (Chan et al. 1991). It comprises

a RING domain at its N-terminus, a BBOX and coiled-coil (CC) region in the middle, and a PRYSPRY (or B30.02) domain at its C-terminus (Torok and Etkin 2001; Davd A. Rhodes et al. 2002; Reymond et al. 2001). Two isoforms are known, TRIM21α and TRIM21β (which lacks the CC region). TRIM21α was found to homo-multimerise through the CC region, while TRIM21β does not multimerize (Reymond et al. 2001).

Similarly to other TRIM proteins, TRIM21 was demonstrated to act as an E3 ubiquitin-protein ligase and ubiquitination was catalysed by the RING domain of TRIM21 (Wada and Kamitani 2006). Ubiquitination studies revealed that TRIM21 can autoubiquitinate itself with monoubiquitin and polyubiquitin chains, with monoubiquitination being the most prevalent modification (Espinosa et al. 2006; Fukuda-Kamitani and Kamitani 2002). Interestingly, poly-ubiquitinated TRIM21 did not accumulate in HEK293T cells treated with a proteasome inhibitor. This suggests that this type of polyubiquitination was not involved in TRIM21 degradation via proteasome (Wada and Kamitani 2006). In fact, the mechanism of TRIM21 degradation is still unknown. Self-polyubiquitination of TRIM21 was reported to be mediated by UBE2D1 (UBCH5a), UBE2D3 (UBCH5c), and UBE2E1 (UBCH6)(Espinosa et al. 2006; Wada and Kamitani 2006) but not by UBCH2, UBCH3, UBCH7, UBE2L6 (UBCH8) and UBCH10 (Espinosa et al. 2008). Interestingly, UBE2D1 was shown to be localised in the cytoplasm while UBE2E1 was present in the nucleus (Plafker et al. 2004; Espinosa et al. 2008).

The cellular location of TRIM21 is somewhat controversial. Some authors suggest TRIM21 is predominantly found in the cytoplasm and to a lesser extent in the nucleus (Keech, Gordon, and McCluskey 1995; Pourmand et al. 1998), while others describe a predominantly nuclear localisation (Ben-Chetrit et al. 1988, 52; Kelekar, Saitta, and Keene 1994). More recently, Espinosa et al. showed that TRIM21 can be found in both the

cytoplasm and the nucleus, and that amino acids 128-245, comprising the intact CC region and the leucine zipper (residues 213-238), are needed for cytoplasmic localisation. In addition, amino-acids 381-470 (part of the SPRY domain) are crucial for nuclear localisation (but only in the absence of the leucine zipper) (Espinosa et al. 2006; Espinosa et al. 2008). However, mutations in the leucine zipper that prevent homo dimerization and multidimerisation did result in increased TRIM21 nuclear accumulation (Espinosa et al. 2008). Additionally, residues 244-267 form a putative nuclear export signal (NES), but mutation of this region did not result in increased TRIM21 nuclear accumulation (Espinosa et al. 2008). It was suggested that TRIM21-mediated ubiquitination supported by UBE2D1 occurs in the cytoplasm, but in order to interact with UBE2E1, TRIM21 must translocate to the nucleus.

A distinct perinuclear localisation of TRIM21 has also been reported (Espinosa et al. 2008). It seems possible that TRIM21 that is found in close proximity to the nucleus may be actively imported into the nucleus. The involvement of exportin-1, a protein that plays a role in the active nuclear export transport of many protein cargos (e.g. TRIM27), was excluded in the case of TRIM21. Exposure to the inflammatory mediators hydrogen peroxide (H_2O_2), nitric oxide (NO) and type 1 interferon (INFα), results in translocation of TRIM21 from the cytoplasm to the nucleus (Nobuhara et al. 2007; Espinosa et al. 2008; Strandberg et al. 2008). Interestingly, TRIM21 has no classical nuclear localisation signal (NLS) (Keech, Gordon, and McCluskey 1995). Nevertheless, the nuclear import may be supported by protein-protein interactions or post-translational modification. Overall, it seems possible that TRIM21 has both cytoplasmic and nuclear substrates and that subcellular compartmentalization may function as a mechanism to regulate TRIM21-mediated ubiquitination.

Surface exposure of TRIM21 has also been reported in apoptotic keratinocytes and apoptotic human salivary gland (HSG) cells, suggesting that the protein can be translocated to the surface of the dying cells. Furthermore, TRIM21 was found in apoptotic blobs and bodies (Ohlsson, Jonsson, and Brokstad 2002; Yang et al. 2000).

A distinct, speckled pattern of cytoplasmic TRIM21 has been reported (Ishii et al. 2003). Further studies revealed that TRIM21 co-localised to cytoplasmic processing bodies (p-bodies) (Eystathioy et al. 2003; Bhanji et al. 2007; Yamochi et al. 2008). These are small dot-like aggregates of specific proteins and RNA that regulate mRNA translation and decay (Parker and Sheth 2007; Kulkarni, Ozgur, and Stoecklin 2010). Target RNAs can be recruited to p-bodies and translationally silenced where they remain until they are released to re-enter translation. Alternatively, RNA can be degraded by the deadenylation-decapping-decay pathway.

The complete composition of p-bodies is still to be characterised, but it is already known that p-bodies contain many components. These can be classified into two categories (Parker and Sheth 2007). The first category contains 'core' proteins which are constitutively present in p-bodies, and are conserved from yeast to mammals. The second category comprises proteins that are found in p-bodies only under certain conditions or in specific cell types or organisms. Core proteins comprise those involved in the repression/decay machinery and include the deadenylating enzymes CCR4–CAF1, PAN2–PAN3 and NOT1-5p, XRN1 (an exoribonuclease that degrades RNA in the 5' to 3' direction), proteins involved in repression of translation such as SCD6P/CAR-1/RAP55 and the decapping enzyme DCP2 with its enhancers DCP1, EDC3, HEDLS, PAT1, DHH1/RCK and the LSM1–7 complex (Kulkarni, Ozgur, and Stoecklin 2010).

Removal of the mRNA cap is catalysed by DCP2 in an irreversible step that leads to mRNA degradation by XRN1. TRIM21 was shown to co-localise and interact with DCP2, through both its N- and C-terminal domains (Yamochi et al. 2008). Moreover, the interaction enhanced DCP2 decapping activity in a dose-dependent manner. These results suggest an association between TRIM21 and processes involved in the regulation of mRNA translation and decay.

The search for other TRIM21 interacting partners revealed that the protein can bind *in vitro* to the constant region (Fc) of human IgG1, IgG2 and IgG4 in a class and subclass specific manner (IgG3, IgA and IgM were not recognised) (Yang et al. 1999; Yang et al. 2000; James et al. 2007; Rhodes and Trowsdale 2007; Keeble et al. 2008; Takahata et al. 2008). Yang proposed that the interaction was based on antibody regions other than the variable region of the IgG and the TRIM21 PRYSPRY and was later confirmed by others (Rhodes and Trowsdale 2007; Keeble et al. 2008). The IgG1 heavy chain can be polyubiquitinated by TRIM21 in mammalian cells which results in IgG1 degradation by the proteasome (Takahata et al. 2008). This was described to be mediated through TRIM21 and a molecular chaperone p97/valosin-containing protein (VCP), a component of endoplasmic reticulum associated degradation (ERAD) system, which recognises misfolded or mutated proteins. It was also established that TRIM21 is a specific Fc receptor, highly conserved within mammals (Keeble et al. 2008).

The biological relevance of the above mentioned phenomenon remained unknown until it was established that antibodies bound to viruses can enter the infected cell where they are rapidly recognised by TRIM21 and targeted for proteasomal degradation. This results in neutralization of viral infections and stimulation of immune signalling (Mallery et al. 2010;

McEwan et al. 2011; McEwan et al. 2013). These results revealed a novel, TRIM21-antibody based model of intracellular immunity.

To summarise, TRIM21 is a protein of complex and diverse molecular functions which regulates important cellular events at the protein level through ubiquitination and proteasomal degradation. It also acts at the RNA level, where it influences mRNA translation, degradation and gene expression. However, important questions remain unanswered. For example, what is the role of the TRIM21-FTO interaction? Does TRIM21 act as an E3 ubiquitin-protein ligase and target FTO for ubiquitination? If so, does the ubiquitination lead to proteasomal degradation? What is the cellular compartment that facilitates the TRIM21 and FTO interaction? Does the TRIM21-FTO interaction play a role in modulating RNA metabolism in p-bodies? Thus, in this chapter, I aimed to answer these questions.

The specific aims were to:

1) Determine which domain of TRIM21 and FTO are required for interaction.
2) Investigate if TRIM21 mediates ubiquitination of FTO and if this leads to FTO degradation.
3) Investigate the role and cytoplasmic location of TRIM21 and FTO interaction.

5.2 Methods

5.2.1 Introduction of an N-terminal Tag and Creation of Tagged and Truncated Versions of TRIM21 and FTO

MYC-tagged TRIM21 and truncated variants.

Mouse *Trim21* was purchased as a fully sequenced cDNA from Source Bioscience (**Figure 27 A**). The *Trim21* cDNA was cloned by the manufacturer into a pCMV-Sport6 vector using *Sal*I and *Not*I cloning sites. An N-terminal MYC-tag *Trim21* was created by cloning the ORF *of TRIM21* cDNA into the pCMV-MYC plasmid (kindly provided by Dr Chris Esapa), (**Figure 27 B**).

HA-tagged FTO and truncated variants.

Mouse *Fto* was kindly provided by Dr James McTaggart in a pCDNA3.1 vector. An N-terminal HA-tagged FTO was created by cloning the FTO sequence into the pCMV-HA-N plasmid (kindly provided by Dr. Chris Esapa), (**Figure 28**).

Oligonucleotides were designed to overlap the coding region of cDNA sequence and included restriction endonuclease sites for *EcoRI* at the 5` terminus and *XhoI* at the 3` terminus. Overhangs were added to create binding sites for the restriction endonuclease and to ensure correct translation of the cDNA sequence. Truncated versions of each protein were created using oligonucleotides to overlapping specific regions of cDNA. The list of primers used in *Trim21* and *Fto* cloning is included in **Table 15** and **Table 16**.

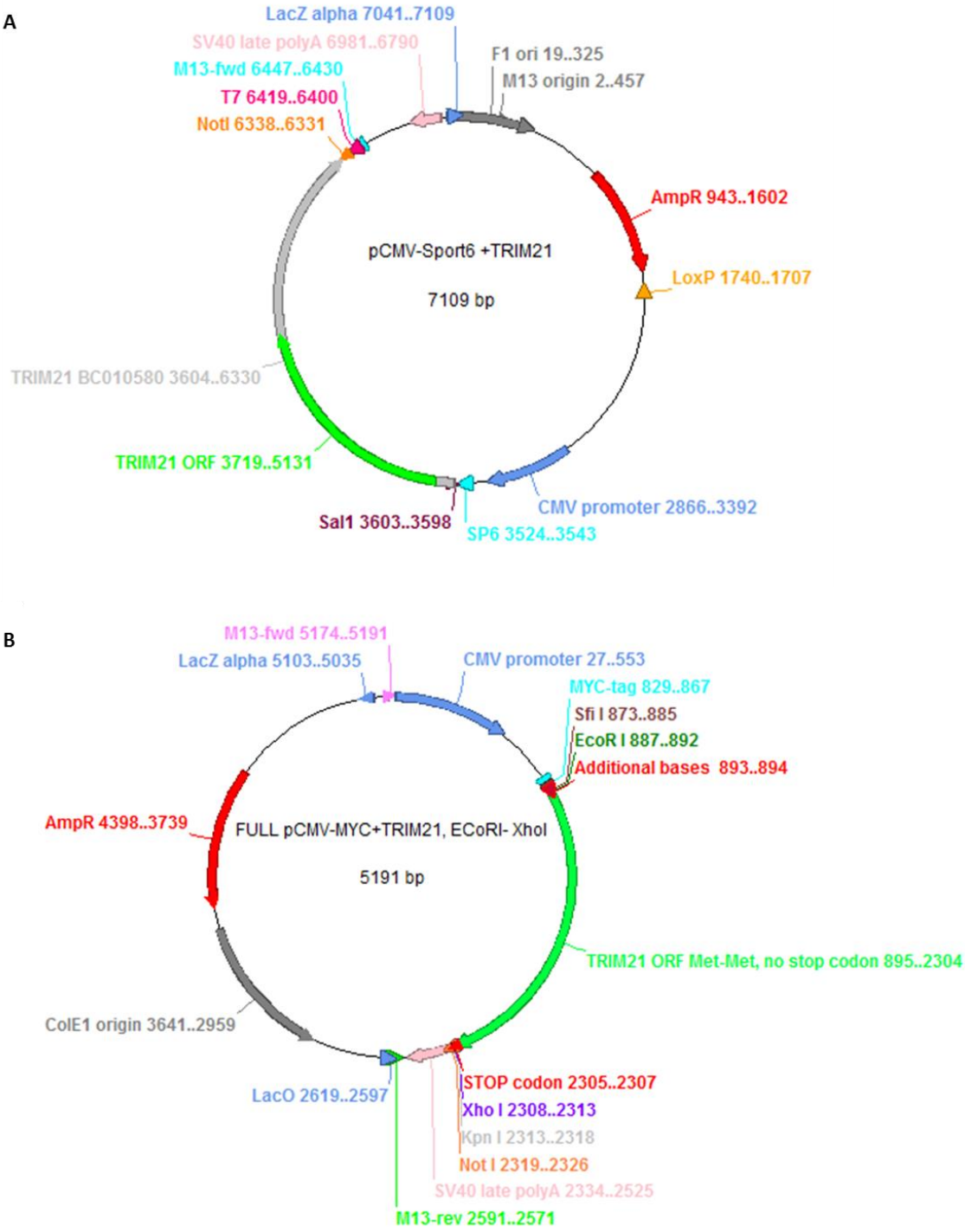

Figure 27. Maps of DNA plasmids used in TRIM21 cloning. A, pCMV-Sport6 with *Trim21* fully sequenced cDNA clone IRAVp968A0819D (Source Bioscience). **B**, Final product of cloning, pCMV-MYC with *Trim21* and a MYC tag at the N-terminus.

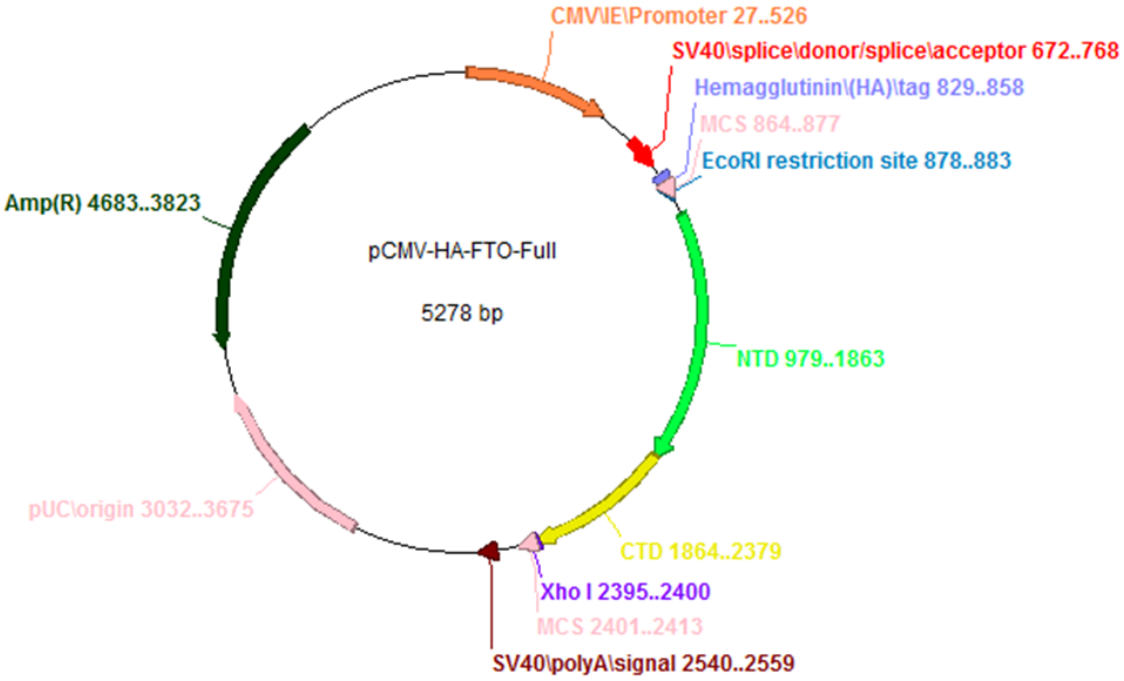

Figure 28. Map of DNA plasmid with a final product of *Fto* cloning into pCMV-HA-N plasmid.

Table 15. *Trim21* cloning primers information.

Name	Sequence (5' to 3')	Amplicon size (bp)
TRIM21ForwEcoRI	CTAGGAATTCAGATGTCACCCTCTACAACCTC	1435
TRIM21RevXhoI	GTACCTCGAGTCACATCTTTAGTGGACAGAGC	
ΔRINGForwEcoRI	CTAGGAATTCAGTTTCTGCTCCGAAACCTCAGG	1252
ΔRINGRevXhoI	GTACCTCGAGTCACATCTTTAGTGGACAGAGC	
ΔBBOXForwEcoRI	CTAGGAATTCAGAAAGAGTTGGCCGAGAAGATG	976
ΔBBOXRevXhoI	GTACCTCGAGTCACATCTTTAGTGGACAGAGC	
ΔSPRYForwEcoRI	CTAGGAATTCAGATGTCACCCTCTACAACCTC	1051
ΔSPRYRevXhoI	GTACCTCGAGTCAGGAGAATCTCTGGGCACCTAG	
ΔPRYEcoRI	CTAGGAATTCAGATGTCACCCTCTACAACCTC	862
ΔPRYRevXhoI	GTACCTCGAGTCACACAGGGCATGTGCTTGTTAG	

Table 16. *Fto* cloning primers information.

Name	Sequence (5' to 3')	Amplicon size (bp)
FTOForwEcoRI	CTAGGAATTCAGATGAAGCGCGTCCAGAC	1531
FTORevXhoI	GTACCTCGAGCTAGGATCTTGCTTCCAGC	
N-termForwEcoRI	CTAGGAATTCAGATGAAGCGCGTCCAGA	1003
N-termRevXhoI	GTACCTCGAGCTAGCCTGTTGAGCACTCTGC	
C-termForwEcoRI	CTAGGAATTCAGACCTTGGATTATATCTTAGAACGC	553
C-termRevXhoI	GTACCTCGAGCTAGGATCTTGCTTCCAGC	

The desired DNA fragments of were amplified by PCR (2.2.6). Amplified DNA fragments were resolved by DNA gel electrophoresis (2.2.1) and visualised by UV light. Desired bands were excised and the DNA was extracted as described in 2.2.2.

5.2.2 Double Digestion of Vector and Insert with Restriction Endonucleases

Purified PCR products and the vectors were double digested with restriction enzymes EcoRI-HF and XhoI (New England Biolabs) using Cut Smart Buffer. Reactions were performed at 37 °C for 1 hour.

Double Digest Reaction Components

Restriction Enzyme	10 Units (1µl)
DNA	1 µg
Buffer	1 x (5µl)
Reaction Volume	50 µl

Enzymes were heat inactivated at 65 °C for 20 minutes. DNA fragments were resolved by DNA gel electrophoresis (2.2.1) and visualised by UV light. Desired bands were excised and the DNA was extracted as described in 2.2.2.

5.2.3 Ligation of Vector and Insert

DNA fragments were ligated with the vector using T4 DNA Ligase (New England Biolabs) with molar ratios of 1:3 of vector to insert. A negative control of vector without an insert was performed in parallel. The reaction mixture was incubated for 30 minutes at 16 °C.

Ligation Reaction Components

10X T4 DNA Ligase Buffer	2 µl
Vector DNA	100 ng
Insert DNA	various
Nuclease-free water	to 20 µl
T4 DNA Ligase	1 µl

After the incubation, 1 µl of ligated DNA was used to transform DH5α™ competent cells as described in 2.2.3. Cells were spread on solid LB media selective plates containing ampicillin (Amp) at a concentration of 50 µg/ml. After overnight (12-16 hours) incubation at 37 °C, single colonies from each plate were picked with a sterile pipette tip and transferred to 5 ml of LB medium containing ampicillin. Plasmid DNA was isolated from the bacterial culture as described in 2.2.4. Purified DNA was sequenced using the standard pCMV forward primer. Successful constructs were fully sequenced using cloning Trim21 and Fto primers (**Table 15** and **Table 16**).

5.2.4 Immunoblotting Analysis

Immunoblotting was performed as described in 2.4.4 using the antibodies listed in **Table 17**.

Table 17. Antibodies used for immunoblotting analysis in the experiments described in Chapter 5. Antibodies were used in pairs (e.g. A1 with B1, A2 with B2).

Label	Name	Dilution	Source	Cat. Number
A1	rabbit anti-FTO	1:1000	raised in-house	
B1	anti-rabbit-HRP	1:2500	GE Healthcare	NA934
A2	mouse anti-MYC	1:4000	Millipore	05-419
B2	anti-mouse-HRP	1:4000	GE Healthcare	NA931
A3	rat anti-HA	1:2500	Roche	11867423001
B3	anti-rat-HRP	1:1000	GE Healthcare	NA935
A4	rabbit anti-GAPDH	1:500	Santa Cruz	Sc-25778
B4	anti-rabbit-HRP	1:1000	GE Healthcare	NA934
A5	rat anti-HA	1:2500	Roche	11867423001
B5	anti-rat 800	1:15000	LI-COR	92632219
A6	mouse anti-αTubulin	1:10000	DSHB	12G10
B6	anti-mouse 680	1:15000	LI-COR	92668020
A7	rabbit anti-TRIM21	1:1000	Abcam	91423
B7	anti-rabbit-HRP	1:1000	GE Healthcare	NA934

HRP-conjugated Secondary Antibody

The presence of proteins was revealed by Amersham ECL Western blotting detection reagent (GE Healthcare, RPN2109) following the manufacturer's instructions. Alternatively, SuperSignal West Pico Chemiluminescent Substrate (Thermo Scientific, 34077) was used to detect small amounts of protein. The membranes were exposed to Hyperfilm ECL Autoradiography Film (Amersham, GE Healthcare) and Xograph Film Processor was used to visualise the protein on the film.

Fluorophore-conjugated Secondary Antibody

The membranes were incubated with a specific primary antibody followed by a 1 hour incubation with a fluorophore-conjugated secondary antibody at room temperature in the dark. Next, the membranes were washed three times for 10 minutes with TBST and one time for 10 minutes with TBS. The membranes were then dried on the filter paper for 15 minutes at room temperature in the dark. Detection of the protein of interest was performed using the Odyssey SA Infrared Imaging System (LI-COR Biosciences). Odyssey channel 800 and 700 was used to detect anti-rat 800 and anti-mouse 680 antibody respectively. The membranes were scanned at 100μm resolution and medium quality. The intensity level for the 700 and the 800 channels was of 2.5 and 7.3, respectively.

5.2.5 Densitometry Analysis of FTO and Tubulin Bands

The quantification of the protein bands visualised by the fluorophore-conjugated secondary antibody was performed using Odyssey SA Infrared Imaging Software (LI-COR Biosciences) in the single-channel mode, on black and white images. A "New Feature" was created

around each studied band using the "Details View" option. The median value of the pixels outside of all sides of the feature was chosen as the method of a background quantification. The integrated intensity of each band was calculated by the software. Relative FTO levels were determined by dividing the integrated intensity values of FTO band in each lane by the integrated intensity values of the corresponding tubulin band. Student's t-test was used to investigate differences between the means. The analysis and graphical representation of the results were performed using GraphPad Prism.

5.2.6 Mammalian Cell Transfections

Transfections were carried out as described in 2.3.2 using the conditions listed in the **Table 18**.

Table 18. Transfection conditions used in the experiments described in Chapter 5.

Culture vessel	12-well plate	T75 flask	T175 flask
Surface area	3.8 cm^2	75 cm^2	175 cm^2
Complete growth medium	1.0 ml	19.7 ml	42.5 ml
Serum-free medium	100 µl	1.9 ml	4.2 ml
DNA	1 µg	19 µg	44 µg
TransIT-LT1 Reagent	3 µl	57 µl	131 µl

Co-transfection of multiple plasmid DNAs was performed by first mixing the plasmid DNAs to give the desired DNA stock solution and then adding TransIT-LT1 Reagent.

5.2.7 Immunocytochemistry

Cells were subjected to the immunocytochemistry analysis according to the protocol described in 2.3.3. Combinations of antibodies used in the experiments described in Chapter 5 are listed in **Table 19**.

Table 19. Antibodies used in the immunocytochemistry analysis in Chapter 5. Antibodies were used in pairs (e.g. A1 with B1, A2 with B2).

Label	Name	Dilution	Source	Cat. Number
A1	rabbit anti-FTO	1:100	raised in-house	
B1	anti-rabbit Alexa-488	1:400	Life Technologies	A-21206
A2	mouse anti-MYC	1:35	Millipore	05-419
B2	anti-mouse Alexa 680	1:100	Life Technologies	A-21057
A3	mouse anti-mono and polyubiquitin	1:100	Enzo	BML-PW8810-0100
B3	anti-mouse Alexa 680	1:100	Life Technologies	A-21051
A4	goat anti-TRIM21	1:20	Santa Cruz	Sc-21367
B4	anti-goat Texas Red	1:100	Abcam	ab6883
A5	mouse anti-DCP2	1:20	Abcam	ab168574
B5	anti-mouse Alexa 633	1:200	Life Technologies	A-21052

5.3 Results

5.3.1 TRIM21 Binds to FTO through a SPRY Domain

The results of the Co-IP, reversed Co-IP and mass spectrometry (MS) experiments presented in Chapter 4 revealed that TRIM21 is a novel FTO binding partner. I therefore next investigated which part of TRIM21 interacts with FTO.

Extensive evidence shows that TRIM21 (**Figure 29 A**) is a member of the tripartite motif family (TRIM) that contains an N-terminal RING-finger domain, a BBOX domain, and a PRYSPRY domain at its C-terminus (Torok and Etkin 2001; Rhodes et al. 2002). Numerous proteins have been shown to bind to TRIM2 and these interactions involved the C-terminal PRYSPRY domain and N-terminal RING domain of TRIM21 (Zhang et al. 2013; Yamochi et al. 2008; Yang et al. 1999). I used the ISIS computational method, which identifies interacting residues by combining the protein sequence and evolutionary information (Ofran and Rost 2007), to predict possible protein binding sites in TRIM21. These are illustrated in **Figure 29 B**.

In order to determine which domains of TRIM21 interact with FTO, a series of MYC-tagged mutants were constructed (**Figure 30 A**) as described in **5.2.1, 5.2.2** and **5.2.3**. ΔRING lacks the first 61 amino acids (aa), including the RING domain that has the ubiquitin-protein ligase activity. ΔBBOX (aa 154-470) lacks both the RING and BBOX domains. ΔSPRY and ΔPRY are C-terminal deletion constructs that lack the SPRY (ΔSPRY) and both SPRY and PRY domains (ΔPRY) respectively.

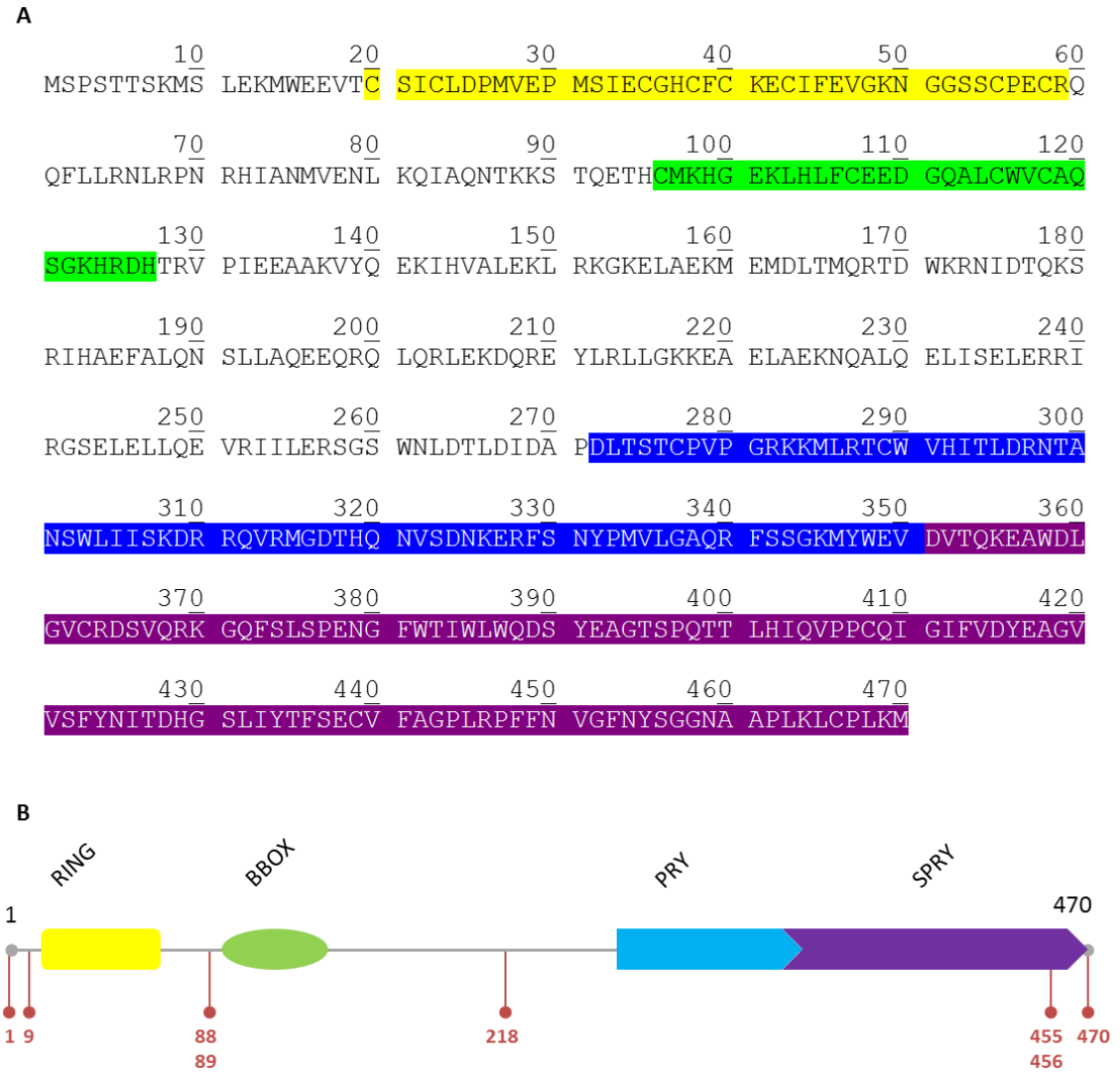

Figure 29. Structural characteristics of TRIM21. A; Amino-acid sequence of mouse TRIM21 in one letter code with colour coded sequences representing different protein domains. **B;** Graphical representation of TRIM21 with putative protein binding sites (in red), predicted using www.predictprotein.org.

Immunoprecipitation of FTO was performed using magnetic Dynabeads conjugated to rabbit anti-FTO antibody (2.4.8, 2.4.9 and 2.4.10). The immunoblotting results show that native FTO was precipitated under all experimental conditions (**Figure 30 B,** upper panel). MYC-TRIM21 and its truncated variants all expressed well and had the expected molecular weights of ~56 kDa for MYC-TRIM21, ~50 kDa for MYC-ΔRING, ~39 kDa for MYC-ΔBBOX, ~42 kDa for MYC-ΔSPRY, and ~35 kDa for MYC-ΔPRY (**Figure 30 B,** lower panel). As shown in **Figure 30 B** lower panel (right side), MYC-TRIM21, MYC-ΔRING, and MYC-ΔBBOX bound

to FTO but the MYC-ΔSPRY and MYC-ΔPRY variants of TRIM21 did not. These results suggest that the SPRY domain is required for binding of TRIM21 to FTO. They further suggest that the RING and BBOX domains are not essential for binding.

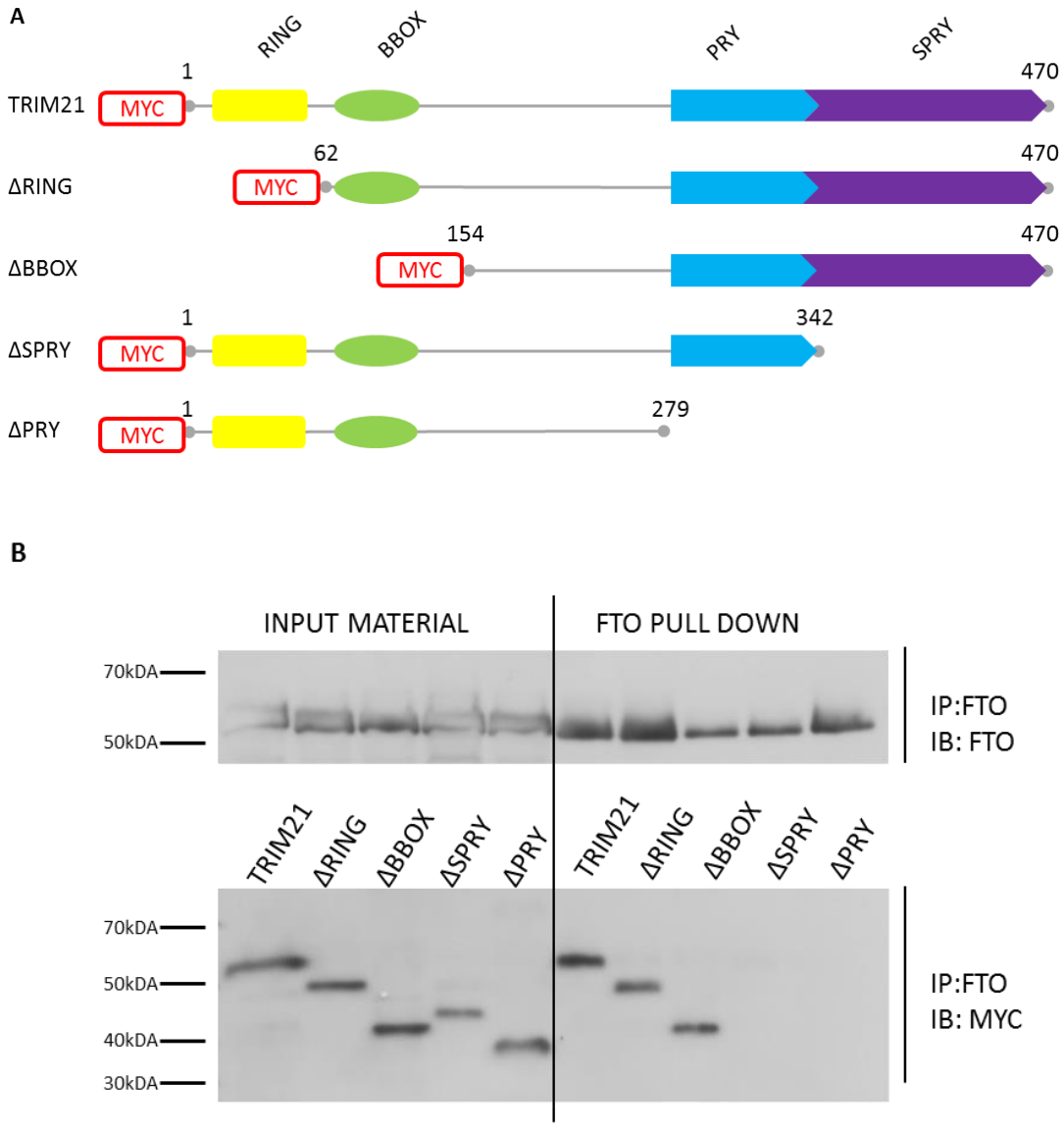

Figure 30. Determination of TRIM21 binding domains involved in TRIM21-FTO interaction. **A**; Schematic representation of MYC-tagged TRIM21 and its truncated mutants. Residues 20-59 comprise the RING domain, residues 96-127 comprise the BBOX domain, residues 272-341 comprise the PRY domain, and residues 342-470 comprise the SPRY domain. A MYC-tag was added at the N-terminus. Numbers indicate amino acid positions. **B**; Immunoblotting analysis of TRIM21 precipitated with FTO. Precipitated FTO and bound MYC-TRIM21 were visualised by immunoblotting using rabbit anti-FTO and mouse anti-MYC antibody. IP, Immunoprecipitation; IB, Immunoblotting. This experiment is representative of two experiments.

5.3.2 Determination of FTO Domain Interacting with TRIM21

I next examined which domain of FTO is required for binding to TRIM21. I created two truncated constructs consisting of the N-terminus alone (aa 1-326) and the C-terminus alone (aa 327-502) (**Figure 31**). Both constructs, and full length FTO, were N-terminally tagged with HA (**5.2.1, 5.2.2** and **5.2.3**). HEK 293 cells were transfected with plasmid DNAs encoding FTO constructs as well as MYC-TRIM21, and Co-IP was performed using magnetic Dynabeads conjugated to the mouse anti-MYC antibody (2.4.8, 2.4.9 and 2.4.10).

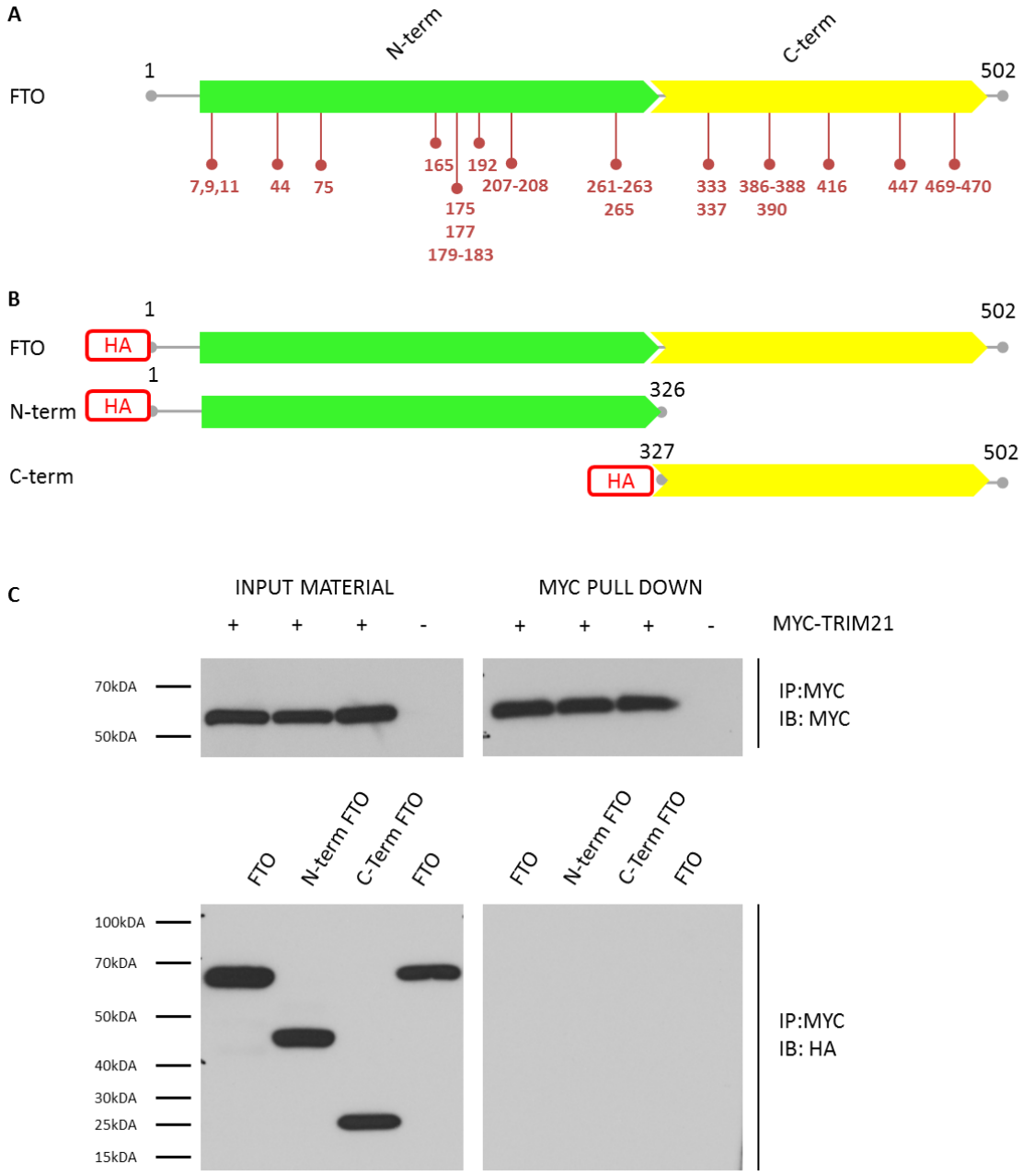

Figure 31. Determination of the FTO binding domains involved in the TRIM21-FTO interaction. A; Graphical representation of FTO with putative protein binding sites (in red), predicted using www.predictprotein.org. B; Schematic representation of HA-tagged FTO and its truncated mutants. Numbers indicate amino acid positions. C; Immunoblotting analysis of FTO precipitated with TRIM21. HA-FTO and MYC-TRIM21 were visualised by immunoblotting using anti-HA and anti-MYC antibody. IP, Immunoprecipitation; IB, Immunoblotting. This experiment is representative of two separate experiments.

Immunoblotting analysis of the input material revealed that all the HA-tagged FTO constructs expressed well (**Figure 31** lower left panel). MYC-TRIM21 was precipitated in all experimental conditions. Surprisingly, none of the HA-tagged FTO constructs were co-precipitated (**Figure 31** lower right panel). This may suggest that introduction of the HA tag in FTO, and/or the HA and MYC tags in TRIM21, can block the interaction between FTO and TRIM21.

5.3.3 TRIM21 Can Ubiquitinate FTO in Mammalian Cells

TRIM21 is an E3 ubiquitin-protein ligase that recruits protein for ubiquitination (Wada and Kamitani 2006). I therefore next aimed to determine whether TRIM21 acts as an E3 ubiquitin protein ligase for FTO.

To study FTO ubiquitination, HEK293 cells grown in T-75 flasks were transfected with various combinations of plasmids encoding FTO with an N-terminal FLAG tag, ubiquitin (UB) tagged with HA, and MYC-TRIM21. Cells transfected with ΔRING, which lacks the catalytic domain of TRIM21, were used as a control. After 48 hours incubation, the cells were cryolysed and FTO was immunoprecipitated using rabbit anti-FTO antibody coupled magnetic Dynabeads (**Figure 32**), (2.4.8, 2.4.9 and 2.4.10) FTO was identified by immunoblotting using rabbit anti-FTO antibody (**Figure 32 A**) and ubiquitination was studied using rat anti-HA antibody (**Figure 32 C**). Expression of MYC-TRIM and MYC-ΔRING was confirmed with mouse anti-MYC immunoblot (**Figure 32 B**).

A band corresponding to FLAG-FTO was identified in pull downs under all experimental conditions. Anti-MYC immunoblotting showed that cells were successfully transfected and that MYC-TRIM21, as well as MYC-ΔRING, bound to FTO. In MYC-TRIM21 transfected cells, a distinctly higher FTO band (+20 kDa, mas of around two HA-UB) and a high molecular weight smear was also detected by anti-FTO antibodies. This distinct band and the smear were also present in the anti-HA (i.e. ubiquitin) immunoblot in MYC-TRIM transfected cells. However, they were not detected in pulldowns from cells transfected with catalytically inactive MYC-ΔRING.

These results suggest that FTO is ubiquitinated by TRIM21 in mammalian cells and that removal of the RING domain abolishes this ubiquitination. The molecular weight of the detected bands and the polyubiquitin smear (observed due to progressive addition of 9.4 kDa HA-UB molecules) suggest that FTO can be polyubiquitinated by TRIM21 but the modification with two ubiquitin molecules was most prevalent. Since di-ubiquitin chain modifications are not common (Woelk et al. 2007) this suggest that FTO was modified with one ubiquitin at two separate sites.

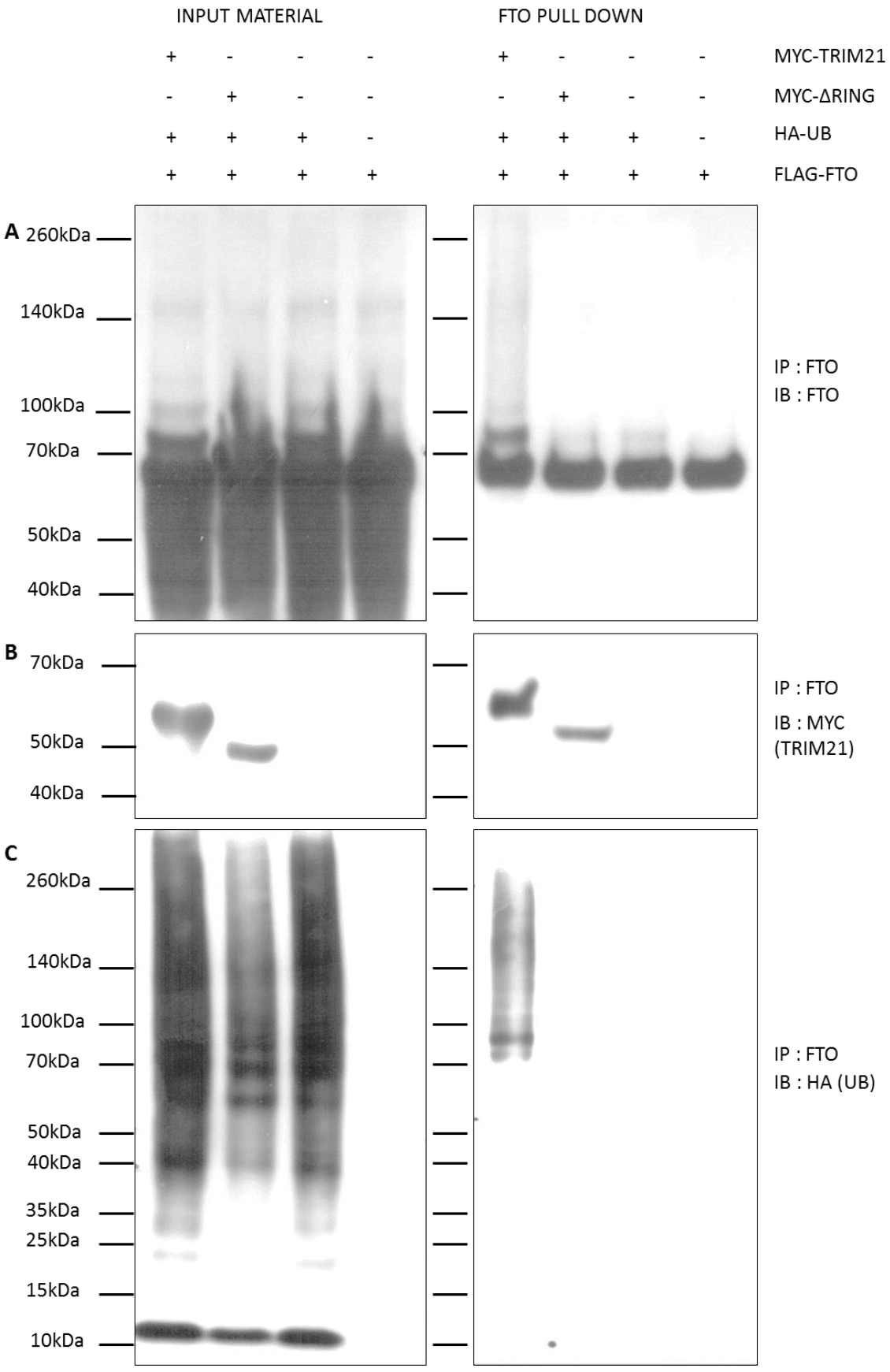
INPUT MATERIAL
FTO PULL DOWN
+ - - - + - - - MYC-TRIM21
- + - - - + - - MYC-ΔRING
+ + + - + + + - HA-UB
+ + + + + + + + FLAG-FTO
A
260kDa
140kDa
100kDa
70kDa
50kDa
40kDa
IP : FTO
IB : FTO
B
70kDa
50kDa
40kDa
IP : FTO
IB : MYC
(TRIM21)
C
260kDa
140kDa
100kDa
70kDa
50kDa
40kDa
35kDa
25kDa
15kDa
10kDa
IP : FTO
IB : HA (UB)

Figure 32. Cell-based analysis of FTO ubiquitination. HEK 293 cells were transfected with plasmids encoding the constructs indicated above the panels. Cells were cryolysed and FTO was immunoprecipitated. Immunoblotting with rabbit anti-FTO (top panel), rat anti-HA (central panel), mouse anti-MYC (bottom panel) was used to identify FLAG-FTO, HA-UB and MYC-TRIM21 (MYC-ΔRING) respectively. IP, Immunoprecipitation; IB, Immunoblotting. These results are representative of one experiment.

5.3.4 Overexpression of Full-Length TRIM21 Did Not Lead to Accelerated Degradation of FTO

Recently, FTO expression levels were shown to be tightly regulated via the ubiquitin and proteasome pathway (Russell and Morgan 2011). Therefore, I next investigated whether polyubiquitination catalysed by TRIM21 results in degradation of FTO.

For this experiment, it was necessary to be able to initiate expression of FTO at a defined time point and then follow its degradation. I therefore used INS-1 cells which conditionally overexpress C-terminally tagged mouse FTO-HA when induced with tetracycline (Russell and Morgan 2011). **Figure 33 A** shows that 12 hours exposure to rising tetracycline concentrations induced FTO-HA expression. This induction was not dose-dependent over the concentration range used, and the protein was detectable even at 50 ng/ml of tetracycline. This is in line with Russell and Morgan's 2011 observations. Interaction of FTO and TRIM21 in untreated INS-1 cells was confirmed by cryolysis and FTO Co-IP followed by immunoblotting (**Figure 33 B**).

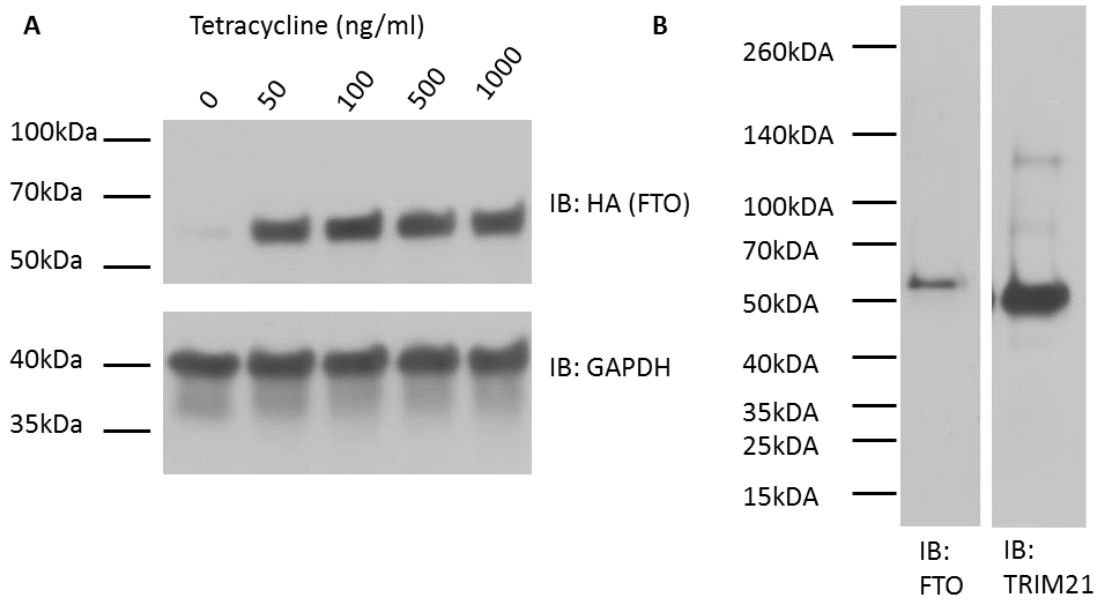

Figure 33. Immunoblotting analysis of conditionally expressed FTO-HA in INS-1 cells. A; Cells were incubated with various tetracycline concentrations for 12 hours and protein was extracted using standard RIPA buffer. Expressed FTO-HA was identified using rat anti-HA antibody (top panel). GAPDH was chosen as a loading control and identified with rabbit anti-GAPDH (bottom panel). **B**; Immunoblot of pull down from uninduced INS-1 cells. IP was performed using magnetic Dynabeads coupled to rabbit anti-FTO antibodies. FTO was detected with rabbit anti-FTO antibodies and TRIM21 was detected with rabbit anti-TRIM21 antibodies. These results are representative of one experiment.

In order to determine whether ubiquitination by TRIM21 has an effect on FTO protein turnover, INS-1 cells grown in T-25 flasks were transfected with MYC-TRIM21. Cells transfected with catalytically inactive MYC-ΔRING were used as a control. After 48 hours incubation, cells were induced for 12 hours with medium supplemented with 100 ng/ml of tetracycline. Next, cells were incubated without the antibiotic for another 10 hours. The presence of FTO, tubulin and MYC-TRIM21 (MYC-ΔRING) was detected by immunoblotting as described in 5.2.4 (**Figure 34 A**). The intensity of the FTO and tubulin bands was quantified with the Odyssey Infrared System and the relative FTO levels were calculated as described in 5.2.5 (**Figure 34 B**). Experiments were performed simultaneously using three biological replicates.

Induction with tetracycline stimulated FTO-HA protein expression to the same level in both MYC-TRIM21 and MYC-ΔRING transfected cells. Removal of the antibiotic resulted in gradual degradation of FTO-HA and after 8-10 hours the expression level was comparable to that in uninduced cells. Importantly, at each time point studied, there was no difference in the relative FTO-HA protein levels in cells transfected with MYC-TRIM21 or catalytically inactive MYC-ΔRING, as assessed by the Student's t-test.

These results indicate that the rate of the FTO degradation was the same in MYC-TRIM21 and MYC-ΔRING transfected cells, and overexpression of full-length TRIM21 did not lead to upregulation of proteasomal degradation of FTO via the ubiquitin-mediated pathway. This may further suggest that role of TRIM21 is not limited to FTO degradation.

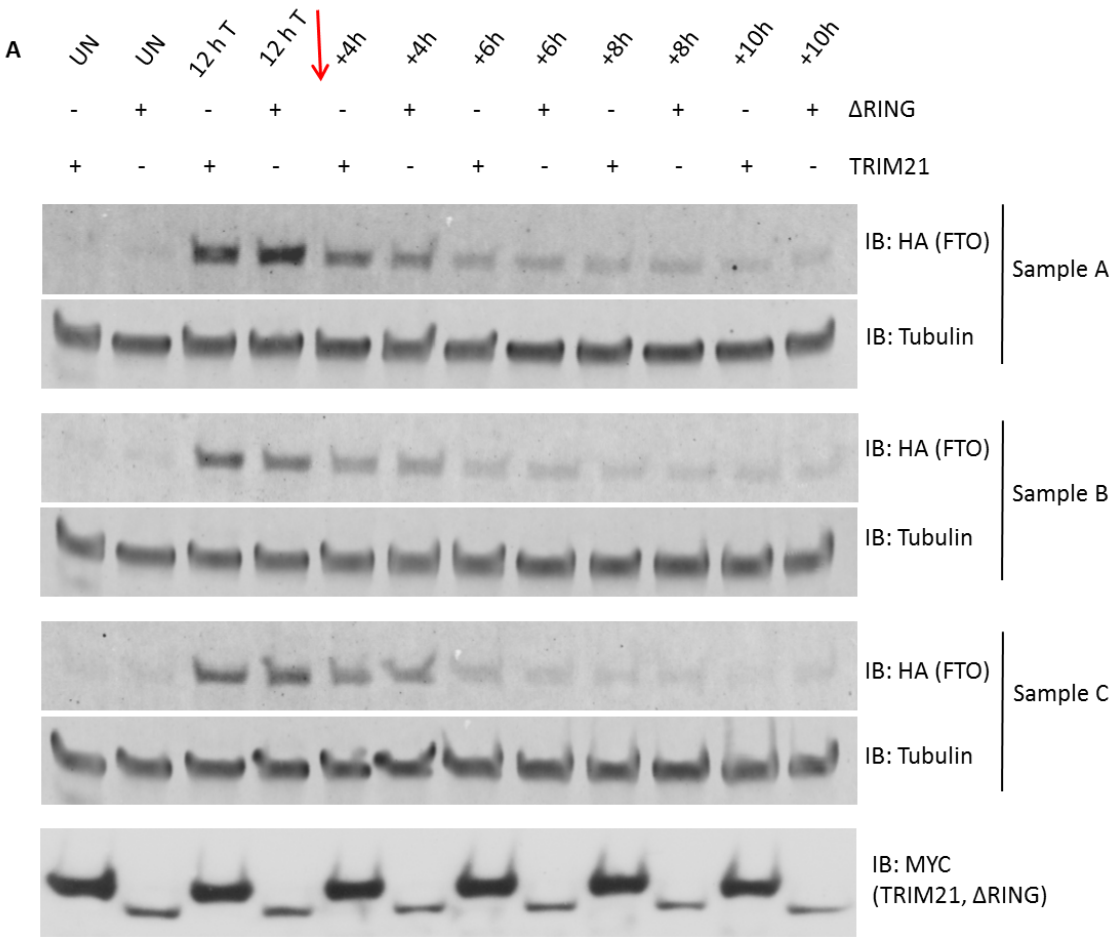
A
UN
UN
12 h T
12 h T
+4h
+4h
+6h
+6h
+8h
+8h
+10h
+10h
ΔRING
TRIM21
IB: HA (FTO)
IB: Tubulin
Sample A
IB: HA (FTO)
IB: Tubulin
Sample B
IB: HA (FTO)
IB: Tubulin
Sample C
IB: MYC
(TRIM21, ΔRING)

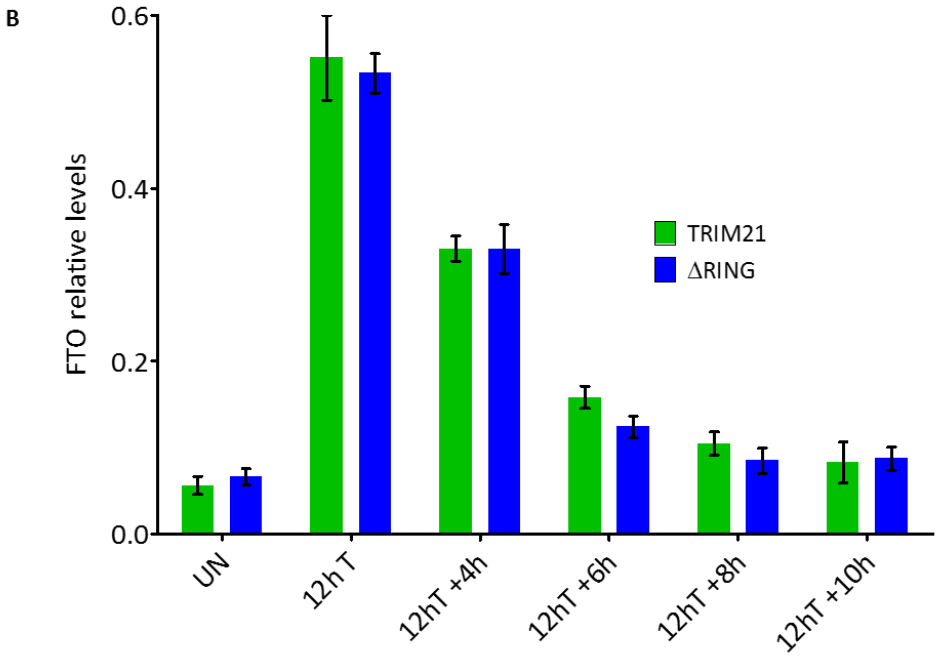
B
FTO relative levels
0.6
0.4
0.2
0.0
TRIM21
ΔRING
UN
12h T
12hT +4h
12hT +6h
12hT +8h
12hT +10h

Figure 34. Cell-based analysis of FTO degradation. A; Immunoblotting analysis of INS-1 cells transfected with plasmid DNAs encoding MYC-TRIM21 and MYC-ΔRING, and induced with 100 ng/ml tetracycline for 12 hours. After antibiotic withdrawal, cells were incubated for another 10 hours and proteins were extracted. FTO-HA and tubulin were visualised using fluorescent secondary antibodies. The presence of MYC-TRIM21 and MYC-ΔRING was confirmed with secondary HRP-conjugated antibodies. **B**, Comparison of the relative levels of FTO in MYC-TRIM21 and MYC-ΔRING overexpressing cells at different time points. Data were analysed using Student's t-test. Data are shown as group mean ± SEM. UN, uninduced; T, Tetracycline; IB, immunoblotting; red arrow indicates the removal of tetracycline.

5.3.5 Ubiquitination by TRIM21 May Regulate FTO Function

Post-translational modification of a protein with ubiquitin can trigger various signalling pathways and cellular events, depending on the number of ubiquitin molecules attached and the type of the linkage between two or more ubiquitin molecules in a polyubiquitin chain (Wilkinson 1987; Glickman and Ciechanover 2002; Schnell and Hicke 2003; Mukhopadhyay and Riezman 2007).

I have shown that overexpression of full-length TRIM21 does not trigger upregulated degradation of FTO in mammalian cells. Why FTO is ubiquitinated by TRIM21 is thus unclear, but possible functions include a conformational change resulting in modulation of the enzymatic activity of FTO, or nuclear export or import. In order to further investigate the possible function of ubiquitination of FTO I aimed to examine ubiquitinated FTO by mass spectrometry.

A

```
          10         20         30         40        !  !50        60
MKRTPTAEER EREAKKLRLL EELEDTWLPY LTPKDDEFYQ QWQLKYPKLI LREASSVSEE

          70         80        !90        100       !110        120
LHKEVQEAFL TLHKHGCLFR DLVRIQGKDL LTPVSRILIG NPGCTYKYLN TRLFTVPWPV

!         130        140        150        160        170        180
KGSNIKHTEA EIAAACETFL KLNDYLQIET IQALEELAAK EKANEDAVPL CMSADFPRVG

          190     !  200        210     !     220        230        240
MGSSYNGQDE VDIKSRAAYN VTLLNFMDPQ KMPYLKEEPY FGMGKMAVSW HHDENLVDRS

          250        260        270        280        290        300
AVAVYSYSCE GPEEESEDDS HLEGRDPDIW HVGFKISWDI ETPGLAIPLH QGDCYFMLDD

          310        320        330        340        350        360
LNATHQHCVL AGSQPRFSST HRVAECSTGT LDYILQRCQL ALQNVCDDVD NDDVSLKSFE

          370        380        390        400        410        420
PAVLKQGEEI HNEVEFEWLR QFWFQGNRYR KCTDWWCQPM AQLEALWKKM EGVTNAVLHE

          430        440        450        460        470        480
VKREGLPVEQ RNEILTAILA SLTARQNLRR EWHARCQSRI ARTLPADQKP ECRPYWEKDD

          490        500
ASMPLPFDLT DIVSELRGQL LEAKP
```

B

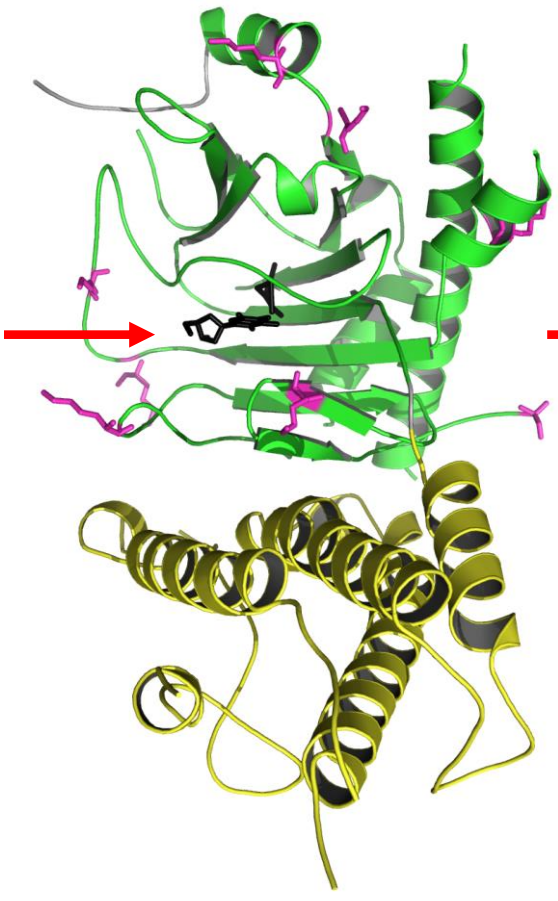

C

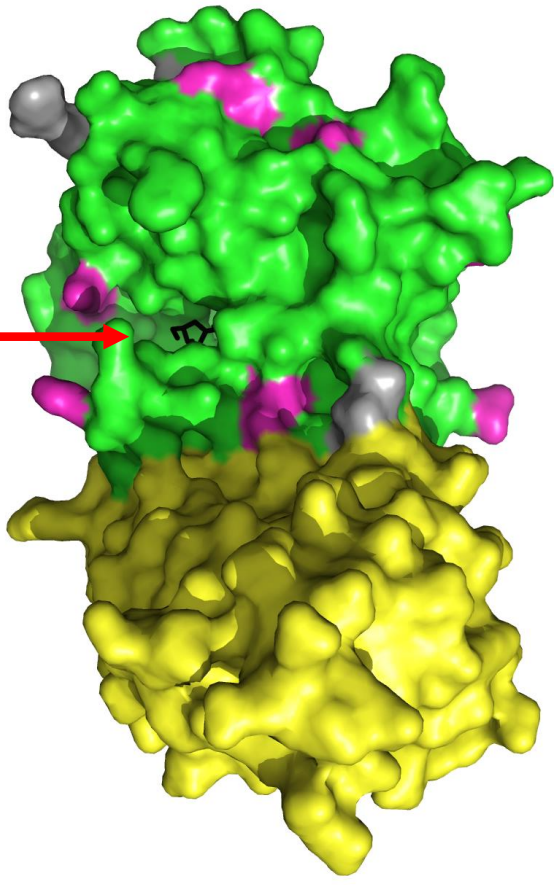

Figure 35. Sequence and structure of human FTO. The N-terminal domain of FTO is marked in green and C-terminal domain in yellow. **A**; Amino-acid sequence of human FTO in the one letter code with the lysines marked in red. Pink bars and exclamation marks represent lysines known to be ubiquitinated. **B-C;** Crystal structure of FTO with lysines known to be ubiquitinated in pink. In black, 3-methylthymidine, Fe (II) ion and N-oxalylglycine. The active site is marked by a red arrow. The crystal structure 3LFM was obtained from the Protein Data Bank PDB (www.pdb.org) and visualised as ribbon (B) and surface (C) forms using the educational version of PyMOL.

First, I used the PhosphoSitePlus database (www.phosphosite.org) to examine known post-translation modifications of FTO. The database search revealed that ubiquitination is the second most common modification of FTO after phosphorylation. In addition, out of 24 known modification sites, most were localised within the N-terminal domain (NTD), which is the Fe2OG dioxygenase domain. Only one phosphorylation site was localised within the C-terminal domain (CTD). Similarly, all ubiquitination sites experimentally identified in cell and tissue samples (K-45, K-48, K-88, K-107, K-121, K-194, K-211 and K-216), were localised in the NTD (**Figure 35 A**). In the crystal structure of FTO given in **Figure 35 B** and **C**, all ubiquitination sites located on the surface of the protein are shown: most of these lie on the side of the deep surface pocket that surrounds the catalytic site. Two of the modified lysines (K-88, K-107) seem to be flanking substrate binding sites (position 96 and 108). Interestingly, mutation of Y108A, which lies adjacent to one of these sites, is known to abolish enzymatic activity (Jia et al. 2011). K -211 and 216 are close to the alpha-ketoglutarate binding site (position 205). Moreover, K-214 and K-216 are located within Loop-1 (213 – 224) which is thought to block FTO binding to double-stranded DNA and RNA.

Overall, the location of the known ubiquitination sites in FTO may suggest that ubiquitination of these lysines can affect the function of FTO, perhaps through modulation of its activity, specificity, protein-protein interaction, FTO dimerization or stability.

To study FTO ubiquitination by MS, HEK293 cells grown in T-175 flasks were transfected with various plasmids encoding FLAG-FTO, HA-UB, MYC-TRIM21 or catalytically inactive MYC-ΔRING. In addition, one flask of cells was treated with PR619 - an inhibitor of deubiquitinating enzymes. After 48 hours incubation, cells were cryolysed and FTO was immunoprecipitated using rabbit anti-FTO antibody coupled magnetic Dynabeads. Co-IP

was carried out at 4 °C, and the Co-IP buffer was supplemented with 1X Deconjugation Stop Buffer (BostonBiochem, B-110). Proteins were separated by gel electrophoresis and visualised by Coomassie stain. Each lane was cut into ten small pieces and proteins from each piece were in-gel digested (2.4.5) and peptides analysed by mass spectrometry. (2.4.6). The proteins detected by MS are listed in **Table Appendix 5**.

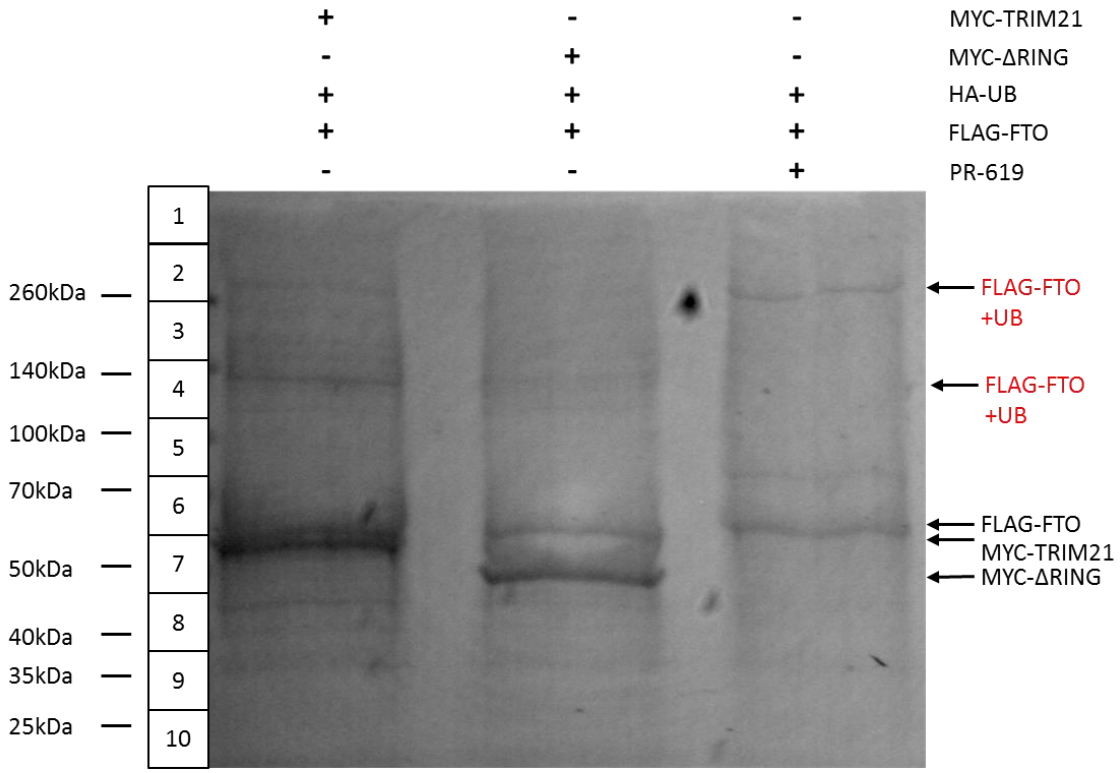

Figure 36. Large scale cell-based analysis of FTO ubiquitination. Coommasie stained gel of FTO pull downs performed with magnetic Dynabeads coupled with rabbit anti-FTO antibodies. Numbers in square boxes refer to gel pieces. These results are representative of two separate experiments.

A band corresponding to immunoprecipitated FLAG-FTO was identified in all experimental conditions (**Figure 36**). Additionally, distinct bands of MYC-TRIM21 and MYC-ΔRING were detected. To identify other bands present on the gel and search for ubiquitinated FTO, each lane was cut in ten pieces and proteins were subjected to in-gel digestion, (to preserve ubiquitination, chloroacetamide was used instead of iodoacetamide to alkylate protein). Extracted peptides were analysed by MS and the Mascot search engine (with detection of GlyGly (K) modification as chosen parameter).

FTO and UB were identified within the same high molecular weight gel slice (gel slice 4) in the MYC-TRIM21 transfected cells, but not in the MYC-ΔRING transfected cells. In fact, no UB was identified in any gel slice from the MYC-ΔRING transfected cells. FTO and UB were detected in cells treated with PR619, but at higher molecular weight (gel slice 2). However, the results did not provide any information about which lysines were modified or the type of polyubiquitin lysine-lysine (K-K) linkage. This may be because the amount of ubiquitinated FTO was insufficient to be detected by MS.

These results support the idea that FTO can be ubiquitinated by TRIM21. Additionally, we can hypothesise that the difference in molecular weight between the FTO + UB gel slice in MYC-TRIM21 and the FTO + UB gel slice in PR619 was a result of a polyubiquitin chain attached to FTO which had a different length.

5.3.6 FTO Interacts with TRIM21 in Cytoplasmic P-bodies

It has been reported that TRIM21 may variously have a cytoplasmic, perinuclear and nuclear localisation (Espinosa et al. 2006; Espinosa et al. 2008). To further understand the role of the TRIM21 and FTO interaction, I used immunocytochemistry to investigate the subcellular localisation of native TRIM21 in HEPA1-6 cells under growth conditions applied in the Co-IP experiments. I also evaluated if TRIM21 and FTO co-localise in the same subcellular compartment under these conditions.

Immunocytochemistry (2.3.3 and 5.2.7) was performed on HEPA1-6 cells grown on cover slips under normal growth conditions. DAPI was used to stain the nucleus and goat anti-

TRIM21 antibody with secondary anti-goat Texas Red were used to visualise native TRIM2 (**Figure 37**). The data show that TRIM21 is not observed in the nucleus of HEPA1-6 cells (where the majority of the FTO is) but localises in a "dot-like" pattern in the cytoplasm. A distinct perinuclear signal is visible, as well as a strong signal from cellular compartments surrounding the nucleus, which may be the endoplasmic reticulum membrane.

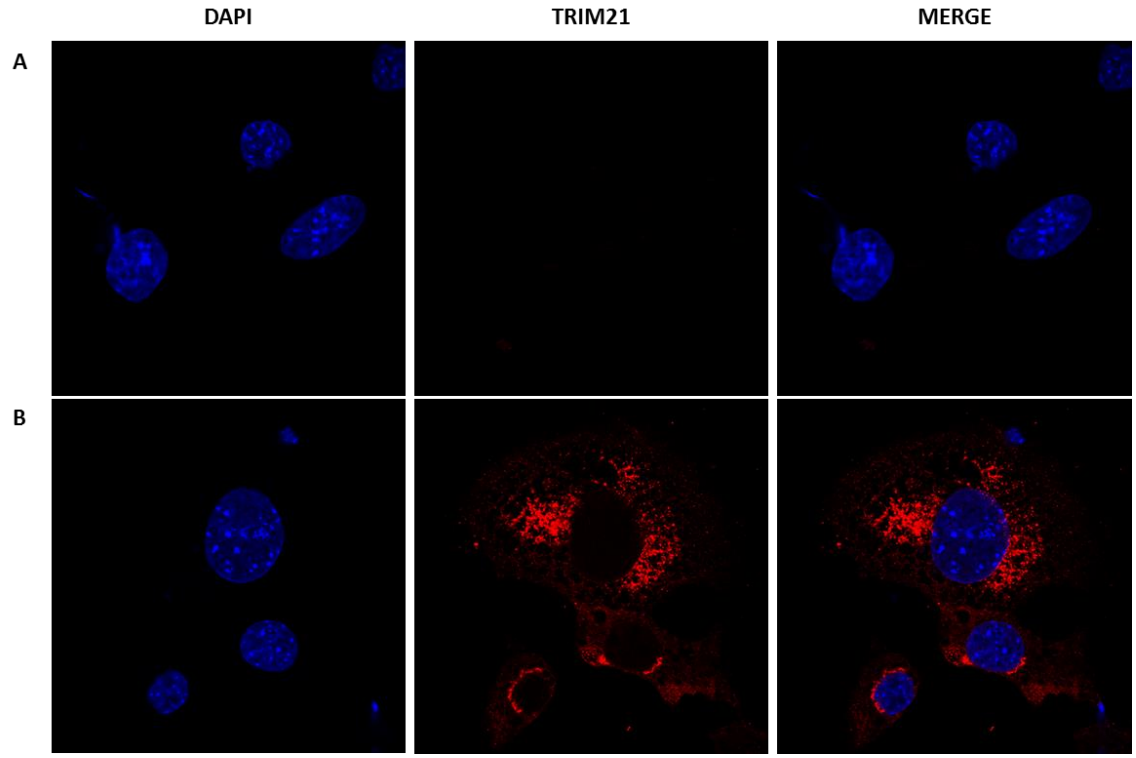

Figure 37. Immunocytochemistry analysis of TRIM21 localisation in HEPA1-6 cells. Confocal images of cells stained with secondary anti-Goat Texas Red antibody (**A**) and cells stained with primary Goat anti-TRIM21 (red) (**B**). DAPI was used to stain the nucleus (blue). These results are representative of two separate experiments.

A similar distributed pattern of TRIM21 was described by Yamochi et al (Yamochi et al. 2008). In that study, TRIM21 was found to co-localise with p-bodies and play a key role in mRNA degradation by enhancing the decapping activity of DCP2 (Yamochi et al. 2008). In Chapter 3, I showed that FTO is primarily confined to the nucleus but is also present at

lower intensity in a dot-like pattern in the cytoplasm. Given that TRIM21 and FTO are binding partners, I hypothesised that FTO might localise with TRIM21 to p-bodies. To test this hypothesis, I stained HEPA1-6 cells for FTO, TRIM21, and DCP2 a marker of p-bodies (**Figure 38**). The presence of FTO, TRIM21 and DCP2 was detected with specific primary antibodies and fluorophore-conjugated secondary antibodies Alexa 488 (green), Texas Red (red) and Alexa 688 (purple) respectively (5.2.7).

The confocal images revealed a strong nuclear localisation of FTO, but also a distinctive spotty cytoplasmic localisation (**Figure 38 B, G**). This is in agreement with the results given in the Chapter 3. The subcellular localisation of TRIM21 and DCP2 was limited to the cytoplasm and showed a similar speckled pattern to that of FTO (**Figure 38 C, H** and **D, I**). More importantly, a merge of all channels demonstrated (in white) foci where FTO, TRIM21 and DCP2 co-localised (**Figure 38 E, F**). Not all foci represent all three proteins together: some consisted only of TRIM21 and FTO, resulting in a yellow staining.

Overall, these results demonstrate that FTO and TRIM21 co-localise in the cytoplasm and both partially co-localise with DCP2. This suggests that FTO can be found in p-bodies where it interacts with TRIM21.

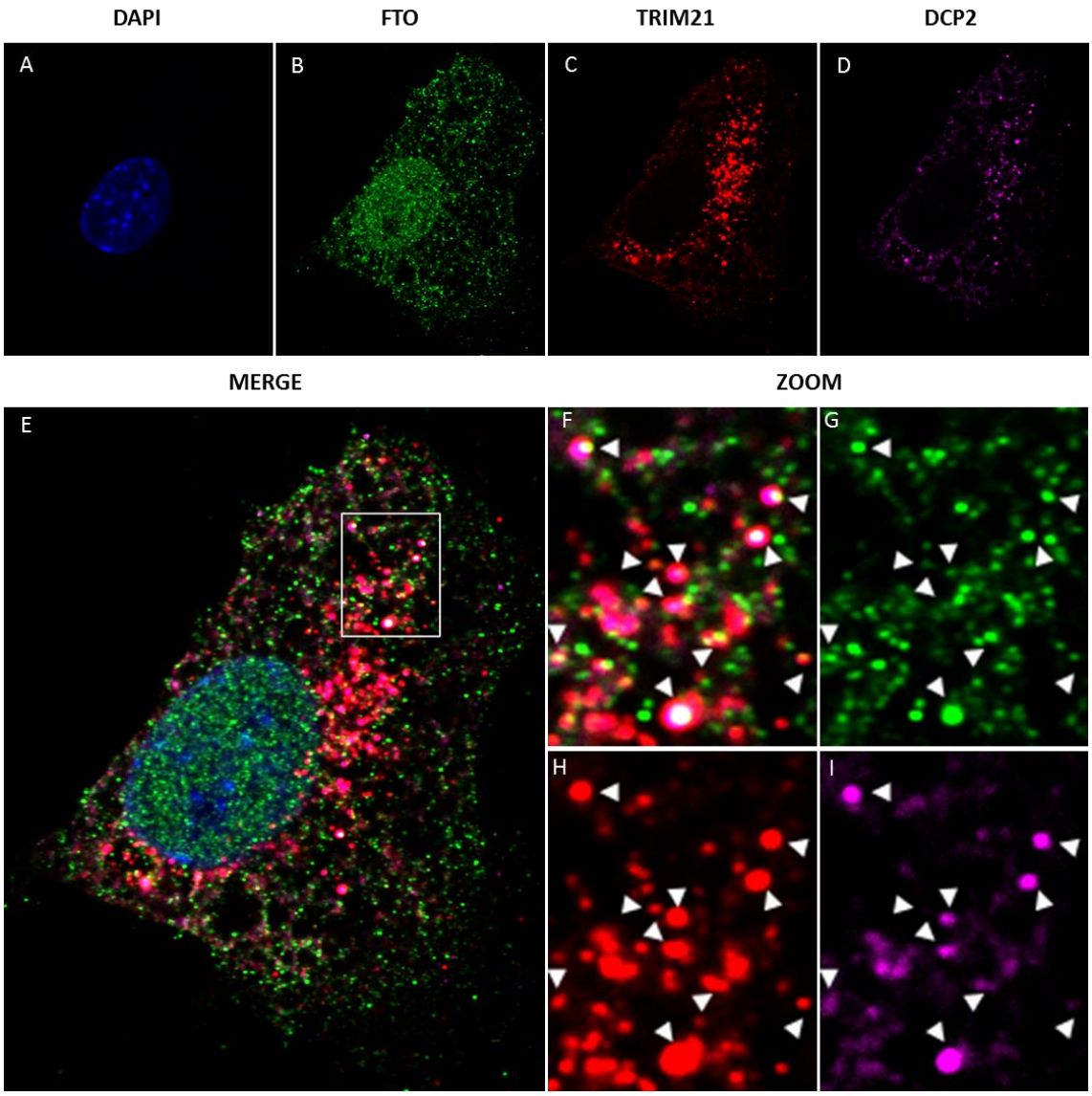

Figure 38. Immunocytochemistry analysis of TRIM21, FTO and DCP2 localisation in HEPA1-6 cells. Confocal images of the nucleus stained with DAPI (**A**), FTO (**B**), TRIM21 (**C**), and DCP2 (**D**)**.** Merge of all four channels (**E**). Higher magnification of a region highlighted in E (**F**). Localisation of FTO, TRIM21 and DCP2 in highlighted region (**G-I**).White arrow indicate foci where FTO, TRIM21 and DCP2 co-localise. Yellow signal represents co-localisation of FTO and TRIM21. These results are representative of one experiment.

5.3.7 TRIM21 Regulates FTO Subcellular Localisation

The interaction of FTO and TRIM21 in p-bodies gives some insight into the role of cytoplasmic FTO. As discussed in Chapter 3, FTO does not contain a classical nuclear export signal (NES) and I hypothesised that the nuclear export may be facilitated through a protein-protein interaction with another protein containing such a signal. Interestingly, TRIM21 contains a putative NES (amino acid sequence: ELELLQEVRIILLER) at residues 244-257. Furthermore, TRIM21 was found in both the cytoplasm and the nucleus, and the coiled-coiled (CC) region was suggested to be necessary for its cytoplasmic localisation (Espinosa et al. 2006; Espinosa et al. 2008). Therefore, I investigated the influence of the TRIM21 interaction and the TRIM21-dependent ubiquitination on the subcellular localisation of FTO.

I transfected HEPA1-6 cells with plasmids encoding the full length and truncated TRIM21 constructs described in 5.3.1. All constructs contained the putative NES, and the CC region. First, cells were subjected to immunocytochemistry analysis to visualise the localisation of overexpressed MYC tagged constructs (in red) (5.2.7).

The confocal images revealed that MYC-TRIM21 is present mainly in the cytoplasm but low levels were also detected in the nucleus (**Figure 39 A**). A similar expression pattern was seen for MYC-ΔRING, and MYC-ΔSPRY (**Figure 39 B, D**). However, MYC-ΔBBOX and MYC-ΔPRY appeared to have increased nuclear levels, while still exhibiting strong cytoplasmic localisation (**Figure 39 C, E**). More importantly, a strong signal in the cytoplasm was observed in the majority of the cells transfected with MYC-TRIM, MYC-ΔRING, MYC-ΔBBOX, MYC-ΔSPRY (**Figure 39 F, G, H, I**) but not with MYC-ΔPRY (**Figure 39 J**). These aggregates

showed different characteristics. Fibre-like aggregates, which formed an "envelop" around the nucleus and extended into the cytoplasm were found in MYC-TRIM21 transfected cells (**Figure 39 F**). In contrast, MYC-ΔRING, MYC-ΔBBOX, MYC-ΔSPRY signal showed spherical "bubble-like" aggregates within the cytoplasm, not around to the nucleus (**Figure 39 G, H, I**).

In order to investigate the effect of overexpressed TRIM21 (and its variants) on the localisation of native FTO, transfected cells were also stained for FTO (green) (**Figure 40**). The confocal images revealed that FTO co-localises with full length MYC-TRIM21, MYC-ΔRING, MYC-ΔBBOX in aggregates that accumulate in the cytoplasm. More importantly, in cells transfected with MYC-TRIM21, MYC-ΔRING, MYC-ΔBBOX, the distribution of FTO was altered – it was no longer mostly present in the nucleus but instead accumulated in the cytoplasm. Furthermore, in cells expressing MYC-ΔSPRY and MYC-ΔPRY (constructs that did not interact with FTO as shown by Co-IP), FTO localisation was unaltered and the majority of signal was present in the nucleus. In MYC-TRIM21 transfected cells, FTO accumulated in a fibre-like structure around the nucleus, similar to the signal seen for full length MYC-TRIM21, and it was barely visible in the nucleus. On the other hand, in MYC-ΔRING and MYC-ΔBBOX transfected cells, FTO co-localised with the MYC-TRIM21 truncates in spherical, "bubble-like" structures.

Additionally, the signal of native FTO seemed stronger in cells expressing MYC-TRIM21, MYC-ΔRING, MYC-ΔBBOX than in neighbouring, untransfected cells (**Figure 41**). This was not observed in cells expressing MYC-ΔSPRY or MYC-ΔPRY.

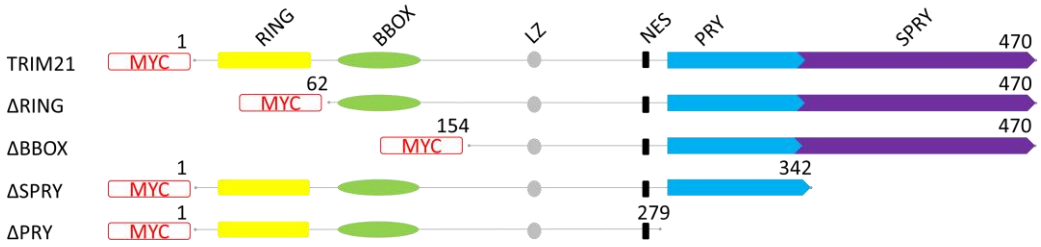
RING
BBOX
LZ
NES
PRY
SPRY
TRIM21
1
MYC
470
ΔRING
62
MYC
470
ΔBBOX
154
MYC
470
ΔSPRY
1
MYC
342
ΔPRY
1
MYC
279

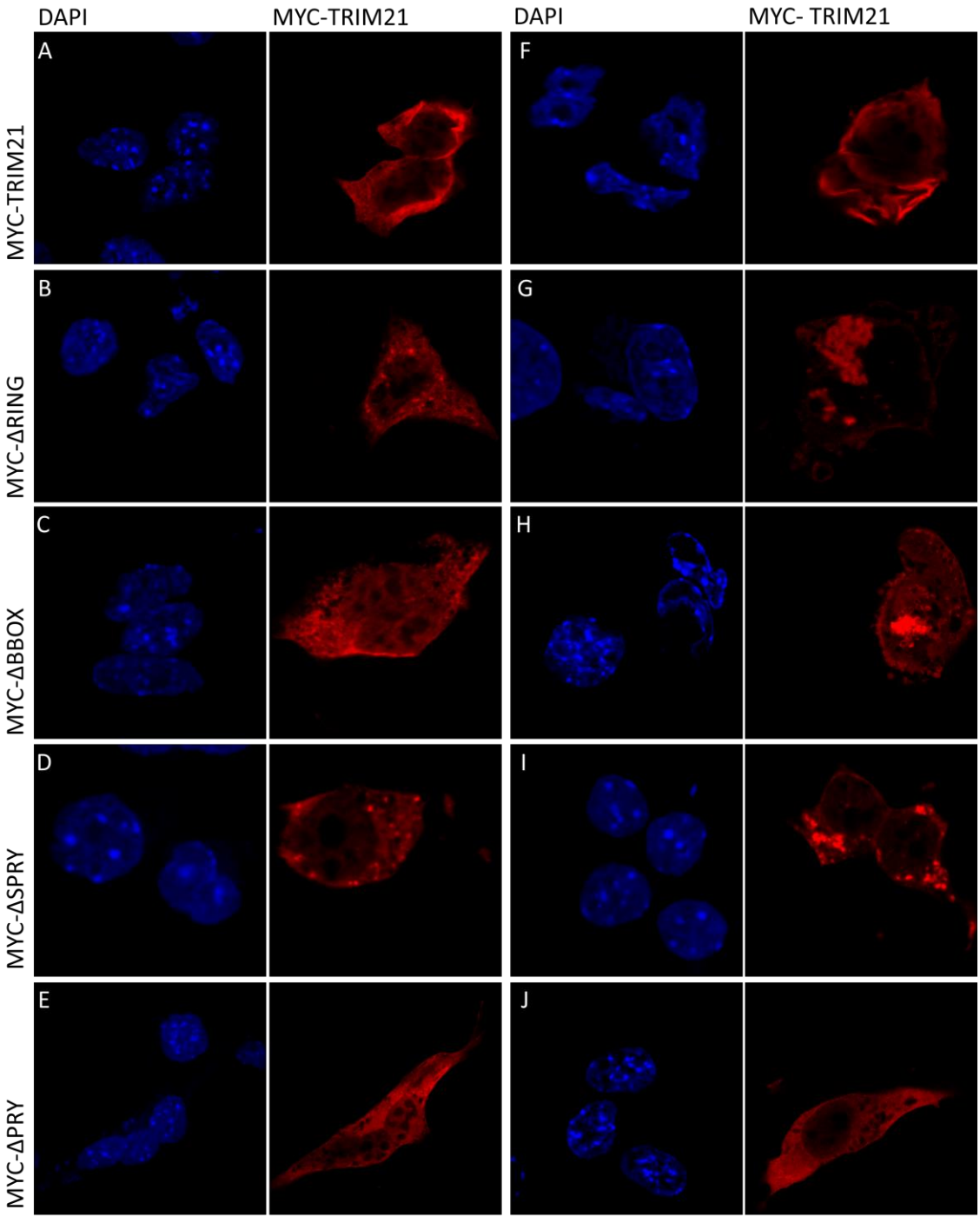
DAPI
MYC-TRIM21
DAPI
MYC- TRIM21
MYC-TRIM21
MYC-ΔRING
MYC-ΔBBOX
MYC-ΔSPRY
MYC-ΔPRY
A
B
C
D
E
F
G
H
I
J

Figure 39. Subcellular localisation of MYC-tagged TRIM21 constructs. Immunocytochemistry of HEPA1-6 cells transfected with full length and truncated variants of MYC-TRIM21 (showed in top panel). **A-J**; Confocal images of transfected cells with nucleus visualised by DAPI (blue) and MYC-TRIM21 with in red. MYC-TRIM21 constructs were detected with mouse anti-MYC antibody.

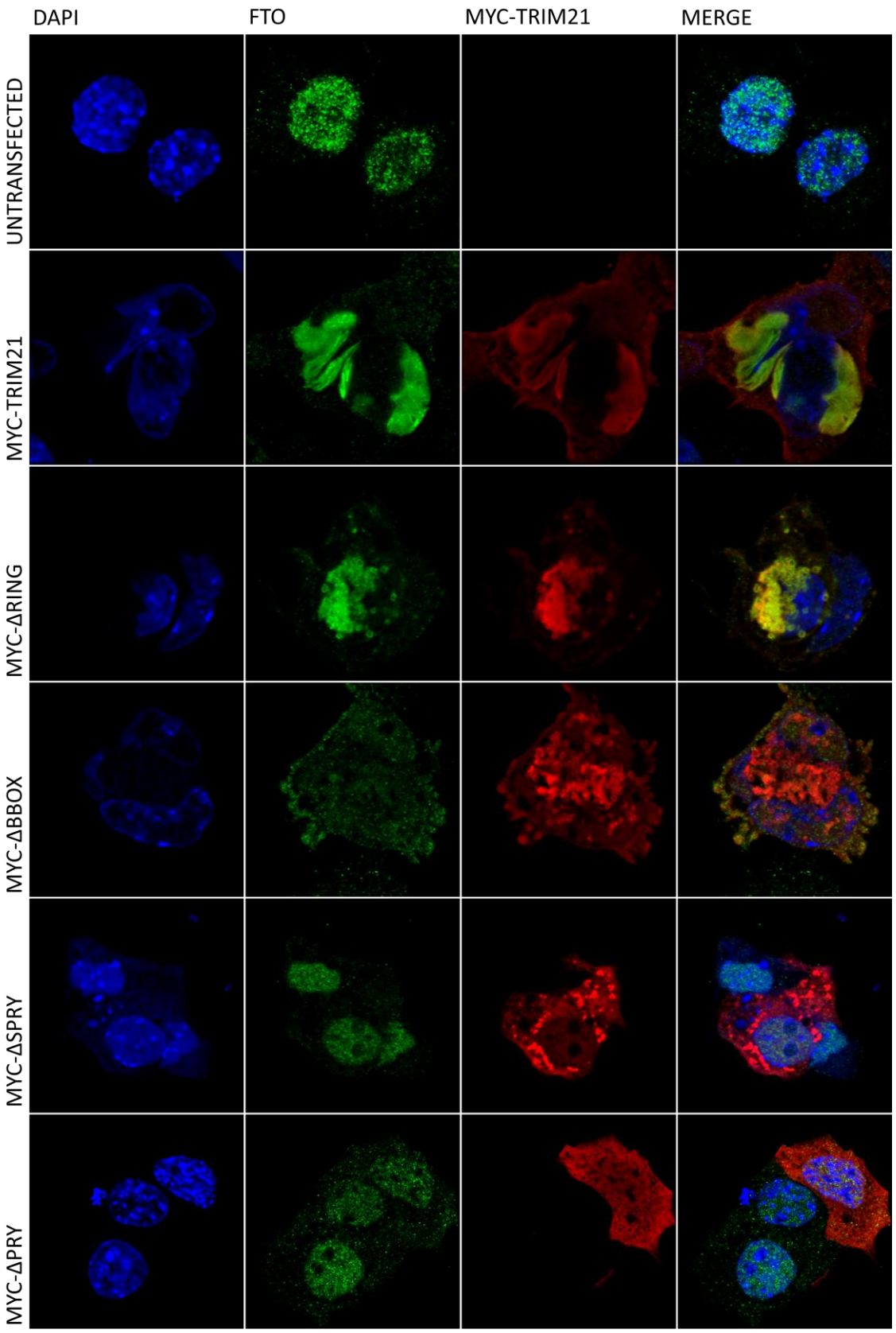

Figure 40. Subcellular localisation of native FTO and MYC-tagged TRIM21 constructs. Immunocytochemistry of HEPA1-6 cells transfected with full length and truncated variants of MYC-TRIM21. FTO was visualised with rabbit anti-FTO antibodies and MYC-TRIM21 constructs were detected with mouse anti-MYC antibodies.

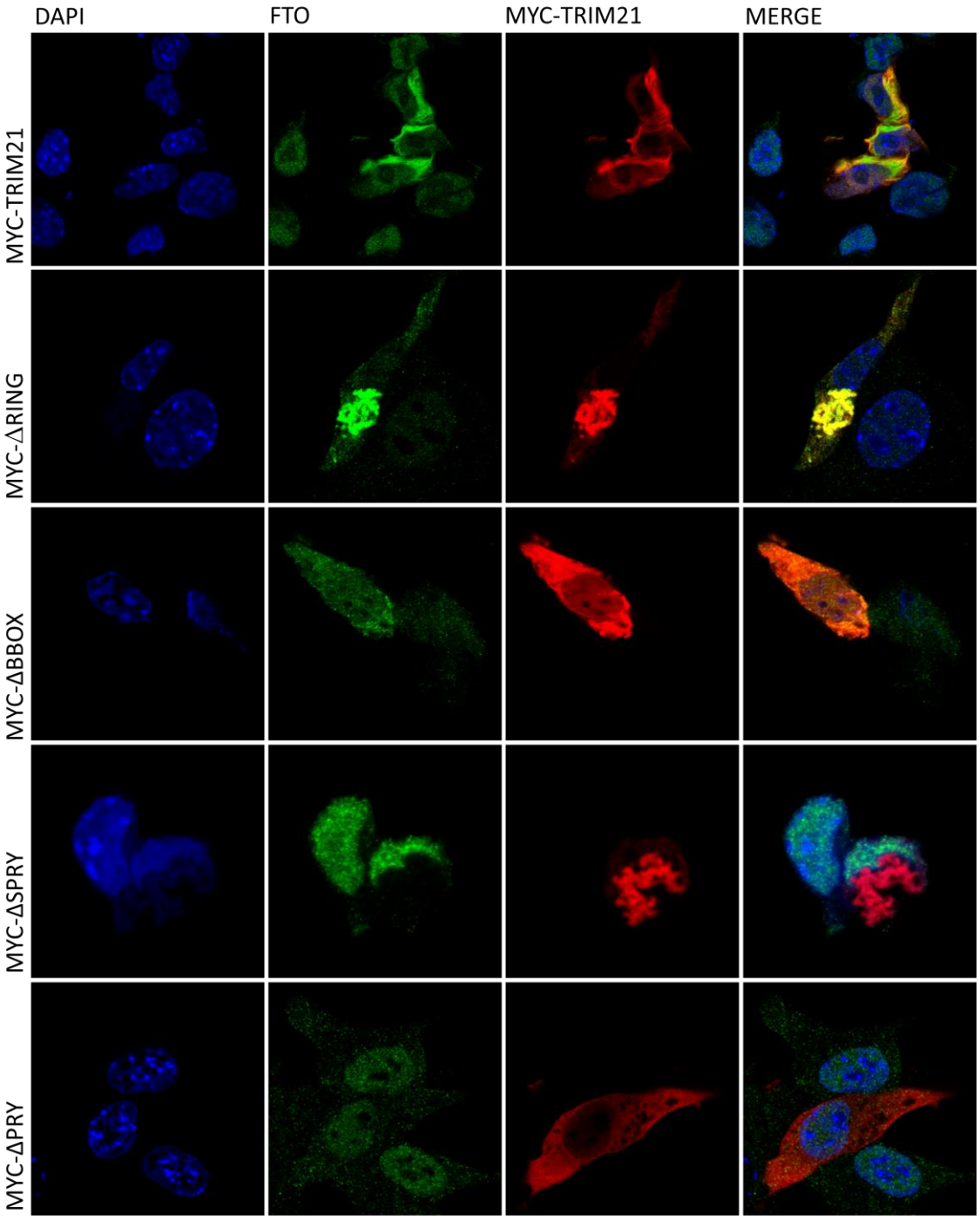

Figure 41. Comparison of FTO levels untransfected cells and cells transfected with various MYC-TRIM21 constructs. Immunocytochemistry of HEPA1-6 cells transfected with full length and truncated variants of MYC-TRIM21. FTO was visualised with rabbit anti-FTO antibodies and MYC-TRIM21 constructs were detected with mouse anti-MYC antibodies. Transfected cells and untransfected controls are present on the same images.

In order to further investigate the character of the accumulated FTO described above, MYC-TRIM21 and MYC-ΔRING transfected cells were stained for FTO (green) and UB (red) (**Figure 42**).

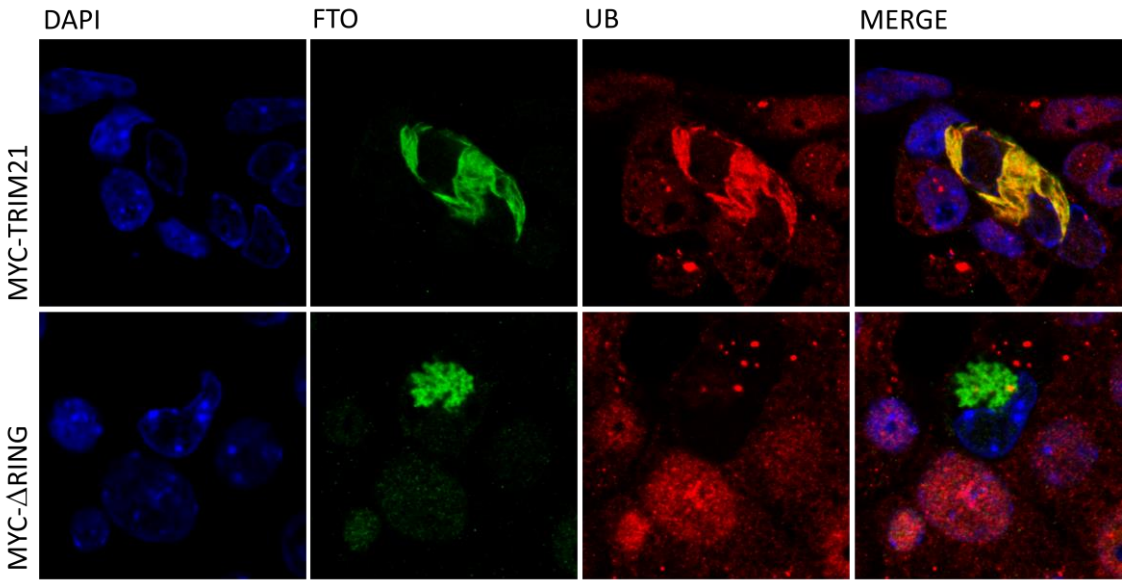

Figure 42. Presence of ubiquitin in FTO cytoplasmic aggregates. Immunocytochemistry of HEPA1-6 cells transfected with full length MYC-TRIM21 and catalytically inactive MYC-ΔRING. Native FTO was visualised with rabbit anti-FTO antibody and UB was visualised with mouse anti-UB antibody.

The confocal images revealed that MYC-TRIM21 and FTO accumulated in the cytoplasm and strongly co-localised with UB. Moreover, in cells transfected with MYC-TRIM21, the intensity of the UB signal seemed to be higher than in neighbouring untransfected cells. In contrast, MYC-ΔRING and FTO accumulated in the cytoplasm did not co-localise with UB, and the signal representing UB seemed to be lower in cells transfected with MYC-ΔRING than in untransfected cells.

Overall, these results demonstrate that overexpression of MYC-TRIM21 results in alteration of the pattern of FTO cellular localisation and causes its accumulation outside the nucleus. Similar findings were observed in cells transfected with truncated variants of TRIM21 that bind to FTO (MYC-ΔRING and MYC-ΔBBOX), but not in cells transfected with variants that do not bind to FTO (MYC-ΔSPRY and MYC-ΔPRY). This confirms that interaction with TRIM21 is the cause of the accumulation outside the nucleus. Moreover, since accumulation in the cytoplasm is observed in MYC-TRIM21 and MYC-ΔRING transfected cells, ubiquitination of FTO by TRIM21 does not regulate translocation. However, the ubiquitination of FTO by TRIM21 may be responsible for the character of the TRIM21-FTO complex. In the presence of ubiquitin, FTO and TRIM21 accumulated in a "fibre-like", perinuclear structures, but when UB was not present FTO and TRIM21 were found in "bubble-like", spotty structures.

In summary, these results indicate that TRIM21 is a regulator of the subcellular localisation of FTO.

5.3.8 Cytoplasmic Accumulation of Native FTO Is Reversed When Both TRIM21 and FTO Are Overexpressed

The results described in 5.3.7 demonstrate an interaction between TRIM21 and FTO when TRIM21 (but not FTO) is overexpressed. Next, I tested if the same phenotype would be observed when both interacting partners were overexpressed. HEPA1-6 cells were simultaneously transfected with plasmids encoding FLAG-FTO as well as plasmids coding MYC-TRIM21 and its truncated variants (**Figure 43**).

Confocal images of the cells overexpressing FLAG-FTO only (**Figure 43** top panel) show mostly nuclear expression of FTO with a weak cytoplasmic signal. Interestingly, in cells expressing both FLAG-FTO and MYC-TRIM21, FLAG-FTO and MYC-ΔRING and FLAG-FTO and MYC-ΔBBOX, accumulation of TRIM21 and its truncated variants in the cytoplasm was observed, but the subcellular localisation of FLAG-FTO did not seem to be affected. Cytoplasmic co-localisation of FLAG-FTO and MYC-TRIM21, MYC-ΔRING, MYC-ΔBBOX was still detectable, but at very low levels. As described in 5.3.7, co-transfection with MYC-ΔSPRY and MYC-ΔPRY showed no effect on FLAG-FTO localisation.

These results demonstrate that overexpression of both TRIM21 and FTO does not lead to accumulation of FTO in the cytoplasm, but instead most of the FTO is localised in the nucleus. This suggests that balance between TRIM21 and FTO levels is important for determining the subcellular localisation of FTO, and that a relative increase in TRIM21 results in accumulation of FTO outside of the nucleus.

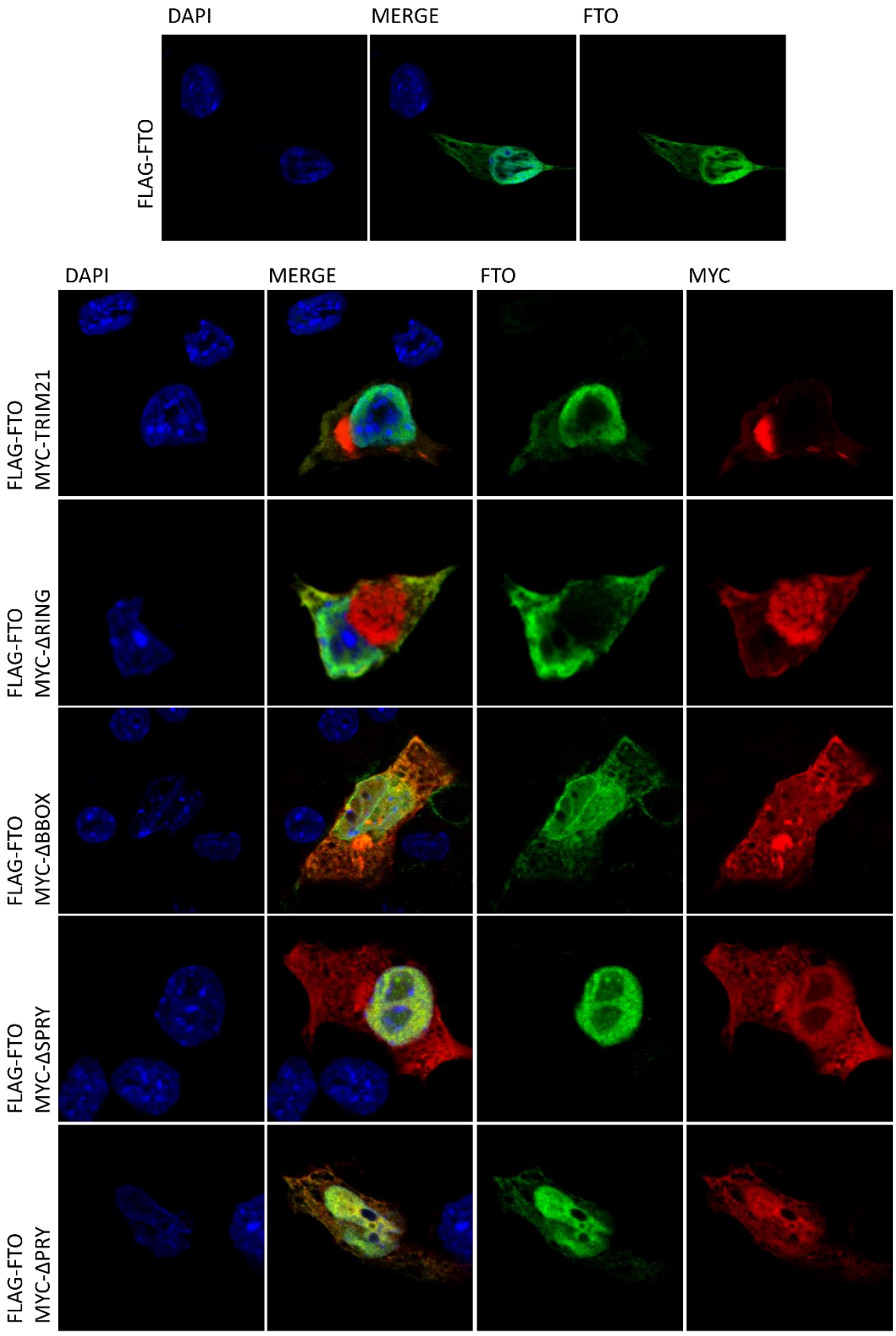

Figure 43. Subcellular localisation of FLAG-FTO and MYC-tagged TRIM21 constructs. Immunocytochemistry of HEPA1-6 cells expressing full length and truncated variants of MYC-TRIM21 as well as FLAG-FTO. FTO was visualised with rabbit anti-FTO antibodies and MYC-TRIM21 constructs were detected with mouse anti-MYC antibodies.

5.4 Discussion

5.4.1 Summary

The aim of this study was to investigate the functional role of TRIM21-FTO interaction. In this chapter, I showed that TRIM21 binds to FTO through an N-terminal SPRY domain, although I was unsuccessful in identifying the FTO domain necessary for this interaction. Furthermore, I showed that TRIM21 can ubiquitinate FTO in cells in a RING-dependent manner, and that ubiquitination did not cause FTO degradation. This demonstrated that TRIM21 and FTO are indeed direct interacting partners. Computational analysis suggested that ubiquitination is the second most prevalent FTO post-translational modification, but I was unable to determine experimentally which FTO residue is ubiquitinated by TRIM21. Immunocytochemistry analysis confirmed that native TRIM21 and FTO interact in cells and that both partially co-localise to cytoplasmic p-bodies. Moreover, overexpression of TRIM21 resulted in accumulation of FTO and its localisation outside of the nucleus. This phenomenon was ubiquitination independent. Overall these results suggest a role for TRIM21 in the regulation of FTO subcellular localisation and imply that FTO may act in the cytoplasmic p-bodies regulating mRNA life cycle.

5.4.2 Characterisation of Structural Basis of the TRIM21-FTO Interaction

The data presented in Chapter 4 confirmed that TRIM21 and FTO are indeed binding partners. To map the binding sites of FTO and TRIM21, I studied interactions of truncated TRIM21 and FTO variants. The identification of the TRIM21 C-terminal SPRY domain as the FTO recognition site is in line with other interactions of TRIM21 and TRIM family members

which are described to be facilitated by PRYSPRY domains (James et al. 2007). The N-terminal RING domain has a ubiquitin-protein ligase activity and recruits cooperating E2 ubiquitin-conjugating enzymes of the ubiquitination system (Pickart 2001). Binding of the RING domain to FTO would most likely block the interaction of TRIM21 with E2s and abolish its ubiquitination capability (Espinosa et al. 2011). PRYSPRY domains have a canonical binding interface comprised of six binding loops and the variability of these loops allow recognition of different targets (James et al. 2007). Two binding pockets are located in each SPRY and PRY sub-domain. Although my Co-IP experiment suggested that SPRY was crucial for FTO binding, it seems likely that two SPRY and PRY sub-domains are involved in FTO recognition.

The SPRYPRY domain of TRIM21 recognises numerous target proteins including interferon regulatory factors (IRF3, IRF7, IRF8) (Higgs and Jefferies 2008; Kong et al. 2007; Higgs et al. 2010), a probable ATP-dependent RNA helicase DDX41 (Zhang et al. 2013), and the Fc fragment of human IgG isotypes 1,2 and 4 (Yang et al. 1999; Yang et al. 2000; James et al. 2007; Rhodes and Trowsdale 2007; Keeble et al. 2008; Takahata et al. 2008). This suggests that TRIM21 is an IgG receptor and is involved in intracellular immunity (Mallery et al. 2010; McEwan et al. 2011; McEwan et al. 2013). Regardless of the results of these studies, I believe that we can exclude the possibility of SPRYPRY domain binding to the anti-FTO antibody during the Co-IP. Although mouse TRIM21 can bind to specific human IgG isotypes (Keeble et al. 2008), there is no evidence suggesting binding of mouse TRIM21 to rabbit IgG. In contrast to multiple human and mouse IgG isotypes, rabbit IgG has only one isotype, which is perhaps not recognised by mouse TRIM21. Moreover, rabbit anti-GFP IgG, used as a control in the initial Co-IP experiment, did not pull-down TRIM21 (Chapter 4). This indicates that the SPRYPRY domain of mouse TRIM21 does not bind to rabbit IgG.

I was unable to determine which FTO domain binds to TRIM21. The reason why none of the HA-tagged FTO constructs were pulled down with TRIM21 (in two separate experiments) is not clear. One possibility is that the presence of two tags (MYC on TRIM21 and HA on FTO) blocked the interaction. However, in a different experiment, MYC-TRIM21 was shown to interact with FLAG-FTO resulting in its ubiquitination. Perhaps, the length or sequence of the amino acid tag added to FTO played a role. The HA tag (YPYDVPDYA) was attached to FTO by a ten amino acid linker, while the FLAG epitope (DYKDDDDK) was directly attached to first amino acid of FTO. Also, different tags might have been subject to post-translation modifications such as phosphorylation (Berggård, Linse, and James 2007), which might inhibit FTO-TRIM21 binding. If I was to speculate, I would imagine that FTO binds to TRIM21 through a the C-terminal domain, which represent a novel, previously unknown motif as opposed to the N-terminal domain that shares similarities with other ALKBHs (Han et al. 2010). Perhaps binding of TRIM21 to the C-terminal domain of FTO would ensure specificity of signalling.

5.4.3 TRIM21 is an E3 Ubiquitin-Protein Ligase for FTO

The post-translational modification (PTM) of a protein with ubiquitin is produced by a hierarchical chain reaction of three enzymes; ubiquitin-activating E1, ubiquitin-conjugating E2 that carries activated ubiquitin, and ubiquitin-protein ligase E3 which recognises the substrate protein and transfers activated ubiquitin from E2 onto the protein or another ubiquitin (Pickart 2001). Substrate specificity depends on the E3 enzyme.

In this chapter I showed that TRIM21 in an E3 ubiquitin-protein ligase for FTO and facilities its ubiquitination in cells in RING-dependent manner. This is in line with the general

mechanism of ubiquitination by RING E3 ubiquitin-protein ligases (Pickart 2001). The RING domains comprise a zinc finger motif containing a series of histidine and cysteine residues that bind two zinc ions (Borden 2000). The ions are catalytically inert, suggesting that the RING domain functions as a skeleton for binding and coordination of other proteins. Given that TRIM21 binds to FTO through the SPRY domain, it means that the RING domain may bind to specific E2 ubiquitin-conjugating enzyme primed with activated ubiquitin. Interestingly, the ubiquitin-conjugating enzyme E2Q2 (UBE2Q2, localises in the cytoplasm) and E2E1 (UBE2E1, nucleus) were found in condition B of the anti-FTO pull-down (Chapter 4, Appendix 4), suggesting they may be involved in FTO ubiquitination. UBE2E1 was previously shown to interact with the RING domain of TRIM21 and support its E3 ligase activity. (Espinosa et al. 2008; Espinosa et al. 2006; Espinosa et al. 2011). This suggests that TRIM21-mediated ubiquitination can regulate cytoplasmic and nuclear proteins.

The UBE2E1 enzyme, along other E2s, also supports auto-ubiquitination of TRIM21 (Espinosa et al. 2008). Thus, it is possible that the ubiquitin smear observed in the FTO pull-down at least partially represents auto-ubiquitinated TRIM21 co-precipitated with FTO. However, the distinctly higher molecular weight FTO band and the high molecular weight smear in the anti-FTO blot clearly demonstrate that FTO was ubiquitinated by TRIM21. This further suggests that the FTO-TRIM21 interaction is direct, not mediated though other proteins, although other molecules (e.g. RNA) may influence TRIM21 and FTO affinity.

The question of which E2 enzyme cooperates with TRIM21 in FTO ubiquitination remains. Perhaps it is one of the co-precipitated UBE2E1 or UBE2Q2. One way of finding which E2 enzyme is involved might be to perform an *in vitro* ubiquitination assay which would include all the necessary components of ubiquitination system, TRIM21, FTO, and a selection of E2s. I have performed this experiment (data not shown) but in the presence of

ATP and Mg^{2+} (which is necessary for the reaction), FTO was degraded, possibly due to contamination with metalloprotease. Hence, I was unable to conclusively asses FTO ubiquitination. A further search for the E2 is necessary, as this would shine more light on the FTO ubiquitination process and its function.

5.4.4 Type and Role of TRIM21-Mediated Ubiquitination of FTO

Ubiquitination regulates a broad range of cellular events (Woelk et al. 2007). The diversity of ubiquitin signalling results from the reversibility and variability of ubiquitin (UB) modification, which is based on a number of ubiquitin molecules as well as on character of the polyubiquitin chain.

The cell-based ubiquitination experiment showed that TRIM21 catalysed polyubiquitin modification of FTO and as well as short modification of ~ 20 kDa, which was the most prevalent. Polyubiquitin modification results from the progressive attachment of numerous UB molecules, and can trigger different responses depending on the type of the linkage between the lysines (K) of each UB attached. The lysine 48 (K-48) linked chain is the best known and triggers protein destruction via the 26S proteasome (Glickman and Ciechanover 2002). Polyubiquitination mediated by TRIM21 was previously reported to direct its targets for degradation (Oke and Wahren-Herlenius 2012). Moreover, FTO was shown to be rapidly degraded via the ubiquitin-proteasome pathway (Russell and Morgan 2011). Therefore, the question was if TRIM21 regulates FTO levels and protein turnover, and thus might regulate its cellular role? However, the data showed that overexpression of full-length TRIM21 did not accelerate degradation of FTO, suggesting that TRIM21-mediated ubiquitination is not limited to degradation of FTO. Agreeably, given that RING E3 ubiquitin-

protein ligases form complexes with E2 ubiquitin-conjugating enzymes in the last step of the ubiquitination process (Pickart 2001), and given that TRIM21 was shown to be a member of Skp1–cullin–F-box (SCF) ubiquitin protein ligase complex SCFSkp2 (Sabile et al. 2006), it is possible that overexpression of TRIM21on its own may not have been sufficient to stimulate ubiquitin-dependant FTO degradation. Another way of looking at TRIM21-mediated FTO degradation would be to knock-down native TRIM21 with siRNA and compare the degradation rate of FTO with cells treated with control siRNA.

The lack effect on FTO degradation suggested other forms of TRIM21-mediated ubiquitination might have occurred. The polyubiquitin chains linked at K-63 trigger non-proteasomal signals and are thought to play a role in inflammatory responses, endocytosis, nerve growth, ribosomal protein synthesis, DNA repair, and transcription regulation (Zhao and Ulrich 2010; Nathan et al. 2013; Woelk et al. 2007). Interestingly, TRIM21 was also shown to mediate formation of the K-63 chains (McEwan et al. 2013). Other chains attached at K-6, K-11, K-27, K-29, K-33, and even the combination of all possible linkages have been reported, but much less is known about their function (Kim et al. 2007; Komander and Rape 2012).

More importantly, modification of FTO with one ubiquitin at two separate sites was the most abundant. Monoubiquitination is also a non-proteolytic modification and affects the location, conformation and activity of many proteins (e.g. histone regulation), as well as various cellular processes including endocytosis, DNA repair, nuclear export, transcription (Schnell and Hicke 2003; Woelk et al. 2007). The evidence that the ubiquitination is the second most common FTO modification, and the location of reported ubiquitinated sites in catalytic N-terminal FTO domain, supports the argument that ubiquitination could have an important effect on the catalytic activity and biological function of FTO.

Overall, information about which lysine of FTO is modified and the type of UB linkage would allow a better understanding of the function of FTO ubiquitination. I was unable to detect ubiquitin modification of FTO by Co-IP and MS. The most probable explanation is that the amount of the cell lysate was not enough to detect ubiquitin modification on immunoprecipitated FTO by MS analysis. Perhaps increasing the amount of transfected cells and using a two-stage IP protocol (first anti-FTO and then anti-UB) could improve the identification. An alternative solution would be to use immunoblotting analysis with an antibody against a specific type of polyubiquitin modification. Nevertheless, I did identify FTO and UB in higher molecular weight bands, although it was not possible to distinguish if the UB came from FTO ubiquitination or TRIM21 auto-ubiquitination.

The question remains - which lysine of FTO is modified with monoubiquitin and what type of poly-ubiquitin chain is formed by TRIM21? Since overexpression of TRIM21 did not accelerate degradation of FTO, perhaps TRIM21 modifies FTO with K-63 and monoubiquitin. Both of these signals lead to non-proteasomal events and are thought to have a similar signal topology (Woelk et al. 2007). The role of TRIM21-mediated FTO ubiquitination also remains unknown, however I was able to eliminate the possibility that polyubiquitination of FTO leads to proteasomal degradation. Moreover, ubiquitination does not trigger nuclear export, since FTO translocation to the cytoplasm (analysed by immunocytochemistry) was also observed in ΔRING-expressing cells. Given the location of lysines reported to be modified with UB, perhaps ubiquitination by TRIM21 regulates FTO catalytic activity or substrate recognition. Importantly, since ubiquitination is a reversible modification, specific de-ubiquitinating enzymes (DUBs) might influence the fate of FTO. I identified de-ubiquitinating enzymes 1 and 47 in the FTO pull-down condition B and C

respectively. It would be interesting to test the role of these enzymes in FTO de-ubiquitination.

5.4.5 FTO Is a Component of Cytoplasmic P-bodies

TRIM21 was shown to interact and co-localise in "dot-like" pattern with human decapping enzyme 2 (DCP2), (Yamochi et al. 2008). DCP2 is a component of p-bodies, which are cytoplasmic aggregates of specific proteins and RNA, that regulate mRNA translational repression and decay (Parker and Sheth 2007; Kulkarni, Ozgur, and Stoecklin 2010). Based on a similar pattern of FTO cytoplasmic localisation described in Chapter 3 and the association of FTO and TRIM21 with mRNA processing, I hypothesised that FTO may interact with TRIM21 in p-bodies.

Using immunocytochemistry I showed that native FTO and TRIM21 co-localise in the cytoplasm and that both partially co-localise with native DCP2 suggesting that FTO is a new component of p-bodies. Partial co-localisation with DCP2 suggests that FTO would not be a constitutive member of p-bodies, but rather might be attracted to these foci under the specific conditions, or by specific proteins (perhaps TRIM21) or mRNA.

Evidence in support of the idea that FTO plays a role in p-bodies is presented in this thesis as well as in other studies. The presence of FTO in p-bodies is in line with the role of FTO in RNA processing identified in Chapter 4, and with the currently proposed role of m^6A methylation in mRNA metabolism and processing (Jia et al. 2011; Jia, Fu, and He 2013). Although this function was initially associated with the nuclear speckles and pre-mRNA

splicing (Zhao et al. 2014), more recently member of human YTH domain family, YTHDF2 was shown to specifically bind to m^{6}A and transfer the m^{6}A containing mRNAs from translatable pool to degradation in p-bodies (Wang et al. 2014). This demonstrated the role of m^{6}A and m^{6}A binding proteins in regulation of both translational status and the lifetime of mRNA in p-bodies. Perhaps FTO, as a demethylase, could regulate binding of m^{6}A specific proteins, and hence influence mRNA translation through the mRNA retention or degradation. This would be in line with reduced rate of mRNA translational observed in *Fto* KO MEFs (Gulati et al. 2013). Additionally, in dopaminergic neurons lacking FTO, lower levels of the proteins encoded by specific mRNAs hyper-methylated due to the FTO loss were reported, while the levels of these mRNAs were increased (Hess et al. 2013). Protein expression and mRNA levels of other hyper-methylated mRNA were not affected. Perhaps this suggest that lack of FTO-dependent demethylation increases mRNA repression and storage. Moreover, TRIM21 was shown to enhance the decapping activity of DCP2 (Yamochi et al. 2008). Removal of the mRNA cap by DCP2 allows the 5' to 3' exonucleolytic decay of non-translating mRNA (Sheth and Parker 2003). Perhaps the presence of FTO in the proximity of TRIM21 and DCP2 would influence mRNA decapping, and so increase and/or decrease mRNA degradation.

In contrast with my data, Jia et al. did not find evidence of FTO localisation to p-bodies using DCP1 as a marker (Jia et al. 2011). However, they were unable to demonstrate FTO in the cytoplasm (which is where p-bodies localise), and even the nuclear FTO signal was limited to a few, very faint foci. Furthermore, the authors used DCP1 as the marker of p-bodies which is only transiently associated with p-bodies. On the other hand, I observed co-localisation of FTO with DCP2, which is stably associated with p-bodies as it performs the important de-capping function (Franks and Lykke-Andersen 2008). The immunocytochemistry data presented here clearly show co-localisation of FTO with DCP2

and TRIM21, which both are components of p-bodies. It would be beneficial to stain for another core component of the p-body, perhaps XRN1 exoribonuclease, to further confirm the presence of FTO in p-bodies. Additionally, the formation of p-bodies could be stimulated in order to help visualise these foci.

5.4.6 Role of TRIM21 Binding in FTO Subcellular Localisation

In Chapter 3 I showed that the majority of FTO was found in the nucleus and that small amounts were present in the cytoplasm. However, how the localisation of FTO is regulated was unknown. The immunocytochemistry data presented in this chapter suggest that TRIM21 potentiates cytoplasmic localisation and reduces nuclear localisation of FTO.

The experiments were performed using cells transfected with pCMV plasmids encoding MYC-TRIM21 constructs. One interpretation of the observed FTO phenotype might be cytotoxicity caused by the transfection reagent or cellular stress due to excess of a foreign protein. However, all TRIM21 constructs were cloned into the same expression vector and the cells were transfected, cultured and stained in parallel, using the same conditions. Thus, because a normal phenotype was observed in cells transfected with MYC-ΔSPRY and MYC-ΔPRY (variants that do not interact with TRIM21), this allows me to conclude that the effects observed in cells expressing TRIM21 variants did not result from transfection toxicity or cell overload with foreign protein.

Interaction of TRIM21 with FTO seems to be the strongest argument for the reduced nuclear and increased cytoplasmic presence of FTO, although indirect cellular effects of

each TRIM21 variant might have played a role. Truncated variants of TRIM21 do not naturally exist in cells and it is difficult to predict the effects of their overexpression. Moreover, they were included in the study to provide an insight into the role of FTO binding and ubiquitination in the observed phenotype of TRIM21 expressing cells, and there is little benefit in discussing their functional effect on the cells.

However, the effects of overexpression of full length TRIM21 may be important for understanding the underlying mechanism of FTO cytoplasmic accumulation. Overexpression of TRIM21 was reported to decrease cell proliferation and increase cell death in a RING-dependent manner in a mouse lymphoma cell line (Espinosa et al. 2006), and to promote apoptosis in a mouse skin melanoma cell line (J. Zhang et al. 2012). Moreover, TRIM21 was redistributed to apoptotic blebs in cardiac monocytes, epithelial cells, salivary gland cells and keratinocytes (McArthur et al. 2002; Miranda et al. 1998; Ohlsson, Jonsson, and Brokstad 2002). However, TRIM21-expressing cells in my experiments did not resemble the phenotype of apoptotic cells described in these studies and did not show positive staining using in-situ cell death analysis (**Appendix 5, Appendix 5.1 Figure Appendix 5**). Thus, alterations in the cellular localisation of FTO in my experiments cannot be taken to be secondary to cell death. TRIM21 lacking the RING domain did not promote cell death (Espinosa et al. 2006). I was unable to assess the status of cells expressing MYC-ΔRING, as they were lost during the staining procedure.

A distinct perinuclear localisation of TRIM21 and a "dot-like" pattern of TRIM21 lacking the RING and BBOX domains has previously been reported in HeLa cells (Espinosa et al. 2008) although not to the extent I observed. Perhaps the pronounced localisation pattern of the overexpressed truncated variants of TRIM21 described in this study is specific for hepatocytes, cells involved in uptake, processing and secretion of many compounds within

the body (Boron and Boulpaep 2008, chap. 46), and the "bubble-like" structures in cells expressing MYC-ΔRING and MYC-ΔBBOX represent exocytotic vesicles.

Cells overexpressing TRIM21 variants which interact with FTO (as determined by Co-IP) had stronger FTO signals than neighbouring, untransfected cells. Given that overexpression of TRIM21 did not accelerate degradation of FTO, it seems possible that binding of TRIM21/MYC-ΔRING/MYC-ΔBBOX blocked the interaction of FTO with other E3 enzymes, which would otherwise direct the protein for degradation. Hence, TRIM21 binding resulted in accumulation of FTO outside of the nucleus. The increased ubiquitin staining in TRIM21-expressing cells, as opposed to untransfected cells or cells expressing MYC-ΔRING, seems to be associated with the RING-dependent ubiquitination. It suggests that UB is a component of full length TRIM21-FTO complex. However, based on my data, I cannot conclude if the UB is attached to TRIM21 (by auto-ubiquitination) or to FTO (by TRIM21-mediated ubiquitination). Nevertheless, the presence of UB may have an effect on shape of the FTO aggregates in the cytoplasm, and perhaps influence the role and fate of the complexes.

The mechanism leading to FTO accumulation in the cytoplasm and its reduction in the nucleus is still unclear, although the nature of this process would depend on subcellular compartment of initial FTO-TRIM21 interaction. One possibility may be that TRIM21 bound to FTO outside nucleus (perhaps in the ER) blocks nuclear import by masking an FTO nuclear localisation signal (NLS). Alternatively, TRIM21, which can shuttle between cytoplasm and nucleus (Espinosa et al. 2008), could bind to FTO in the nucleus, and stimulate FTO nuclear export. Once TRIM21 dissociates from the complex, a strong NLS in FTO would direct it back to the nucleus. This scenario would be in line with nucleocytoplasmic translocation observed by Gulati et al. (Gulati et al. 2014).

Admittedly, native TRIM21 was not present in the nucleus when detected with anti-TRIM21 antibody, however MYC-TRIM21 and its truncated variants showed variable nuclear and cytoplasmic staining. This is in line with other studies showing TRIM21 mostly in the cytoplasm (Keech, Gordon, and McCluskey 1995; Pourmand et al. 1998), the nucleus (Ben-Chetrit et al. 1988, 52; Kelekar, Saitta, and Keene 1994) or both cytoplasm and nucleus (Espinosa et al. 2006; Espinosa et al. 2008). The difference in the TRIM21 localisation pattern presented in this chapter may result from antibody specificity. Anti-TRIM21 bound to the C-terminus of the TRIM21 molecule, whereas anti-MYC bound to the N-terminal MYC tag on TRIM21. Post-translational modification of TRIM21 epitopes, dependent on the subcellular compartment, might blocked anti-TRIM21 antibody from binding to nuclear TRIM21 (van Zeijl et al. 2000).

Although FTO was shown to be present in the cytoplasm and co-localise with TRIM21 to p-bodies, a strong accumulation of FTO outside of the nucleus and decreased nuclear presence have only been observed in the TRIM21-overexpressing cells. It is reasonable to suggest that the overexpression of TRIM21 most likely up-regulated a cellular event, which perhaps is controlled by the balance of amounts of each TRIM21 and FTO. The presented data suggest that TRIM21 would have a dominant positive effect on FTO translocation. Therefore, when both TRIM21 and FTO were overexpressed, the normal FTO localisation pattern observed in native cells was restored. It would be interesting to investigate the effect of overexpression of FTO on TRIM21 subcellular localisation. If TRIM21 is dominant in TRIM21-FTO interaction, I would expect that FTO overexpression would not impact TRIM21 localisation.

5.4.7 Future Plan

FTO is ubiquitinated by TRIM21 but the character of this ubiquitination remains unknown. I would like to use an *in vitro* ubiquitination assay to confirm FTO ubiquitination by TRIM21. I would subject ubiquitinated FTO to MS analysis to identify which lysines within FTO were modified, and the type of ubiquitin linkage. Alternatively, I would use immunoblotting with a linkage-specific antibody. The ubiquitination assay should also reveal which E2 enzyme cooperates with TRIM21 in the ubiquitination reaction. This would shine more light on the FTO ubiquitination process.

It is important to understand the biological role of FTO ubiquitination. I would like to investigate the effect of TRIM21-mediated ubiquitination on the catalytic activity of FTO and substrate recognition. This could be determined by subjecting *in vitro* ubiquitinated FTO and unmodified FTO to an *in vitro* demethylation assay, which would assess the reactivity and selectivity of both FTO proteins against a panel of methylated oligonucleotides.

Moreover, it would be interesting to investigate the link between TRIM21-FTO interaction and m^6A demethylation of mRNA. I would like to determine if overexpression of TRIM21 and the resulting change in FTO cellular localisation has an effect on m^6A levels in mRNA. If so, this would suggest the cellular sub-compartment where FTO plays its role. Furthermore, given the recently described role of FTO in adipogenesis (Merkestein et al. 2015; Zhao et al. 2014), it would interesting to test if TRIM21 overexpression impairs differentiation of pre-adipocytes.

I would like to further investigate the FTO role in p-bodies and mRNA translational repression and decay. It would be interesting to use Co-IP with cross-linking to search for other components of p-bodies. Furthermore, I would like to investigate translational rate and life-time of mRNA shown to be demethylated by FTO in condition when FTO is overexpressed or knock-down.

5.4.8 Conclusions

I have identified TRIM21 as an E3 ubiquitin-protein ligase that mediates ubiquitination of FTO which does not lead to proteasomal degradation. FTO and TRIM21 interact in cytoplasmic p-bodies, suggesting FTO has a role in mRNA translational regression and decay. Moreover, TRIM21 alters the subcellular localisation of FTO increasing its cytoplasmic presence and reducing its nuclear abundancy. Overall, these data suggest that TRIM21 may be a regulator of FTO cytoplasmic location and TRIM21-mediated ubiquitination may affect cellular function of FTO.

6 *Fto* Conditional Muscle Specific Knock-Out

6.1 Introduction

Animal studies have provided strong support for the role of FTO in body composition and offered some insights into its effect on food intake and metabolism. Global germline loss of *Fto* in homozygous *Fto*$^{-/-}$ mice lead to a significant reduction in adipose tissue, lean body mass and body length, but also resulted in postnatal growth retardation and frequent postnatal death (Fischer et al. 2009). Whole body conditional *Fto* knock-out generated using a *Meox2*-Cre mouse line, resulted in significantly lower lean mass in males and females, growth retardation or perinatal lethality but also increased fat mass in females (Gao et al. 2010). Knock-out of *Fto* in adult life (week 6) using a tamoxifen induced *Ubc*-Cre line did not affect viability, body length and food intake but caused a reduction in body weight and lean mass (week 9) and surprisingly, an increase in fat mass over the next 10 weeks (McMurray et al. 2013). Furthermore, global overexpression of FTO led to a dose-dependent increase in body and fat mass and hyperphagia, irrespective of whether mice were fed on a standard or a high-fat diet (Church et al. 2010). These animal models clearly indicate that FTO influences body composition through changes in lean mass and fat mass.

Recent microarray studies on gastrocnemius muscle dissected from mice overexpressing FTO (Merkestein et al. 2014) showed that expression of around ~270 genes were changed at least 1.5 fold, with some genes showing up to an 8.7-fold change. Several genes that are related to cell cycle and DNA repair were down regulated. Pathway analysis revealed that a high percentage of genes whose expression was altered were part of a pathway involved in

methylation. Finally, the gastrocnemius muscle of FTO overexpression mice had the highest number of genes changed that were associated with obesity.

Given the changes in lean mass in FTO knock-out mice and expression differences in skeletal muscle, I decided to investigate whether FTO function in muscle has an effect on body mass composition.

The specific aims of this chapter were to:

1) Investigate whether specific loss of FTO expression in skeletal muscle affects body composition and development.
2) Investigate whether specific loss of FTO expression causes changes in glucose homeostasis and muscle function.

To do so, I conditionally deleted the *Fto* gene specifically in muscle. I then carried out metabolic phenotyping on genetically modified mice and their wild-type littermates. I also collected post mortem tissue samples for protein and DNA analysis, as well as histological studies.

6.2 Methods

6.2.1 Generation of Condition Muscle *Fto* Knock-Out Mice Model

To investigate the biological effects of genetic disruption of *Fto* in muscle, we generated mice in which *Fto* was selectively knocked out in muscle. The overall strategy is demonstrated in **Figure 44.** Mice with *Fto* exon 3 flanked with LoxP sites (FTO-KO-FLOX-B6) were previously generated by Dr Chris Church (McMurray et al. 2013).

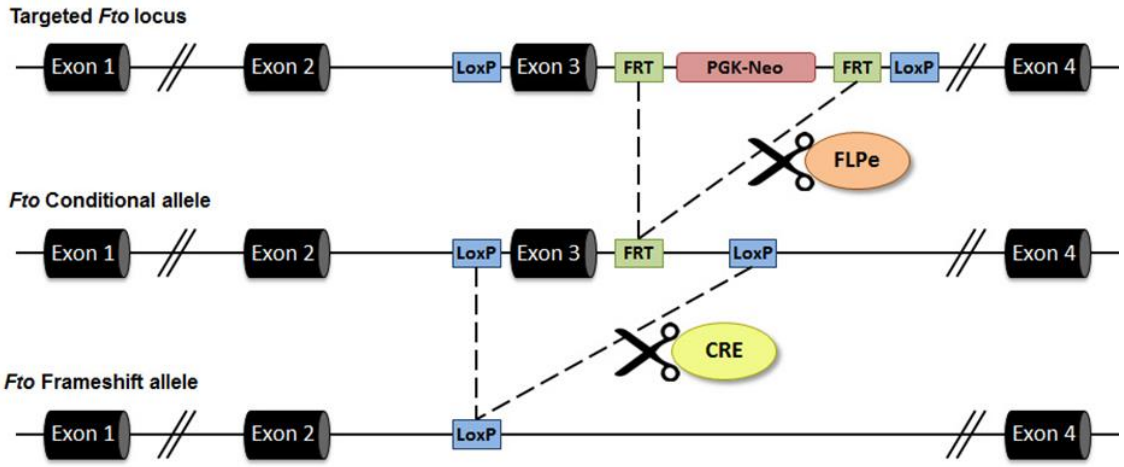

Figure 44. Strategy for generating conditional muscle *Fto* knock-out mice model. The targeted *Fto* locus contained a Neo selection cassette under control of a strong PGK promoter, flanked by FRT recombination sites. The Neo selection cassette enabled selection of positive 129 ES cell clones. PGK-Neo has been removed by crossing LoxP-Exon3-FRT-PGKNeo-FRT-LoxP mice to line expressing FLPe recombinase under the control of the β-actin promoter, generating an *Fto* conditional allele ($Fto^{+/flox}$). Mice carrying an *Fto* conditional allele were then crossed to line expressing Cre recombinase under the control of the muscle creatine kinase promoter (*Mck*-Cre) for conditional knock-out of *Fto* in muscle.

All mice were on a congenic C57BL/6J background (later called wild type, WT). A stock of mice carrying *Mck*-Cre recombinase (Brüning et al. 1998) were maintained by crossing the mice with the C57BL/6J mice. Mice carrying the *Fto* conditional allele ($Fto^{+/flox}$) were

crossed with mice carrying *Mck*-Cre recombinase to produce heterozygous (*Fto*$^{+/flox}$) mice expressing *Mck*-Cre. These mice were crossed again with (*Fto*$^{+/flox}$) to produce mice homozygous for *Fto* flox and carrying *Mck*-Cre recombinase (Fto$^{flox/flox}$,*Mck*-Cre). These mice lack *Fto* specifically in muscle.

6.2.2 *Fto* Conditional Muscle Knock-Out Phenotyping

Homozygous mice (Fto$^{flox/flox}$,*Mck*-Cre) entered a phenotyping pipeline at 3 weeks of age and proceeded as shown in **Figure 45** until the termination point at week 20. Wild type (WT) mice (*Fto*$^{+/+}$), WT mice with both Fto alleles floxed (*Fto*$^{flox/flox}$) and Cre mice (*Fto*$^{+/+}$,*Mck*-Cre) also underwent phenotyping to control for any effects due to the engineering of the floxed allele or due to the expression of Cre-recombinase (**Table 20**).

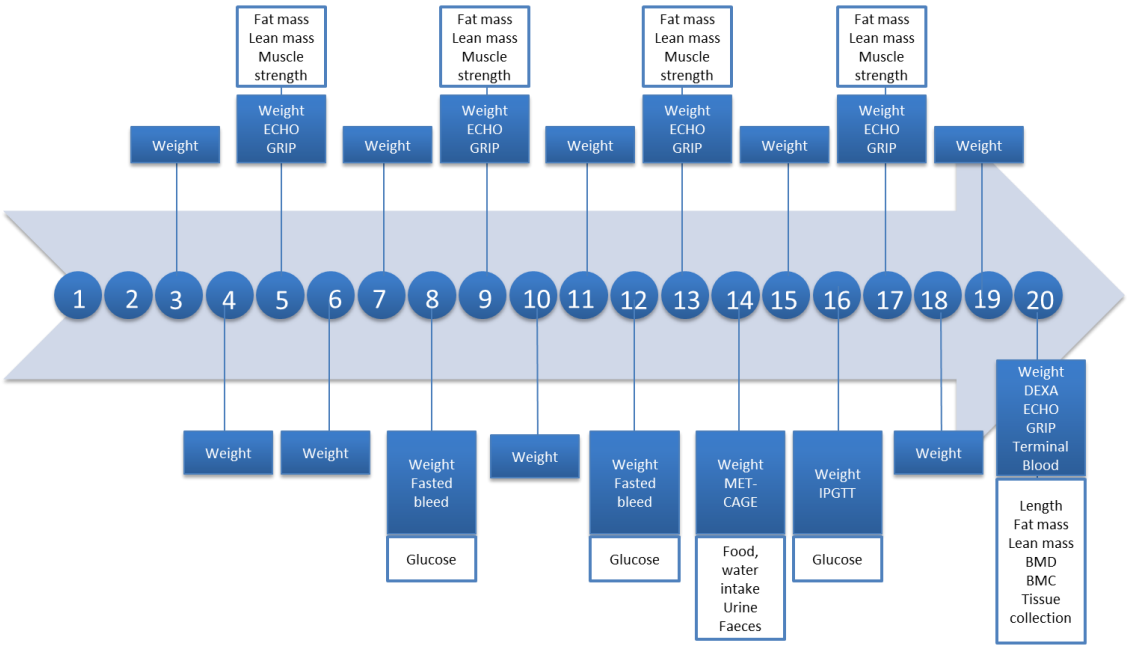

Figure 45. Phenotyping pipeline for conditional muscle knock-out mice and controls. Numbers represent the age of the animal in weeks. Abbreviations: ECHO, ECHO-MRI; GRIP, grip strength test; DEXA, dual energy X-ray absorptiometry; MET-CAGE, metabolic cage; IPGTT, Intraperitoneal Glucose Tolerance Test; BMD, bone mineral density; BMC, bone mineral content.

Table 20. Genotype groups in the phenotyping pipeline.

Genotype	Description	Abbreviation
Fto$^{+/+}$	Mice with wild-type *Fto* allele, no Cre	WTWT
Fto$^{+/+}$,*Mck*-Cre	Mice with wild-type *Fto* allele, carrying Cre	WTCRE
Fto$^{flox/flox}$	Homozygous mice with floxed *Fto* allele, no Cre	HOMWT
Fto$^{flox/flox}$,*Mck*-Cre	Homozygous mice with floxed *Fto* allele, carrying Cre	HOMCRE

6.2.3 One-Way Analysis of Variance (ANOVA)

One-way ANOVA was used to determine whether there were differences between group means of more than two groups in the population ('Laerd Statistics' 2015). During the analysis, the null hypothesis, which assumes that there are no differences in population means between the groups, was tested.

$$H_0: \text{all group means are equal (i.e., } \mu_1 = \mu_2 = \mu_3 = ... = \mu_k)$$

Where:

- μ = population mean
- k = number of groups

Evidence against the null hypothesis allows to accept the alternative hypothesis, which was that differences between the group population means really did exist.

$$H_A: \text{at least one group mean is different (they are not all the same)}$$

Statistical significance of $p \leq 0.05$ was accepted in this analysis, meaning that the probability of finding differences in the means of groups was less than 5 in 100 (5%) given that the null hypothesis was true.

The following assumptions were tested to provide valid one-way ANOVA results:

1. There are no outliers in any group (or overall).
2. The data (or residuals) are approximately normally distributed.
3. There is homogeneity of variances.

The first assumption was tested using a boxplot to identify the outliers ('Laerd Statistics' 2015). Data points were classified by SPSS as outliers and extreme outliers if there were more than 1.5 box-lengths and 3 box lengths respectively from the edge of their box. After careful examination, all outliers and extreme outliers proved to be genuine data points and were included in the analysis since there was no reason to reject them as invalid.

The Shapiro-Wilk Test of Normality was used to determine whether the data were normally distributed for each category of the independent variable (e.g. genotype) ('Laerd Statistics' 2015). The null hypothesis of the Shapiro-Wilk test is that the data's distribution is equal to a normal distribution, and the alternative hypothesis is that the data's distribution is not equal to a normal distribution. If the significance value for the test was $p<0.05$, the assumption of normality has been violated, rejecting the null hypothesis. On the rare occasions where the data are not normally distributed, analyses were run regardless as the one-way ANOVA is fairly robust to deviations from normality, particularly if the sample sizes (numbers in each group) are equal, or nearly equal (Lix, Keselman, and Keselman 1996).

The assumption of homogeneity of variances was tested using Levene's Test of Equality of Variances ('Laerd Statistics' 2015). If Levene's test was statistically significant (p<0.05), the assumption of homogeneity of variances has been violated (lack of equal variances). On that occasion, a modified version of the one-way ANOVA was required (called the Welch ANOVA). In the Welch ANOVA, if the Robust Tests of Equality of Means was statistically significant (p≤0.05) it meant there were statistically significant differences in group means.

In the example result of Welch ANOVA: Welchs' F(3, 38.219)=4.229, p=0.011, the meaning of each part as follows:

F	Indicates that we are comparing to an F-distribution.
3 in (3, 38.219)	Indicates the Between Groups degrees of freedom
38.219 in (3,38.219)	Indicates the Within Groups [Error] degrees of freedom
4.229	Indicates the obtained value of the F-statistic
p =0.011	Indicates the probability of obtaining the observed F-value if the null hypothesis is correct.

Although one-way ANOVA can indicate that not all the group means are equal in the population, it does not provide information about which group is different. To investigate this, a post-hoc test was applied which examined all possible group combinations ('Laerd Statistics' 2015). When the assumption of homogeneity of variances was met (equal variances), a Bonferroni post-hoc test was applied. However, when the assumption was violated, the Games-Howell post-hoc test was used instead. The significance level of post-hoc multiple comparison for both tests was p≤0.05.

6.2.4 Mixed ANOVA Analysis

The mixed ANOVA was used to determine if there is an interaction effect between two independent variables (e.g. genotype and time) on dependent variable (e.g. body weight, blood glucose concentration) and if there is a main effect of any of the independent variables on the dependent variable ('Laerd Statistics' 2015). The following assumptions have been tested to provide valid results:

1. There are no outliers in any group (or overall).
2. The data (or residuals) are approximately normally distributed.
3. There is homogeneity of variances.
4. There is homogeneity of covariances.
5. There is sphericity.

First two assumptions have been discussed in 6.2.3. The mixed ANOVA assumes that there are equal variances between the levels of the between-subjects factor, (e.g. genotype), at each level of the within-subjects factor, (e.g. time) for the dependent variable, (e.g. body weight). In the mixed ANOVA, the homogeneity of variances was tested with Levene's Test of Equality of Error Variances ('Laerd Statistics' 2015). If Levene's test was statistically significant (p<0.05), the assumption was violated. Lack of homogeneity of variances prevents from further analysis and the data must be transformed to correct the unequal variances.

The Box's Test of Equality of Covariance Matrices was used to validate the fourth assumption ('Laerd Statistics' 2015). If this test was statistically significant (p<0.001), the assumption of homogeneity of covariances have been violated. If the homogeneity of

covariances was met, the analysis was performed to determine whether an interaction existed. When the assumption was violated, the mixed ANOVA was run anyway or the analysis was split into separate repeated measures ANOVAs for each group or interpretation of the interaction was omitted in the analysis.

The assumption of sphericity was tested with Mauchly's Test of Sphericity, which tested the null hypothesis that the variances of the differences are equal ('Laerd Statistics' 2015). If Mauchly's test of sphericity was statistically significant (p<0.05), the null hypothesis was rejected and the alternative hypothesis that the variances of the differences are not equal was accepted (sphericity has been violated). If the data did not violate the assumption of sphericity, analysis was interpreted using the "Sphericity Assumed" rows. If the assumption was violated, a correction was applied to provide valid results. Statistic called the Epsilon (ε) represents the degree to which the sphericity is present. An epsilon of 1 indicates that the condition of sphericity is exactly met. The further epsilon decreases below 1 the greater the violation of sphericity. Greenhouse-Geisser and the Huynd-Feldt corrections attempt to overcome the fact that sphericity has been violated and estimate epsilon (ε). Greenhouse-Geisser correction was used when the estimated epsilon (ε) is less than 0.75 and Huynd-Feldt correction was used if estimated epsilon (ε) is greater than 0.75.

The mixed ANOVA was run using Repeated Measures Analysis in SPSS ('Laerd Statistics' 2015). The interaction effect was studied with the Tests of Within-Subjects Effects, mainly the time*genotype section. If the significance value is p<0.05 there is a statistically significant interaction and simple main effect for genotype was studied using Univatiate Analysis in SPSS (testing for differences in body weight between genotype groups at each week) which is equivalent to running three separate one-way ANOVAs. The simple main effect for time analysis (testing for differences in body weigh between time points for each

genotype group) was always significant reflecting a natural phenomenon of weight gain related to aging.

The main effect of genotype on body mass was studied by Tests of Between-Subjects Effects ('Laerd Statistics' 2015). If the significance value is $p<0.05$ there is a statistically significant overall difference in body weight between different genotype groups collapse across time (time is effectively being ignored and four genotype groups are being compared). The differences can be consulted in the Multiple Comparisons table using appropriate post-hoc test. The main effect of time on body weight was always significant for the reasons explained in the previous paragraph.

6.2.5 Immunoblotting Analysis

Immunoblotting was performed as described in 2.4.4 using the antibodies listed in **Table 21**.

Table 21. Antibodies used for immunoblotting analysis in the experiments described in Chapter 6. Antibodies were used in pairs (e.g. A1 with B1, A2 with B2).

Label	Name	Dilution	Source	Cat. Number
A1	rabbit anti-FTO	1:1000	raised in-house	
B1	anti-rabbit-HRP	1:2500	GE Healthcare	NA934
A2	rat anti-HSC70	1:1000	Abcam	Ab19136
B2	anti-rat CY2	1:1000	Abcam	Ab6952

6.3 Results

In order to evaluate the function of FTO in skeletal muscle I used a mouse line expressing Cre recombinase under muscle creatine kinase (*Mck*-Cre) to delete exon 3 of the *Fto* gene. Muscle creatine kinase in rodents is expressed predominantly in skeletal muscle and heart (Johnson, Wold, and Hauschka 1989; Trask and Billadello 1990; Lyons et al. 1991). To ensure that any observed phenotypes could be properly ascribed to loss of FTO protein in HOMCRE mice, I included three colony littermate control groups in the phenotyping cohorts. These were HOMWT to control for effects due to the floxed allele, WTCRE to control for any effects due to expression of *Mck*-Cre recombinase in muscle, and WTWT mice as a baseline reference. Any phenotype observed in HOMCRE mice could be credited to *Fto* loss in muscle only if the statistically significant differences are observed between HOMCRE and each of all three colony littermate control groups.

6.3.1 Characterisation of Muscle Creatine Kinase (*Mck*)-Cre

In order to verify and assess the tissue specificity of Cre recombinase expressed under the *Mck* promoter, mice were crossed with the reporter line R26R-LACZ (Gt(ROSA)26Sor^{tm1Sor}) which has a beta-galactosidase gene preceded by a LoxP-flanked transcriptional termination sequence. This resulted in excision of the transcriptional termination sequence in cells expressing Cre recombinase under the *Mck* promoter and expression of beta-galactosidase under the *LacZ* promoter. Mice were sacrificed at 9 weeks of age and tissues were collected and stained as described in 2.1.11. All the cells expressing beta-galactosidase should be stained an intense blue due to X-gal hydrolysis. The results showed that the *Mck* promoter was predominantly active in the skeletal muscle cells (**Figure 46 C,E, F**) and heart

muscle cells (**Figure 46 H**), but also in muscle cells present in tongue, bronchi, bladder, stomach and oesophagus, small intestine and large intestine (**Figure 46 D,G,I,J,K,L**).

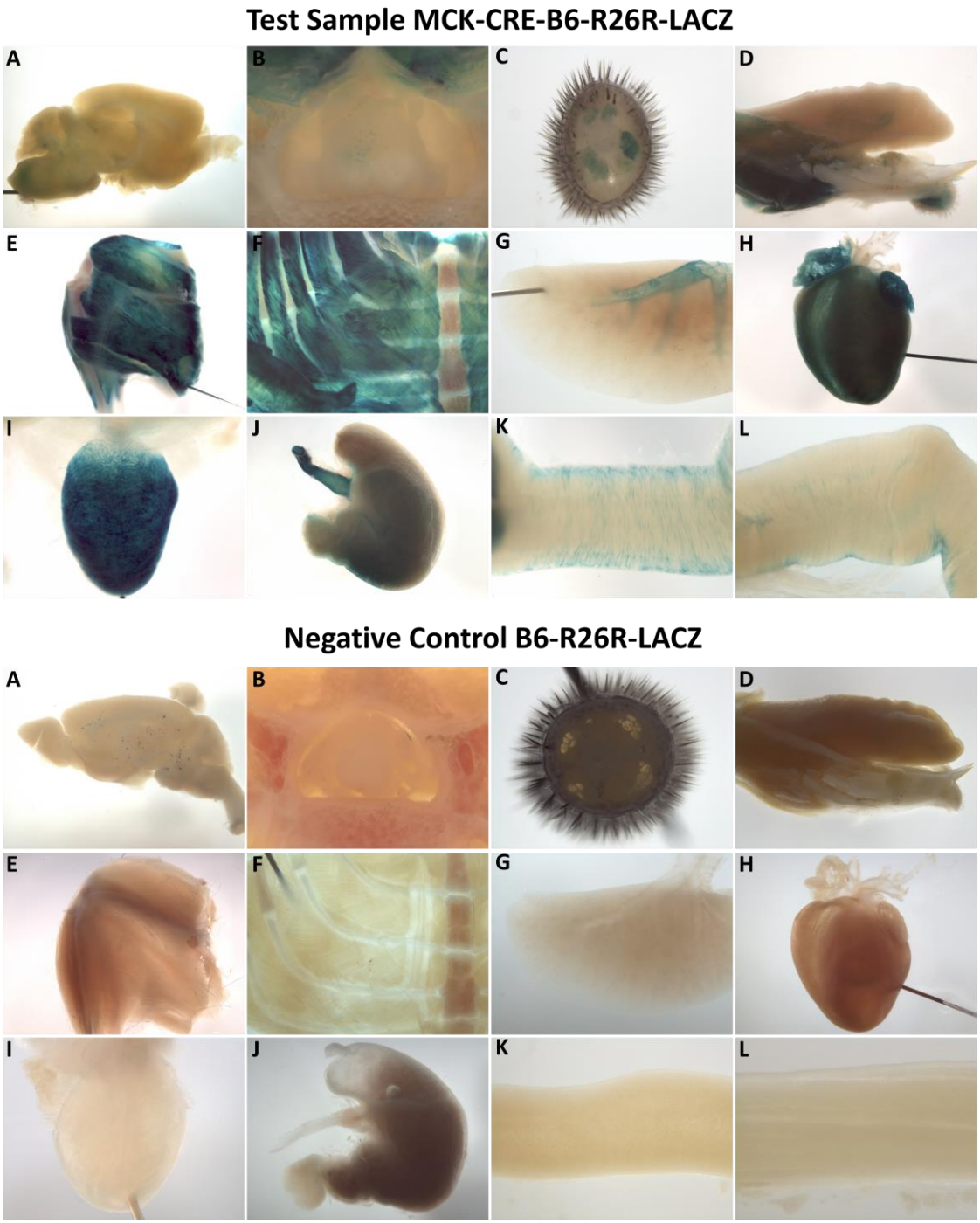

Figure 46. X-gal staining for cell expressing beta-galactosidase. Tissues were collected from 9 weeks old mice. A-brain; B-spinal cord; C-tail; D-tongue and lower jaw; E-hind leg; F-rib cage; G-lungs; H-heart; I-bladder; J-stomach; K-small intestines; L-large intestines. Staining was performed by the histology team at Harwell MRC.

6.3.2 Deletion of Exon 3 of the *Fto* Gene Resulted in FTO Protein Knock-Down

Deletion of FTO at the protein level was tested using immunoblotting (6.2.5). Male mice at 7 weeks of age were sacrificed and heart and gastrocnemius muscle were collected (2.1.4). Knock-out of *Fto* in heart and skeletal muscle of $Fto^{flox/flox}$,*Mck*-Cre (HOMCRE) mice is shown in **Figure 47**. The results showed that FTO bands were detected in the WTWT ($Fto^{+/+}$, WT) and HOMWT ($Fto^{flox/flox}$, WT) muscle and heart lysates, but not in muscle and heart dissected from the HOMCRE mouse. These results show that *Fto* gene deletion led to FTO knock-down at the protein level.

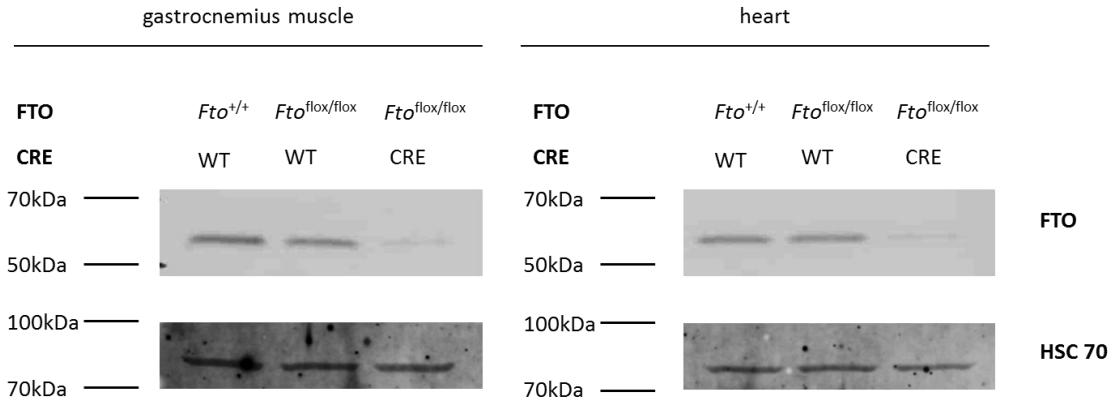

Figure 47. Loss of FTO in heart and skeletal muscle as a result of *Fto* gene knock-out. FTO bands were detected by rabbit anti-FTO antibody and HRP-conjugated secondary antibody. HSC 70 (70 kDa heat shock protein) was used as a loading control and detected with rat anti-HSC70 antibody and CY-2 fluorescently labelled secondary antibody. HSC 70 was visualised with Typhoon 9400 fluorescent gel scanner.

6.3.3 *Fto* Muscle Knock-Out Did Not Affect Mice Viability and Body Length

Postnatal lethality and growth retardation were previously observed in global germline homozygous $Fto^{-/-}$ mice (Fischer et al. 2009; Gao et al. 2010; McMurray et al. 2013) when

compared to wild type littermates. These mice were born at the expected Mendelian ratios but homozygous *Fto*$^{-/-}$ mice died more frequently at 4 weeks of age (Fischer et al. 2009; McMurray et al. 2013). A similar phenotype was reported in conditional *Meox2*-Cre *Fto*$^{-/-}$ mice, with only 50 % surviving until weaning (Gao et al. 2010). The authors suggested that FTO is not essential for embryonic development but plays a role after birth.

Overall, in the muscle-specific *Fto* knock-out study 793 mice were born (**Table 22**) and 236 died prior to weaning (within 21 days after birth) giving a survival rate of 70.24%, which was in line with a reported value of 73.39% for Harwell stock colony inbred C57BL/6J pups. In total, *Mck*-Cre *Fto*$^{-/-}$ (HOMCRE) mice were born with a genotype distribution (12.3 %) in line with the Mendelian distribution (12.5% expected) (**Table 23**). However, a chi-square goodness-of-fit test for the total number of mice from all the specific genotypes indicated that there were statistically significant differences in the total number of mice from all the specific genotypes compared to the proportions calculated based on the Mendelian distribution ($\chi 2(5)=11.635$, $p=0.040$). The significance was lost when calculated separately for males and females. The binomial distribution of the genotype proportions further revealed the total number of HOMWT mice (50) was statistically different than expected ($p=0.042$) This means that the variations from Mendelian distribution were not due to *Fto* deletion in muscle.

Out of 189 mice monitored over week 3-20 and included in the phenotyping experiments, none died suddenly, although seven were culled as they were sick. None of these mice lacked *Fto* in muscle. One WT female was removed from further analysis due to overgrown teeth and a resulting low body mass.

Table 22. Summary of mice born within *Fto* muscle knock-out breeding scheme.

Mating Identifier	Pups recorded	Dead before 21 day
FTOKOFLOX-MCK-CRE/4	92	28
FTOKOFLOX-MCK-CRE/5	33	10
FTOKOFLOX-MCK-CRE/6	45	16
FTOKOFLOX-MCK-CRE/7	113	49
FTOKOFLOX-MCK-CRE/8	107	23
FTOKOFLOX-MCK-CRE/9	60	9
FTOKOFLOX-MCK-CRE/10	72	31
FTOKOFLOX-MCK-CRE/11	42	11
FTOKOFLOX-MCK-CRE/12	36	7
FTOKOFLOX-MCK-CRE/13	55	20
FTOKOFLOX-MCK-CRE/14	37	10
FTOKOFLOX-MCK-CRE/15	39	11
FTOKOFLOX-MCK-CRE/16	61	11
All	793	236

Table 23. Mendelian distribution of genotyped mice born in the experiment. n-numbers, O- observed, E-expected, χ2- the chi-square goodness-of-fit.

Genotype	Males			Females			Total			E. %
	O. n	E. n	%	O. n	E. n	%	O. n	E. n	%	
WTWT	38	29.8	16.0	40	33.3	15.0	78	63.0	15.5	12.5
WTCRE	36	29.8	15.1	42	33.3	15.8	78	63.0	15.5	12.5
HOMWT	27	29.8	11.3	23	33.3	8.6	50	63.0	9.9	12.5
HOMCRE	32	29.8	13.4	30	33.3	11.3	62	63.0	12.3	12.5
HETWT	44	59.5	18.5	67	66.5	25.2	111	126.0	22.0	25
HETCRE	61	59.5	25.6	64	66.5	24.1	125	126.0	24.8	25
Total	238	238	100	266	266	100	504	504	100	100
χ2	χ2(5)=8.101, *p*=0.151			χ2(5)=7.248, *p*=0.203			χ2(5)=11.635, *p*=0.040			

To assess if *Fto* knock-out in muscle caused growth retardation, the body length from nose to anus was measured in mice at 20 weeks of age. Descriptive statistics are included in the **Table Appendix 6**. A one-way ANOVA was conducted separately for females and males and mice were classified into genotype groups (**Table Appendix 7**).

In males, body length was statistically significantly different between different genotype groups, Welchs' $F(3, 38.219)=4.229$, $p=0.011$ (6.2.3). Games-Howell post-hoc analysis revealed that the only significant difference in body length was between WTCRE (10.19±0.05 cm) and HOMWT (9.97±0.03 cm), $p=0.015$ (**Figure 48**). This may suggest a mild effect of flexed *Fto* allele on body length in male mice. The body length of HOMCRE (10.07±0.03 cm) mice was also nominally lower compared to WTCRE and WTWT (10.16±0.08 and 10.19±0.05 cm) but was not statistically significant. There was no significant difference between HOMCRE and HOMWT.

In females, the nominal body length decreased from 9.67±0.04 cm in WTWT to 9.61±0.04 cm in WTCRE; to 9.53±0.04 cm in HOMWT and to the lowest 9.48±48 cm in HOMCRE mice. There was a statistically significantly difference between genotype groups as assessed by one-way ANOVA $F(3, 83)=3.182$, $p=0.028$. Bonferroni post-hoc analysis revealed that the only significant difference was between WTWT and HOMCRE $p=0.033$. Consistent with a mild effect of floxed *Fto* allele on body length in male mice, a mild floxed effect in HOMWT females was observed.

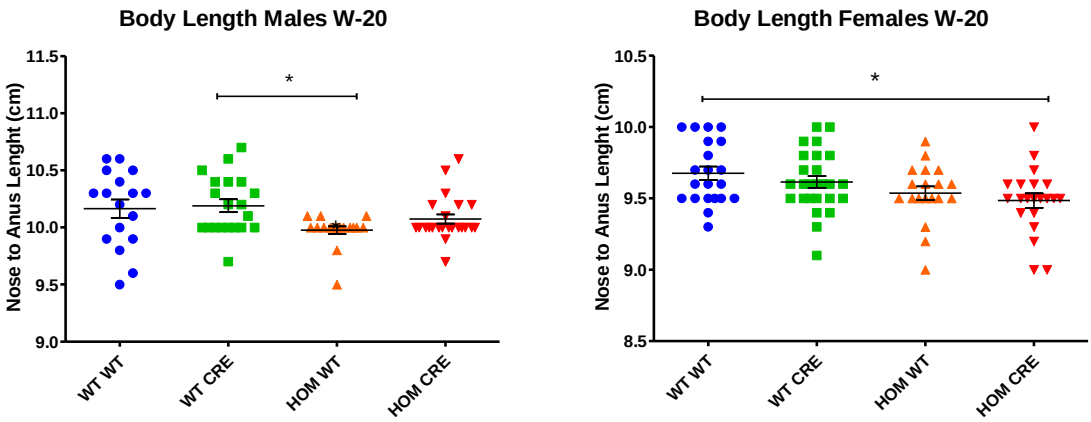

Figure 48. Body length of *Fto* muscle knock-out males and females. Body length of *Fto* muscle knock-out mice measured from nose to anus at week 20 and compared to litter mates. **A** Males; WTWT n=17, WTCRE n=20, HOMWT n=17, HOMCRE n=23. **B** Females; WTWT n=17, WTCRE n=22, HOMWT n=15, HOMCRE n=17. Data were analysed with one-way ANOVA as described in 6.2.3. Data are represented by single data points with mean ± SEM marked. *$p \leq 0.05$.

Overall, these results revealed that mice lacking *Fto* in muscle did not show increased postnatal lethality or growth retardation as was observed in global germline homozygous *Fto*$^{-/-}$ mice (Fischer et al. 2009; Gao et al. 2010; McMurray et al. 2013).

6.4 Analysis of Phenotypes in Male Mice

6.4.1 *Fto* Knock-Out in Muscle Did Not Affect Body Weight in Males

To investigate whether muscle specific *Fto* knock-out had an effect on body mass, male mice were weighed repeatedly from week 4 until the termination at week 20 (**Figure 49**). Mice were classified into groups based on their date of birth, and body weight was checked once a week (2.1.8). Animals were fasted over-night at weeks 8, 12 and 16, which resulted in a

small body mass decrease. After fasting, animals quickly recovered and continued to gain weight.

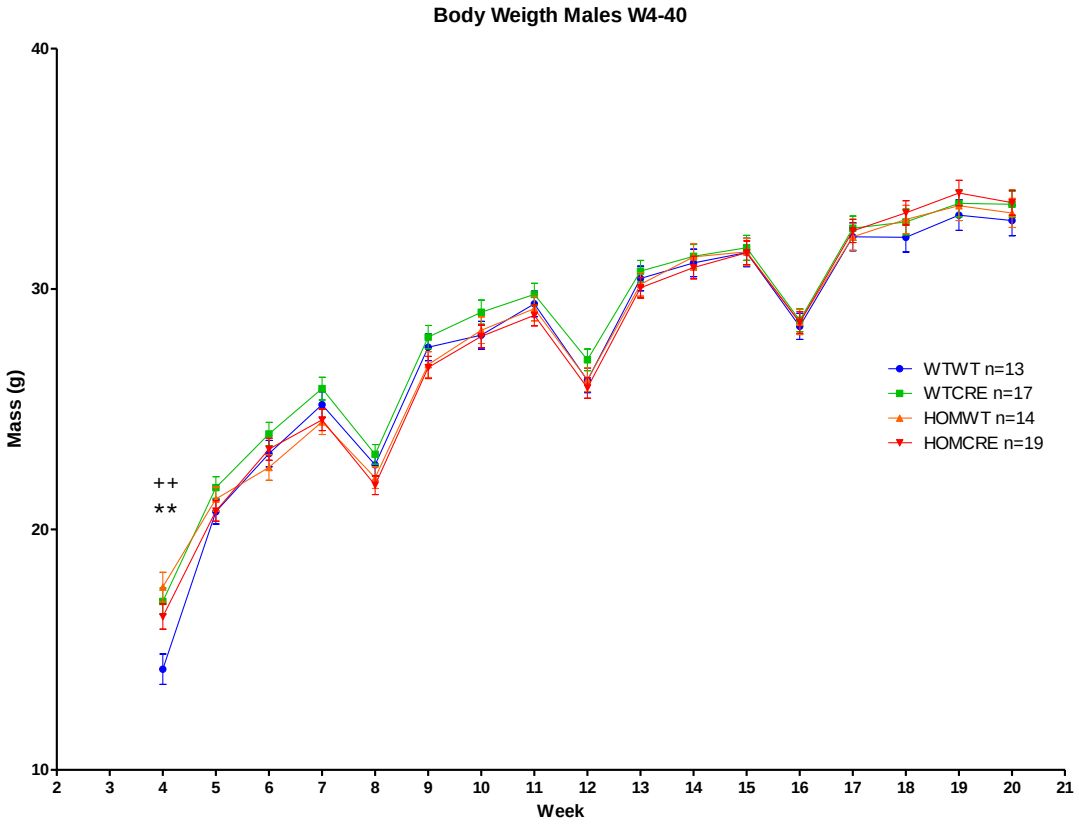

Figure 49. Repeated weekly body mass measurements of *Fto* muscle knock-out male mice. Data were analysed with mixed ANOVA as described in 6.2.4. Decrease of body mass in week 8, 12 and 16 is due to overnight fasting. Data are represented by group mean ± SEM. Statistically significant differences between WTWT and WTCRE are marked with "*", between WTWT and HOMWT by "+". **/++$p \leq 0.01$.

A mixed ANOVA was conducted and time (17 weeks) was chosen as a Within-Subject Factor and Genotype as a Between Subject Factor (**Table Appendix 8**). In males, Mauchly's Test of Sphericity had been violated ($p<0.001$) and a Greenhouse-Geisser correction was then used. The simple main effect analysis for genotype showed statistically significant differences in body weight at week 4, $F(3, 59)=5.781$ $p=0.002$, partial $\eta^2 = 0.227$. Bonferroni post-hoc analysis revealed that body mass was significantly higher at week 4 in WTCRE (17.01±0.55 g) $p=0.008$, and in HOMWT (17.60±0.61 g), $p=0.002$ comparing to WTWT

(14.18±0.63 g). The increase in body weight in HOMCRE (16.37±0.52 g) was also nearly statistically significant p=0.059. However, there were no statistically significant differences in weight over weeks 5-20. Furthermore, data analysed for the main effect of genotype group also showed that there was no statistically significant difference in body weight between genotype groups $F(3, 59) = 0.477$, $p = 0.700$, partial $\eta^2 = 0.024$.

Consistent with body mass analysis, food and water consumed by males measured over 24 hours at 14 weeks of age was unaltered (**Figure 50 A** and **B**) as determined by one-way ANOVA with homogeneity of variances met (food intake - $F(3, 82)=0.618$, p=0.606; water intake- $F(3, 82)=0.416$, p=0.742), (**Table Appendix 9**). Faeces and urine output were also unaffected (**Figure 50 C** and **D**) (one-way ANOVA with homogeneity of variances met: faeces output $F(3, 82)=0.617$, p=0.606; urine output $F(3, 82)=0.501$, p=0.501), (**Table Appendix 9**).

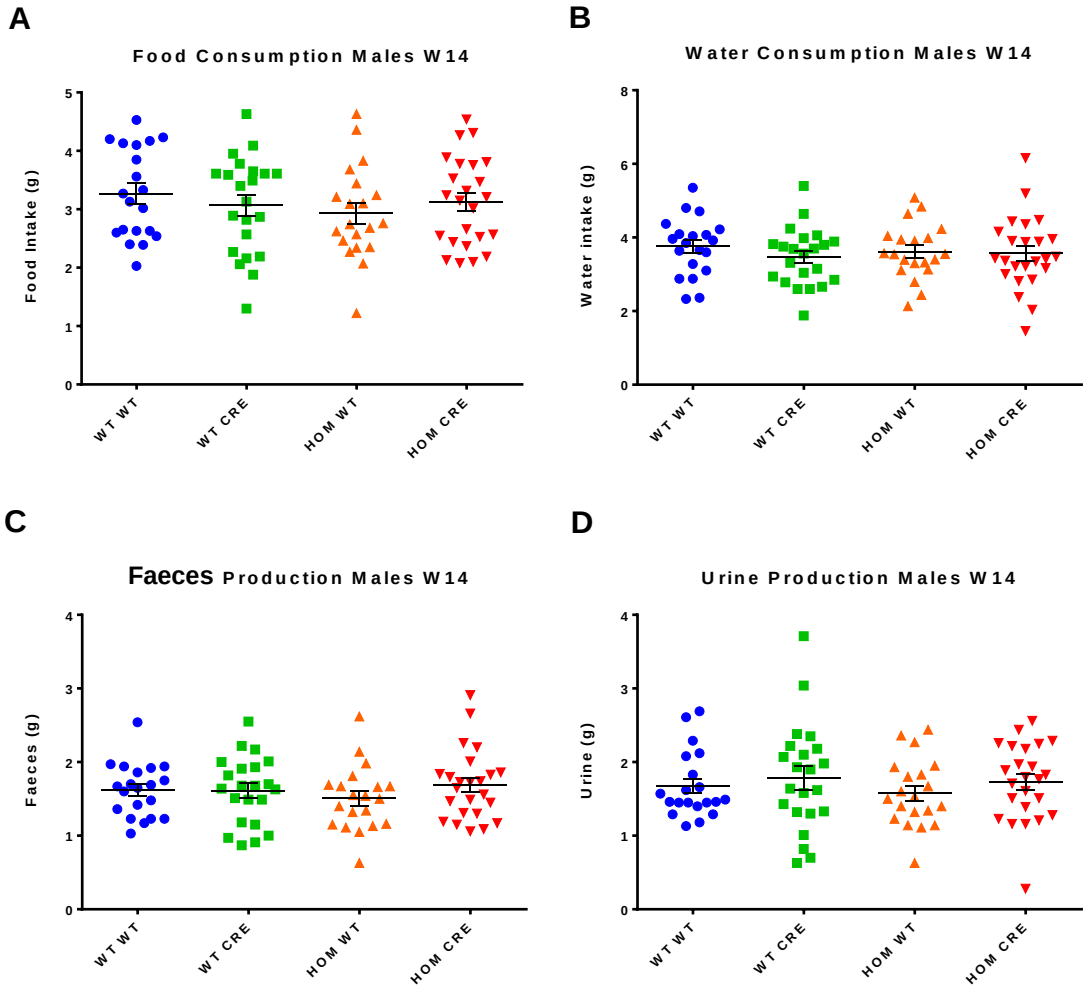

Figure 50. Food and water consumption, and faeces and urine output of *Fto* muscle knock-out males. Parameters were measured over 24 hour at week 14 in metabolic cages, as described in 2.1.9. A-D, WTWT n=20, WTCRE n=22, HOMWT n=20, HOMCRE n=24. Data were analysed with one-way ANOVA as described in 6.2.3. Data are represented by single data points with mean ± SEM marked.

Overall these results suggest that FTO knock-down in muscle did not affect body weight, food and water consumption, or faeces and urine production in male mice.

6.4.2 HOMCRE Males Have Increased White Adipose Tissue (WAT) Mass But Not Due to *Fto* Muscle Specific Knock-Out

At the end of the phenotyping pipeline (week 20) animals were subjected to dual-energy X-ray absorptiometry (DEXA) (2.1.8) and tissues were collected post-mortem (2.1.4).

Figure 51 shows DEXA measurements and tissue mass of 20-week old male mice. Descriptive statistics and the results of post-hoc analysis are presented in **Table Appendix 10** and **Table Appendix 11**. One way ANOVA (homogeneity of variances met) revealed that bone mineral density (BMD) was significantly different between the genotype groups $F(3, 74)=3.892$, $p=0.012$. Bonferroni post-hoc analysis revealed a significant decrease of BMD in HOMCRE (0.0541±0.0005 g/cm^2) but only when compared to WTCRE (0.0561±0.0005 g/cm^2), $p=0.035$ (**Figure 51 A**). BMD of HOMWT was also nominally lower (0.0544±0.0007 cm^2) when compared to WTWT and WTCRE but did not reach significance level of post-hoc multiple comparison.

There was a trend towards a lower bone mineral content (BMC) (**Figure 51 B**) in HOMCRE males (0.5284±0.0087 g) compared to WTCRE (0.5696±0.0109 g), but ANOVA analysis revealed that the differences did not reach statistical significance, ANOVA, $F(3, 74)=3.673$, $p=0.053$.

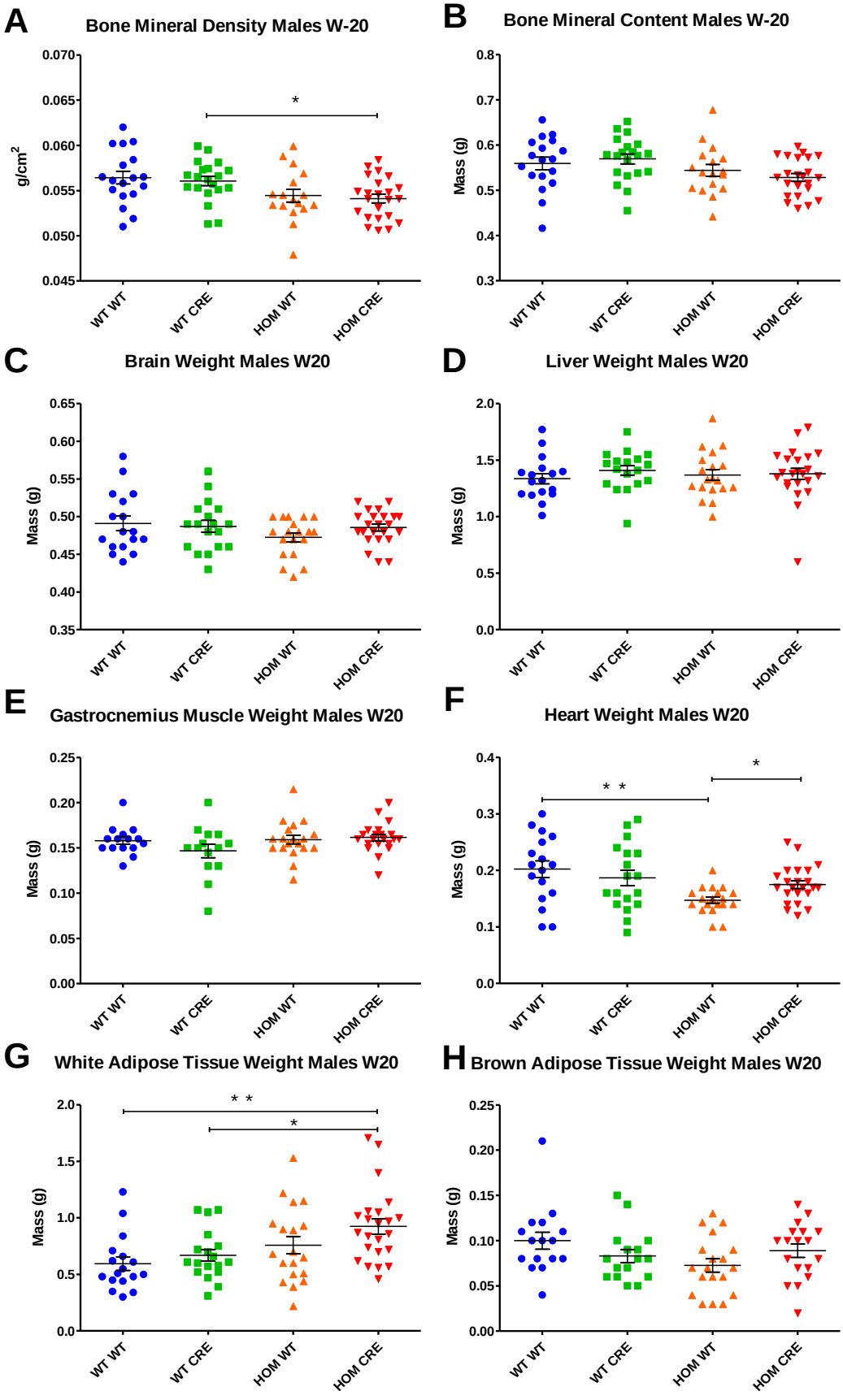
A
Bone Mineral Density Males W-20
g/cm2
0.070
0.065
0.060
0.055
0.050
0.045
*
WT WT
WT CRE
HOM WT
HOM CRE
B
Bone Mineral Content Males W-20
Mass (g)
0.8
0.7
0.6
0.5
0.4
0.3
C
Brain Weight Males W20
Mass (g)
0.65
0.60
0.55
0.50
0.45
0.40
0.35
D
Liver Weight Males W20
Mass (g)
2.0
1.5
1.0
0.5
0.0
E
Gastrocnemius Muscle Weight Males W20
Mass (g)
0.25
0.20
0.15
0.10
0.05
0.00
F
Heart Weight Males W20
Mass (g)
0.4
0.3
0.2
0.1
0.0
* *
*
G
White Adipose Tissue Weight Males W20
Mass (g)
2.0
1.5
1.0
0.5
0.0
* *
*
H
Brown Adipose Tissue Weight Males W20
Mass (g)
0.25
0.20
0.15
0.10
0.05
0.00

Figure 51. DEXA measurements and tissue mass of 20-week old male mice. DEXA measurements were performed on anaesthetised mice and tissues were collected post-mortem. **A-B**, WTWT n=18, WTCRE n=20, HOMWT n=17, HOMCRE n=23. **C**, **D**, **F**, **G**, WTWT n=11, WTCRE n=18, HOMWT n=19, HOMCRE n=23. **E**, WTWT n=15, WTCRE n=14, HOMWT n=19, HOMCRE n=21. **H**, WTWT n=16, WTCRE n=16, HOMWT n=19, HOMCRE n=23. Data were analysed with one-way ANOVA as described in 6.2.3. Data are represented by single data points with mean ± SEM marked. *$p \leq 0.05$, **$p \leq 0.01$.

Analysis of adipose tissue revealed statistically significant differences between genotypes in White Adipose Tissue (WAT) mass (F(3, 73)=4.837, p=0.004) in 20-week old males, (**Figure 51 G**). Bonferroni post-hoc analysis shown significantly increased WAT mass in HOMCRE (0.9243±0.0677 g) compared to WTWT (0.5947±0.06001 g), p=0.004 and compared to WTCRE (0.7513±0.0356 g), p=0.041, but not significantly different when compared to HOMWT (0.7595±0.0773 g) p=0.429. Overall, these data suggest that the increase in WAT mass observed in HOMCRE males did not result from *Fto* deletion in muscle.

Analysis of Brown Adipose Tissue (BAT) mass showed no statistically significant differences, (F(3, 70)=2.152, p=0.101), however nominal BAT mass of HOMWT males was lower than other genotype groups (**Figure 51 H**). Furthermore, analysis of cardiac mass showed statistically significant differences between genotype groups, Welchs' F(3, 36.525)=6.866, p=0.001. Games-Howell post-hoc analysis revealed that the cardiac mass was significantly lower in HOMWT (0.1474±0.0055 g) comparing to WTWT (0.2024±0.0146 g), p=0.010 and HOMCRE (0.1748 ±0.0068 g), p=0.016 (**Figure 51 F**). There was a trend for reduced cardiac mass in HOMWT comparing to WTCRE (0.1867±0.0137 g), but the difference was not statistically significant p=0.065. The results of BAT and cardiac mass analysis further suggest a mild effect of floxed *Fto* allele.

There were no statistically significant differences between genotype groups in brain mass (Welchs' F(3, 37.341)=1.425, p=0.0251) (**Figure 51 C**), liver mass (ANOVA F(3, 73)=0.374, p=0.772),(**Figure 51 D**) or the gastrocnemius muscle mass (ANOVA F(3, 65)=1.609, p=0.196),(**Figure 51 E**).

6.4.3 Increased Fat Mass and Decreased Lean Mass Account for Unaltered Total Body Mass in HOMCRE Males

To further investigate the body composition of *Fto* muscle specific knock-out mice, the animals were subjected to Echo-MRI (2.1.8) at various stages of the phenotypic pipeline (5, 9, 13, 17 and 20 weeks of age), (**Figure 52**). This enabled absolute lean mass and absolute fat mass to be determined. The relative fat and relative lean mass were calculated by dividing the fat (lean) mass by the total body weight (**Figure 52**). A one-way ANOVA was conducted to determine if there were any differences in the body composition between the genotype groups (**Table Appendix 12** and **Table Appendix 14**). There was homogeneity of variances for all the groups and all the analysis, thus a standard ANOVA was used with a Bonferroni post-hoc multiple comparison (**Table Appendix 13** and **Table Appendix 15**).

Consistent with the analysis of WAT dissected from the 20-week old male mice, the *Fto* muscle specific knock-out males (HOMCRE) had significantly greater absolute fat mass than WTWT males from 9 weeks of age (**Figure 52 C**, **E**, **G**, **I**). Their fat mass was also greater than WTCRE mice at 17 and 20 weeks of age (**Figure 52 G**, **I**). Moreover, HOMCRE males had significantly decreased absolute lean mass compared to WTCRE at 9 and 13 weeks of age (**Figure 52 D**, **F**). However, there were no significant differences in absolute lean mass or fat mass between HOMWT and HOMCRE males, suggesting that these differences are not due to loss of FTO. These data also illustrate that the nominal fat mass and the nominal lean mass of HOMWT was different compared to WTWT and WTCRE, although the differences were not statistically significant.

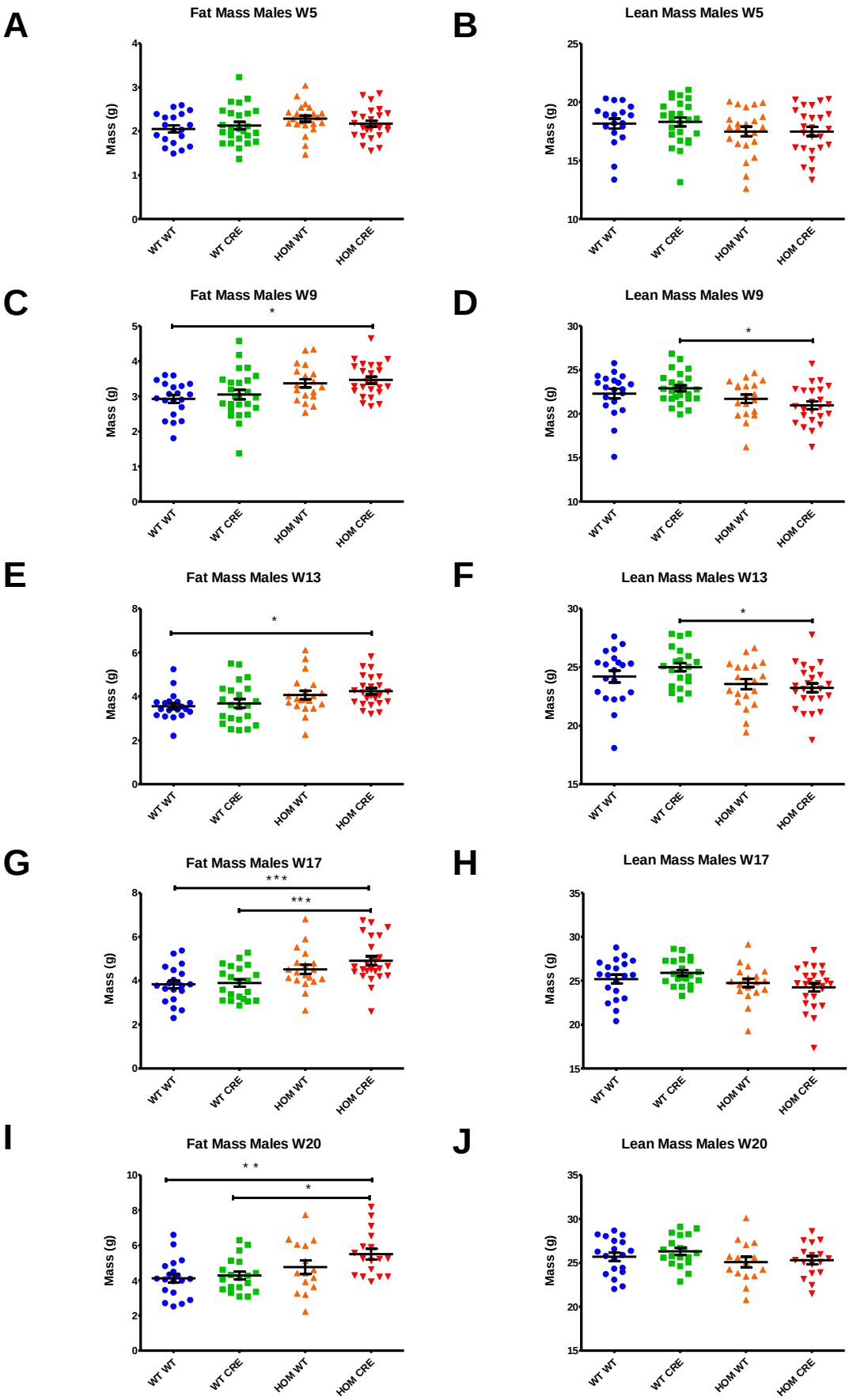
A
Fat Mass Males W5
Mass (g)
WT WT
WT CRE
HOM WT
HOM CRE
B
Lean Mass Males W5
C
Fat Mass Males W9
*
D
Lean Mass Males W9
*
E
Fat Mass Males W13
*
F
Lean Mass Males W13
*
G
Fat Mass Males W17
***
***
H
Lean Mass Males W17
I
Fat Mass Males W20
* *
*
J
Lean Mass Males W20

Figure 52. Absolute Fat Mass and Relative Lean Mass of *Fto* muscle specific knock-out males at 5, 9, 13, 17 and 20 weeks of age. Animals were subjected to Echo-MRI as described in 2.1.8. Data were analysed with one-way ANOVA as described in 6.2.3. Numbers of animals included in each study are listed in WTWT, WTCRE, HOMWT, HOMCRE order: **A**-**B**, 22, 26, 21, 23; **C**-**F**, 22, 27, 20, 21; **G**-**H**, 21, 27, 20, 20; **I-J**, 19, 25, 18, 19. Data are represented by single data points with mean ± SEM marked. *$p \leq 0.05$, **$p \leq 0.01$, ***$p \leq 0.001$.

To reduce intersubject variability, data were also analysed as a relative lean mass and relative fat mass (**Figure 53**). These data demonstrate an even more pronounced increase of relative fat mass and a greater decrease in relative lean mass in *Fto* muscle specific knock-out mice. HOMCRE males had increased relative fat mass compared to WTWT and WTCRE, (**Figure 53 A, C, E, G, I**). The differences became significant at 9 weeks of age and continued until the termination week 20.

A

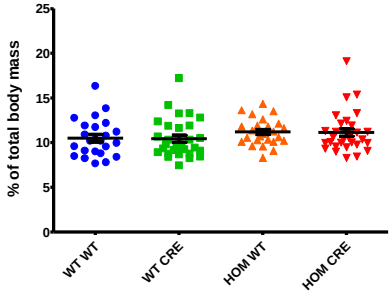
% Fat Mass Males W5
% of total body mass
WT WT
WT CRE
HOM WT
HOM CRE

B

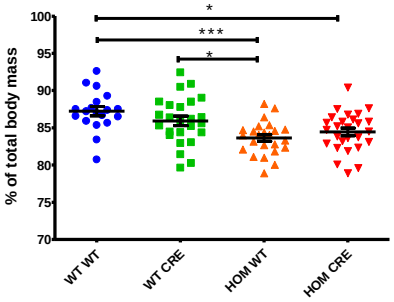
% Lean Mass Males W5
% of total body mass
WT WT
WT CRE
HOM WT
HOM CRE

C

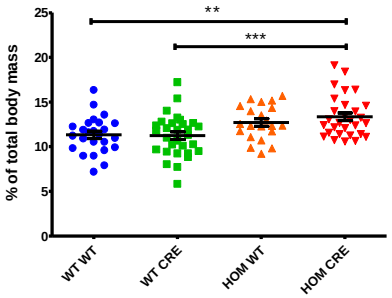
% Fat Mass Males W9
% of total body mass
WT WT
WT CRE
HOM WT
HOM CRE

D

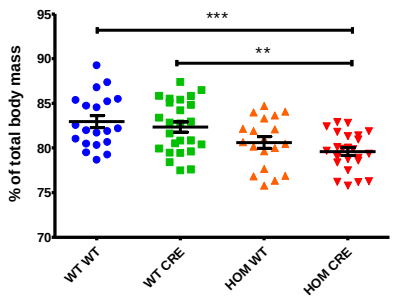
% Lean Mass Males W9
% of total body mass
WT WT
WT CRE
HOM WT
HOM CRE

E

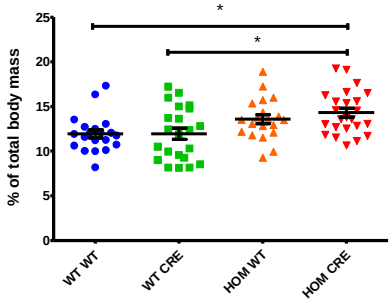
% Fat Mass Males W13
% of total body mass
WT WT
WT CRE
HOM WT
HOM CRE

F

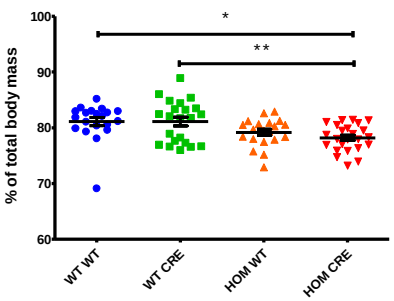
% Lean Mass Males W13
% of total body mass
WT WT
WT CRE
HOM WT
HOM CRE

G

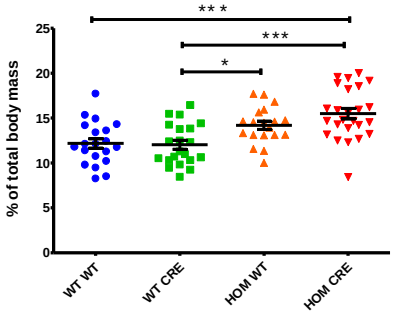
% Fat Mass Males W17
% of total body mass
WT WT
WT CRE
HOM WT
HOM CRE

H

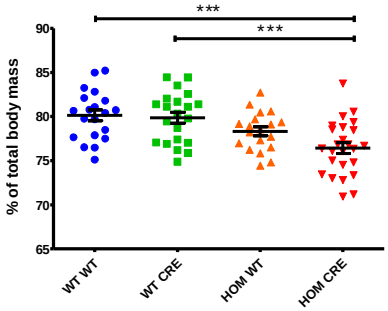
% Lean Mass Males W17
% of total body mass
WT WT
WT CRE
HOM WT
HOM CRE

I

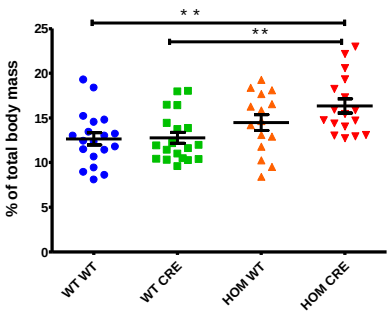
% Fat Mass Males W20
% of total body mass
WT WT
WT CRE
HOM WT
HOM CRE

J

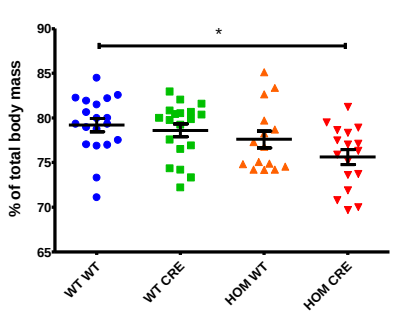
% Lean Mass Males W20
% of total body mass
WT WT
WT CRE
HOM WT
HOM CRE

Figure 53. Relative Fat Mass and Relative Lean Mass of *Fto* muscle specific knock-out males at 5, 9, 13, 17 and 20 weeks of age. Animals were subjected to Echo-MRI (2.1.8). Relative fat/lean mass was calculated by dividing fat/lean mass by total body weight. Data were analysed with one-way ANOVA as described in 6.2.3. Numbers of animals included in each study are listed in WTWT, WTCRE, HOMWT, HOMCRE order: **A**-**B**, 19, 25, 23, 25; **C**-**D**, 20, 25, 19, 24; **E**-**F**, 20, 22, 20, 24; **G**-**H**, 20, 21, 19, 25; **I-J**, 19, 19, 15, 17. Data are represented by single data points with mean ± SEM marked. *$p \leq 0.05$, **$p \leq 0.01$, ***$p \leq 0.001$.

Further analysis showed that the HOMCRE males had significantly less relative lean mass compared to WTWT (throughout all weeks) and WTCRE (week 9-17) (**Figure 53 B**, **D**, **F**, **H**, **J**).

Moreover, HOMWT males showed increased relative fat mass and decreased relative lean mass compared to WTWT and WTCRE throughout all weeks, however the differences in relative lean mass were statistically significant only at week 5 (HOMWT and WTWT, $p<0.001$; HOMWT and WTCRE, $p=0.023$) and the differences in relative fat mass were statistically significant only at week 17 (HOMWT and WTCRE, $p=0.036$).

Overall, these results illustrate that the HOMCRE males had increased absolute and relative fat mass as well as decreased absolute and relative lean mass when compared to some control groups, however the observed phenotypic differences did not result from loss of FTO in muscle as the comparison between HOMWT and HOMCRE was not significantly different.

6.4.4 *Fto* Muscle Specific Knock-Out Did Not Affect Muscle Strength in Males

To investigate the effect of muscle specific *Fto* knock-out on muscle strength, animals were subjected to a grip strength test (2.1.10). Each measurement was repeated three times and the average value was calculated. The results of grip strength test at the 5, 9, 13, 17 and 20 weeks of age are shown in **Figure 54**. A one-way ANOVA was conducted to determine if there were any differences in the muscle strength between the genotype groups (**Table**

Appendix 16). Depending on the outcome of homogeneity test, Bonferroni or Games-Howell post-hoc multiple comparison was applied (**Table Appendix 17**).

The results of the analysis showed that *Fto* muscle specific knock-out male (HOMCRE) mice, despite having less relative lean mass than WTWT males, had significantly greater muscle strength at week 13 (p=0.001), 17 (p<0.001) and 20 (p=0.012). At week 9 muscle strength also appeared slightly greater, but the difference were not statistically significant. HOMWT males also showed significantly greater muscle strength than WTWT mice (week 9, p=0.027; week 13, p<0.00; week 17, p<0.00; week 20 p=0.001), but also compared to HOMCRE at week 5 (p=0.045), and WTCRE at week 17 (p=0.015). Also at week 17, WTCRE show significantly increased muscle strength compared to WTWT males (p=0.022).

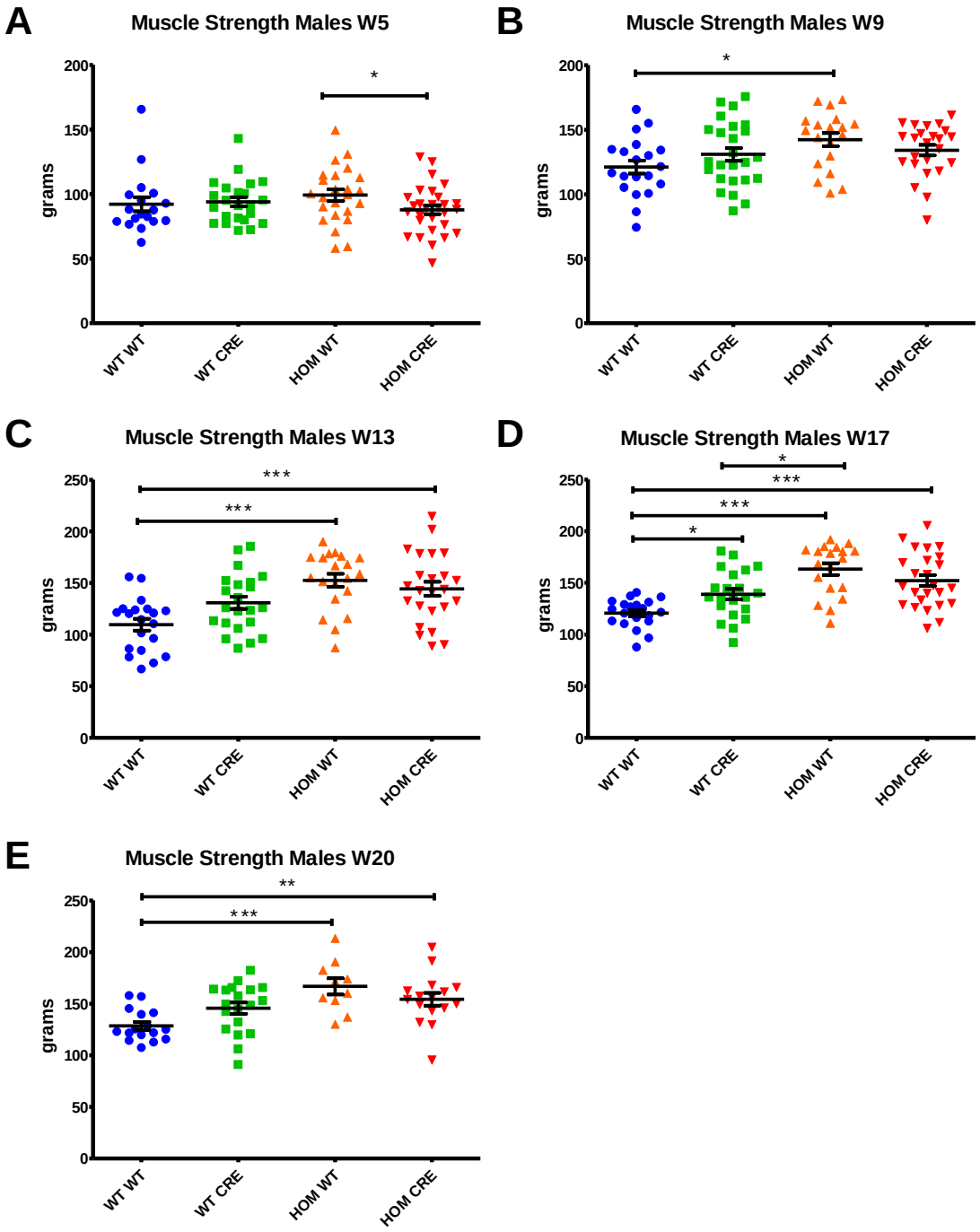

Figure 54. Muscle strength of *Fto* muscle specific knock-out males at 5, 9, 13, 17 and 20 weeks of age. Muscle strength was measured by a grip strength test of combined forelimbs and hind limbs. Each measurement was repeated three times and the average value was calculated (2.1.10). Data were analysed with one-way ANOVA as described in 6.2.3. Numbers of animals included in each study are listed in WTWT, WTCRE, HOMWT, HOMCRE order: **A**, 15, 20, 22, 26; **B**, 20, 25, 19, 24; **C**, 20, 22, 20, 24; **D**, 20, 21, 19, 25; **E**, 16, 19, 10, 16. Data points represent the average value calculated based on three measurements. Total mean ± SEM of each group are marked. *p<0.05, **p<0.01, ***p<0.001.

Overall, these results revealed phenotypic differences in muscle strength in the studied male mice, although the effects were not due to muscle specific *Fto* knock-out. Furthermore, the data showed that despite a reduction in absolute and relative lean mass, muscle strength of HOMCRE males was not decreased, and in fact it was greater than certain control groups. Interestingly, muscle strength of HOMWT males was also increased, further suggesting a link between the observed phenotype and floxed *Fto* allele.

6.4.5 *Fto* Knock-Out in Muscle Has No Effect on Glucose Tolerance

To assess if *Fto* knock-out in muscle had an effect on glucose homeostasis, mice were subjected to an intraperitoneal glucose tolerance test (IPGTT), (2.1.6) at 16 weeks of age. Average absolute blood glucose levels, individual normalised trials and area under the curve (AUC) calculated for males are shown in **Figure 55**.

A mixed ANOVA was conducted with Time (0, 60 and 120 minutes) chosen as a Within-Subject Factor and Genotype as a Between Subject Factor. Mauchly's Test of Sphericity indicated that the assumption of sphericity had been violated (p<0.001) and Huynh-Feldt correction was used. The simple main effect analysis for genotype showed no statistically significant differences in glucose at any time point (**Table Appendix 18**). Additionally, data analysed for the main effect of genotype group also showed no overall significant effect of genotype on glucose homeostasis, $F(3, 71)=1.445$, p =0.237 , partial η^2 = 0.058.

To calculate the AUC, blood glucose levels were normalised to time 0 blood glucose level of each individual animal (**Figure 55 B**). One-way ANOVA (homogeneity of variances met)

indicated significant differences between the groups, $F(3, 71)=2.836$, p =0.44. Bonferroni post-hoc analysis revealed that AUC of HOMWT males (208.7389±35.87642) was significantly lower than HOWMCRE males (255.195±57.99024), p=0.031.

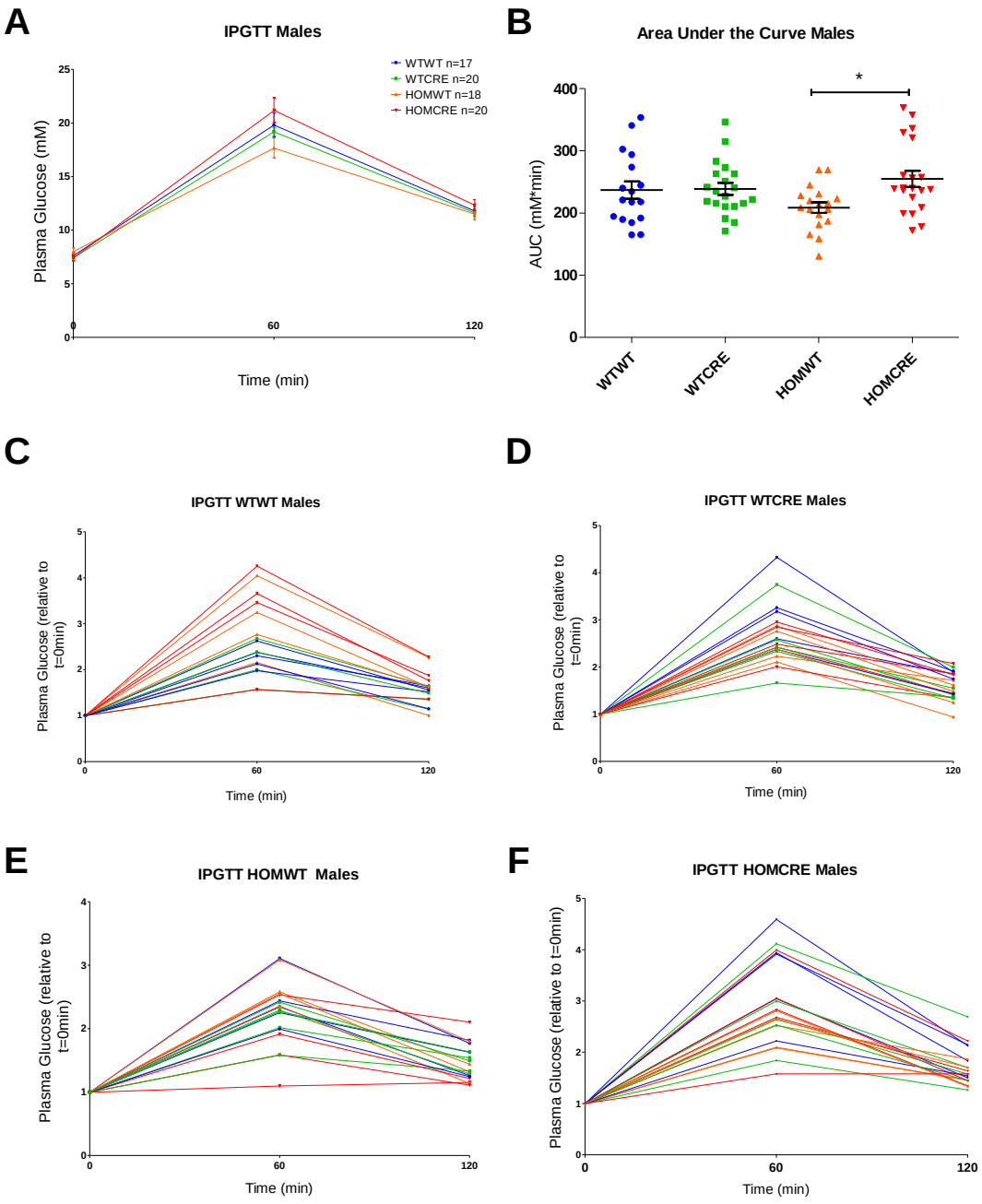

Figure 55. Intraperitoneal glucose tolerance test (IPGTT) and area under the curve (AUC) for *Fto* muscle specific knock-out males at 16 weeks of age. Mice were fasted overnight (16 hours) and blood samples were collected from the tail vein (time 0 min). Subsequently, mice were injected IP with glucose and blood was collected after 60 and 120 min after the injection (2.1.6). Plasma was analysed as described in 2.1.7. **A**, Data were analysed with mixed ANOVA as described in 6.2.4. Data points represent absolute group mean ± SEM. **B**, Data were analysed with one-way ANOVA as described in 6.2.3. Data are represented by single data points with mean ± SEM marked. **C-D**, Individual blood glucose curves normalised to time 0 blood glucose. *p≤0.05.

6.5 Analysis of Phenotypes in Female Mice

6.5.1 *Fto* Knock-Out in Muscle Did Not Affect Body Weight in Females, but the Floxed *Fto* Allele Resulted in Body Weight Loss

In order to assess the effect of *Fto* knock-out in muscle on body mass in females, a mixed ANOVA was conducted on the repeated body mass measurements taken from the same female mice (**Table Appendix 19**). Time (17 weeks) was chosen as a Within-Subject Factor and Genotype as a Between Subject Factor. Mauchly's Test of Sphericity indicated that the assumption of sphericity had been violated (p<0.001) and Greenhouse-Geisser correction was used. The results showed no statistically significant interaction between the genotype and time on body weight, F(9.335, 205.367)=0.760, p=0.658 partial η^2=0.033.

The main effect of genotype analysis showed that there was a statistically significant difference in body mass between genotype groups F(3, 66) = 3.572, p = 0.019, partial η^2 = 0.140. Post-hoc Games-Howell multiple comparison revealed that overall across time, HOMCRE females have significantly lower body mass compared to WTWT females (p=0.027) (**Figure 56**). Moreover, HOMCRE females seemed to have less body mass compared to WTCRE female, but the difference was not statistically significant (p=0.084). Similarly, HOMWT seemed to weigh less that WTWT and WTCRE, but the differences were not statistically significant (p=0.107 and p=0.207 respectively). HOMCRE and HOMWT female mice are not significantly different in weight from one another (p=1.000). These results suggest that the floxed *Fto* allele caused the observed phenotype.

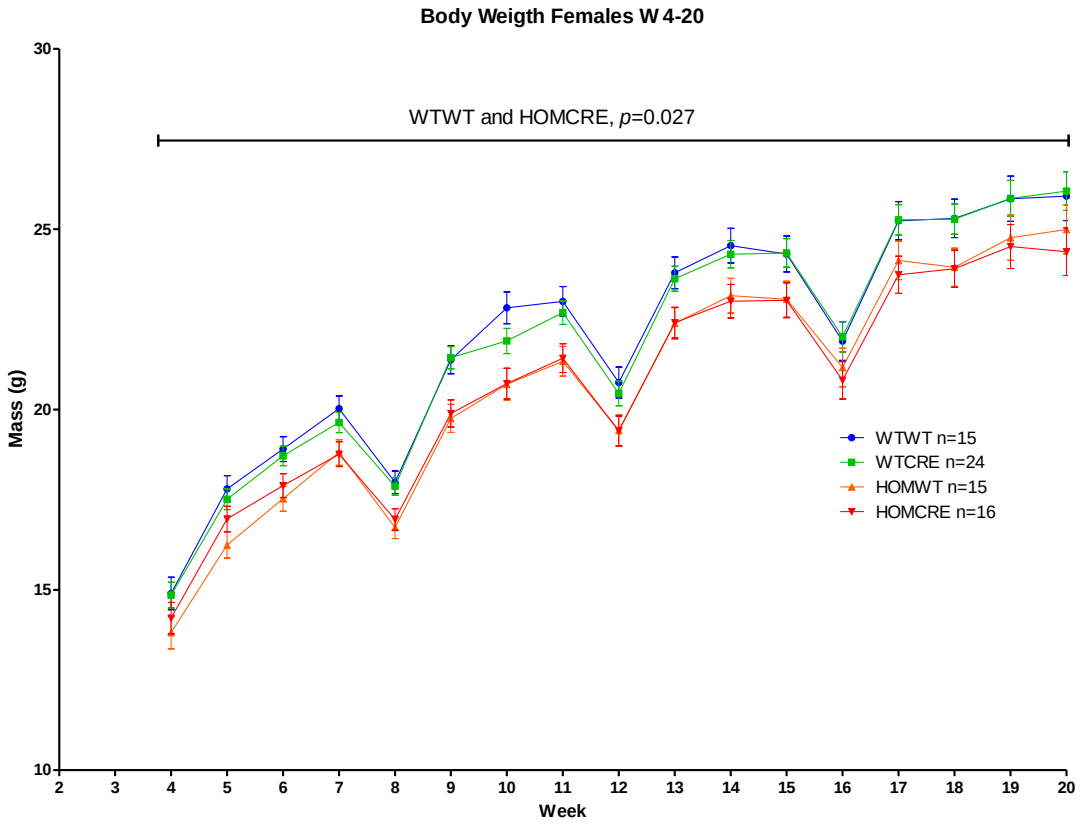

Figure 56. Repeated weekly body mass measurements of the same *Fto* muscle knock-out female mice. Data were analysed with mixed ANOVA as described in 6.2.4. Decrease of body mass in weeks 8, 12 and 16 is due to overnight fasting. Data are represented by group mean ± SEM.

To further assess the impact of the floxed allele on body weight, I expanded the data set of the body weight measurements and included the non-repeated measurements of the body weight of female mice which due to other tests or sickness were not repeatedly weighed throughout the entire phenotyping pipeline (**Table Appendix 20**), (**Figure 57**). A one-way ANOVA (homogeneity of variances met) was conducted to assess differences in body mass in each week of the phenotyping pipeline separately. The results of Bonferroni post-hoc multiple comparisons are included in the **Table Appendix 21**.

In line with the previous results, HOMCRE females had significantly lower body mass compared to WTWT (weeks 9-11, 14 and 17; **Figure 57** marked with "+") and WTCRE

(weeks 9, 11; **Figure 57** marked with "o"). Interestingly, with the additional data included, HOMWT females were now significantly lighter when compared to WTWT (weeks 5-11, 13-15 and 17-18; **Figure 57** marked with "*") and also WTCRE (6, 9, 11, 13; **Figure 57** marked with "x"), supporting the view that the floxed *Fto* allele reduced body weight.

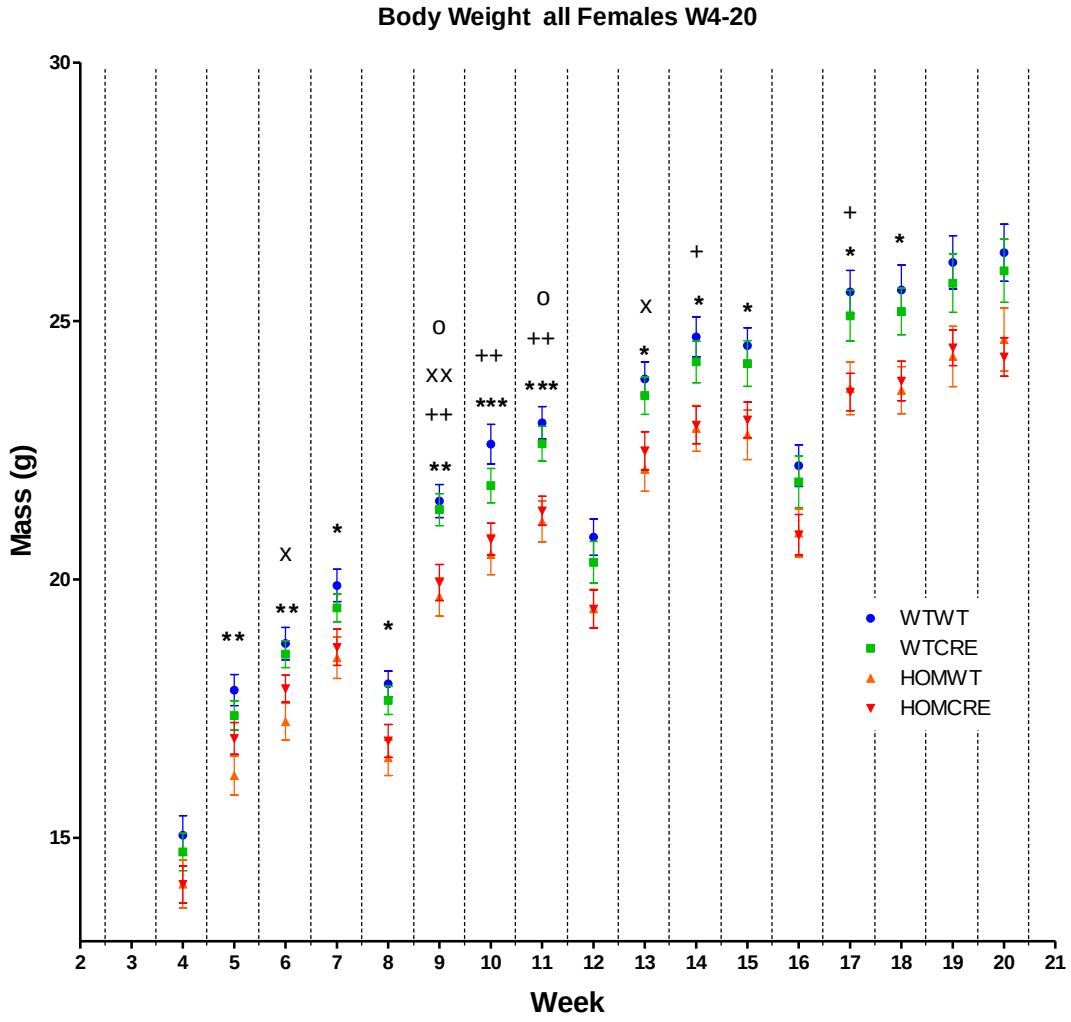

Figure 57. Body mass of all *Fto* muscle knock-out females ever included in the phenotyping pipeline. Data were analysed with one-way ANOVA as described in 6.2.3. Decrease of body mass in weeks 8, 12 and 16 is due to overnight fasting. Data are represented by group mean ± SEM. Statistically significant differences between WTWT and HOMWT are marked with "*", between WTWT and HOMCRE by "+", between WTCRE and HOMWT by "x", between WTCRE and HOMCRE by "o". */+/x/o $p \leq 0.05$, **/++/xx/oo $p \leq 0.01$, ***/+++/ xxx/ooo $p \leq 0.001$.

Consistent with the analysis of male mice, food consumption ($F(3, 46.683)=2.275$, $p=0.092$), and faeces production ($F(3, 84)=0.856$, $p=0.467$), was unaltered in female mice (**Table Appendix 22**, **Figure 58**). However there were differences in water consumption ($F(3, 86)=3.696$, $p=0.015$) and urine production ($F(3, 84)=4.649$, $p=0.005$). Bonferroni post hoc multiple comparisons (**Table Appendix 23**) revealed that HOMWT females consumed significantly less water than WTWT ($p=0.010$) and produced less urine ($p=0.006$). The difference in urine production was also significant compared to WTCRE females ($p=0.017$).

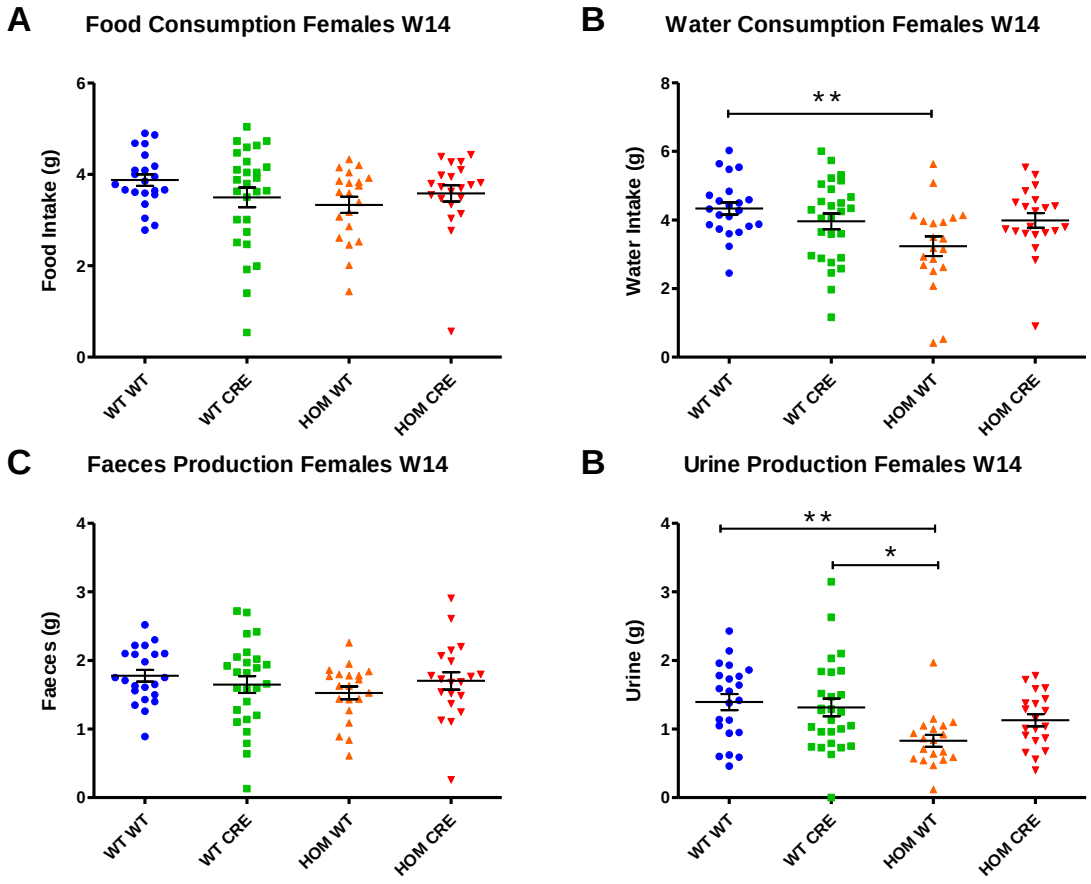

Figure 58. Food and water consumption, and faeces and urine output of *Fto* muscle knock-out females. Parameters were measured at week 14 over 24 hour in the metabolic cage as described in 2.1.9. **A-B**, WTWT n=22, WTCRE n=27, HOMWT n=20, HOMCRE n=21; **C-D**, WTWT n=22, WTCRE n=27, HOMWT n=19, HOMCRE n=20 Data was analysed with one-way ANOVA as described in 6.2.3. Data are represented by single data points with mean ± SEM marked. *$p\leq0.05$, **$p\leq0.01$.

6.5.2 Terminal DEXA and Dissections Revealed No Differences in WAT and BAT Female Mice at Termination Point

Results of dual-energy X-ray absorptiometry (DEXA) performed on females at 20 weeks of age and the mass of tissues collected at post-mortem are summarised in **Table Appendix 24**.

A one-way ANOVA (homogeneity of variances met) showed that bone mineral density (BMD) and bone mineral content (BMC) were significantly different between the genotype groups (BMD $F(3, 83)=4.789$, $p=0.044$; BMC $F(3, 83)=6.376$, $p=0.001$). Bonferroni post-hoc analysis (**Table Appendix 24**) revealed that HOMCRE females (0.051±0.001 g/cm^2) had a significantly lower BMD than WTWT mice (0.054±0.000 g/cm^2), $p=0.003$ (**Figure 59 A**). HOMCRE females (0.474±0.008 g) appeared also to have lower BMC compared to WTWT and WTCRE but the differences did not reach statistical significance ($p=0.067$, $p=0.360$). Interestingly, HOMWT females (0.5696±0.0109 g) also had a significantly lower BMC (0.457±0.009 g) than WTWT (0.506±0.007 g, $p=0.001$) and WTCRE (0.497±0.009 g, $p=0.009$), (**Figure 59 B**)**.** Lastly, HOMCRE and HOMWT female mice were not significantly different from each other.

There were no statistically significant differences between genotype groups in brain mass, liver mass, the mass of gastrocnemius muscle, and cardiac mass (**Figure 59 C**,**D**,**E**,**F**). Importantly, there were also no statistical significant differences in white and brown adipose tissue mass in females at week 20 (**Figure 59 G**, **H**), (**Table Appendix 25**).

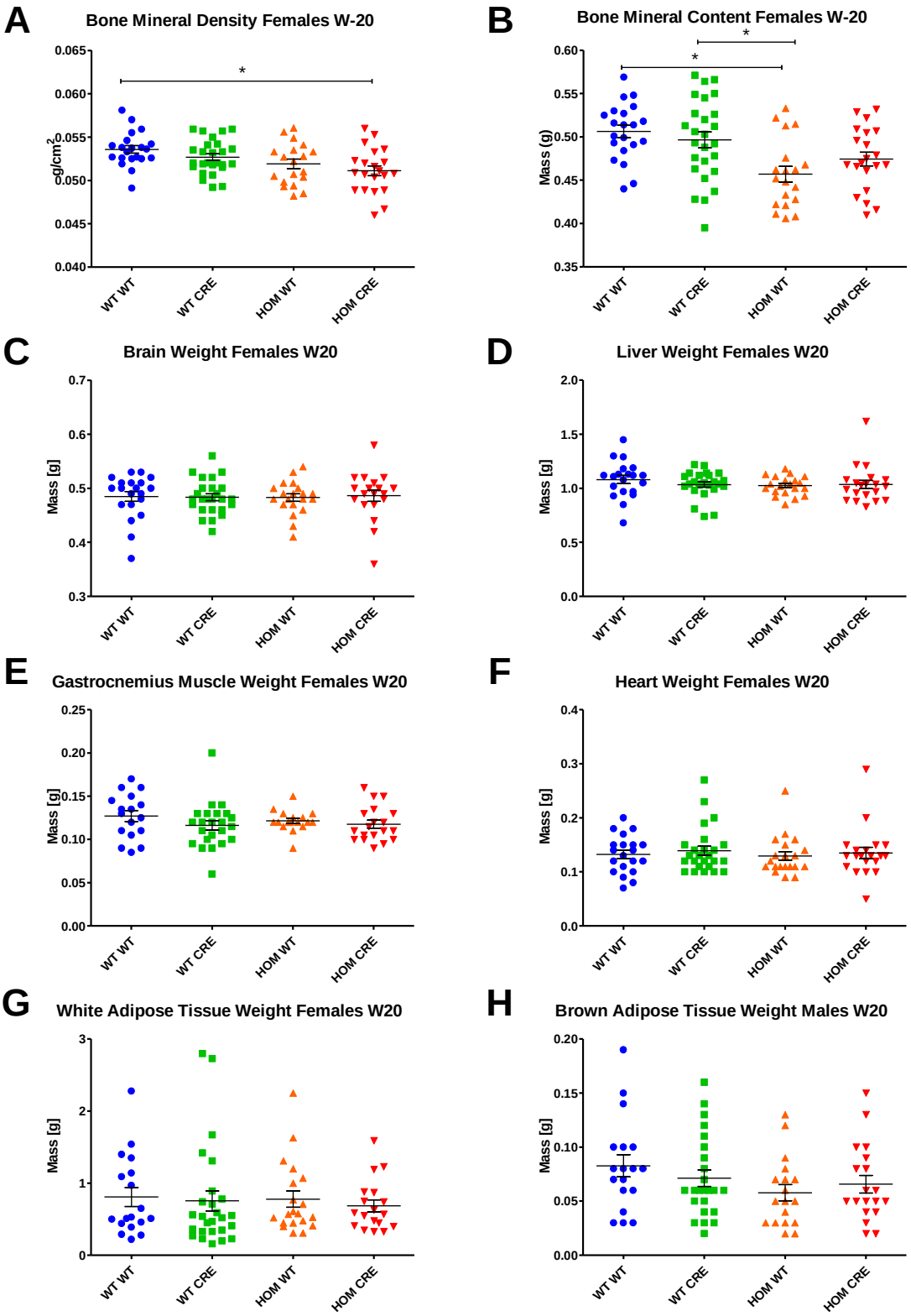
A
Bone Mineral Density Females W-20
g/cm2
0.065
0.060
0.055
0.050
0.045
0.040
*
WT WT
WT CRE
HOM WT
HOM CRE
B
Bone Mineral Content Females W-20
Mass (g)
0.60
0.55
0.50
0.45
0.40
0.35
*
*
WT WT
WT CRE
HOM WT
HOM CRE
C
Brain Weight Females W20
Mass [g]
0.7
0.6
0.5
0.4
0.3
WT WT
WT CRE
HOM WT
HOM CRE
D
Liver Weight Females W20
Mass [g]
2.0
1.5
1.0
0.5
0.0
WT WT
WT CRE
HOM WT
HOM CRE
E
Gastrocnemius Muscle Weight Females W20
Mass [g]
0.25
0.20
0.15
0.10
0.05
0.00
WT WT
WT CRE
HOM WT
HOM CRE
F
Heart Weight Females W20
Mass [g]
0.4
0.3
0.2
0.1
0.0
WT WT
WT CRE
HOM WT
HOM CRE
G
White Adipose Tissue Weight Females W20
Mass [g]
3
2
1
0
WT WT
WT CRE
HOM WT
HOM CRE
H
Brown Adipose Tissue Weight Males W20
Mass [g]
0.20
0.15
0.10
0.05
0.00
WT WT
WT CRE
HOM WT
HOM CRE

Figure 59. DEXA measurements and tissue mass of 20-week old females. DEXA measurements were performed on anaesthetised mice and tissues were collected post-mortem. Numbers of animals included in each study are listed in WTWT, WTCRE, HOMWT, HOMCRE order: **A-B**, 21, 26, 19, 21; **C**, 20, 25, 20, 19**; D**,F 20, 25, 20, 20; **E**, 17, 23, 17, 19; **G**, 18, 26, 20, 18; **H**, 18, 24, 18, 19. Data were analysed with one-way ANOVA as described in 6.2.3. Data are represented by single data points with mean ± SEM marked. *$p \leq 0.05$.

6.5.3 Decreased Body Mass in FTO Floxed and FTO Knock-Out Mice Was Caused by a Reduction in Absolute Lean Mass

The body composition of females with the *Fto* gene specifically knocked-out in muscle was studied at 5, 9, 13, 17 and 20 weeks of age using echo Echo-MRI (2.1.8). The results of absolute fat mass and lean mass measurements are presented in **Figure 60** and **Table Appendix 26**. Relative fat and relative lean mass were calculated by dividing fat (lean) mass by total body weight (**Figure 61, Table Appendix 28**). A one-way ANOVA was conducted to determine if there were any differences in the body composition between the genotype groups (**Table Appendix 26** and **Table Appendix 28**).

A one-way ANOVA conducted for each week showed no statistically significant differences in absolute fat mass (**Table Appendix 26**), but significant changes in absolute lean mass were found. Bonferroni post-hoc multiple comparisons (**Table Appendix 27**) revealed that HOMCRE females had decreased absolute lean mass compared to WTWT and WTCRE from 9 weeks of age. Moreover, HOMWT females had significantly lower absolute lean mass compared to WTWT and WTCRE across all weeks studied. This suggested that the reduction in body mass observed in HOMWT and HOMCRE females was due to a reduction in absolute lean mass. Also, the results further supported the link between observed phenotype and floxed *Fto* allele, whether recombined or not.

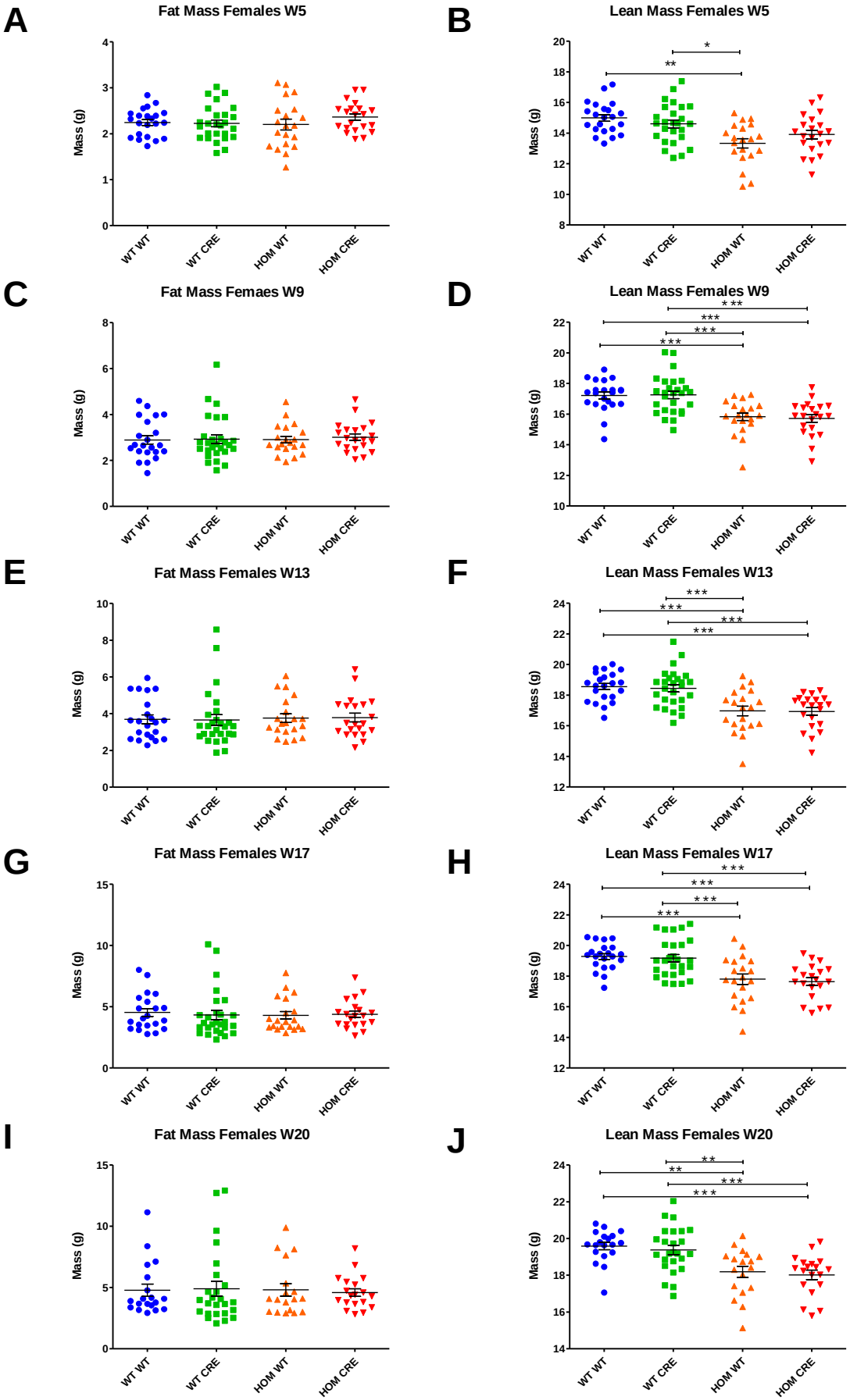
A
Fat Mass Females W5
Mass (g)
WT WT
WT CRE
HOM WT
HOM CRE
B
Lean Mass Females W5
C
Fat Mass Femaes W9
D
Lean Mass Females W9
E
Fat Mass Females W13
F
Lean Mass Females W13
G
Fat Mass Females W17
H
Lean Mass Females W17
I
Fat Mass Females W20
J
Lean Mass Females W20

Figure 60. Absolute Fat Mass and Relative Lean Mass of *Fto* muscle specific knock-out females at 5, 9, 13, 17 and 20 weeks of age. Animals were subjected to Echo-MRI as described in 2.1.8. Data were analysed with one-way ANOVA as described in 6.2.3. Numbers of animals included in each study are listed in WTWT, WTCRE, HOMWT, HOMCRE order: **A**-**B**, 22, 26, 21, 23; **C**-**F**, 22, 27, 20, 21; **G**-**H**, 21, 27, 20, 20; **I-J**, 19, 25, 18, 19. Data are represented by single data points with mean ± SEM marked. *$p \leq 0.05$, **$p \leq 0.01$, ***$p \leq 0.001$.

The differences in lean mass mostly disappeared when data were presented as relative lean mass (**Table Appendix 28**). However, at 5 weeks of age, there was a significant reduction in relative lean mass in HOMWT and HOMCRE females compared to WTWT (**Table Appendix 29**) and a significant increase in relative fat mass in HOMCRE when compared to WTWT females. This shows that absolute lean mass was the main factor that decisively affected body weight, as the effect of lean mass disappeared when corrected for the body weight.

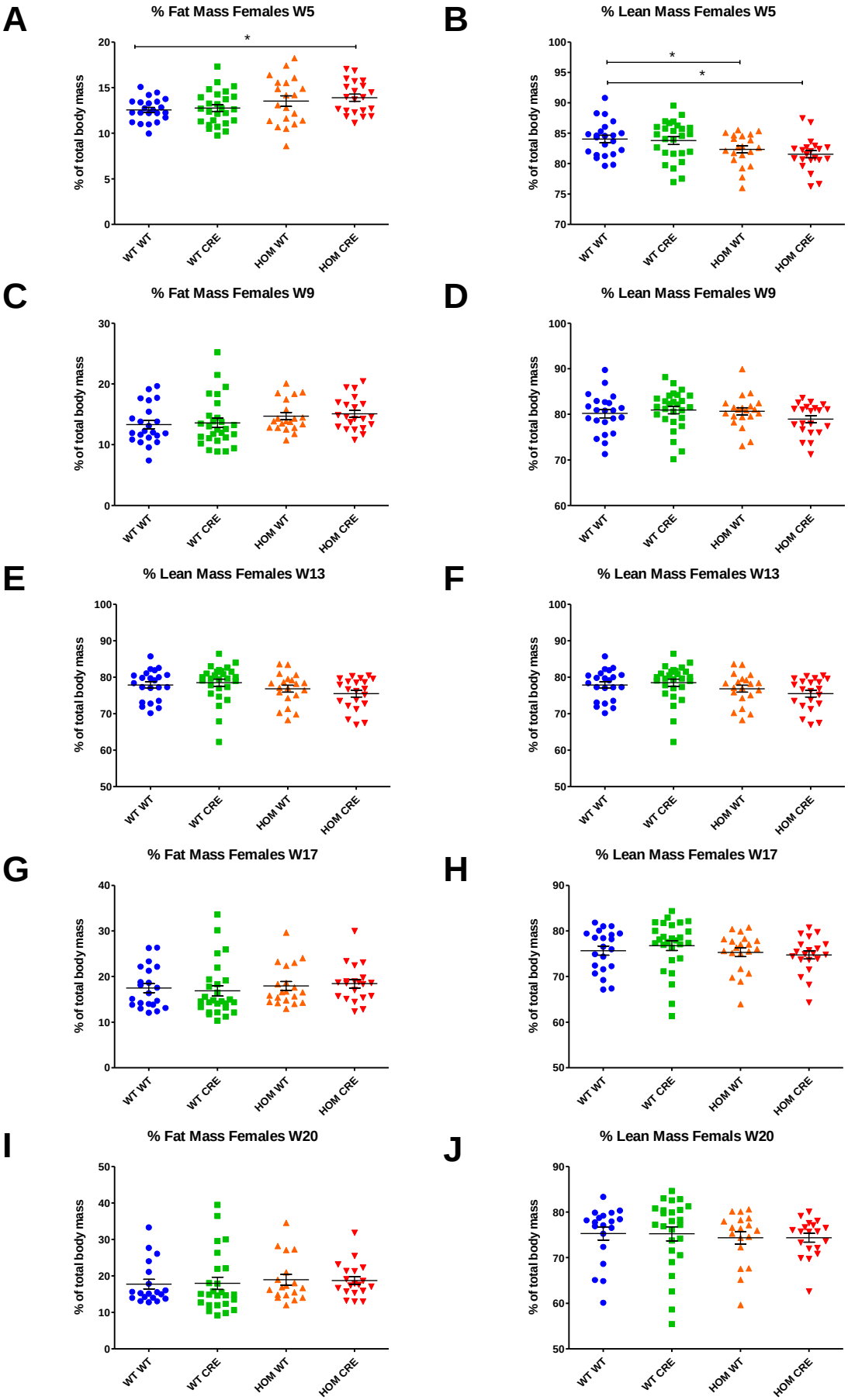
A
% Fat Mass Females W5
% of total body mass
WT WT
WT CRE
HOM WT
HOM CRE
B
% Lean Mass Females W5
C
% Fat Mass Females W9
D
% Lean Mass Females W9
E
% Lean Mass Females W13
F
% Lean Mass Females W13
G
% Fat Mass Females W17
H
% Lean Mass Females W17
I
% Fat Mass Females W20
J
% Lean Mass Femals W20

Figure 61. Relative Fat Mass and Relative Lean Mass of *Fto* muscle specific knock-out females at 5, 9, 13, 17 and 20 weeks of age. Animals were subjected to Echo-MRI as described in 2.1.8. Relative fat/lean mass was calculated by dividing fat/lean mass by total body weight. Data were analysed with one-way ANOVA as described in 6.2.3. Numbers of animals included in each study are listed in WTWT, WTCRE, HOMWT, HOMCRE order: **A**-**B**, 22, 26, 21, 23; **C**-**F**, 22, 27, 20, 21; **G**-**H**, 21, 27, 20, 20; **I-J**, 19, 25, 18, 19. Data are represented by single data points with mean ± SEM marked. *$p \leq 0.05$.

6.5.4 Reduction of Lean Mass Did Not Affect Muscle Strength in Females

Muscle strength was assessed by the grip strength test (2.1.10) at 5, 9, 13, 17 and 20 weeks of age **Figure 62**. Even though a distinct reduction in absolute lean mass was observed in HOMWT and HOMCRE females, there were no differences in the muscle strength between the groups when analysed by one-way ANOVA (homogeneity of variances met), (**Table Appendix 30**).

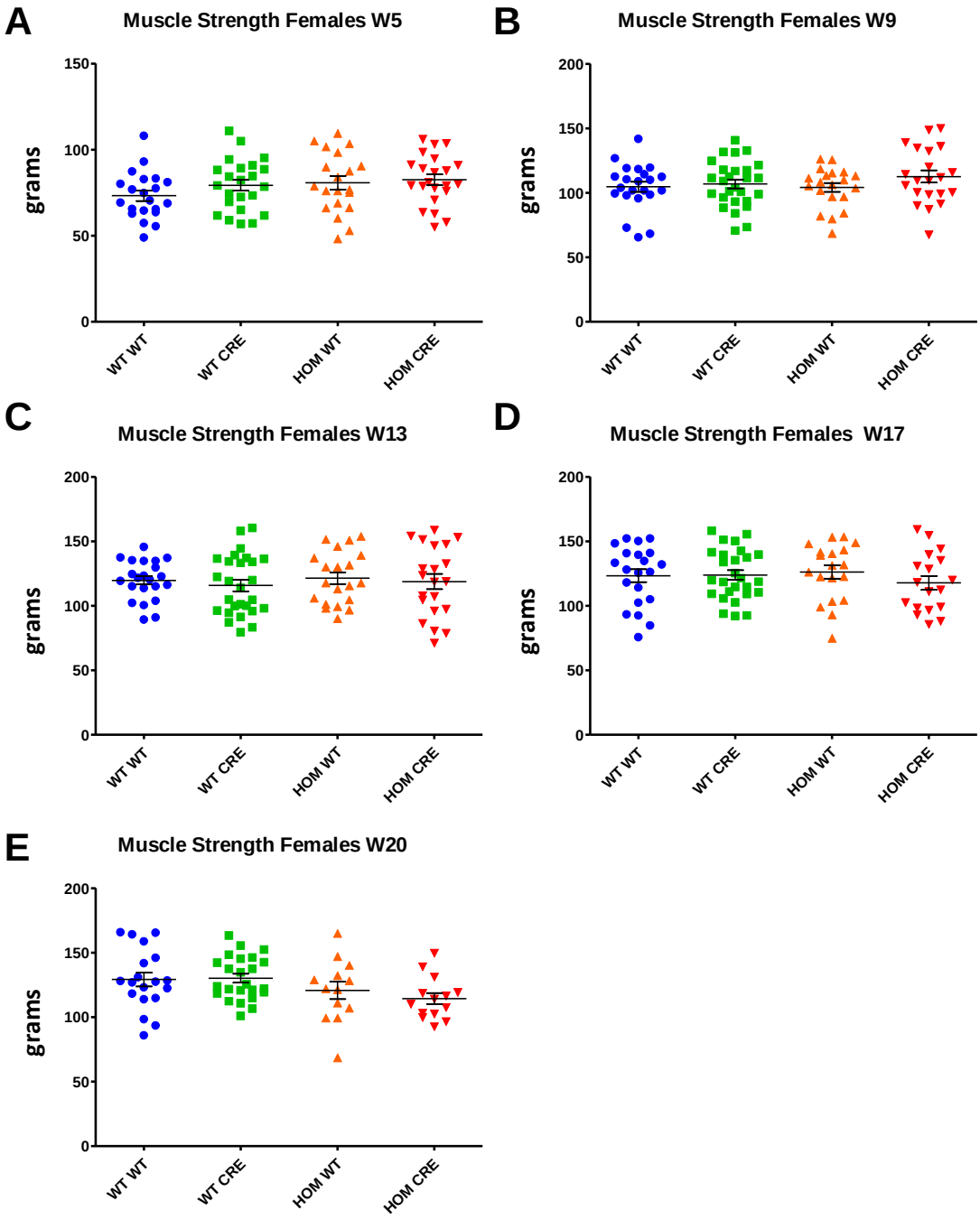

Figure 62. Muscle strength of *Fto* muscle specific knock-out females at 5, 9, 13, 17 and 20 weeks of age. Muscle strength was measured by a grip strength test of combined forelimbs and hind limbs. Each measurement was repeated three times and the average value was calculated (2.1.10). Data were analysed with one-way ANOVA as described in 6.2.3. Numbers of animals included in each study are listed in WTWT, WTCRE, HOMWT, HOMCRE order: **A**, 15, 20, 22, 26; **B**, 20, 25, 19, 24; **C**, 20, 22, 20, 24; **D**, 20, 21, 19, 25; **E**, 16, 19, 10, 16. Data points represent the average value calculated based on three measurements. Total mean ± SEM of each group are marked.

6.5.5 Glucose Homeostasis in Female Mice Is Not Affected by *Fto* Knock-Out

Glucose homeostasis in female mice was assessed by an intraperitoneal glucose tolerance test (IPGTT) (2.1.6) at 16 weeks of age. The average absolute blood glucose levels, individual normalised trials and the area under the curve (AUC) are shown in **Figure 63**. A mixed ANOVA was conducted with Time (0, 60 and 120 minutes) chosen as a Within-Subject Factor and Genotype as a Between Subject Factor. Mauchly's Test of Sphericity indicated that the assumption of sphericity had been violated ($p<0.001$) and Huynh-Feldt correction was used.

There results showed no statistically significant interaction between the genotype and time on the blood glucose level, $F(6, 133.982)= 0.405$, $p =0.854$, partial $\eta^2 = 0.016$ suggesting that genotype had no effect of glucose metabolism in female mice. Analysis of the main effect of genotype also showed no overall significant effect of genotype on glucose homeostasis, $F(3, 76)=0.856$, $p =0.468$, partial $\eta^2 = 0.033$.

Similarly, there were no significant differences in the AUC, as assessed by one-way ANOVA (homogeneity of variances met), $F(3, 76)=0.242$, $p=0.867$), (**Table Appendix 31**).

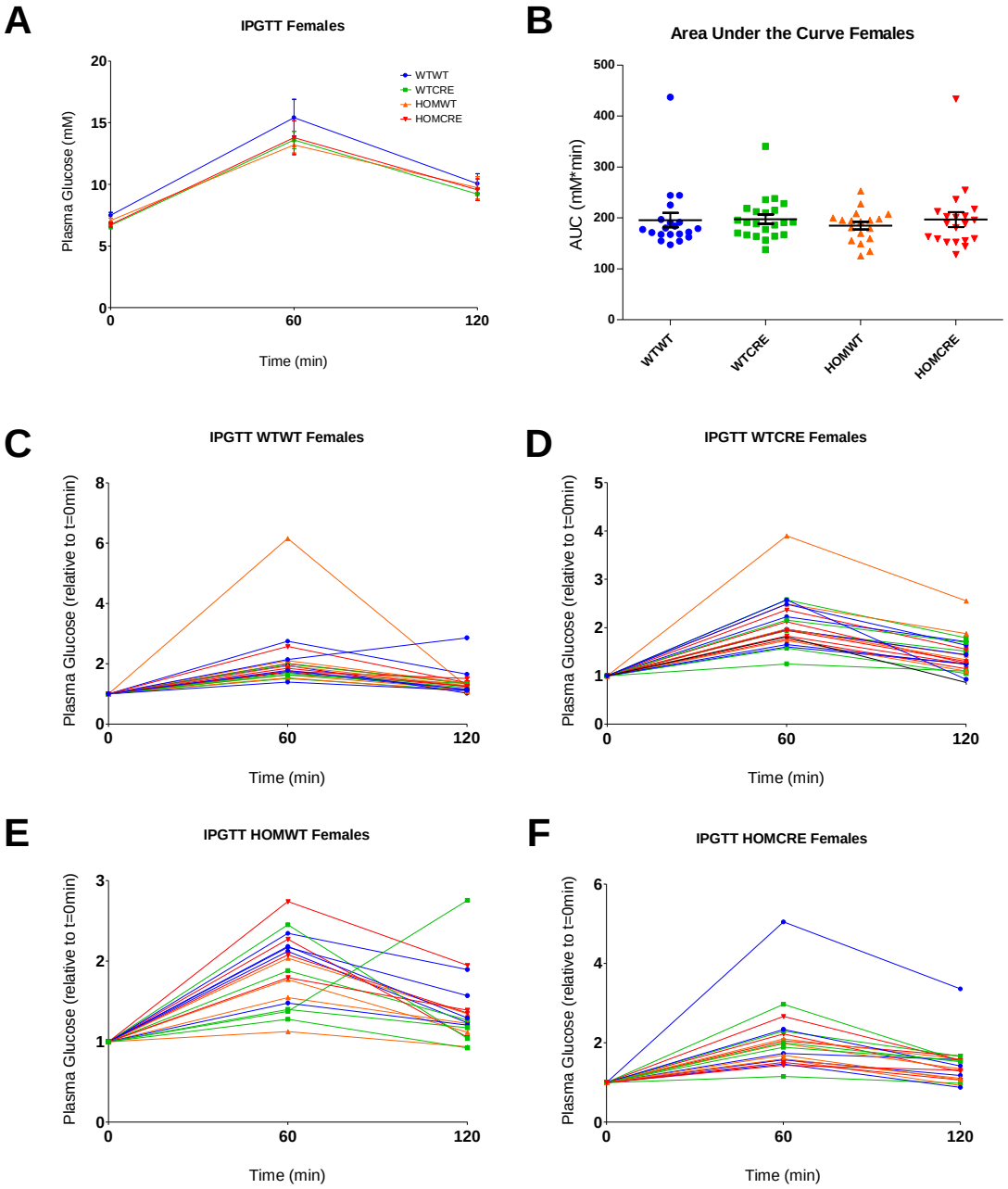

Figure 63. Intraperitoneal glucose tolerance test (IPGTT) and area under the curve (AUC) for *Fto* muscle specific knock-out females at 16 weeks of age. Mice were fasted overnight (16 hours) and blood samples were collected from the tail vein (time 0 min). Subsequently, mice were injected IP with glucose and blood was collected after 60 and 120 min after the injection (2.1.6). Plasma was analysed as described in 2.1.7. **A**, Data were analysed with mixed ANOVA as described in 6.2.4. Data points represent absolute group mean ± SEM. **B**, Data were analysed with one-way ANOVA as described in 6.2.3. Data are represented by single data points with mean ± SEM marked. **C-D**, Individual blood glucose curves normalised to time 0 blood glucose.

6.6 Discussion

6.6.1 Summary

These data show that constitutive deletion of *Fto* specifically in muscle does not influence body weight and body composition in contrast to results obtained following global *Fto* germline knock-out, adult global *Fto* knock-out and in mice globally overexpressing FTO (Church et al. 2010; McMurray et al. 2013). Mice lacking *Fto* in muscle did not show perinatal lethality or any growth abnormalities. Moreover, food intake and glucose homeostasis were unchanged. Lastly, loss of *Fto* in muscle did not decrease skeletal muscle strength. Overall, these results suggest that it is unlikely that effects of FTO on body weight phenotype observed in man and mice are mediated via muscle.

6.6.2 Conditional Loss of *Fto* in Muscle Using *Mck*-Cre

In this study, I used Cre recombinase under the control of the muscle creatine kinase promoter (*Mck*-Cre) (Brüning et al. 1998) to knock-out *Fto* in muscle via Cre/LoxP system (Kos 2004). A strong signal of *Mck* expression in skeletal and cardiac muscle and a weak signal detected in the smooth muscle cells are in line with the previously reported expression of *Mck* in rodents (Johnson, Wold, and Hauschka 1989; Trask and Billadello 1990; Lyons et al. 1991). Given that the expression levels of *Mck* in skeletal muscle were reported to be 10^4 fold higher than in non-muscle tissues, and expression of *Mck* in cardiac muscle were greater only by 2-3 orders of magnitude than in non-muscle tissues (Johnson,

Wold, and Hauschka 1989).Thus, I have primarily tested the effects of *Fto* deletion in skeletal muscle and to a smaller extent in heart.

6.6.3 Effects of Floxed *Fto* Allele

Although I did not identify any changes in the phenotype that could be assigned directly to loss of *Fto* in skeletal muscle, analysis of the collected data revealed various nominal and statistically significant differences in HOMWT and HOMCRE mice (summarised in **Table Appendix 32**).The same direction of observed changes (e.g. increase of relative fat mass and decrease of relative lean mass in males, decrease of absolute lean mass in females) in both of the genotype groups suggests a link between the genotype of these two groups and the observed phenotype. Since HOMWT and HOMCRE are the only groups carrying the floxed *Fto* allele (HOMCRE have recombined while HOMWT have unrecombined alleles), this suggests that the floxed allele carried by these mice might affect their body composition. SNP genotyping of the mice used in this study (data not shown) supports this hypothesis and revealed that both HOMWT and HOMCRE mice have DNA from the 129S1/SvImJ mouse genetic background around the *Fto* locus on chromosome 8.

The presence of 129S1/SvImJ DNA in HOMWT and HOMCRE mice around the LoxP sites flanking exon 3 of *Fto* (location of *Fto* gene in mice chromosome 8; 91.31-91.66 Mb) may explain the phenotypic differences observed in this study. A number of quantitative trait loci (QTL) associated with body weight, body composition and obesity have been identified in the chromosome 8 of C57BL/6J and 129S1/SvImJ mice (Su et al. 2008; Ishimori et al. 2004b; Ishimori et al. 2004a). Strong sex specific effects of some QTLs on body fat have also been highlighted in C57BL/6J x 129S1/SvImJ cross. Moreover phenotypic differences

between C57BL/6J and 129S1/SvImJ strains have been reported (Reed, Bachmanov, and Tordoff 2007; 'MPD-Compare C57BL/6J vs. 129S1/SvImJ' 2015). Mice on 129S1/SvImJ background have increased grip strength which is in line with the results in my male mice (Seburn, Xing, and Burgess 2008). 129S1/SvImJ females have lower lean mass (The Jackson Laboratory 2003; Center for Genome Dynamics (CGD) 2009; Ackert-Bicknell et al. 2008) and lower whole body weight by nearly 2 grams, although not statistically significant in that particular study (Donahue et al. 2004). 129S1/SvImJ males have less relative lean mass (Tordoff and Bachmanov 2002) and more relative fat mass (Center for Genome Dynamics (CGD) 2009; Donahue 2002). All mentioned above differences support findings presented in this chapter.

One explanation for the presence of 129S1/SvImJ DNA comes from the strategy used by Dr Chris Church for generation of the mice with *Fto* exon 3 flanked with LoxP sites (McMurray et al. 2013). First, Church created construct with LoxP sites flanking exon 3 of *Fto* and a FRT flanked neomycin (Neo) resistance cassette. Then, the vector was recombined into embryonic stem (ES) cells from 129S1/SvImJ mice. After selection of the positive clone, the ES cell was injected into the C57BL/6J blastocysts and the obtained chimeras were bred to C57BL/6J mice for germline transmission. Further breeding to C57BL/6J will have eliminated other unlinked ES cell derived 129S1/ScInj DNA. However, 129S1/SvImJ DNA linked to the floxed allele (that was made in 129S1/ScInj ES cells), selected by floxed allele genotype, would be retained in subsequent generations although random recombination events would reduce the size of the 129S1/ScInj interval.

Overall, the genetic basis of C57BL/6J and 129S1/SvImJ mice body composition are complex and this chapter highlights the need for careful design of experiments using animal models and consideration of the genetic background. Importantly, I have included all the

necessary Cre and floxed allele controls in my study, which allowed me to definitively conclude that none of the observed phenotypic differences can account for the loss of the *Fto* gene in muscle and that the reported effects of FTO on body composition are not mediated by an intrinsic muscle FTO effect.

6.6.4 Perinatal Lethality and Growth Retardation

The loss of function mutation (R316Q) in *FTO* in humans (Boissel et al. 2009) as well as global germline loss of *Fto* caused high perinatal lethality and growth retardation (Fischer et al. 2009; McMurray et al. 2013), which was not observed to the same extend when *Fto* was knocked out in adult mice (McMurray et al. 2013). Data in these and other studies clearly demonstrate that FTO is required for normal development and growth. However, absence of perinatal lethality or any growth abnormalities in mice lacking *Fto* in muscle suggest that the effects in man and mice are not mediated by action of FTO in muscle.

However, there is an important factor that should be taken into consideration when interpreting these data. Transcription of endogenous *Mck* begins during the skeletal myoblast differentiation and is detectable in mice only after approximately embryonic day 13 (Lyons et al. 1991). At birth, *Mck* expression levels in rats are around 40%, and the maximal levels are reached by day 10 after birth (Brüning et al. 1998). However, expression of the *Fto* gene is detected already from embryonic day 8.5 onwards (Peters, Ausmeier, and Rüther 1999). This may suggest that the full *Fto* knock-out in muscle in this study was achieved after birth, and FTO might have been present in muscle at early stages of embryonic development. Thus, if FTO plays a role in development (perhaps from early days of embryonic life *in utero*) it is reasonable to suggest that by using *Mck*-Cre and knocking

out *Fto* in muscle at the later stages of embryonic development or around birth, I might have missed the early effects of *Fto* in muscle.

Nevertheless, as the effects on body weight and body composition were reported even when *Fto* was globally deleted in mice at 6 weeks of age (McMurray et al. 2013), there would also have been an effect in my studies if FTO function in muscle was causal in adult mice for the observed traits.

6.6.5 Body Composition

Fto knock-out in muscle did not lead to a reduction in lean mass. This is in contrast with all previously reported global *Fto* knock-out mice models, as well as mice with homozygous dominant loss of function mutation I367F in FTO (Fischer et al. 2009; Church et al. 2009; McMurray et al. 2013; Gao et al. 2010). Recently, the role of FTO in the regulation of cell growth, translation and protein synthesis via amino acid sensing and mTORC1 pathway was proposed, suggesting that loss of FTO deprives cells of amino acids (Cheung et al. 2012; Gulati et al. 2013). Since skeletal muscle stores most of the body's protein mass, loss of FTO in muscle and reduced mTORC1 signalling leading to increased autophagy was suggested as a mechanism causing reduced lean mass (Gulati and Yeo 2013). However, since the muscle *Fto* knock-out did not cause a reduction in lean mass, this does not support a role for FTO in the regulation of protein synthesis and cell growth in muscle cells and suggests that regulation of lean mass by FTO observed in global *Fto* knock-out models is mediated through its action in different tissue(s).

The brain, particularly the hypothalamus, a centre of energy homeostasis (Schwartz et al. 2000; Hall 2010, 845–850; Yeo and Heisler 2012), may be regulating lean mass. However, mediobasal hypothalamic knock-out of *Fto* in adult mice using AAV-Cre did not cause a reduction in lean mass (McMurray et al. 2013), perhaps suggesting a role for other brain regions. Neuronal *Fto* knock-out using *Nestin*-Cre, which resulted in broader loss of *Fto* in the brain, indeed led to reduction of lean mass (Gao et al. 2010). Although, due to the lack of appropriate *Nestin*-Cre control and known body weight and growth retarded phenotype of *Nestin*-Cre line (Harno, Cottrell, and White 2013), the role of brain FTO on lean mass is still unclear.

FTO regulates fat accumulation as a reduction of fat mass was reported in germline global *Fto* knock-out mice (Fischer et al. 2009; McMurray et al. 2013) and mice with a I367F point mutation (Church et al. 2009), although an increase in fat mass was observed in global and brain conditional *Fto* knock-out (Gao et al. 2010) and adult onset *Fto* knock-out (McMurray et al. 2013). However, since no change in fat mass was observed as a consequence of *Fto* knock-out in muscle, this suggests that these effects are not mediated through FTO presence in muscle. This is in line with lack of difference in expression levels of *Fto* mRNA and protein in muscle reported in obese nondiabetic subjects when compared to age matched controls (Bravard et al. 2011).

Recently, expression of FTO was reported to decrease during adipogenesis, inversely affecting global m^6A levels (Zhao et al. 2014). Moreover, knock-down of FTO in pre-adipocytes significantly impaired differentiation suggesting a role of FTO m^6A demethylation activity in adipogenesis. These findings focused attention on the role of FTO in adipogenesis and suggests that loss of FTO activity in pre-adipocytes/adipocytes might be mediating loss of fat mass observed in *Fto* knock-out mouse models (Fischer et al. 2009;

McMurray et al. 2013). It would be interesting to examine the phenotype of mice in which *Fto* was specifically deleted in adipocyte precursor cells during early embryogenesis before adipocyte development, perhaps using a paired-related homeobox 1 (*Prx1*)–Cre, since it is activated in mid-gestation (Cristancho and Lazar 2011).

6.6.6 Muscle FTO and Food Intake

Fto knock-out in muscle did not affect food intake. This contrasted with up-regulated food intake reported in mice where *Fto* was knocked out globally or specifically in brain (Fischer et al. 2009; Gao et al. 2010). This demonstrates that FTO in muscle does not influence energy intake. Perhaps this is not surprising as central nervous system (particularly the hypothalamus), rather than muscle, have been associated with regulation of hunger, appetite and satiety for a long time (Schwartz et al. 2000; Hall 2010, 845–850; Yeo and Heisler 2012).

In common with mice lacking *Fto* in muscle, energy intake was unchanged in mice homozygous for the dominant point mutation I367F in FTO (Church et al. 2009) and adult global *Fto* knock-out mice (McMurray et al. 2013). However, as both of these studies reported effects on body composition, without changes in food intake, this further supports the conclusion that FTO action in muscle does not influence body composition.

6.6.7 Muscle and Glucose Homeostasis

Skeletal muscle is one of the primary tissues in which cells fail to appropriately respond to insulin in insulin resistance condition, which is commonly associated with obesity and type 2 diabetes (T2D) (Teo, Wagers, and Kulkarni 2013). *FTO* risk alleles have also been associated with pathogenesis of T2D (Zeggini et al. 2007; Scott et al. 2007; Zeggini et al. 2008). Recently *Fto* mRNA and protein levels were found to be increased in muscle of T2D patients, although glucose disposal and insulin sensitivity were unaffected (Bravard et al. 2011). Interestingly, global *Fto* knock-out mice had improved insulin sensitivity (Fischer et al. 2009).

However, mice specifically lacking *Fto* in muscle did not have higher plasma glucose levels after an overnight fasting, in contrast to T2D patients (Bravard et al. 2011). Moreover, these mice did not show any signs of change in rate of glucose uptake from the blood as assessed by IPGTT. This supports the lack of change in glucose disposal reported by Bravard et al. and is in line with a lack of correlation of muscle *FTO* levels with insulin sensitivity or secretion (Grunnet et al. 2009). This suggests that FTO in muscle does not influence insulin sensitivity, and changes to *Fto* expression in T2D patients might be a secondary effect. Furthermore, this suggests that improved insulin sensitivity in global *Fto* knock-out-mice was not mediated by muscle.

6.6.8 Effects of FTO on Cardiac and Skeletal Muscle

Cardiac abnormalities were reported in some human individuals with R316Q in FTO (Boissel et al. 2009). Moreover, global *Fto* knock-out in mice was previously reported to

affect cardiac function and reduce heart weight (Carnevali et al. 2014). However, loss of *Fto* in heart did not affect heart weight, suggesting that cardiac dysfunctions observed by Carnevali et al. were not mediated by *Fto* loss in the cardiac muscle itself. Most likely the effects observed in global *Fto* knock-out mice were mediated by the sympathetic nervous system, which regulates heart rate and contractions (Silverthorn and Silverthorn 2009, 379–386). This would be in line with increased sympathetic nervous system activity observed in mice with homozygous mutation I367F in FTO (Church et al. 2009) and increased sympathetic activation in *Fto* germline knock-out mice suggested by Fischer et al. (Fischer et al. 2009).

Although a reduction in muscle mass due to *Fto* deletion has been reported in several studies (Fischer et al. 2009; Church et al. 2009; McMurray et al. 2013; Gao et al. 2010), effects on skeletal muscle strength have never been assessed. Data presented in this chapter suggests that specific *Fto* deletion in muscle does not affect skeletal muscle strength. This is in line with no effect of *Fto* deletion in muscle on muscle mass, as strength of muscle depends mostly on its size (Hall 2010, p.1031). Nevertheless, it would be interesting to investigate whether *Fto* deletion had any effect on muscle fibres or a proportion of glycolytic or oxidative fibres.

6.6.9 Conclusions

Muscle specific loss of *Fto* in mice does not affect body weight or body composition, thus it is unlikely that the action of FTO in muscle plays a role in the obesity phenotype associated with genetic variations in the *FTO* gene in man. Moreover, the genetic background of mice

can affect the body phenotype, thus correct controls must be used to appropriately assess the roles of specific genes on body composition.

7 General Discussion

Less than a decade ago, genome-wide association studies (GWAS) found the first genetic variations associated with obesity in the first intron of the fat mass and obesity associated (*FTO*) gene (Frayling et al. 2007; Scuteri et al. 2007). Since then, the association of *FTO* with obesity has been widely replicated ('Catalog of Published Genome-Wide Association Studies' 2015), and the molecular, cellular and physiological functions of FTO have been studied (Chapter 1).

Until recently, research showed that FTO is exclusively located in the nucleus (Gerken et al. 2007; Church et al. 2009; Fischer et al. 2009; Jia et al. 2011; Berulava et al. 2012) and this subcellular compartment was suggested to facilitate FTO-dependent demethylation of ssRNA and ssDNA (Gerken et al. 2007; Jia et al. 2008; Han et al. 2010; Jia et al. 2011). Also, at the beginning of this study, proteins interacting with FTO were unknown. Moreover, although an effect on body weight, body composition resulting from *FTO* loss or overexpression had been reported in men (Boissel et al. 2009; van den Berg et al. 2010) and mice (Fischer et al. 2009; Gao et al. 2010; Church et al. 2010; McMurray et al. 2013; Tung et al. 2015), the biological mechanisms regulating these effects, and in which tissue, are still poorly defined. Thus, in this study I aimed to broaden our understanding of the role of FTO by examining its functions at the molecular, cellular and whole body level.

Firstly, I investigated the subcellular localisation of FTO. I found that native FTO can be detected in the cytoplasm, and that nuclear FTO is exported through the nuclear membrane during early prophase of mitotic cell division. Based on these findings, I then developed a co-immunoprecipitation (Co-IP) protocol to investigate proteins interacting with native

FTO. I identified a large number of new candidate binding partners (CBPs) of FTO, many of which are involved in RNA post-transcriptional modification and processing. I then went on to confirm that TRIM21, an E3 ubiquitin-protein ligase identified in Co-IP is a real FTO interacting partner and is able to ubiquitinate FTO in cells. However, I found that ubiquitination does not lead to FTO degradation. Moreover, I showed that TRIM21 co-localises with cytoplasmic FTO in p-bodies (foci that regulate mRNA translation and decay), and that TRIM21 mediates accumulation of FTO outside of the nucleus. Additionally, to probe the physiological function of FTO, I created a muscle specific *Fto* knock-out mouse model given the reported effects of FTO loss on lean mass, and found that action of FTO in muscle does not contribute to the body composition phenotype reported in mouse.

Overall, this thesis provides evidence which supports the hypothesis that FTO can act in the cytoplasm, where it may be involved in RNA processing. These functions of FTO may be regulated by TRIM21, either through protein interaction or ubiquitination. Moreover, my data show it is unlikely that FTO-dependent effects on body composition are mediated through action of FTO in skeletal muscle.

7.1 TRIM21 is a Novel Binding Partner Which Affects FTO in Cells

Interaction of FTO with other proteins is likely to affect its molecular and cellular role. TRIM21, an E3 ubiquitin-protein ligase (also known as Sjögren syndrome type A antigen), was pulled down with native FTO in two independent experiments. My experiments showed that TRIM21 interacts with FTO in multiple tissues, mediates ubiquitination of FTO, and influences its cellular localisation. This shows that TRIM21 is a real FTO binding

partner. The possible implications of this interaction are discussed below in relation to the other findings presented in this thesis.

7.2 Nucleocytoplasmic Transport of FTO

Knowledge of the cellular compartment in which FTO is located can provide crucial information about its substrate, binding partners and function. Evidence of FTO being found in the cytoplasm presented in this thesis contradicts that of previous studies reporting exclusive nuclear localisation of FTO (Gerken et al. 2007; Church et al. 2009; Fischer et al. 2009; Jia et al. 2011; Berulava et al. 2012), but is in line with more recent studies that also report cytoplasmic location of FTO (Gulati et al. 2013; Vujovic et al. 2013; Gulati et al. 2014).

In Chapter 3, I showed that FTO is exported from the nucleus through the nuclear membrane. These finding are in common with Vujovic et al. (2013) who observed accumulation of FTO in the cytoplasm in neurons of fasted rats (Vujovic et al. 2013) and support the idea that FTO shuttles between the cytoplasm and the nucleus as proposed by Gulati et al. (Gulati et al. 2014). However, the molecular events regulating this process are yet to be discovered. As predicted by my computational analysis, the nuclear import of FTO may be facilitated by the classical nuclear localisation signal (NLS) and importin α-β pathway. FTO does not contain a nuclear export signal (NES), thus nuclear export may be mediated by an interacting partner of FTO. Exportin 2 (XPO2), a novel FTO binding partner, was suggested as a potential candidate (Gulati et al. 2014). My data demonstrate that overexpression of TRIM21 potentiates the cytoplasmic localisation and reduces the nuclear localisation of FTO. However, I was unable to determine whether this was caused by inhibition of nuclear import, or up-regulation of nuclear export. Since both TRIM21 and FTO

were found to co-localise in the cytoplasm, it seems possible that TRIM21 binds to FTO and silences its NLS, thus preventing FTO from translocating to the nucleus. Identification of region of FTO which is recognised by TRIM21 could help test this hypothesis, however I was unable to determine which domain of FTO interacts with TRIM21 using Co-IP.

It is also possible that TRIM21 influences export of FTO from the nucleus, in which case both proteins would have to interact in the nucleus. In support of this idea, I found staining of overexpressed TRIM21 in the nucleus as well as in the cytoplasm, which is in line with previous studies (Keech, Gordon, and McCluskey 1995; Pourmand et al. 1998; Ben-Chetrit et al. 1988; Kelekar, Saitta, and Keene 1994). Interestingly, TRIM21 was shown to translocate to the nucleus upon exposure to inflammatory mediators including hydrogen peroxide (H_2O_2), nitric oxide (NO) and type 1 interferon (INFα) (Nobuhara et al. 2007; Espinosa et al. 2008; Strandberg et al. 2008). It would be interesting to examine whether TRIM21 would potentiate the presence of FTO in the cytoplasm on exposure to inflammatory mediators.

FTO nuclear export may be associated with its role in mRNA processing (Jia et al. 2011; Jia, Fu, and He 2013; Berulava et al. 2012; Zhao et al. 2014). Perhaps FTO can be exported from the nucleus by interacting with another nuclear protein, which binds to mRNAs following splicing and facilitates their nuclear export. A possible partner could be HNRNPA1, which was identified in one of the FTO pull-down. HNRNPA1, a mRNA binding protein which shuttles between the nucleus and the cytoplasm, is involved in post-splicing events including mRNA export, cap-dependent translation, and also regulation of mRNA stability and translational repression (Guil, Long, and Cáceres 2006). Thus, in future experiments, it would be important to test whether HNRNPA1 (or similar proteins mediating mRNA

export) interact with FTO, and also examine other routes of FTO nuclear export related to post splicing events and mRNA export.

7.3 Is Cytoplasmic FTO Involved in Nutrition Sensing?

The presence of FTO in the cytoplasm supports the idea that FTO acts as a sensor of amino acids and regulates cell growth, mRNA translation and protein synthesis via the mTORC1 pathway (Gulati et al. 2013). It seems probable that the lack of FTO in the cytoplasm, due to loss of the *Fto* gene, compromised the formation and/or stability of the multi-tRNA synthetase complex (MSC) and reduced the translation rate in MEFs reported by Gulati et al. Since the mTORC1 pathway regulates cell growth based on amino acid availability, impaired amino acid sensing due to loss of FTO in the cytoplasm would lead to reduced cell growth and translation, as reported in *Fto* knock-out MEFs (Gulati et al. 2013). However, my data show that deletion of the *Fto* gene in muscle does not cause a reduction in lean mass, suggesting that FTO does not regulate the mTORC1 pathway in muscle.

Further support of a link between the cytoplasmic location of FTO and physiological response to nutrients was suggested by Vujovic et al. who showed that fasting for 48 hours in rats caused translocation of the majority of FTO to the cytoplasm where it accumulated around the outer edge of the nucleus (Vujovic et al. 2013). Up-regulation of *Fto* mRNA and protein expression was also reported. This was observed in neurons of the paraventricular and ventromedial nucleus and lateral hypothalamic area, but not in neurons of the arcuate nucleus (ARC). Interestingly, the effects reported by Vujovic at el. resemble the FTO localisation pattern I observed in cells overexpressing TRIM21. The translocation and accumulation of FTO outside of the nucleus may have been caused by an imbalance in the

relative levels of TRIM21 and FTO. There are no studies examining the role of TRIM21 in nutrient sensing, thus it would be interesting to study whether a 48h fast leads to increased TRIM21 levels in neurons and whether FTO and TRIM21 co-localise in the cytoplasm in these neurons.

7.4 The Relation between FTO and the Cell Cycle

Little is known about the function of FTO in relation to the cell cycle or mitotic cell division. Ingenuity Pathway Analysis (IPA) analysis predicted that the CBPs I identified in the FTO pull-down are involved in the regulation of cellular function and maintenance, as well as the regulation of the cell cycle. However, further work and confirmation of specific interactions is required to clarify whether this is the case.

To broaden our understanding of FTO function in relation to the cell cycle, I examined the subcellular location of FTO at various stages of the cell cycle. Although a dramatic translocation of FTO from the nucleus to the cytoplasm was observed during early prophase, it is not clear whether this process plays a primary role in cell cycle progression or if it is a secondary consequence. Both my immunofluorescence data, and data of others, show that during interphase, the majority of FTO is located in the nucleus in regions of active transcription and pre-mRNA splicing (Jia et al. 2011; Jia, Fu, and He 2013; Berulava et al. 2012; Zhao et al. 2014). The nuclear export of FTO during prophase may suggest that when chromosomes condense, FTO is no longer needed in the nucleus, perhaps because it is involved in gene transcription or RNA post-transcriptional events, and so is transported to the cytoplasm. Although FTO co-localises with TRIM21 in mRNA processing bodies (p-bodies)during interphase, p-bodies disassemble during mitosis (Aizer et al. 2013), hence

the abundance of cytoplasmic FTO cannot be explained by the increased presence of FTO in p-bodies.

Importantly, TRIM21 has been shown to be required for S-phase progression in mammalian cells (Sabile et al. 2006). TRIM21 participates in the ubiquitination of the cyclin-dependent protein kinase inhibitor 1B (CDKN1B, also known as p-27), which leads to its degradation. CDKN1B blocks S-phase progression, and thus its degradation promotes re-entry to the cell cycle. Interestingly, expression of both the *Cdkn1B* and *Cdkn1A* genes were down-regulated in the hypothalamus of mice carrying two extra copies of *Fto* (Merkestein et al. 2014). Moreover, very recently, up-regulated expression of cycline genes *Ccnd1* and *Ccnd3* and increased mitotic clonal expansion was shown in MEFs overexpressing FTO (Merkestein et al. 2015). It would be interesting to examine whether the interaction of FTO with TRIM21 has an effect on TRIM21-mediated S-phase progression in cells.

7.5 Regulation of FTO Protein Levels

FTO protein is ubiquitously expressed throughout the body, mostly at medium and high levels ('The Human Protein Atlas' 2014). Changes in FTO levels have various molecular and cellular effects (Jia et al. 2011; Meyer et al. 2012; Berulava et al. 2012; Gulati et al. 2013; Hess et al. 2013; Karra et al. 2013; Zhao et al. 2014), and were shown to regulate body phenotype in mice (Fischer et al. 2009; McMurray et al. 2013; Gao et al. 2010; Gerken et al. 2007; Church et al. 2010; Tung et al. 2015). Moreover, various stimuli, including nutrition, were reported to influence FTO levels *in vitro* (Cheung et al. 2012; Gan et al. 2013) and *in vivo* (Gerken et al. 2007; Fredriksson et al. 2008; Stratigopoulos et al. 2008; Olszewski et al. 2009; Tung et al. 2010; Wang et al. 2011; Vujovic et al. 2013). Although mechanisms

influencing FTO levels may involve transcriptional control, likely by CUTL1 (Stratigopoulos et al. 2008), protein levels of FTO must inevitably be also controlled by mechanisms leading to its degradation.

Recently, FTO was shown to be rapidly degraded via the ubiquitin and proteasome pathway (Russell and Morgan 2011). Thus, since TRIM21 is an E3 ubiquitin-protein ligase and interacts with FTO in various tissues, it seemed possible that TRIM21 acts as a highly conserved regulator of FTO degradation. However, my data revealed that overexpression of TRIM21 does not promote degradation of FTO. Interestingly, overexpression of TRIM21 in cells seemed to cause the opposite effect, as the native FTO signal in these cells was stronger than in TRIM21-untransfected cells. Thus, although TRIM21 does not affect FTO levels via protein degradation, perhaps it regulates them by protecting FTO from degradation by blocking FTO ubiquitination by another E3 ligase. This further suggests that events leading to the up-regulation or down-regulation of TRIM21 can affect FTO levels and FTO-mediated cellular events.

Given the association between FTO levels and cellular/ whole body phenotype, it would be important to continue to search for E3(s) ligases that regulate FTO degradation or examine other non-proteasomal pathways from FTO degradation. This knowledge, when combined with an understanding of the role of FTO in the regulation of body composition, may lead to the development of compounds that could counteract or potentiate FTO-mediated effects on this phenotype.

7.6 FTO Mediated m^{6}A Demethylation - RNA Processing and RNA Cycle

Although m^{6}A modification in mRNA has been known for 30 years (Jia, Fu, and He 2013), the recent discovery of FTO as the first described m^{6}A demethylase (Jia et al. 2011), stimulated a rapid growth of research in this area and has led to a greater understanding of the role of reversible m^{6}A methylation in RNA processing (Chapter 1, 1.4.9). Such studies also provided the first insights into the biological importance of FTO-mediated m^{6}A demethylation suggesting it plays an important role in alternative splicing (Jia et al. 2011; Berulava et al. 2012; Hess et al. 2013; Karra et al. 2013; Zhao et al. 2014; Shen et al. 2015).

My data indicates that FTO is found in mRNA processing bodies (p-bodies) where it interacts with TRIM21, an enhancer of the decapping enzyme DCP2. This strongly suggests a new level of FTO-mediated regulation of mRNA processing - the translational level. This is supported by recent data suggesting that m^{6}A can affect mRNA stability, and that YTH-family proteins can selectively bind to m^{6}A and transport mRNA to p-bodies (Wang et al. 2014; Fu et al. 2014).

It is not clear what mechanism triggers FTO translocation to p-bodies. FTO is clearly present in the cytoplasm (Gulati et al. 2013; Vujovic et al. 2013; Gulati et al. 2014). Together with my data, showing the increased signal of FTO in the cytoplasm during prophase, this supports the idea of FTO being able to translocate from the nucleus to the cytoplasm. Thus, one possibility is that nuclear FTO can be exported and directed to the p-bodies. Another idea is that following synthesis of FTO in the cytoplasm, FTO is sent directly to p-bodies.

The events regulating TRIM21 translocation to p-bodies are also unknown, although binding or ubiquitination of FTO by TRIM21 may play a role.

However, the question remains - what is the role of FTO-dependent demethylation in p-bodies? TRIM21 was reported to enhance the decapping activity of DCP2 (Yamochi et al. 2008). This suggests a role for TRIM21 in mRNA degradation, because the removal of the mRNA cap by DCP2 is thought to be irreversible and result in mRNA degradation (Franks and Lykke-Andersen 2008). So could FTO further stimulate mRNA degradation? Unpublished data from our group, and that by Gulati et al. showed that loss of *Fto* decreased mRNA translation in MEFs (Gulati et al. 2013). This is in line with data showing that the presence of m^6A is recognised by YTHDF2, which then directs mRNA to p-bodies and leads to mRNA degradation (Wang et al. 2014). Thus, it seems most probable that the presence of FTO, and removal of m^6A, would cause the opposite effect and reduce mRNA degradation. Moreover, lack of FTO led to decreased levels of the proteins encoded by specific mRNAs which are demethylated by FTO, while the levels of these mRNAs increased (Hess et al. 2013). This suggests that these mRNAs were not degraded but stored, which is in line with the capability of p-bodies to stock translationally silenced mRNAs (Parker and Sheth 2007). Given that FTO was also shown to interact with several aminoacyl-tRNA synthetases (AARSs) and to play a role in the formation and/or stability of the multi-tRNA synthetase complex (MSC) (Gulati et al. 2013), this implies that FTO-dependent demethylation of m^6A might rescue translationally repressed mRNAs in p-bodies and initiate their translation.

Overall, I hypothesise that FTO may facilitate the carefully controlled cycling of specific mRNAs between p-bodies (where they are translationally repressed), and polysomes (where they are actively translated). This concept of an mRNA cycle, due to constant competition between translation and repression of mRNA, is becoming widely accepted

(Parker and Sheth 2007; Franks and Lykke-Andersen 2008; Olszewska, Bujarski, and Kurpisz 2012). Overall, data presented in this thesis and recent studies suggest a role for FTO in the complex regulation of gene expression at the mRNA level.

7.7 Is FTO Involved in the Response to Nutrient Mediated Inflammation?

A chronic inflammatory response is now a well-established feature of obesity (Wellen and Hotamisligil 2005; Hotamisligil 2006; Wellen and Thompson 2010). Inflammation emerges as a result of cellular metabolic stress caused by nutrient excess. High levels of nutrients increase oxidative metabolism and elevate production of reactive oxygen species (ROS). This leads to endoplasmic reticulum (ER) stress, and activation of inflammatory pathways, including the NF-κB (nuclear factor kappa-light-chain-enhancer of activated B cells) pathway, which is mainly activated through action of the inhibitor of kappa B kinase (IKK) (Gloire, Legrand-Poels, and Piette 2006).

Interestingly, TRIM21 was shown to down-regulate NF-κB signalling by monoubiquitinating IKKβ, a subunit of IKK (Wada et al. 2009). IKKβ and IKKγ regulate NF-κB signalling through phosphorylation of the inhibitory protein IκBα, which prior to this is bound to NF-κB in the cytoplasm, masking its NLS, and thus preventing NF-κB from translocating to the nucleus and initiating cellular events. Phosphorylation and subsequent ubiquitination of IκBα leads to its degradation, which activates NF-κB signalling. TRIM21-mediated monoubiquitination of IKKβ led to down-regulation of its activity and suppression of NF-κB-dependent gene expression (Wada et al. 2009).

Although in this thesis I focused my research on the direct effects of TRIM21 on FTO, it seems equally probable that FTO can influence the role of TRIM21 by interacting with the NF-κB pathway and intracellular inflammation events related to nutrition. Several lines of evidence support this hypothesis. FTO was shown to regulate translation and the mTORC1 pathway (Gulati et al. 2013), which allows the cell to adapt to up-regulated levels of nutrients and respond to ROS (Wellen and Thompson 2010). Moreover, phosphorylation of AKT (RAC-alpha serine/threonine-protein kinase), whose activation is linked to ROS production (Wellen and Thompson 2010), was reported to be affected in MEFs lacking *Fto* (Osborn et al. 2014). Furthermore, very recently, FTO was linked to the hypothalamic NF-κB signalling (Tung et al. 2015). Tung et al. showed that in the hypothalamus of mice fed on a high fat diet (HFD), the expression of genes in the NF-κB pathway was down-regulated in $Fto^{+/-}$ and $Fto^{-/-}$ mice in a gene-copy-dependent manner, whereas it was up-regulated in control mice. This was not observed in other brain regions or peripheral tissues. Moreover, FTO was identified as a binding partner of TRIP4, a transcriptional coactivator of NF-κB, and was suggested to regulate the specificity of NF-κB transcription in the hypothalamus (Tung et al. 2015).

Overall, the interaction of FTO with TRIM21 found in multiple tissues (including brain) in Co-IP experiments reported in this thesis, and research reporting that both of these proteins are linked to NF-κB signalling strongly suggests a possible association of FTO and TRIM21 interaction (and ubiquitination) with NF-κB signalling. It would therefore be interesting to determine whether *Fto* loss or overexpression influences TRIM21-mediated ubiquitination of IKKβ or suppression of NF-κB-dependent gene expression.

7.8 Which Tissue Mediates the Effects of FTO on Body Composition?

It is clearly evident that global alterations of FTO levels affect body composition (Fischer et al. 2009; Gao et al. 2010; McMurray et al. 2013; Church et al. 2010; Tung et al. 2015). Moreover, mouse and human studies show that mutations in FTO can have similar effects (Boissel et al. 2009; Church et al. 2009). The key question is which tissues are involved in this effect.

Since lean mass and fat mass are most affected by FTO, it seemed reasonable to suggest that FTO plays an important role in either muscle or adipose tissue, or both. To address the first possibility, I generated mice which lacked *Fto* in muscle. However, these mice did not show any phenotypic changes that could be accounted for deletion of *Fto*. Furthermore, a study performed in parallel to mine (by Dr Myrte Merkestein from our group) revealed that deletion of *Fto* in adipose tissue also had no effect on body phenotype. It is important to bear in mind that both of these studies involved the use of Cre recombinase under the control of promoters that are expressed late in embryonic development [muscle creatine kinase~E13 (Lyons et al. 1991), and adiponectin~E15 (Qiao et al. 2012)]. This may be particularly important in the light of recent findings which suggested that FTO plays an important role in the early phase of adipogenesis (Zhao et al. 2014; Merkestein et al. 2015). Further work is required to clarify whether deleting *Fto* before the pre-adipocyte differentiation would affect body composition phenotype *in vivo*.

Although identification of TRIM21 as an interacting partner of FTO does not directly implicate a function in metabolically important tissues, [the highest expression of human

TRIM21 is found in lung, bone marrow, placenta, fallopian tube ('The Human Protein Atlas' 2014)], the link between TRIM21 and inflammatory signalling may provide important clues. The interface between the immune response and metabolic regulation has become apparent as a central homeostatic mechanism, which seems to be triggered predominantly in adipose tissue (particularly visceral fat) and liver (Hotamisligil 2006; Wellen and Hotamisligil 2005). In dietary and genetic obesity, ER stress and expression of inflammatory genes are elevated with increasing adiposity (Hotamisligil 2006; Wellen and Hotamisligil 2005). Both adipocytes and hepatocytes are in close proximity to immune cells as well as blood vessels, and form networks of interaction with muscle and pancreas, but also other tissues. Thus, since FTO and TRIM21 interaction was identified in liver cells, I believe it would be interesting to investigate effects of *Fto* loss or overexpression in this tissue.

Recent research which suggests that nutritional excess induces an inflammatory response mediated by NF-κB and IKKβ in the hypothalamus (Tang, Purkayastha, and Cai 2015), and data from *Fto* knock-out mice on a HFD, which showed down-regulation of NF-κB exclusively in the hypothalamus (Tung et al. 2015), supports the idea that the hypothalamus is crucial in mediating FTO regulation of body phenotype. Earlier research also suggested links between hypothalamic FTO and energy homeostasis (Gerken et al. 2007; Stratigopoulos et al. 2008; Olszewski et al. 2009; P. Wang et al. 2011; Tung et al. 2010; Vujovic et al. 2013; Tung et al. 2015; McTaggart et al. 2011). Interestingly, loss of *Fto* in the mediobasal hypothalamus of adult mice using Adeno-Associated Virus encoding Cre recombinase did not affect body composition (McMurray et al. 2013). Perhaps a specific *Fto* knock-out in the hypothalamus early on during development would provide more insight.

7.9 Future Directions

The research on FTO in the last decade clearly demonstrated a role of FTO on body composition. Moreover, the search for the molecular and cellular mechanism of FTO-mediated obesity has given insight into some fascinating, and perhaps unexpected functions. In this thesis, I have presented data that further suggest new roles of FTO. However, how these functions (and those suggested by others) may be linked together, but how they lead to obesity in humans remains unknown.

It would be important to further examine the role of cytoplasmic FTO and study the mechanisms regulating nucleocytoplasmic trafficking of FTO. This could be achieved by using fluorescent imaging techniques that allow monitoring of protein movements in living cells. Moreover, given the relation between FTO subcellular localisation and nutrient availability, it would be interesting to examine the subcellular localisation of FTO in cells but also peripheral tissues, and regions of the CNS in mice on various feeding regimes, diets or environmental stimuli.

The data on the TRIM21-FTO interaction suggested a new cellular role for FTO. It would be beneficial to continue the search for novel FTO binding partners. This should involve native FTO, and could be based on animal tissues. This approach could be repeated on animals challenged with a high fat diet or inflammatory mediators, and analysis of FTO binding partners could reveal how FTO signalling pathway adapts to these stimuli.

Moreover, TRIM21 is currently the only know protein to modify FTO post-translationally. Given the possible regulatory roles of post-translational modifications (PTMs), and database records demonstrating numerous PTM sites of FTO, in the future research, it will be important to not only study FTO cellular localisation, functions and life-cycle, but also examine the effects of various PTMs on these aspects of the biological role of FTO.

Undoubtedly, FTO acts as a Fe (II) and 2OG oxygenase and is expressed throughout the body. The investigation of the role of FTO catalytic activity *in vivo* will most likely provide crucial insight into its function. This could be achieved by generating mice models which express a catalytic inactive form of FTO. It would be interesting to see if these mice show a similar phenotype to humans with the catalytic null mutation or with mice lacking *Fto* globally. If a high frequency of lethality would be observed, perhaps inactivation of the catalytic activity in later stage of development, or in specific tissues, would lead to improved viability. Depending of the outcome of such a study it could be followed up by examination of the effects of chemical compounds which bind to the FTO active site. This could lead in the future to the development of therapies for obese patients.

FTO molecular function is increasingly being linked with mRNA epigenetics through demethylation of m^6A. To understand the physiological effects of this phenomenon on body composition, it is crucial to know which genes are affected. This could be addressed by global analysis of the m^6A epitranscriptome, perhaps comparing wild type mice with mice with *Fto* overexpressed and deleted. A similar study has been performed on midbrain and striatum from *Fto* knock-out mice, and led to the identification of interesting transcripts. High-throughput analysis of other tissues is necessary to uncover the full role of m^6A modification in these mice. Another approach would be to use cross-linking immunoprecipitation with an anti-FTO antibody combined with high-throughput

sequencing (CLIP-Seq) to look specifically at transcripts demethylated by FTO. Once the genes affected by FTO are identified, the next step would be to understand what triggers the FTO-mediated regulation of their expression. Could it be exposure to environmental factors related to obesity, including nutrition excess or inflammatory response? Or could the abundance of FTO protein be related to genetic variations?

Finally, the tissue mediating the effects of FTO on body composition remains unknown. Thus, it is important to continue to search (perhaps starting with *Fto* knock-out in pre-adipocytes). Although caution must be taken when designing each mouse model and necessary control groups must be included in each study.

References

Aas, Per Arne, Marit Otterlei, Pål Ø Falnes, Cathrine B. Vågbø, Frank Skorpen, Mansour Akbari, Ottar Sundheim, et al. 2003. 'Human and Bacterial Oxidative Demethylases Repair Alkylation Damage in Both RNA and DNA.' *Nature* 421 (6925): 859–63. doi:10.1038/nature01363.

Ackert-Bicknell, C, WG Beamer, CJ Rosen, and JP Sundberg. 2008. 'MPD - Phenotype Project / Data Set: Ackert1.' *Aging Study: Bone Mineral Density and Body Composition of 32 Inbred Strains of Mice.* http://phenome.jax.org/db/q?rtn=projects/details&sym=Ackert1.

Adeyemo, Adebowale, Guanjie Chen, Jie Zhou, Daniel Shriner, Ayo Doumatey, Hanxia Huang, and Charles Rotimi. 2010. 'FTO Genetic Variation and Association with Obesity in West Africans and African Americans.' *Diabetes* 59 (6): 1549–54. doi:10.2337/db09-1252.

Aizer, Adva, Pinhas Kafri, Alon Kalo, and Yaron Shav-Tal. 2013. 'The P Body Protein Dcp1a Is Hyper-Phosphorylated during Mitosis.' *PloS One* 8 (1): e49783. doi:10.1371/journal.pone.0049783.

Alberts, Bruce, Alexander Johnson, Julian Lewis, Martin Raff, Keith Roberts, and Peter Walter. 2002. *Molecular Biology of the Cell*. 4th ed. Garland Science.

Andreasen, Camilla H., Kirstine L. Stender-Petersen, Mette S. Mogensen, Signe S. Torekov, Lise Wegner, Gitte Andersen, Arne L. Nielsen, et al. 2008. 'Low Physical Activity Accentuates the Effect of the FTO rs9939609 Polymorphism on Body Fat Accumulation.' *Diabetes* 57 (1): 95–101. doi:10.2337/db07-0910.

'Antibody Labelling and Immobilization Sites.' 2015. Accessed March 11. https://www.lifetechnologies.com/gr/en/home/life-science/protein-biology/protein-biology-learning-center/protein-biology-resource-library/pierce-protein-methods/antibody-labeling-immobilization-sites.html.

Attaoua, Redha, Samira Ait El Mkadem, Serban Radian, Simona Fica, Felicia Hanzu, Alice Albu, Monica Gheorghiu, Mihai Coculescu, and Florin Grigorescu. 2008. 'FTO Gene Associates to Metabolic Syndrome in Women with Polycystic Ovary Syndrome.' *Biochemical and Biophysical Research Communications* 373 (2): 230–34. doi:10.1016/j.bbrc.2008.06.039.

Balthasar, Nina, Louise T. Dalgaard, Charlotte E. Lee, Jia Yu, Hisayuki Funahashi, Todd Williams, Manuel Ferreira, et al. 2005. 'Divergence of Melanocortin Pathways in the Control of Food Intake and Energy Expenditure.' *Cell* 123 (3): 493–505. doi:10.1016/j.cell.2005.08.035.

Barber, T. M., A. J. Bennett, C. J. Groves, U. Sovio, A. Ruokonen, H. Martikainen, A. Pouta, et al. 2008. 'Association of Variants in the Fat Mass and Obesity Associated (FTO) Gene with Polycystic Ovary Syndrome.' *Diabetologia* 51 (7): 1153–58. doi:10.1007/s00125-008-1028-6.

Ben-Chetrit, E., E. K. Chan, K. F. Sullivan, and E. M. Tan. 1988. 'A 52-kD Protein Is a Novel Component of the SS-A/Ro Antigenic Particle.' *The Journal of Experimental Medicine* 167 (5): 1560–71.

Berentzen, T., S. I. I. Kring, C. Holst, E. Zimmermann, T. Jess, T. Hansen, O. Pedersen, S. Toubro, A. Astrup, and T. I. A. Sørensen. 2008. 'Lack of Association of Fatness-Related FTO Gene Variants with Energy Expenditure or Physical Activity.' *The Journal of Clinical Endocrinology and Metabolism* 93 (7): 2904–8. doi:10.1210/jc.2008-0007.

Berggård, Tord, Sara Linse, and Peter James. 2007. 'Methods for the Detection and Analysis of Protein-Protein Interactions.' *Proteomics* 7 (16): 2833–42. doi:10.1002/pmic.200700131.

Bernales, Sebastián, Feroz R. Papa, and Peter Walter. 2006. 'Intracellular Signaling by the Unfolded Protein Response.' *Annual Review of Cell and Developmental Biology* 22: 487–508. doi:10.1146/annurev.cellbio.21.122303.120200.

Berndt, Sonja I., Stefan Gustafsson, Reedik Mägi, Andrea Ganna, Eleanor Wheeler, Mary F. Feitosa, Anne E. Justice, et al. 2013. 'Genome-Wide Meta-Analysis Identifies 11 New Loci for Anthropometric Traits and Provides Insights into Genetic Architecture.' *Nature Genetics* 45 (5): 501–12. doi:10.1038/ng.2606.

Berulava, Tea, and Bernhard Horsthemke. 2010. 'The Obesity-Associated SNPs in Intron 1 of the FTO Gene Affect Primary Transcript Levels.' *European Journal of Human Genetics: EJHG* 18 (9): 1054–56. doi:10.1038/ejhg.2010.71.

Berulava, Tea, Matthias Ziehe, Ludger Klein-Hitpass, Emil Mladenov, Jürgen Thomale, Ulrich Rüther, and Bernhard Horsthemke. 2012. 'FTO Levels Affect RNA Modification and the Transcriptome.' *European Journal of Human Genetics: EJHG*, August. doi:10.1038/ejhg.2012.168.

Bhanji, Rahima A., Theophany Eystathioy, Edward K. L. Chan, Donald B. Bloch, and Marvin J. Fritzler. 2007. 'Clinical and Serological Features of Patients with Autoantibodies to GW/P Bodies.' *Clinical Immunology (Orlando, Fla.)* 125 (3): 247–56. doi:10.1016/j.clim.2007.07.016.

Bjørnstad, Linn G., Trine J. Meza, Marit Otterlei, Solveig M. Olafsrud, Leonardo A. Meza-Zepeda, and Pål Ø. Falnes. 2012. 'Human ALKBH4 Interacts with Proteins Associated with Transcription.' *PLoS ONE* 7 (11): e49045. doi:10.1371/journal.pone.0049045.

Boissel, Sarah, Orit Reish, Karine Proulx, Hiroko Kawagoe-Takaki, Barbara Sedgwick, Giles S H Yeo, David Meyre, et al. 2009. 'Loss-of-Function Mutation in the Dioxygenase-Encoding FTO Gene Causes Severe Growth Retardation and Multiple Malformations.' *American Journal of Human Genetics* 85 (1): 106–11. doi:10.1016/j.ajhg.2009.06.002.

Bollepalli, Sureka, Lawrence M. Dolan, Ranjan Deka, and Lisa J. Martin. 2010. 'Association of FTO Gene Variants with Adiposity in African-American Adolescents.' *Obesity (Silver Spring, Md.)* 18 (10): 1959–63. doi:10.1038/oby.2010.82.

Bonifacino, Juan S., and Esteban C. Dell'Angelica. 2001. 'Immunoprecipitation.' In *Current Protocols in Cell Biology*. John Wiley & Sons, Inc. http://onlinelibrary.wiley.com/doi/10.1002/0471143030.cb0702s00/abstract.

Borden, K. L. 2000. 'RING Domains: Master Builders of Molecular Scaffolds?' *Journal of Molecular Biology* 295 (5): 1103–12. doi:10.1006/jmbi.1999.3429.

Boron, Walter F., and Emile L. Boulpaep. 2008. *Medical Physiology*. Elsevier Health Sciences.

Bouchard, C., A. Tremblay, J. P. Després, A. Nadeau, P. J. Lupien, G. Thériault, J. Dussault, S. Moorjani, S. Pinault, and G. Fournier. 1990. 'The Response to Long-Term Overfeeding in Identical Twins.' *The New England Journal of Medicine* 322 (21): 1477–82. doi:10.1056/NEJM199005243222101.

Bradfield, Jonathan P., H. Rob Taal, Nicholas J. Timpson, André Scherag, Cecile Lecoeur, Nicole M. Warrington, Elina Hypponen, et al. 2012. 'A Genome-Wide Association Meta-Analysis Identifies New Childhood Obesity Loci.' *Nature Genetics* 44 (5): 526–31. doi:10.1038/ng.2247.

Bravard, Amélie, Etienne Lefai, Emmanuelle Meugnier, Sandra Pesenti, Emmanuel Disse, Julien Vouillarmet, Nöel Peretti, et al. 2011. 'FTO Is Increased in Muscle during Type 2 Diabetes, and Its Overexpression in Myotubes Alters Insulin Signaling, Enhances Lipogenesis and ROS Production, and Induces Mitochondrial Dysfunction.' *Diabetes* 60 (1): 258–68. doi:10.2337/db10-0281.

Bressler, Jan, Myriam Fornage, Ellen W. Demerath, David S. Knopman, Keri L. Monda, Kari E. North, Alan Penman, Thomas H. Mosley, and Eric Boerwinkle. 2013. 'Fat Mass and Obesity Gene and Cognitive Decline: The Atherosclerosis Risk in Communities Study.' *Neurology* 80 (1): 92–99. doi:10.1212/WNL.0b013e3182768910.

Brüning, J. C., M. D. Michael, J. N. Winnay, T. Hayashi, D. Hörsch, D. Accili, L. J. Goodyear, and C. R. Kahn. 1998. 'A Muscle-Specific Insulin Receptor Knockout Exhibits Features of

the Metabolic Syndrome of NIDDM without Altering Glucose Tolerance.' *Molecular Cell* 2 (5): 559–69.

Burden, David W. 2012. 'Guide to the Disruption of Biological Samples.' Guide. http://opsdiagnostics.com. http://opsdiagnostics.com/applications/homogenization_guide_download.htm.

Burton, Paul R., David G. Clayton, Lon R. Cardon, Nick Craddock, Panos Deloukas, Audrey Duncanson, Dominic P. Kwiatkowski, et al. 2007. 'Genome-Wide Association Study of 14,000 Cases of Seven Common Diseases and 3,000 Shared Controls.' *Nature* 447 (7145): 661–78. doi:10.1038/nature05911.

Calvo, Jennifer A., Lisiane B. Meira, Chun-Yue I. Lee, Catherine A. Moroski-Erkul, Nona Abolhassani, Koli Taghizadeh, Lindsey W. Eichinger, et al. 2012. 'DNA Repair Is Indispensable for Survival after Acute Inflammation.' *The Journal of Clinical Investigation* 122 (7): 2680–89. doi:10.1172/JCI63338.

Carnevali, Luca, Gallia Graiani, Stefano Rossi, Mumna Al Banchaabouchi, Emilio Macchi, Federico Quaini, Nadia Rosenthal, and Andrea Sgoifo. 2014. 'Signs of Cardiac Autonomic Imbalance and Proarrhythmic Remodeling in FTO Deficient Mice.' *PLoS ONE* 9 (4): e95499. doi:10.1371/journal.pone.0095499.

'Catalog of Published Genome-Wide Association Studies.' 2015. Accessed February 4. http://www.genome.gov/gwastudies/.

Cecil, Joanne E, Roger Tavendale, Peter Watt, Marion M Hetherington, and Colin N A Palmer. 2008. 'An Obesity-Associated FTO Gene Variant and Increased Energy Intake in Children.' *The New England Journal of Medicine* 359 (24): 2558–66. doi:10.1056/NEJMoa0803839.

'CELLO.' 2014. Accessed November 29. http://cello.life.nctu.edu.tw/.

Center for Genome Dynamics (CGD). 2009. 'MPD - Phenotype Project / Data Set: CGDpheno1.' *Multi-System Survey of Mouse Physiology in 72 Inbred Strains of Mice (ANOVA-Adjusted Methodology).* http://phenome.jax.org/db/q?rtn=projects/details&sym=CGDpheno1.

Chambers, John C., Paul Elliott, Delilah Zabaneh, Weihua Zhang, Yun Li, Philippe Froguel, David Balding, James Scott, and Jaspal S. Kooner. 2008. 'Common Genetic Variation near MC4R Is Associated with Waist Circumference and Insulin Resistance.' *Nature Genetics* 40 (6): 716–18. doi:10.1038/ng.156.

Chan, E K, J C Hamel, J P Buyon, and E M Tan. 1991. 'Molecular Definition and Sequence Motifs of the 52-kD Component of Human SS-A/Ro Autoantigen.' *Journal of Clinical Investigation* 87 (1): 68–76.

Chen, B. J., P. Carroll, and L. Samson. 1994. 'The Escherichia Coli AlkB Protein Protects Human Cells against Alkylation-Induced Toxicity.' *Journal of Bacteriology* 176 (20): 6255–61.

Chen, Jiang, Christine Laclef, Alejandra Moncayo, Elizabeth R. Snedecor, Ning Yang, Li Li, Ken-Ichi Takemaru, Ralf Paus, Sylvie Schneider-Maunoury, and Richard A. Clark. 2015. 'The Ciliopathy Gene Rpgrip1l Is Essential for Hair Follicle Development.' *The Journal of Investigative Dermatology* 135 (3): 701–9. doi:10.1038/jid.2014.483.

Cheung, M K, P Gulati, S O'Rahilly, and G S H Yeo. 2012. 'FTO Expression Is Regulated by Availability of Essential Amino Acids.' *International Journal of Obesity (2005)*, May. doi:10.1038/ijo.2012.77.

Cho, Yoon Shin, Min Jin Go, Young Jin Kim, Jee Yeon Heo, Ji Hee Oh, Hyo-Jeong Ban, Dankyu Yoon, et al. 2009. 'A Large-Scale Genome-Wide Association Study of Asian Populations Uncovers Genetic Factors Influencing Eight Quantitative Traits.' *Nature Genetics* 41 (5): 527–34. doi:10.1038/ng.357.

Church, Chris, Sheena Lee, Eleanor A L Bagg, James S McTaggart, Robert Deacon, Thomas Gerken, Angela Lee, et al. 2009a. 'A Mouse Model for the Metabolic Effects of the Human Fat Mass and Obesity Associated FTO Gene.' *PLoS Genetics* 5 (8): e1000599. doi:10.1371/journal.pgen.1000599.

Church, Chris, Sheena Lee, Eleanor A. L. Bagg, James S. McTaggart, Robert Deacon, Thomas Gerken, Angela Lee, et al. 2009b. 'A Mouse Model for the Metabolic Effects of the Human Fat Mass and Obesity Associated FTO Gene' 5 (8). doi:10.1371/journal.pgen.1000599.

Church, Chris, Lee Moir, Fiona McMurray, Christophe Girard, Gareth T Banks, Lydia Teboul, Sara Wells, et al. 2010. 'Overexpression of Fto Leads to Increased Food Intake and Results in Obesity.' *Nat Genet* 42 (12): 1086–92. doi:10.1038/ng.713.

Clement, Karine, and Thorkild I. A. Sorensen, eds. 2007. *Obesity: Genomics and Postgenomics*. 1 edition. New York: CRC Press.

'ClustalW2, Multiple Sequence Alignment, EMBL-EBI.' 2015. Accessed March 30. http://www.ebi.ac.uk/Tools/msa/clustalw2/.

Cook, Atlanta, Fulvia Bono, Martin Jinek, and Elena Conti. 2007. 'Structural Biology of Nucleocytoplasmic Transport.' *Annual Review of Biochemistry* 76: 647–71. doi:10.1146/annurev.biochem.76.052705.161529.

Cooper, Geoffrey M. 2000. *The Cell*. 2nd ed. Sinauer Associates.

Cotsapas, Chris, Elizabeth K. Speliotes, Ida J. Hatoum, Danielle M. Greenawalt, Radu Dobrin, Pek Y. Lum, Christine Suver, et al. 2009. 'Common Body Mass Index-Associated Variants Confer Risk of Extreme Obesity.' *Human Molecular Genetics* 18 (18): 3502–7. doi:10.1093/hmg/ddp292.

Cristancho, Ana G., and Mitchell A. Lazar. 2011. 'Forming Functional Fat: A Growing Understanding of Adipocyte Differentiation.' *Nature Reviews Molecular Cell Biology* 12 (11): 722–34. doi:10.1038/nrm3198.

Delaney, James C., and John M. Essigmann. 2004. 'Mutagenesis, Genotoxicity, and Repair of 1-Methyladenine, 3-Alkylcytosines, 1-Methylguanine, and 3-Methylthymine in alkB Escherichia Coli.' *Proceedings of the National Academy of Sciences of the United States of America* 101 (39): 14051–56. doi:10.1073/pnas.0403489101.

Delaney, James C., Lisa Smeester, Cintyu Wong, Lauren E. Frick, Koli Taghizadeh, John S. Wishnok, Catherine L. Drennan, Leona D. Samson, and John M. Essigmann. 2005. 'AlkB Reverses Etheno DNA Lesions Caused by Lipid Oxidation in Vitro and in Vivo.' *Nature Structural & Molecular Biology* 12 (10): 855–60. doi:10.1038/nsmb996.

Delous, Marion, Lekbir Baala, Rémi Salomon, Christine Laclef, Jeanette Vierkotten, Kàlmàn Tory, Christelle Golzio, et al. 2007. 'The Ciliary Gene RPGRIP1L Is Mutated in Cerebello-Oculo-Renal Syndrome (Joubert Syndrome Type B) and Meckel Syndrome.' *Nature Genetics* 39 (7): 875–81. doi:10.1038/ng2039.

de Recondo, A M, and J Abadiedebat. 1976. 'Regenerating Rat Liver DNA Polymerases: Disimilitude or Relationship between Nuclear and Cytoplasmic Enzymes?' *Nucleic Acids Research* 3 (8): 1823–37.

Dina, Christian, David Meyre, Sophie Gallina, Emmanuelle Durand, Antje Korner, Peter Jacobson, Lena M S Carlsson, et al. 2007. 'Variation in FTO Contributes to Childhood Obesity and Severe Adult Obesity.' *Nat Genet* 39 (6): 724–26. doi:10.1038/ng2048.

Dominissini, Dan, Sharon Moshitch-Moshkovitz, Schraga Schwartz, Mali Salmon-Divon, Lior Ungar, Sivan Osenberg, Karen Cesarkas, et al. 2012. 'Topology of the Human and Mouse m6A RNA Methylomes Revealed by m6A-Seq.' *Nature* 485 (7397): 201–6. doi:10.1038/nature11112.

Donahue, L. 2002. 'MPD - Phenotype Project / Data Set: Donahue1.' *Bone Mineral Density, Body Composition, and Craniofacial Characterization in 30 Inbred Strains of Mice.* http://phenome.jax.org/db/q?rtn=projects/details&sym=Donahue1.

Donahue, L, WG Beamer, MA Bogue, and GA Churchill. 2004. 'MPD - Phenotype Project / Data Set: Donahue2.' *Characterization of Skeletal Geometry and Bone Strength in 10 Inbred Strains of Mice.* http://phenome.jax.org/db/q?rtn=projects/details&sym=Donahue2.

Dorajoo, R., A. I. F. Blakemore, X. Sim, R. T.-H. Ong, D. P. K. Ng, M. Seielstad, T.-Y. Wong, et al. 2012. 'Replication of 13 Obesity Loci among Singaporean Chinese, Malay and Asian-

Indian Populations.' *International Journal of Obesity (2005)* 36 (1): 159–63. doi:10.1038/ijo.2011.86.

Do, Ron, Swneke D. Bailey, Katia Desbiens, Alexandre Belisle, Alexandre Montpetit, Claude Bouchard, Louis Pérusse, Marie-Claude Vohl, and James C. Engert. 2008. 'Genetic Variants of FTO Influence Adiposity, Insulin Sensitivity, Leptin Levels, and Resting Metabolic Rate in the Quebec Family Study.' *Diabetes* 57 (4): 1147–50. doi:10.2337/db07-1267.

Duncan, Tod, Sarah C. Trewick, Pertti Koivisto, Paul A. Bates, Tomas Lindahl, and Barbara Sedgwick. 2002. 'Reversal of DNA Alkylation Damage by Two Human Dioxygenases.' *Proceedings of the National Academy of Sciences of the United States of America* 99 (26): 16660–65. doi:10.1073/pnas.262589799.

'Dynabeads® Co-Immunoprecipitation Kit.' 2014. Accessed October 26. http://www.lifetechnologies.com/uk/en/home/references/protocols/proteins-expression-isolation-and-analysis/antibody-protocol/dynabeads-co-immunoprecipitation-kit.html.

Elks, Cathy E., John R. B. Perry, Patrick Sulem, Daniel I. Chasman, Nora Franceschini, Chunyan He, Kathryn L. Lunetta, et al. 2010. 'Thirty New Loci for Age at Menarche Identified by a Meta-Analysis of Genome-Wide Association Studies.' *Nature Genetics* 42 (12): 1077–85. doi:10.1038/ng.714.

'EMBL-EBI Expression Atlast.' 2014. Accessed October 13. http://www.ebi.ac.uk/gxa/experiments/E-MTAB-1733?_specific=on&queryFactorType=ORGANISM_PART&queryFactorValues=&geneQuery=TRIM21&exactMatch=true.

'Ensembl Genome Browser.' 2015. Accessed February 11. http://www.ensembl.org/index.html.

Espinosa, Alexander, Janosch Hennig, Aurélie Ambrosi, Madhanagopal Anandapadmanaban, Martina Sandberg Abelius, Yi Sheng, Filippa Nyberg, Cheryl H. Arrowsmith, Maria Sunnerhagen, and Marie Wahren-Herlenius. 2011. 'Anti-Ro52 Autoantibodies from Patients with Sjögren's Syndrome Inhibit the Ro52 E3 Ligase Activity by Blocking the E3/E2 Interface.' *The Journal of Biological Chemistry* 286 (42): 36478–91. doi:10.1074/jbc.M111.241786.

Espinosa, Alexander, Vilija Oke, Ase Elfving, Filippa Nyberg, Ruxandra Covacu, and Marie Wahren-Herlenius. 2008. 'The Autoantigen Ro52 Is an E3 Ligase Resident in the Cytoplasm but Enters the Nucleus upon Cellular Exposure to Nitric Oxide.' *Experimental Cell Research* 314 (20): 3605–13. doi:10.1016/j.yexcr.2008.09.011.

Espinosa, Alexander, Wei Zhou, Monica Ek, Malin Hedlund, Susanna Brauner, Karin Popovic, Linn Horvath, et al. 2006. 'The Sjogren's Syndrome-Associated Autoantigen Ro52 Is an E3 Ligase That Regulates Proliferation and Cell Death.' *Journal of Immunology (Baltimore, Md.: 1950)* 176 (10): 6277–85.

Eystathioy, Theophany, Edward K. L. Chan, Ken Takeuchi, Michael Mahler, LeeAnne M. Luft, Douglas W. Zochodne, and Marvin J. Fritzler. 2003. 'Clinical and Serological Associations of Autoantibodies to GW Bodies and a Novel Cytoplasmic Autoantigen GW182.' *Journal of Molecular Medicine (Berlin, Germany)* 81 (12): 811–18. doi:10.1007/s00109-003-0495-y.

Falnes, Pål Ø, Rune F. Johansen, and Erling Seeberg. 2002. 'AlkB-Mediated Oxidative Demethylation Reverses DNA Damage in Escherichia Coli.' *Nature* 419 (6903): 178–82. doi:10.1038/nature01048.

Fan, Zhen-Chuan, and Ya-Xiong Tao. 2009. 'Functional Characterization and Pharmacological Rescue of Melanocortin-4 Receptor Mutations Identified from Obese Patients.' *Journal of Cellular and Molecular Medicine* 13 (9b): 3268–82. doi:10.1111/j.1582-4934.2009.00726.x.

Farooqi, I. Sadaf, Julia M. Keogh, Giles S. H. Yeo, Emma J. Lank, Tim Cheetham, and Stephen O'Rahilly. 2003. 'Clinical Spectrum of Obesity and Mutations in the Melanocortin 4

Receptor Gene.' *The New England Journal of Medicine* 348 (12): 1085–95. doi:10.1056/NEJMoa022050.
Fawcett, Katherine A., and Inês Barroso. 2010. 'The Genetics of Obesity: FTO Leads the Way.' *Trends in Genetics* 26 (6): 266–74. doi:10.1016/j.tig.2010.02.006.
Fischer, Julia, Linda Koch, Christian Emmerling, Jeanette Vierkotten, Thomas Peters, Jens C. Bruning, and Ulrich Ruther. 2009. 'Inactivation of the Fto Gene Protects from Obesity.' *Nature* 458 (7240): 894–98. doi:10.1038/nature07848.
Fischer, Julia, Linda Koch, Christian Emmerling, Jeanette Vierkotten, Thomas Peters, Jens C. Brüning, and Ulrich Rüther. 2010. 'Fischer et Al. Reply.' *Nature* 464 (7289): E2–E2. doi:10.1038/nature08808.
Fox, Caroline S., Yongmei Liu, Charles C. White, Mary Feitosa, Albert V. Smith, Nancy Heard-Costa, Kurt Lohman, et al. 2012. 'Genome-Wide Association for Abdominal Subcutaneous and Visceral Adipose Reveals a Novel Locus for Visceral Fat in Women.' *PLoS Genet* 8 (5): e1002695. doi:10.1371/journal.pgen.1002695.
Frank, M. B. 1999. 'Characterization of DNA Binding Properties and Sequence Specificity of the Human 52 kDa Ro/SS-A (Ro52) Zinc Finger Protein.' *Biochemical and Biophysical Research Communications* 259 (3): 665–70. doi:10.1006/bbrc.1999.0835.
Frank, M B, V R McCubbin, and C Heldermon. 1995. 'Expression and DNA Binding of the Human 52 kDa Ro/SSA Autoantigen.' *Biochemical Journal* 305 (Pt 2): 359–62.
Franks, Tobias M., and Jens Lykke-Andersen. 2008. 'The Control of mRNA Decapping and P-Body Formation.' *Molecular Cell* 32 (5): 605–15. doi:10.1016/j.molcel.2008.11.001.
Frayling, Timothy M., Nicholas J. Timpson, Michael N. Weedon, Eleftheria Zeggini, Rachel M. Freathy, Cecilia M. Lindgren, John R. B. Perry, et al. 2007. 'A Common Variant in the FTO Gene Is Associated with Body Mass Index and Predisposes to Childhood and Adult Obesity.' *Science* 316 (5826): 889–94. doi:10.1126/science.1141634.
Fredriksson, Robert, Maria Hägglund, Pawel K. Olszewski, Olga Stephansson, Josefin A. Jacobsson, Agnieszka M. Olszewska, Allen S. Levine, Jonas Lindblom, and Helgi B. Schiöth. 2008. 'The Obesity Gene, FTO, Is of Ancient Origin, up-Regulated during Food Deprivation and Expressed in Neurons of Feeding-Related Nuclei of the Brain.' *Endocrinology* 149 (5): 2062–71. doi:10.1210/en.2007-1457.
Frick, Lauren E., James C. Delaney, Cintyu Wong, Catherine L. Drennan, and John M. Essigmann. 2007. 'Alleviation of 1,N6-Ethanoadenine Genotoxicity by the Escherichia Coli Adaptive Response Protein AlkB.' *Proceedings of the National Academy of Sciences of the United States of America* 104 (3): 755–60. doi:10.1073/pnas.0607377104.
Fu, Dragony, Jennifer A. N. Brophy, Clement T. Y. Chan, Kyle A. Atmore, Ulrike Begley, Richard S. Paules, Peter C. Dedon, Thomas J. Begley, and Leona D. Samson. 2010. 'Human AlkB Homolog ABH8 Is a tRNA Methyltransferase Required for Wobble Uridine Modification and DNA Damage Survival.' *Molecular and Cellular Biology* 30 (10): 2449–59. doi:10.1128/MCB.01604-09.
Fu, Dragony, Jennifer J. Jordan, and Leona D. Samson. 2013. 'Human ALKBH7 Is Required for Alkylation and Oxidation-Induced Programmed Necrosis.' *Genes & Development* 27 (10): 1089–1100. doi:10.1101/gad.215533.113.
Fu, Dragony, and Leona D. Samson. 2012. 'Direct Repair of 3,N(4)-Ethenocytosine by the Human ALKBH2 Dioxygenase Is Blocked by the AAG/MPG Glycosylase.' *DNA Repair* 11 (1): 46–52. doi:10.1016/j.dnarep.2011.10.004.
Fukuda-Kamitani, Taeko, and Tetsu Kamitani. 2002. 'Ubiquitination of Ro52 Autoantigen.' *Biochemical and Biophysical Research Communications* 295 (4): 774–78.
Fu, Ye, Qing Dai, Wen Zhang, Jin Ren, Tao Pan, and Chuan He. 2010. 'The AlkB Domain of Mammalian ABH8 Catalyzes Hydroxylation of 5-Methoxycarbonylmethyluridine at the Wobble Position of tRNA.' *Angewandte Chemie (International Ed. in English)* 49 (47): 8885–88. doi:10.1002/anie.201001242.

Fu, Ye, Dan Dominissini, Gideon Rechavi, and Chuan He. 2014. 'Gene Expression Regulation Mediated through Reversible m^{6}A RNA Methylation.' *Nature Reviews. Genetics* 15 (5): 293–306. doi:10.1038/nrg3724.

Gan, Xiaohong Tracey, Ganjian Zhao, Cathy X. Huang, Adrianna C. Rowe, Daniel M. Purdham, and Morris Karmazyn. 2013. 'Identification of Fat Mass and Obesity Associated (FTO) Protein Expression in Cardiomyocytes: Regulation by Leptin and Its Contribution to Leptin-Induced Hypertrophy.' *PloS One* 8 (9): e74235. doi:10.1371/journal.pone.0074235.

Gao, Xue, Yong-Hyun Shin, Min Li, Fei Wang, Qiang Tong, and Pumin Zhang. 2010. 'The Fat Mass and Obesity Associated Gene FTO Functions in the Brain to Regulate Postnatal Growth in Mice.' Edited by Krisztian Stadler. *PLoS ONE* 5 (11): e14005. doi:10.1371/journal.pone.0014005.

Gaudet, Mia M., Hannah P. Yang, Jesus Gonzalez Bosquet, Catherine S. Healey, Shahana Ahmed, Alison M. Dunning, Doug F. Easton, et al. 2010. 'No Association between FTO or HHEX and Endometrial Cancer Risk.' *Cancer Epidemiology, Biomarkers & Prevention: A Publication of the American Association for Cancer Research, Cosponsored by the American Society of Preventive Oncology* 19 (8): 2106–9. doi:10.1158/1055-9965.EPI-10-0515.

Gerken, Thomas, Christophe A. Girard, Yi-Chun Loraine Tung, Celia J. Webby, Vladimir Saudek, Kirsty S. Hewitson, Giles S. H. Yeo, et al. 2007. 'The Obesity-Associated FTO Gene Encodes a 2-Oxoglutarate-Dependent Nucleic Acid Demethylase.' *Science* 318 (5855): 1469–72. doi:10.1126/science.1151710.

Glickman, Michael H., and Aaron Ciechanover. 2002. 'The Ubiquitin-Proteasome Proteolytic Pathway: Destruction for the Sake of Construction.' *Physiological Reviews* 82 (2): 373–428. doi:10.1152/physrev.00027.2001.

Gloire, Geoffrey, Sylvie Legrand-Poels, and Jacques Piette. 2006. 'NF-kappaB Activation by Reactive Oxygen Species: Fifteen Years Later.' *Biochemical Pharmacology* 72 (11): 1493–1505. doi:10.1016/j.bcp.2006.04.011.

Graff, Mariaelisa, Julius S. Ngwa, Tsegaselassie Workalemahu, Georg Homuth, Sabine Schipf, Alexander Teumer, Henry Völzke, et al. 2013. 'Genome-Wide Analysis of BMI in Adolescents and Young Adults Reveals Additional Insight into the Effects of Genetic Loci over the Life Course.' *Human Molecular Genetics* 22 (17): 3597–3607. doi:10.1093/hmg/ddt205.

Graham, John M., and David Rickwood. 1997. *Subcellular Fractionation: A Practical Approach*. IRL Press at Oxford University Press.

Grunnet, Louise G., Emma Nilsson, Charlotte Ling, Torben Hansen, Oluf Pedersen, Leif Groop, Allan Vaag, and Pernille Poulsen. 2009. 'Regulation and Function of FTO mRNA Expression in Human Skeletal Muscle and Subcutaneous Adipose Tissue.' *Diabetes* 58 (10): 2402–8. doi:10.2337/db09-0205.

Guilbert, J. J. 2003. 'The World Health Report 2002 - Reducing Risks, Promoting Healthy Life.' *Education for Health (Abingdon, England)* 16 (2): 230. doi:10.1080/1357628031000116808.

Guil, Sonia, Jennifer C. Long, and Javier F. Cáceres. 2006. 'hnRNP A1 Relocalization to the Stress Granules Reflects a Role in the Stress Response.' *Molecular and Cellular Biology* 26 (15): 5744–58. doi:10.1128/MCB.00224-06.

Gulati, Pawan, Edward Avezov, Marcella Ma, Robin Antrobus, Paul Lehner, Stephen O'Rahilly, and Giles S. H. Yeo. 2014. 'Fat Mass and Obesity-Related (FTO) Shuttles between the Nucleus and Cytoplasm.' *Bioscience Reports* 34 (5). doi:10.1042/BSR20140111.

Gulati, Pawan, Man Ka Cheung, Robin Antrobus, Chris D. Church, Heather P. Harding, Yi-Chun Loraine Tung, Debra Rimmington, et al. 2013. 'Role for the Obesity-Related FTO Gene in the Cellular Sensing of Amino Acids.' *Proceedings of the National Academy of Sciences of the United States of America* 110 (7): 2557–62. doi:10.1073/pnas.1222796110.

Gulati, Pawan, and Giles S. H. Yeo. 2013. 'The Biology of FTO: From Nucleic Acid Demethylase to Amino Acid Sensor.' *Diabetologia* 56 (10): 2113–21. doi:10.1007/s00125-013-2999-5.

Güttler, Thomas, and Dirk Görlich. 2011. 'Ran-Dependent Nuclear Export Mediators: A Structural Perspective.' *The EMBO Journal* 30 (17): 3457–74. doi:10.1038/emboj.2011.287.

Hakanen, Maarit, Olli T. Raitakari, Terho Lehtimäki, Nina Peltonen, Katja Pahkala, Lauri Sillanmäki, Hanna Lagström, Jorma Viikari, Olli Simell, and Tapani Rönnemaa. 2009. 'FTO Genotype Is Associated with Body Mass Index after the Age of Seven Years but Not with Energy Intake or Leisure-Time Physical Activity.' *The Journal of Clinical Endocrinology and Metabolism* 94 (4): 1281–87. doi:10.1210/jc.2008-1199.

Hall, John E. 2010. *Guyton and Hall Textbook of Medical Physiology*. 12 edition. Philadelphia, Pa: Saunders.

Hamanaka, Robert B., and Navdeep S. Chandel. 2010. 'Mitochondrial Reactive Oxygen Species Regulate Cellular Signaling and Dictate Biological Outcomes.' *Trends in Biochemical Sciences* 35 (9): 505–13. doi:10.1016/j.tibs.2010.04.002.

Han, Zhifu, Tianhui Niu, Junbiao Chang, Xiaoguang Lei, Mingyan Zhao, Qiang Wang, Wei Cheng, Jinjing Wang, Yi Feng, and Jijie Chai. 2010. 'Crystal Structure of the FTO Protein Reveals Basis for Its Substrate Specificity.' *Nature* 464 (7292): 1205–9. doi:10.1038/nature08921.

Harno, Erika, Elizabeth C. Cottrell, and Anne White. 2013. 'Metabolic Pitfalls of CNS Cre-Based Technology.' *Cell Metabolism* 18 (1): 21–28. doi:10.1016/j.cmet.2013.05.019.

Hassanein, Mohamed T., Helen N. Lyon, Thutrang T. Nguyen, Ermeg L. Akylbekova, Kevin Waters, Guillaume Lettre, Bamidele Tayo, et al. 2010. 'Fine Mapping of the Association with Obesity at the FTO Locus in African-Derived Populations.' *Human Molecular Genetics* 19 (14): 2907–16. doi:10.1093/hmg/ddq178.

Haupt, Axel, Claus Thamer, Jürgen Machann, Kerstin Kirchhoff, Norbert Stefan, Otto Tschritter, Fausto Machicao, Fritz Schick, Hans-Ulrich Häring, and Andreas Fritsche. 2008. 'Impact of Variation in the FTO Gene on Whole Body Fat Distribution, Ectopic Fat, and Weight Loss.' *Obesity* 16 (8): 1969–72. doi:10.1038/oby.2008.283.

Hay, Nissim, and Nahum Sonenberg. 2004. 'Upstream and Downstream of mTOR.' *Genes & Development* 18 (16): 1926–45. doi:10.1101/gad.1212704.

Heard-Costa, Nancy L., M. Carola Zillikens, Keri L. Monda, Åsa Johansson, Tamara B. Harris, Mao Fu, Talin Haritunians, et al. 2009. 'NRXN3 Is a Novel Locus for Waist Circumference: A Genome-Wide Association Study from the CHARGE Consortium.' *PLoS Genet* 5 (6): e1000539. doi:10.1371/journal.pgen.1000539.

Heid, Iris M., Anne U. Jackson, Joshua C. Randall, Thomas W. Winkler, Lu Qi, Valgerdur Steinthorsdottir, Gudmar Thorleifsson, et al. 2010. 'Meta-Analysis Identifies 13 New Loci Associated with Waist-Hip Ratio and Reveals Sexual Dimorphism in the Genetic Basis of Fat Distribution.' *Nature Genetics* 42 (11): 949–60. doi:10.1038/ng.685.

Hess, Martin E., Simon Hess, Kate D. Meyer, Linda A. W. Verhagen, Linda Koch, Hella S. Brönneke, Marcelo O. Dietrich, et al. 2013. 'The Fat Mass and Obesity Associated Gene (Fto) Regulates Activity of the Dopaminergic Midbrain Circuitry.' *Nature Neuroscience* 16 (8): 1042–48. doi:10.1038/nn.3449.

Hewitson, K. S., N. Granatino, R. W. D. Welford, M. A. McDonough, and C. J. Schofield. 2005. 'Oxidation by 2-Oxoglutarate Oxygenases: Non-Haem Iron Systems in Catalysis and Signalling.' *Philosophical Transactions. Series A, Mathematical, Physical, and Engineering Sciences* 363 (1829): 807–28; discussion 1035–40. doi:10.1098/rsta.2004.1540.

Hietakangas, Ville, and Stephen M. Cohen. 2009. 'Regulation of Tissue Growth through Nutrient Sensing.' *Annual Review of Genetics* 43: 389–410. doi:10.1146/annurev-genet-102108-134815.

Higgs, Rowan, and Caroline A. Jefferies. 2008. 'Targeting IRFs by Ubiquitination: Regulating Antiviral Responses.' *Biochemical Society Transactions* 36 (Pt 3): 453–58. doi:10.1042/BST0360453.

Higgs, Rowan, Elisa Lazzari, Claire Wynne, Joan Ní Gabhann, Alexander Espinosa, Marie Wahren-Herlenius, and Caroline A. Jefferies. 2010. 'Self Protection from Anti-Viral Responses--Ro52 Promotes Degradation of the Transcription Factor IRF7 Downstream of the Viral Toll-Like Receptors.' *PloS One* 5 (7): e11776. doi:10.1371/journal.pone.0011776.

Hill, James O., Holly R. Wyatt, and John C. Peters. 2012. 'Energy Balance and Obesity.' *Circulation* 126 (1): 126–32. doi:10.1161/CIRCULATIONAHA.111.087213.

Hill, J. O., and R. Commerford. 1996. 'Physical Activity, Fat Balance, and Energy Balance.' *International Journal of Sport Nutrition* 6 (2): 80–92.

Hinney, Anke, Thomas Bettecken, Patrick Tarnow, Harald Brumm, Kathrin Reichwald, Peter Lichtner, André Scherag, et al. 2006. 'Prevalence, Spectrum, and Functional Characterization of Melanocortin-4 Receptor Gene Mutations in a Representative Population-Based Sample and Obese Adults from Germany.' *The Journal of Clinical Endocrinology & Metabolism* 91 (5): 1761–69. doi:10.1210/jc.2005-2056.

Hinney, Anke, Thuy Trang Nguyen, André Scherag, Susann Friedel, Günter Brönner, Timo Dirk Müller, Harald Grallert, et al. 2007. 'Genome Wide Association (GWA) Study for Early Onset Extreme Obesity Supports the Role of Fat Mass and Obesity Associated Gene (FTO) Variants.' *PloS One* 2 (12): e1361. doi:10.1371/journal.pone.0001361.

Hinney, Anke, Carla I. G. Vogel, and Johannes Hebebrand. 2010. 'From Monogenic to Polygenic Obesity: Recent Advances.' *European Child & Adolescent Psychiatry* 19 (3): 297–310. doi:10.1007/s00787-010-0096-6.

Ho, April J., Jason L. Stein, Xue Hua, Suh Lee, Derrek P. Hibar, Alex D. Leow, Ivo D. Dinov, et al. 2010. 'A Commonly Carried Allele of the Obesity-Related FTO Gene Is Associated with Reduced Brain Volume in the Healthy Elderly.' *Proceedings of the National Academy of Sciences of the United States of America* 107 (18): 8404–9. doi:10.1073/pnas.0910878107.

Horton, Paul, Keun-Joon Park, Takeshi Obayashi, Naoya Fujita, Hajime Harada, C. J. Adams-Collier, and Kenta Nakai. 2007. 'WoLF PSORT: Protein Localization Predictor.' *Nucleic Acids Research* 35 (Web Server issue): W585–87. doi:10.1093/nar/gkm259.

Hotamisligil, Gökhan S. 2006. 'Inflammation and Metabolic Disorders.' *Nature* 444 (7121): 860–67. doi:10.1038/nature05485.

Huang, Tony T., Shelly M. Wuerzberger-Davis, Zhao-Hui Wu, and Shigeki Miyamoto. 2003. 'Sequential Modification of NEMO/IKKgamma by SUMO-1 and Ubiquitin Mediates NF-kappaB Activation by Genotoxic Stress.' *Cell* 115 (5): 565–76.

Huszar, D., C. A. Lynch, V. Fairchild-Huntress, J. H. Dunmore, Q. Fang, L. R. Berkemeier, W. Gu, et al. 1997. 'Targeted Disruption of the Melanocortin-4 Receptor Results in Obesity in Mice.' *Cell* 88 (1): 131–41.

Iles, Mark M., Matthew H. Law, Simon N. Stacey, Jiali Han, Shenying Fang, Ruth Pfeiffer, Mark Harland, et al. 2013. 'A Variant in FTO Shows Association with Melanoma Risk Not due to BMI.' *Nature Genetics* 45 (4): 428–32, 432e1. doi:10.1038/ng.2571.

Ingalls, A. M., M. M. Dickie, and G. D. Snell. 1950. 'Obese, a New Mutation in the House Mouse.' *The Journal of Heredity* 41 (12): 317–18.

'IPA®, QIAGEN Redwood City.' 2014. Accessed November 14. http://www.ingenuity.com/.

Ishii, Tomonori, Kei Ohnuma, Akikazu Murakami, Naruhiko Takasawa, Tadanori Yamochi, Satoshi Iwata, Masahiko Uchiyama, Nam H. Dang, Hirotoshi Tanaka, and Chikao Morimoto. 2003. 'SS-A/Ro52, an Autoantigen Involved in CD28-Mediated IL-2 Production.' *Journal of Immunology (Baltimore, Md.: 1950)* 170 (7): 3653–61.

Ishimori, Naoki, Renhua Li, Peter M. Kelmenson, Ron Korstanje, Kenneth A. Walsh, Gary A. Churchill, Kristina Forsman-Semb, and Beverly Paigen. 2004a. 'Quantitative Trait

Loci Analysis for Plasma HDL-Cholesterol Concentrations and Atherosclerosis Susceptibility between Inbred Mouse Strains C57BL/6J and 129S1/SvImJ.' *Arteriosclerosis, Thrombosis, and Vascular Biology* 24 (1): 161–66. doi:10.1161/01.ATV.0000104027.52895.D7.

Ishimori, Naoki, Renhua Li, Peter M. Kelmenson, Ron Korstanje, Kenneth A. Walsh, Gary A. Churchill, Kristina Forsman-Semb, and Beverly Paigen. 2004b. 'Quantitative Trait Loci That Determine Plasma Lipids and Obesity in C57BL/6J and 129S1/SvImJ Inbred Mice.' *Journal of Lipid Research* 45 (9): 1624–32. doi:10.1194/jlr.M400098-JLR200.

Jaffe, Joseph, Malka Hochberg, Joseph Riss, Tal Hasin, Lea Reich, and Reuven Laskov. 1995. 'Cloning, Sequencing and Expression of Two Isoforms of the Murine Oct-1 Transcription Factor.' *Biochimica et Biophysica Acta (BBA) - Gene Structure and Expression* 1261 (2): 201–9. doi:10.1016/0167-4781(94)00246-Y.

James, Leo C., Anthony H. Keeble, Zahra Khan, David A. Rhodes, and John Trowsdale. 2007. 'Structural Basis for PRYSPRY-Mediated Tripartite Motif (TRIM) Protein Function.' *Proceedings of the National Academy of Sciences* 104 (15): 6200–6205. doi:10.1073/pnas.0609174104.

Jia, Guifang, Ye Fu, and Chuan He. 2013. 'Reversible RNA Adenosine Methylation in Biological Regulation.' *Trends in Genetics : TIG* 29 (2): 108–15. doi:10.1016/j.tig.2012.11.003.

Jia, Guifang, Ye Fu, Xu Zhao, Qing Dai, Guanqun Zheng, Ying Yang, Chengqi Yi, et al. 2011. 'N6-Methyladenosine in Nuclear RNA Is a Major Substrate of the Obesity-Associated FTO.' *Nature Chemical Biology* 7 (12): 885–87. doi:10.1038/nchembio.687.

Jia, Guifang, Cai-Guang Yang, Shangdong Yang, Xing Jian, Chengqi Yi, Zhiqiang Zhou, and Chuan He. 2008. 'Oxidative Demethylation of 3-Methylthymine and 3-Methyluracil in Single-Stranded DNA and RNA by Mouse and Human FTO.' *FEBS Letters* 582 (23-24): 3313–19. doi:10.1016/j.febslet.2008.08.019.

Johnson, J E, B J Wold, and S D Hauschka. 1989. 'Muscle Creatine Kinase Sequence Elements Regulating Skeletal and Cardiac Muscle Expression in Transgenic Mice.' *Molecular and Cellular Biology* 9 (8): 3393–99.

Jonsson, A., F. Renström, V. Lyssenko, E. C. Brito, B. Isomaa, G. Berglund, P. M. Nilsson, L. Groop, and P. W. Franks. 2009. 'Assessing the Effect of Interaction between an FTO Variant (rs9939609) and Physical Activity on Obesity in 15,925 Swedish and 2,511 Finnish Adults.' *Diabetologia* 52 (7): 1334–38. doi:10.1007/s00125-009-1355-2.

Jou, Chin. 2014. 'The Biology and Genetics of Obesity--a Century of Inquiries.' *The New England Journal of Medicine* 370 (20): 1874–77. doi:10.1056/NEJMp1400613.

Kaklamani, Virginia, Nengjun Yi, Maureen Sadim, Kalliopi Siziopikou, Kui Zhang, Yanfei Xu, Sarah Tofilon, Surbhi Agarwal, Boris Pasche, and Christos Mantzoros. 2011. 'The Role of the Fat Mass and Obesity Associated Gene (FTO) in Breast Cancer Risk.' *BMC Medical Genetics* 12: 52. doi:10.1186/1471-2350-12-52.

Kamata, Hideaki, Shi-Ichi Honda, Shin Maeda, Lufen Chang, Hajime Hirata, and Michael Karin. 2005. 'Reactive Oxygen Species Promote TNFalpha-Induced Death and Sustained JNK Activation by Inhibiting MAP Kinase Phosphatases.' *Cell* 120 (5): 649–61. doi:10.1016/j.cell.2004.12.041.

Karra, Efthimia, Owen G. O'Daly, Agharul I. Choudhury, Ahmed Yousseif, Steven Millership, Marianne T. Neary, William R. Scott, et al. 2013. 'A Link between FTO, Ghrelin, and Impaired Brain Food-Cue Responsivity.' *The Journal of Clinical Investigation* 123 (8): 3539–51. doi:10.1172/JCI44403.

Kataoka, H., and M. Sekiguchi. 1985. 'Molecular Cloning and Characterization of the alkB Gene of Escherichia Coli.' *Molecular & General Genetics: MGG* 198 (2): 263–69.

Keeble, Anthony H., Zahra Khan, Alan Forster, and Leo C. James. 2008. 'TRIM21 Is an IgG Receptor That Is Structurally, Thermodynamically, and Kinetically Conserved.' *Proceedings of the National Academy of Sciences of the United States of America* 105 (16): 6045–50. doi:10.1073/pnas.0800159105.

Keech, C. L., T. P. Gordon, and J. McCluskey. 1995. 'Cytoplasmic Accumulation of the 52 kDa Ro/SS-A Nuclear Autoantigen in Transfected Cell Lines.' *Journal of Autoimmunity* 8 (5): 699–712. doi:10.1006/jaut.1995.0052.

Kelekar, A, M R Saitta, and J D Keene. 1994. 'Molecular Composition of Ro Small Ribonucleoprotein Complexes in Human Cells. Intracellular Localization of the 60- and 52-kD Proteins.' *Journal of Clinical Investigation* 93 (4): 1637–44.

Kelly, T., W. Yang, C.-S. Chen, K. Reynolds, and J. He. 2008. 'Global Burden of Obesity in 2005 and Projections to 2030.' *International Journal of Obesity* 32 (9): 1431–37. doi:10.1038/ijo.2008.102.

Kilpeläinen, Tuomas O., Lu Qi, Soren Brage, Stephen J. Sharp, Emily Sonestedt, Ellen Demerath, Tariq Ahmad, et al. 2011. 'Physical Activity Attenuates the Influence of FTO Variants on Obesity Risk: A Meta-Analysis of 218,166 Adults and 19,268 Children.' *PLoS Medicine* 8 (11): e1001116. doi:10.1371/journal.pmed.1001116.

Kilpeläinen, Tuomas O., M. Carola Zillikens, Alena Stančákova, Francis M. Finucane, Janina S. Ried, Claudia Langenberg, Weihua Zhang, et al. 2011. 'Genetic Variation near IRS1 Associates with Reduced Adiposity and an Impaired Metabolic Profile.' *Nature Genetics* 43 (8): 753–60. doi:10.1038/ng.866.

Kim, J. H., B. Hahm, Y. K. Kim, M. Choi, and S. K. Jang. 2000. 'Protein-Protein Interaction among hnRNPs Shuttling between Nucleus and Cytoplasm.' *Journal of Molecular Biology* 298 (3): 395–405. doi:10.1006/jmbi.2000.3687.

Kodiha, M., P. Bański, D. Ho-Wo-Cheong, and U. Stochaj. 2008. 'Dissection of the Molecular Mechanisms That Control the Nuclear Accumulation of Transport Factors Importin-Alpha and CAS in Stressed Cells.' *Cellular and Molecular Life Sciences: CMLS* 65 (11): 1756–67. doi:10.1007/s00018-008-7588-2.

Kondo, H., Y. Nakabeppu, H. Kataoka, S. Kuhara, S. Kawabata, and M. Sekiguchi. 1986. 'Structure and Expression of the alkB Gene of Escherichia Coli Related to the Repair of Alkylated DNA.' *The Journal of Biological Chemistry* 261 (33): 15772–77.

Kong, Hee Jeong, D. Eric Anderson, Chang Hoon Lee, Moon Kyoo Jang, Tomohiko Tamura, Prafullakumar Tailor, Hyun Kook Cho, et al. 2007. 'Cutting Edge: Autoantigen Ro52 Is an Interferon Inducible E3 Ligase That Ubiquitinates IRF-8 and Enhances Cytokine Expression in Macrophages.' *Journal of Immunology (Baltimore, Md.: 1950)* 179 (1): 26–30.

Kos, Claudine H. 2004. 'Cre/loxP System for Generating Tissue-Specific Knockout Mouse Models.' *Nutrition Reviews* 62 (6 Pt 1): 243–46.

Kosugi, Shunichi, Masako Hasebe, Masaru Tomita, and Hiroshi Yanagawa. 2009. 'Systematic Identification of Cell Cycle-Dependent Yeast Nucleocytoplasmic Shuttling Proteins by Prediction of Composite Motifs.' *Proceedings of the National Academy of Sciences* 106 (25): 10171–76. doi:10.1073/pnas.0900604106.

Kowalak, J A, S C Pomerantz, P F Crain, and J A McCloskey. 1993. 'A Novel Method for the Determination of Post-Transcriptional Modification in RNA by Mass Spectrometry.' *Nucleic Acids Research* 21 (19): 4577–85.

Kowalska, I., M. T. Malecki, M. Straczkowski, J. Skupien, M. Karczewska-Kupczewska, A. Nikolajuk, M. Szopa, et al. 2009. 'The FTO Gene Modifies Weight, Fat Mass and Insulin Sensitivity in Women with Polycystic Ovary Syndrome, Where Its Role May Be Larger than in Other Phenotypes.' *Diabetes & Metabolism* 35 (4): 328–31. doi:10.1016/j.diabet.2009.03.004.

Krejčí, Alena. 2012. 'Metabolic Sensors and Their Interplay with Cell Signalling and Transcription.' *Biochemical Society Transactions* 40 (2): 311–23. doi:10.1042/BST20110767.

Kristiansson, Kati, Markus Perola, Emmi Tikkanen, Johannes Kettunen, Ida Surakka, Aki S. Havulinna, Alena Stancáková, et al. 2012. 'Genome-Wide Screen for Metabolic Syndrome Susceptibility Loci Reveals Strong Lipid Gene Contribution but No Evidence for Common Genetic Basis for Clustering of Metabolic Syndrome Traits.'

Circulation. Cardiovascular Genetics 5 (2): 242–49. doi:10.1161/CIRCGENETICS.111.961482.

Kulkarni, Meeta, Sevim Ozgur, and Georg Stoecklin. 2010. 'On Track with P-Bodies.' *Biochemical Society Transactions* 38 (Pt 1): 242–51. doi:10.1042/BST0380242.

Kurowski, Michal A., Ashok S. Bhagwat, Grzegorz Papaj, and Janusz M. Bujnicki. 2003. 'Phylogenomic Identification of Five New Human Homologs of the DNA Repair Enzyme AlkB.' *BMC Genomics* 4 (1): 48. doi:10.1186/1471-2164-4-48.

Kutay, U., F. R. Bischoff, S. Kostka, R. Kraft, and D. Görlich. 1997. 'Export of Importin Alpha from the Nucleus Is Mediated by a Specific Nuclear Transport Factor.' *Cell* 90 (6): 1061–71.

la Cour, Tanja, Lars Kiemer, Anne Mølgaard, Ramneek Gupta, Karen Skriver, and Søren Brunak. 2004. 'Analysis and Prediction of Leucine-Rich Nuclear Export Signals.' *Protein Engineering Design and Selection* 17 (6): 527–36. doi:10.1093/protein/gzh062.

'Laerd Statistics.' 2015. Accessed April 19. https://statistics.laerd.com/.

Lancha, Andoni, Gema Frühbeck, and Javier Gómez-Ambrosi. 2012. 'Peripheral Signalling Involved in Energy Homeostasis Control.' *Nutrition Research Reviews* 25 (2): 223–48. doi:10.1017/S0954422412000145.

Lappalainen, T., M. Kolehmainen, U. S. Schwab, A. M. Tolppanen, A. Stančáková, J. Lindström, J. G. Eriksson, et al. 2011. 'Association of the FTO Gene Variant (rs9939609) with Cardiovascular Disease in Men with Abnormal Glucose Metabolism--the Finnish Diabetes Prevention Study.' *Nutrition, Metabolism, and Cardiovascular Diseases: NMCD* 21 (9): 691–98. doi:10.1016/j.numecd.2010.01.006.

Li, Ming-Ming, Anja Nilsen, Yue Shi, Markus Fusser, Yue-He Ding, Ye Fu, Bo Liu, et al. 2013. 'ALKBH4-Dependent Demethylation of Actin Regulates Actomyosin Dynamics.' *Nature Communications* 4 (May): 1832. doi:10.1038/ncomms2863.

Lindgren, Cecilia M., Iris M. Heid, Joshua C. Randall, Claudia Lamina, Valgerdur Steinthorsdottir, Lu Qi, Elizabeth K. Speliotes, et al. 2009. 'Genome-Wide Association Scan Meta-Analysis Identifies Three Loci Influencing Adiposity and Fat Distribution.' *PLoS Genet* 5 (6): e1000508. doi:10.1371/journal.pgen.1000508.

Li, W. D., D. R. Reed, J. H. Lee, W. Xu, R. L. Kilker, B. R. Sodam, and R. A. Price. 1999. 'Sequence Variants in the 5' Flanking Region of the Leptin Gene Are Associated with Obesity in Women.' *Annals of Human Genetics* 63 (Pt 3): 227–34.

Lix, Lisa M., Joanne C. Keselman, and H. J. Keselman. 1996. 'Consequences of Assumption Violations Revisited: A Quantitative Review of Alternatives to the One-Way Analysis of Variance "F" Test'. *Review of Educational Research* 66 (4): 579. doi:10.2307/1170654.

Loenarz, Christoph, and Christopher J. Schofield. 2011. 'Physiological and Biochemical Aspects of Hydroxylations and Demethylations Catalyzed by Human 2-Oxoglutarate Oxygenases.' *Trends in Biochemical Sciences* 36 (1): 7–18. doi:10.1016/j.tibs.2010.07.002.

Loos, Ruth J. F., Cecilia M. Lindgren, Shengxu Li, Eleanor Wheeler, Jing Hua Zhao, Inga Prokopenko, Michael Inouye, et al. 2008. 'Common Variants near MC4R Are Associated with Fat Mass, Weight and Risk of Obesity.' *Nature Genetics* 40 (6): 768–75. doi:10.1038/ng.140.

Loughlin, John, Kalliope Panoutsopoulou, Lorraine Southam, Nigel W. Rayner, Aaron G. Day-Williams, Margarida C. Lopes, Vesna Boraska, et al. 2012. 'Identification of New Susceptibility Loci for Osteoarthritis (arcOGEN): A Genome-Wide Association Study.' *Lancet* 380 (9844): 815–23. doi:10.1016/S0140-6736(12)60681-3.

Lu, Lining, Chenxu Zhu, Bo Xia, and Chengqi Yi. 2014. 'Oxidative Demethylation of DNA and RNA Mediated by Non-Heme Iron-Dependent Dioxygenases.' *Chemistry, an Asian Journal* 9 (8): 2018–29. doi:10.1002/asia.201402148.

Lu, Yingchang, and Ruth JF Loos. 2013. 'Obesity Genomics: Assessing the Transferability of Susceptibility Loci across Diverse Populations.' *Genome Medicine* 5 (6): 55. doi:10.1186/gm459.

Lyons, G. E., S. Muhlebach, A. Moser, R. Masood, B. M. Paterson, M. E. Buckingham, and J. C. Perriard. 1991. 'Developmental Regulation of Creatine Kinase Gene Expression by Myogenic Factors in Embryonic Mouse and Chick Skeletal Muscle.' *Development* 113 (3): 1017–29.

Mahajan, Anubha, Min Jin Go, Weihua Zhang, Jennifer E. Below, Kyle J. Gaulton, Teresa Ferreira, Momoko Horikoshi, et al. 2014. 'Genome-Wide Trans-Ancestry Meta-Analysis Provides Insight into the Genetic Architecture of Type 2 Diabetes Susceptibility.' *Nature Genetics* 46 (3): 234–44. doi:10.1038/ng.2897.

Mallery, Donna L., William A. McEwan, Susanna R. Bidgood, Greg J. Towers, Chris M. Johnson, and Leo C. James. 2010. 'Antibodies Mediate Intracellular Immunity through Tripartite Motif-Containing 21 (TRIM21).' *Proceedings of the National Academy of Sciences of the United States of America* 107 (46): 19985–90. doi:10.1073/pnas.1014074107.

Ma, Marcella, Heather P. Harding, Stephen O'Rahilly, David Ron, and Giles S. H. Yeo. 2012. 'Kinetic Analysis of FTO (fat Mass and Obesity-Associated) Reveals That It Is Unlikely to Function as a Sensor for 2-Oxoglutarate.' *The Biochemical Journal* 444 (2): 183–87. doi:10.1042/BJ20120065.

Manolio, Teri A. 2010. 'Genomewide Association Studies and Assessment of the Risk of Disease.' *The New England Journal of Medicine* 363 (2): 166–76. doi:10.1056/NEJMra0905980.

Ma, Xiaoju Max, and John Blenis. 2009. 'Molecular Mechanisms of mTOR-Mediated Translational Control.' *Nature Reviews Molecular Cell Biology* 10 (5): 307–18. doi:10.1038/nrm2672.

McArthur, Carole, Yan Wang, Patricia Veno, Jianghong Zhang, and Russell Fiorella. 2002. 'Intracellular Trafficking and Surface Expression of SS-A (Ro), SS-B (La), poly(ADP-Ribose) Polymerase and Alpha-Fodrin Autoantigens during Apoptosis in Human Salivary Gland Cells Induced by Tumour Necrosis Factor-Alpha.' *Archives of Oral Biology* 47 (6): 443–48.

McEwan, William A., Donna L. Mallery, David A. Rhodes, John Trowsdale, and Leo C. James. 2011. 'Intracellular Antibody-Mediated Immunity and the Role of TRIM21.' *BioEssays: News and Reviews in Molecular, Cellular and Developmental Biology* 33 (11): 803–9. doi:10.1002/bies.201100093.

McEwan, William A., Jerry C. H. Tam, Ruth E. Watkinson, Susanna R. Bidgood, Donna L. Mallery, and Leo C. James. 2013. 'Intracellular Antibody-Bound Pathogens Stimulate Immune Signaling via the Fc Receptor TRIM21.' *Nature Immunology* 14 (4): 327–36. doi:10.1038/ni.2548.

McKeon, F. D., M. W. Kirschner, and D. Caput. 1986. 'Homologies in Both Primary and Secondary Structure between Nuclear Envelope and Intermediate Filament Proteins.' *Nature* 319 (6053): 463–68. doi:10.1038/319463a0.

McMurray, Fiona, Chris D. Church, Rachel Larder, George Nicholson, Sara Wells, Lydia Teboul, Y. C. Loraine Tung, et al. 2013. 'Adult Onset Global Loss of the Fto Gene Alters Body Composition and Metabolism in the Mouse.' *PLoS Genet* 9 (1): e1003166. doi:10.1371/journal.pgen.1003166.

McTaggart, James S., Sheena Lee, Michaela Iberl, Chris Church, Roger D. Cox, and Frances M. Ashcroft. 2011. 'FTO Is Expressed in Neurones throughout the Brain and Its Expression Is Unaltered by Fasting.' Edited by Nicholas John Timpson. *PLoS ONE* 6 (11): e27968. doi:10.1371/journal.pone.0027968.

Merkestein, Myrte, Samantha Laber, Fiona McMurray, Daniel Andrew, Gregor Sachse, Jeremy Sanderson, Mengdi Li, et al. 2015. 'FTO Influences Adipogenesis by Regulating Mitotic Clonal Expansion.' *Nature Communications* 6 (April). doi:10.1038/ncomms7792.

Merkestein, Myrte, James S. McTaggart, Sheena Lee, Holger B. Kramer, Fiona McMurray, Mathilde Lafond, Lily Boutens, Roger Cox, and Frances M. Ashcroft. 2014. 'Changes in Gene Expression Associated with FTO Overexpression in Mice.' *PloS One* 9 (5): e97162. doi:10.1371/journal.pone.0097162.

Meyer, Kate D., and Samie R. Jaffrey. 2014. 'The Dynamic Epitranscriptome: N6-Methyladenosine and Gene Expression Control.' *Nature Reviews Molecular Cell Biology* 15 (5): 313–26. doi:10.1038/nrm3785.

Meyer, Kate D., Yogesh Saletore, Paul Zumbo, Olivier Elemento, Christopher E. Mason, and Samie R. Jaffrey. 2012. 'Comprehensive Analysis of mRNA Methylation Reveals Enrichment in 3' UTRs and Near Stop Codons.' *Cell* 149 (7): 1635–46. doi:10.1016/j.cell.2012.05.003.

Meyer, Sylke, Claudia Temme, and Elmar Wahle. 2004. 'Messenger RNA Turnover in Eukaryotes: Pathways and Enzymes.' *Critical Reviews in Biochemistry and Molecular Biology* 39 (4): 197–216. doi:10.1080/10409230490513991.

Meyre, David, Jérôme Delplanque, Jean-Claude Chèvre, Cécile Lecoeur, Stéphane Lobbens, Sophie Gallina, Emmanuelle Durand, et al. 2009. 'Genome-Wide Association Study for Early-Onset and Morbid Adult Obesity Identifies Three New Risk Loci in European Populations.' *Nature Genetics* 41 (2): 157–59. doi:10.1038/ng.301.

Meyre, David, Karine Proulx, Hiroko Kawagoe-Takaki, Vincent Vatin, Ruth Gutiérrez-Aguilar, Debbie Lyon, Marcella Ma, et al. 2010. 'Prevalence of Loss-of-Function FTO Mutations in Lean and Obese Individuals.' *Diabetes* 59 (1): 311–18. doi:10.2337/db09-0703.

Miranda, M. E., C. E. Tseng, W. Rashbaum, R. L. Ochs, C. A. Casiano, F. Di Donato, E. K. Chan, and J. P. Buyon. 1998. 'Accessibility of SSA/Ro and SSB/La Antigens to Maternal Autoantibodies in Apoptotic Human Fetal Cardiac Myocytes.' *Journal of Immunology (Baltimore, Md.: 1950)* 161 (9): 5061–69.

Monda, Keri L., Gary K. Chen, Kira C. Taylor, Cameron Palmer, Todd L. Edwards, Leslie A. Lange, Maggie C. Y. Ng, et al. 2013. 'A Meta-Analysis Identifies New Loci Associated with Body Mass Index in Individuals of African Ancestry.' *Nature Genetics* 45 (6): 690–96. doi:10.1038/ng.2608.

Montague, C. T., I. S. Farooqi, J. P. Whitehead, M. A. Soos, H. Rau, N. J. Wareham, C. P. Sewter, et al. 1997. 'Congenital Leptin Deficiency Is Associated with Severe Early-Onset Obesity in Humans.' *Nature* 387 (6636): 903–8. doi:10.1038/43185.

'MPD-Compare C57BL/6J vs. 129S1/SvImJ.' 2015. Accessed April 6. http://phenome.jax.org/db/q?rtn=strains%2Fdetails2&x=34&y=15&S7=on&S3=on.

Mueller, Tina A., Katheryn Meek, and Robert P. Hausinger. 2010. 'Human AlkB Homologue 1 (ABH1) Exhibits DNA Lyase Activity at Abasic Sites.' *Dna Repair* 9 (1): 58–65. doi:10.1016/j.dnarep.2009.10.011.

Mukhopadhyay, Debdyuti, and Howard Riezman. 2007. 'Proteasome-Independent Functions of Ubiquitin in Endocytosis and Signaling.' *Science* 315 (5809): 201–5. doi:10.1126/science.1127085.

Namjou, Bahram, Mehdi Keddache, Keith Marsolo, Michael Wagner, Todd Lingren, Beth Cobb, Cassandra Perry, et al. 2013. 'EMR-Linked GWAS Study: Investigation of Variation Landscape of Loci for Body Mass Index in Children.' *Frontiers in Genetics* 4: 268. doi:10.3389/fgene.2013.00268.

Nan, Cassandra, Boliang Guo, Claire Warner, Tom Fowler, Timothy Barrett, Dorret Boomsma, Tracy Nelson, et al. 2012. 'Heritability of Body Mass Index in Pre-Adolescence, Young Adulthood and Late Adulthood.' *European Journal of Epidemiology* 27 (4): 247–53. doi:10.1007/s10654-012-9678-6.

'NetNES 1.1 Server.' 2014. Accessed November 28. http://www.cbs.dtu.dk/services/NetNES/.

'NLS Mapper.' 2014. Accessed November 28. http://nls-mapper.iab.keio.ac.jp/cgi-bin/NLS_Mapper_form.cgi.

Nobuhara, Yumiko, Seiji Kawano, Goichi Kageyama, Daisuke Sugiyama, Jun Saegusa, and Shunichi Kumagai. 2007. 'Is SS-A/Ro52 a Hydrogen Peroxide-Sensitive Signaling Molecule?' *Antioxidants & Redox Signaling* 9 (3): 385–91. doi:10.1089/ars.2007.9.ft-23.

Nordstrand, Line M., Jessica Svärd, Elisabeth Larsen, Anja Nilsen, Rune Ougland, Kari Furu, Guro F. Lien, et al. 2010. 'Mice Lacking Alkbh1 Display Sex-Ratio Distortion and Unilateral Eye Defects.' *PLoS ONE* 5 (11): e13827. doi:10.1371/journal.pone.0013827.

Noselli, S., and N. Perrimon. 2000. 'Signal Transduction. Are There Close Encounters between Signaling Pathways?' *Science (New York, N.Y.)* 290 (5489): 68–69.

Noselli, Stephane, and Norbert Perrimon. 2000. 'Are There Close Encounters Between Signaling Pathways?' *Science* 290 (5489): 68–69. doi:10.1126/science.290.5489.68.

Ofran, Yanay, and Burkhard Rost. 2007. 'ISIS: Interaction Sites Identified from Sequence.' *Bioinformatics* 23 (2): e13–16. doi:10.1093/bioinformatics/btl303.

Ohlsson, M., R. Jonsson, and K. A. Brokstad. 2002. 'Subcellular Redistribution and Surface Exposure of the Ro52, Ro60 and La48 Autoantigens during Apoptosis in Human Ductal Epithelial Cells: A Possible Mechanism in the Pathogenesis of Sjögren's Syndrome.' *Scandinavian Journal of Immunology* 56 (5): 456–69.

Okada, Yukinori, Michiaki Kubo, Hiroko Ohmiya, Atsushi Takahashi, Natsuhiko Kumasaka, Naoya Hosono, Shiro Maeda, et al. 2012. 'Common Variants at CDKAL1 and KLF9 Are Associated with Body Mass Index in East Asian Populations.' *Nature Genetics* 44 (3): 302–6. doi:10.1038/ng.1086.

Oke, Vilija, and Marie Wahren-Herlenius. 2012. 'The Immunobiology of Ro52 (TRIM21) in Autoimmunity: A Critical Review.' *Journal of Autoimmunity* 39 (1-2): 77–82. doi:10.1016/j.jaut.2012.01.014.

Olszewska, Marta, Józef J. Bujarski, and Maciej Kurpisz. 2012. 'P-Bodies and Their Functions during mRNA Cell Cycle: Mini-Review.' *Cell Biochemistry and Function* 30 (3): 177–82. doi:10.1002/cbf.2804.

Olszewski, Pawel K, Robert Fredriksson, Agnieszka M Olszewska, Olga Stephansson, Johan Alsiö, Katarzyna J Radomska, Allen S Levine, and Helgi B Schiöth. 2009. 'Hypothalamic FTO Is Associated with the Regulation of Energy Intake Not Feeding Reward.' *BMC Neuroscience* 10: 129. doi:10.1186/1471-2202-10-129.

Olszewski, Pawel K., Katarzyna J. Radomska, Kedar Ghimire, Anica Klockars, Caroline Ingman, Agnieszka M. Olszewska, Robert Fredriksson, Allen S. Levine, and Helgi B. Schiöth. 2011. 'Fto Immunoreactivity Is Widespread in the Rodent Brain and Abundant in Feeding-Related Sites, but the Number of Fto-Positive Cells Is Not Affected by Changes in Energy Balance.' *Physiology & Behavior* 103 (2): 248–53. doi:10.1016/j.physbeh.2011.01.022.

Osborn, Daniel P. S., Rosa Maria Roccasecca, Fiona McMurray, Victor Hernandez-Hernandez, Sriparna Mukherjee, Inês Barroso, Derek Stemple, Roger Cox, Philip L. Beales, and Sonia Christou-Savina. 2014. 'Loss of FTO Antagonises Wnt Signaling and Leads to Developmental Defects Associated with Ciliopathies.' *PloS One* 9 (2): e87662. doi:10.1371/journal.pone.0087662.

Osborn, D. P. S., S. Mukherjee, R. M. Roccasecca, I. Barosso, D. Stemple, P. L. Beales, and S. Christou-Savina. 2012. 'A Novel Role for the Obesity-Associated Gene FTO in Ciliogenesis and Wnt Signalling.' *Cilia* 1 (Suppl 1): P75. doi:10.1186/2046-2530-1-S1-P75.

Ougland, Rune, David Lando, Ida Jonson, John A. Dahl, Marivi Nabong Moen, Line M. Nordstrand, Torbjørn Rognes, et al. 2012. 'ALKBH1 Is a Histone H2A Dioxygenase Involved in Neural Differentiation.' *STEM CELLS* 30 (12): 2672–82. doi:10.1002/stem.1228.

Ougland, Rune, Chun-Mei Zhang, Aivar Liiv, Rune F. Johansen, Erling Seeberg, Ya-Ming Hou, Jaanus Remme, and Pål Ø. Falnes. 2004. 'AlkB Restores the Biological Function of

mRNA and tRNA Inactivated by Chemical Methylation.' *Molecular Cell* 16 (1): 107–16. doi:10.1016/j.molcel.2004.09.002.

Padeken, Jan, and Patrick Heun. 2014. 'Nucleolus and Nuclear Periphery: Velcro for Heterochromatin.' *Current Opinion in Cell Biology* 28 (June): 54–60. doi:10.1016/j.ceb.2014.03.001.

Parker, Roy, and Ujwal Sheth. 2007. 'P Bodies and the Control of mRNA Translation and Degradation.' *Molecular Cell* 25 (5): 635–46. doi:10.1016/j.molcel.2007.02.011.

Parker, Roy, and Haiwei Song. 2004. 'The Enzymes and Control of Eukaryotic mRNA Turnover.' *Nature Structural & Molecular Biology* 11 (2): 121–27. doi:10.1038/nsmb724.

Pei, Yu-Fang, Lei Zhang, Yongjun Liu, Jian Li, Hui Shen, Yao-Zhong Liu, Qing Tian, et al. 2014. 'Meta-Analysis of Genome-Wide Association Data Identifies Novel Susceptibility Loci for Obesity.' *Human Molecular Genetics* 23 (3): 820–30. doi:10.1093/hmg/ddt464.

Perry, John R. B., Benjamin F. Voight, Loïc Yengo, Najaf Amin, Josée Dupuis, Martha Ganser, Harald Grallert, et al. 2012. 'Stratifying Type 2 Diabetes Cases by BMI Identifies Genetic Risk Variants in LAMA1 and Enrichment for Risk Variants in Lean Compared to Obese Cases.' *PLoS Genetics* 8 (5): e1002741. doi:10.1371/journal.pgen.1002741.

Peters, T., K. Ausmeier, and U. Rüther. 1999. 'Cloning of Fatso (Fto), a Novel Gene Deleted by the Fused Toes (Ft) Mouse Mutation.' *Mammalian Genome: Official Journal of the International Mammalian Genome Society* 10 (10): 983–86.

Peters, Thomas, Katrin Ausmeier, Renate Dildrop, and Ulrich Rüther. 2002. 'The Mouse Fused Toes (Ft) Mutation Is the Result of a 1.6-Mb Deletion Including the Entire Iroquois B Gene Cluster.' *Mammalian Genome* 13 (4): 186–88. doi:10.1007/s00335-001-2142-7.

Phizicky, E. M., and S. Fields. 1995. 'Protein-Protein Interactions: Methods for Detection and Analysis.' *Microbiological Reviews* 59 (1): 94–123.

Pickart, C. M. 2001. 'Mechanisms Underlying Ubiquitination.' *Annual Review of Biochemistry* 70: 503–33. doi:10.1146/annurev.biochem.70.1.503.

Plafker, Scott M., Kendra S. Plafker, Allan M. Weissman, and Ian G. Macara. 2004. 'Ubiquitin Charging of Human Class III Ubiquitin-Conjugating Enzymes Triggers Their Nuclear Import.' *The Journal of Cell Biology* 167 (4): 649–59 . doi:10.1083/jcb.200406001.

Pourmand, N., I. Blange, N. Ringertz, and I. Pettersson. 1998. 'Intracellular Localisation of the Ro 52kD Auto-Antigen in HeLa Cells Visualised with Green Fluorescent Protein Chimeras.' *Autoimmunity* 28 (4): 225–33.

Preller, A., and J. E. Wilson. 1992. 'Localization of the Type III Isozyme of Hexokinase at the Nuclear Periphery.' *Archives of Biochemistry and Biophysics* 294 (2): 482–92.

Prescott, Jennifer, Deborah J. Thompson, Peter Kraft, Stephen J. Chanock, Tina Audley, Judith Brown, Jean Leyland, et al. 2012. 'Genome-Wide Association Study of Circulating Estradiol, Testosterone, and Sex Hormone-Binding Globulin in Postmenopausal Women.' *PloS One* 7 (6): e37815. doi:10.1371/journal.pone.0037815.

'Psort.' 2015. Accessed March 4. http://www.psort.org/.

Qiao, Liping, Hyung Sun Yoo, Alysha Madon, Brice Kinney, William W. Hay, and Jianhua Shao. 2012. 'Adiponectin Enhances Mouse Fetal Fat Deposition.' *Diabetes* 61 (12): 3199–3207. doi:10.2337/db12-0055.

Rampersaud, Evadnie, Braxton D. Mitchell, Toni I. Pollin, Mao Fu, Haiqing Shen, Jeffery R. O'Connell, Julie L. Ducharme, et al. 2008. 'Physical Activity and the Association of Common FTO Gene Variants with Body Mass Index and Obesity.' *Archives of Internal Medicine* 168 (16): 1791–97. doi:10.1001/archinte.168.16.1791.

Rankinen, Tuomo, Aamir Zuberi, Yvon C. Chagnon, S. John Weisnagel, George Argyropoulos, Brandon Walts, Louis Pérusse, and Claude Bouchard. 2006. 'The Human Obesity Gene Map: The 2005 Update.' *Obesity* 14 (4): 529–644. doi:10.1038/oby.2006.71.

Rao, V. Srinivasa, K. Srinivas, G. N. Sujini, and G. N. Sunand Kumar. 2014. 'Protein-Protein Interaction Detection: Methods and Analysis.' *International Journal of Proteomics* 2014 (February): e147648. doi:10.1155/2014/147648.

Reed, Danielle R., Alexander A. Bachmanov, and Michael G. Tordoff. 2007. 'Forty Mouse Strain Survey of Body Composition.' *Physiology & Behavior* 91 (5): 593–600. doi:10.1016/j.physbeh.2007.03.026.

Reitz, Christiane, Giuseppe Tosto, Richard Mayeux, Jose A. Luchsinger, NIA-LOAD/NCRAD Family Study Group, and Alzheimer's Disease Neuroimaging Initiative. 2012. 'Genetic Variants in the Fat and Obesity Associated (FTO) Gene and Risk of Alzheimer's Disease.' *PloS One* 7 (12): e50354. doi:10.1371/journal.pone.0050354.

Reymond, Alexandre, Germana Meroni, Anna Fantozzi, Giuseppe Merla, Stefano Cairo, Lucilla Luzi, Daniela Riganelli, et al. 2001. 'The Tripartite Motif Family Identifies Cell Compartments.' *The EMBO Journal* 20 (9): 2140–51. doi:10.1093/emboj/20.9.2140.

Rhodes, Davd A., Gudrun Ihrke, Anna T. Reinicke, Georg Malcherek, Michael Towey, David A. Isenberg, and John Trowsdale. 2002. 'The 52000 MW Ro/SS-A Autoantigen in Sjögren's Syndrome/systemic Lupus Erythematosus (Ro52) Is an Interferon-γ Inducible Tripartite Motif Protein Associated with Membrane Proximal Structures.' *Immunology* 106 (2): 246–56. doi:10.1046/j.1365-2567.2002.01417.x.

Rhodes, David A., and John Trowsdale. 2007. 'TRIM21 Is a Trimeric Protein That Binds IgG Fc via the B30.2 Domain.' *Molecular Immunology* 44 (9): 2406–14. doi:10.1016/j.molimm.2006.10.013.

Ringvoll, Jeanette, Marivi N. Moen, Line M. Nordstrand, Lisiane B. Meira, Bo Pang, Anders Bekkelund, Peter C. Dedon, et al. 2008. 'AlkB Homologue 2–Mediated Repair of Ethenoadenine Lesions in Mammalian DNA.' *Cancer Research* 68 (11): 4142–49. doi:10.1158/0008-5472.CAN-08-0796.

Robbens, Steven, Pierre Rouzé, J. Mark Cock, Jürg Spring, Alexandra Z. Worden, and Yves Van de Peer. 2008. 'The FTO Gene, Implicated in Human Obesity, Is Found Only in Vertebrates and Marine Algae.' *Journal of Molecular Evolution* 66 (1): 80–84. doi:10.1007/s00239-007-9059-z.

Roberts, S. B., N. Segil, and N. Heintz. 1991. 'Differential Phosphorylation of the Transcription Factor Oct1 during the Cell Cycle.' *Science (New York, N.Y.)* 253 (5023): 1022–26.

Rodríguez, C. I., F. Buchholz, J. Galloway, R. Sequerra, J. Kasper, R. Ayala, A. F. Stewart, and S. M. Dymecki. 2000. 'High-Efficiency Deleter Mice Show That FLPe Is an Alternative to Cre-loxP.' *Nature Genetics* 25 (2): 139–40. doi:10.1038/75973.

Rose, Nathan R., Michael A. McDonough, Oliver N. F. King, Akane Kawamura, and Christopher J. Schofield. 2011. 'Inhibition of 2-Oxoglutarate Dependent Oxygenases.' *Chemical Society Reviews* 40 (8): 4364–97. doi:10.1039/c0cs00203h.

Russell, Mark A., and Noel G. Morgan. 2011. 'Conditional Expression of the FTO Gene Product in Rat INS-1 Cells Reveals Its Rapid Turnover and a Role in the Profile of Glucose-Induced Insulin Secretion.' *Clinical Science (London, England: 1979)* 120 (9): 403–13. doi:10.1042/CS20100416.

Sabile, Abdelmajid, Andrea Michael Meyer, Christiane Wirbelauer, Daniel Hess, Ulrike Kogel, Martin Scheffner, and Wilhelm Krek. 2006. 'Regulation of p27 Degradation and S-Phase Progression by Ro52 RING Finger Protein.' *Molecular and Cellular Biology* 26 (16): 5994–6004. doi:10.1128/MCB.01630-05.

Sanchez-Pulido, Luis, and Miguel A. Andrade-Navarro. 2007. 'The FTO (fat Mass and Obesity Associated) Gene Codes for a Novel Member of the Non-Heme Dioxygenase Superfamily.' *BMC Biochemistry* 8 (1): 23. doi:10.1186/1471-2091-8-23.

Sanchez-Pulido, Luis, and Miguel A Andrade-Navarro. n.d. 'The FTO (fat Mass and Obesity Associated) Gene Codes for a Novel Member of the Non-Heme Dioxygenase Superfamily.' *BMC Biochemistry* 8: 23–23. doi:10.1186/1471-2091-8-23.

Sandoval, Darleen, Daniela Cota, and Randy J. Seeley. 2008. 'The Integrative Role of CNS Fuel-Sensing Mechanisms in Energy Balance and Glucose Regulation.' *Annual Review of Physiology* 70: 513–35. doi:10.1146/annurev.physiol.70.120806.095256.

Scherag, André, Christian Dina, Anke Hinney, Vincent Vatin, Susann Scherag, Carla I. G. Vogel, Timo D. Müller, et al. 2010. 'Two New Loci for Body-Weight Regulation Identified in a Joint Analysis of Genome-Wide Association Studies for Early-Onset Extreme Obesity in French and German Study Groups.' *PLoS Genet* 6 (4): e1000916. doi:10.1371/journal.pgen.1000916.

Schnell, Joshua D., and Linda Hicke. 2003. 'Non-Traditional Functions of Ubiquitin and Ubiquitin-Binding Proteins.' *Journal of Biological Chemistry* 278 (38): 35857–60. doi:10.1074/jbc.R300018200.

Schofield, C. J., and Z. Zhang. 1999. 'Structural and Mechanistic Studies on 2-Oxoglutarate-Dependent Oxygenases and Related Enzymes.' *Current Opinion in Structural Biology* 9 (6): 722–31.

Schwartz, Michael W., Stephen C. Woods, Daniel Porte, Randy J. Seeley, and Denis G. Baskin. 2000. 'Central Nervous System Control of Food Intake.' *Nature* 404 (6778): 661–71. doi:10.1038/35007534.

Scott, Laura J., Karen L. Mohlke, Lori L. Bonnycastle, Cristen J. Willer, Yun Li, William L. Duren, Michael R. Erdos, et al. 2007. 'A Genome-Wide Association Study of Type 2 Diabetes in Finns Detects Multiple Susceptibility Variants.' *Science (New York, N.Y.)* 316 (5829): 1341–45. doi:10.1126/science.1142382.

Scuteri, Angelo, Serena Sanna, Wei-Min Chen, Manuela Uda, Giuseppe Albai, James Strait, Samer Najjar, et al. 2007. 'Genome-Wide Association Scan Shows Genetic Variants in the FTO Gene Are Associated with Obesity-Related Traits.' *PLoS Genetics* 3 (7): e115. doi:10.1371/journal.pgen.0030115.

Seburn, KL, S Xing, and RW Burgess. 2008. 'MPD - Phenotype Project / Data set:Seburn2.' *Aging Study: Grip Strength and Gait Analysis in 32 Inbred Strains of Mice.* http://phenome.jax.org/db/q?rtn=projects/projdet&reqprojid=248.

Sen, C. K., and L. Packer. 1996. 'Antioxidant and Redox Regulation of Gene Transcription.' *FASEB Journal: Official Publication of the Federation of American Societies for Experimental Biology* 10 (7): 709–20.

Shen, Fan, Wei Huang, Jing-Tao Huang, Jun Xiong, Ying Yang, Ke Wu, Gui-Fang Jia, et al. 2015. 'Decreased N(6)-Methyladenosine in Peripheral Blood RNA from Diabetic Patients Is Associated with FTO Expression rather than ALKBH5.' *The Journal of Clinical Endocrinology and Metabolism* 100 (1): E148–54. doi:10.1210/jc.2014-1893.

Sheth, Ujwal, and Roy Parker. 2003. 'Decapping and Decay of Messenger RNA Occur in Cytoplasmic Processing Bodies.' *Science (New York, N.Y.)* 300 (5620): 805–8. doi:10.1126/science.1082320.

Silventoinen, K., B. Rokholm, J. Kaprio, and T. I. A. Sørensen. 2010. 'The Genetic and Environmental Influences on Childhood Obesity: A Systematic Review of Twin and Adoption Studies.' *International Journal of Obesity (2005)* 34 (1): 29–40. doi:10.1038/ijo.2009.177.

Silverthorn, Dee Unglaub, and Andrew C. Silverthorn. 2009. *Human Physiology: An Integrated Approach*. Pearson/Benjamin Cummings.

Smemo, Scott, Juan J. Tena, Kyoung-Han Kim, Eric R. Gamazon, Noboru J. Sakabe, Carlos Gómez-Marín, Ivy Aneas, et al. 2014. 'Obesity-Associated Variants within FTO Form Long-Range Functional Connections with IRX3.' *Nature* 507 (7492): 371–75. doi:10.1038/nature13138.

Solberg, Anja, Adam B. Robertson, Jan Magnus Aronsen, Øivind Rognmo, Ivar Sjaastad, Ulrik Wisløff, and Arne Klungland. 2013. 'Deletion of Mouse Alkbh7 Leads to Obesity.' *Journal of Molecular Cell Biology* 5 (3): 194–203. doi:10.1093/jmcb/mjt012.

Songe-Møller, Lene, Erwin van den Born, Vibeke Leihne, Cathrine B. Vågbø, Terese Kristoffersen, Hans E. Krokan, Finn Kirpekar, Pål Ø Falnes, and Arne Klungland. 2010. 'Mammalian ALKBH8 Possesses tRNA Methyltransferase Activity Required

for the Biogenesis of Multiple Wobble Uridine Modifications Implicated in Translational Decoding.' *Molecular and Cellular Biology* 30 (7): 1814–27. doi:10.1128/MCB.01602-09.

Speakman, John R. 2010. 'FTO Effect on Energy Demand versus Food Intake.' *Nature* 464 (7289): E1–E1. doi:10.1038/nature08807.

Speliotes, Elizabeth K., Cristen J. Willer, Sonja I. Berndt, Keri L. Monda, Gudmar Thorleifsson, Anne U. Jackson, Hana Lango Allen, et al. 2010. 'Association Analyses of 249,796 Individuals Reveal 18 New Loci Associated with Body Mass Index.' *Nature Genetics* 42 (11): 937–48. doi:10.1038/ng.686.

Strandberg, Linn, Aurelie Ambrosi, Alexander Espinosa, Lars Ottosson, Maija-Leena Eloranta, Wei Zhou, Ase Elfving, Edward Greenfield, Vijay K. Kuchroo, and Marie Wahren-Herlenius. 2008. 'Interferon-Alpha Induces up-Regulation and Nuclear Translocation of the Ro52 Autoantigen as Detected by a Panel of Novel Ro52-Specific Monoclonal Antibodies.' *Journal of Clinical Immunology* 28 (3): 220–31. doi:10.1007/s10875-007-9157-0.

Stratigopoulos, George, Stephanie L Padilla, Charles A LeDuc, Elizabeth Watson, Andrew T Hattersley, Mark I McCarthy, Lori M Zeltser, Wendy K Chung, and Rudolph L Leibel. 2008. 'Regulation of Fto/Ftm Gene Expression in Mice and Humans.' *American Journal of Physiology. Regulatory, Integrative and Comparative Physiology* 294 (4): R1185–96. doi:10.1152/ajpregu.00839.2007.

Strobel, A., T. Issad, L. Camoin, M. Ozata, and A. D. Strosberg. 1998. 'A Leptin Missense Mutation Associated with Hypogonadism and Morbid Obesity.' *Nature Genetics* 18 (3): 213–15. doi:10.1038/ng0398-213.

Stunkard, A. J., T. I. Sørensen, C. Hanis, T. W. Teasdale, R. Chakraborty, W. J. Schull, and F. Schulsinger. 1986. 'An Adoption Study of Human Obesity.' *The New England Journal of Medicine* 314 (4): 193–98. doi:10.1056/NEJM198601233140401.

Stunkard, Albert J., Jennifer R. Harris, Nancy L. Pedersen, and Gerald E. McClearn. 1990. 'The Body-Mass Index of Twins Who Have Been Reared Apart.' *New England Journal of Medicine* 322 (21): 1483–87. doi:10.1056/NEJM199005243222102.

Su, Z., R. Korstanje, S.-W. Tsaih, and B. Paigen. 2008. 'Candidate Genes for Obesity Revealed from a C57BL/6J × 129S1/SvImJ Intercross.' *International Journal of Obesity* 32 (7): 1180–89. doi:10.1038/ijo.2008.56.

Tabassum, Rubina, Ganesh Chauhan, Om Prakash Dwivedi, Anubha Mahajan, Alok Jaiswal, Ismeet Kaur, Khushdeep Bandesh, et al. 2013. 'Genome-Wide Association Study for Type 2 Diabetes in Indians Identifies a New Susceptibility Locus at 2q21.' *Diabetes* 62 (3): 977–86. doi:10.2337/db12-0406.

Takahata, Mutsumi, Miyuki Bohgaki, Tadasuke Tsukiyama, Takeshi Kondo, Masahiro Asaka, and Shigetsugu Hatakeyama. 2008. 'Ro52 Functionally Interacts with IgG1 and Regulates Its Quality Control via the ERAD System.' *Molecular Immunology* 45 (7): 2045–54. doi:10.1016/j.molimm.2007.10.023.

Tanaka, Toshiko, Julius S. Ngwa, Frank J. A. van Rooij, M. Carola Zillikens, Mary K. Wojczynski, Alexis C. Frazier-Wood, Denise K. Houston, et al. 2013. 'Genome-Wide Meta-Analysis of Observational Studies Shows Common Genetic Variants Associated with Macronutrient Intake.' *The American Journal of Clinical Nutrition* 97 (6): 1395–1402. doi:10.3945/ajcn.112.052183.

Tang, Xiaoting, and James E. Bruce. 2009. 'Chemical Cross-Linking for Protein-Protein Interaction Studies.' *Methods in Molecular Biology (Clifton, N.J.)* 492: 283–93. doi:10.1007/978-1-59745-493-3_17.

Tang, Yizhe, Sudarshana Purkayastha, and Dongsheng Cai. 2015. 'Hypothalamic Microinflammation: A Common Basis of Metabolic Syndrome and Aging.' *Trends in Neurosciences* 38 (1): 36–44. doi:10.1016/j.tins.2014.10.002.

Tanofsky-Kraff, Marian, Joan C. Han, Kavitha Anandalingam, Lauren B. Shomaker, Kelli M. Columbo, Laura E. Wolkoff, Merel Kozlosky, et al. 2009. 'The FTO Gene rs9939609

Obesity-Risk Allele and Loss of Control over Eating.' *The American Journal of Clinical Nutrition* 90 (6): 1483–88. doi:10.3945/ajcn.2009.28439.

Teo, Adrian Kee Keong, Amy J. Wagers, and Rohit N. Kulkarni. 2013. 'New Opportunities: Harnessing Induced Pluripotency for Discovery in Diabetes and Metabolism.' *Cell Metabolism* 18 (6): 775–91. doi:10.1016/j.cmet.2013.08.010.

'The Human Protein Atlas.' 2014. Accessed October 13. http://www.proteinatlas.org/ENSG00000132109/cell/CAB004566.

The Jackson Laboratory. 2003. 'MPD - Phenotype Project / Data Set: Jaxwest1.' *Multi-System Analysis of Physiology on 7 Inbred Strains of Mice.* http://phenome.jax.org/db/q?rtn=projects/details&sym=Jaxwest1.

Thorleifsson, Gudmar, G. Bragi Walters, Daniel F. Gudbjartsson, Valgerdur Steinthorsdottir, Patrick Sulem, Anna Helgadottir, Unnur Styrkarsdottir, et al. 2009. 'Genome-Wide Association Yields New Sequence Variants at Seven Loci That Associate with Measures of Obesity.' *Nature Genetics* 41 (1): 18–24. doi:10.1038/ng.274.

Timpson, Nicholas J, Pauline M Emmett, Timothy M Frayling, Imogen Rogers, Andrew T Hattersley, Mark I McCarthy, and George Davey Smith. 2008. 'The Fat Mass- and Obesity-Associated Locus and Dietary Intake in Children.' *The American Journal of Clinical Nutrition* 88 (4): 971–78.

Tönjes, Anke, Eleftheria Zeggini, Peter Kovacs, Yvonne Böttcher, Dorit Schleinitz, Kerstin Dietrich, Andrew P. Morris, et al. 2010. 'Association of FTO Variants with BMI and Fat Mass in the Self-Contained Population of Sorbs in Germany.' *European Journal of Human Genetics: EJHG* 18 (1): 104–10. doi:10.1038/ejhg.2009.107.

Tord Berggård, Sara Linse. 2007. 'Methods for the Detection and Analysis of Protein-Protein Interactions.' *Proteomics* 7 (16): 2833–42. doi:10.1002/pmic.200700131.

Tordoff, MG, and AA Bachmanov. 2002. 'MPD - Phenotype Project / Data Set: Tordoff3.' *Survey of Calcium and Sodium Intake, Blood pH and Calcium Level, and Bone and Body Composition Data in 40 Inbred Strains of Mice.* http://phenome.jax.org/db/q?rtn=projects/details&sym=Tordoff3.

Torok, M., and L. D. Etkin. 2001. 'Two B or Not Two B? Overview of the Rapidly Expanding B-Box Family of Proteins.' *Differentiation; Research in Biological Diversity* 67 (3): 63–71. doi:10.1046/j.1432-0436.2001.067003063.x.

Trachootham, Dunyaporn, Jerome Alexandre, and Peng Huang. 2009. 'Targeting Cancer Cells by ROS-Mediated Mechanisms: A Radical Therapeutic Approach?' *Nature Reviews Drug Discovery* 8 (7): 579–91. doi:10.1038/nrd2803.

Trask, Robert V., and Joseph J. Billadello. 1990. 'Tissue-Specific Distribution and Developmental Regulation of M and B Creatine Kinase mRNAs.' *Biochimica et Biophysica Acta (BBA) - Gene Structure and Expression* 1049 (2): 182–88. doi:10.1016/0167-4781(90)90039-5.

Trayhurn, Paul. 2005. 'The Biology of Obesity.' *The Proceedings of the Nutrition Society* 64 (1): 31–38.

Trewick, Sarah C., Timothy F. Henshaw, Robert P. Hausinger, Tomas Lindahl, and Barbara Sedgwick. 2002. 'Oxidative Demethylation by Escherichia Coli AlkB Directly Reverts DNA Base Damage.' *Nature* 419 (6903): 174–78. doi:10.1038/nature00908.

Trinkle-Mulcahy, Laura, and Angus I. Lamond. 2008. 'Nuclear Functions in Space and Time: Gene Expression in a Dynamic, Constrained Environment.' *FEBS Letters* 582 (14): 1960–70. doi:10.1016/j.febslet.2008.04.029.

Tung, Y. C. Loraine, Pawan Gulati, Che-Hsiung Liu, Debra Rimmington, Rowena Dennis, Marcella Ma, Vladimir Saudek, Stephen O'Rahilly, Anthony P. Coll, and Giles S. H. Yeo. 2015. 'FTO Is Necessary for the Induction of Leptin Resistance by High-Fat Feeding.' *Molecular Metabolism* 4 (4): 287–98. doi:10.1016/j.molmet.2015.01.011.

Tung, Yi-Chun Loraine, Eduard Ayuso, Xiaoye Shan, Fatima Bosch, Stephen O'Rahilly, Anthony P. Coll, and Giles S. H. Yeo. 2010. 'Hypothalamic-Specific Manipulation of Fto, the Ortholog of the Human Obesity Gene FTO, Affects Food Intake in Rats.' *PloS One* 5 (1): e8771. doi:10.1371/journal.pone.0008771.

'UK Proteomics Core Facility.' 2014. Accessed October 31. http://www.research.uky.edu/core/proteomics/primer.html.

Vaisse, C., K. Clement, E. Durand, S. Hercberg, B. Guy-Grand, and P. Froguel. 2000. 'Melanocortin-4 Receptor Mutations Are a Frequent and Heterogeneous Cause of Morbid Obesity.' *The Journal of Clinical Investigation* 106 (2): 253–62. doi:10.1172/JCI9238.

van den Berg, Linda, Henriette Delemarre-van de Waal, Joan C Han, Bauke Ylstra, Paul Eijk, Maria Nesterova, Peter Heutink, and Constantine A Stratakis. 2010. 'Investigation of a Patient with a Partial Trisomy 16q Including the Fat Mass and Obesity Associated Gene (FTO): Fine Mapping and FTO Gene Expression Study.' *American Journal of Medical Genetics. Part A* 152A (3): 630–37. doi:10.1002/ajmg.a.33229.

van den Born, Erwin, Cathrine B. Vågbø, Lene Songe-Møller, Vibeke Leihne, Guro F. Lien, Grazyna Leszczynska, Andrzej Malkiewicz, et al. 2011. 'ALKBH8-Mediated Formation of a Novel Diastereomeric Pair of Wobble Nucleosides in Mammalian tRNA.' *Nature Communications* 2 (February): 172. doi:10.1038/ncomms1173.

van der Hoeven, F., T. Schimmang, A. Volkmann, M. G. Mattei, B. Kyewski, and U. Rüther. 1994. 'Programmed Cell Death Is Affected in the Novel Mouse Mutant Fused Toes (Ft).' *Development (Cambridge, England)* 120 (9): 2601–7.

van Zeijl, Mieke J., Christa Testerink, Jan W. Kijne, and Mei Wang. 2000. 'Subcellular Differences in Post-Translational Modification of Barley 14-3-3 Proteins.' *FEBS Letters* 473 (3): 292–96. doi:10.1016/S0014-5793(00)01545-3.

Veal, Elizabeth A., Alison M. Day, and Brian A. Morgan. 2007. 'Hydrogen Peroxide Sensing and Signaling.' *Molecular Cell* 26 (1): 1–14. doi:10.1016/j.molcel.2007.03.016.

Vierkotten, Jeanette, Renate Dildrop, Thomas Peters, Baolin Wang, and Ulrich Rüther. 2007. 'Ftm Is a Novel Basal Body Protein of Cilia Involved in Shh Signalling.' *Development (Cambridge, England)* 134 (14): 2569–77. doi:10.1242/dev.003715.

Voight, Benjamin F., Laura J. Scott, Valgerdur Steinthorsdottir, Andrew P. Morris, Christian Dina, Ryan P. Welch, Eleftheria Zeggini, et al. 2010. 'Twelve Type 2 Diabetes Susceptibility Loci Identified through Large-Scale Association Analysis.' *Nature Genetics* 42 (7): 579–89. doi:10.1038/ng.609.

von Mering, Christian, Roland Krause, Berend Snel, Michael Cornell, Stephen G. Oliver, Stanley Fields, and Peer Bork. 2002. 'Comparative Assessment of Large-Scale Data Sets of Protein-Protein Interactions.' *Nature* 417 (6887): 399–403. doi:10.1038/nature750.

Vrbikova, Jana, and Vojtech Hainer. 2009. 'Obesity and Polycystic Ovary Syndrome.' *Obesity Facts* 2 (1): 26–35. doi:10.1159/000194971.

Vujovic, Predrag, Stefan Stamenkovic, Nebojsa Jasnic, Iva Lakic, Sinisa F. Djurasevic, Gordana Cvijic, and Jelena Djordjevic. 2013. 'Fasting Induced Cytoplasmic Fto Expression in Some Neurons of Rat Hypothalamus.' *PloS One* 8 (5): e63694. doi:10.1371/journal.pone.0063694.

Wada, Keiji, and Tetsu Kamitani. 2006. 'Autoantigen Ro52 Is an E3 Ubiquitin Ligase.' *Biochemical and Biophysical Research Communications* 339 (1): 415–21. doi:10.1016/j.bbrc.2005.11.029.

Wada, Keiji, Motoko Niida, Makoto Tanaka, and Tetsu Kamitani. 2009. 'Ro52-Mediated Monoubiquitination of IKK{beta} down-Regulates NF-{kappa}B Signalling.' *Journal of Biochemistry* 146 (6): 821–32. doi:10.1093/jb/mvp127.

Wåhlén, Kerstin, Eva Sjölin, and Johan Hoffstedt. 2008. 'The Common rs9939609 Gene Variant of the Fat Mass- and Obesity-Associated Gene FTO Is Related to Fat Cell Lipolysis.' *Journal of Lipid Research* 49 (3): 607–11. doi:10.1194/jlr.M700448-JLR200.

Wan, Emily S., Michael H. Cho, Nadia Boutaoui, Barbara J. Klanderman, Jody S. Sylvia, John P. Ziniti, Sungho Won, et al. 2011. 'Genome-Wide Association Analysis of Body Mass in Chronic Obstructive Pulmonary Disease.' *American Journal of Respiratory Cell and Molecular Biology* 45 (2): 304–10. doi:10.1165/rcmb.2010-0294OC.

Wang, Kai, Wei-Dong Li, Clarence K. Zhang, Zuoheng Wang, Joseph T. Glessner, Struan F. A. Grant, Hongyu Zhao, Hakon Hakonarson, and R. Arlen Price. 2011. 'A Genome-Wide Association Study on Obesity and Obesity-Related Traits.' *PloS One* 6 (4): e18939. doi:10.1371/journal.pone.0018939.

Wang, Pei, Feng-Jiao Yang, Hui Du, Yun-Feng Guan, Tian-Ying Xu, Xue-Wen Xu, Ding-Feng Su, and Chao-Yu Miao. 2011. 'Involvement of Leptin Receptor Long Isoform (LepRb)-STAT3 Signaling Pathway in Brain Fat Mass- and Obesity-Associated (FTO) Downregulation during Energy Restriction.' *Molecular Medicine (Cambridge, Mass.)* 17 (5-6): 523–32. doi:10.2119/molmed.2010.00134.

Wang, Tao, Weiping Jia, and Cheng Hu. 2014. 'Advancement in Genetic Variants Conferring Obesity Susceptibility from Genome-Wide Association Studies.' *Frontiers of Medicine*, December. doi:10.1007/s11684-014-0373-8.

Wang, Xiao, Zhike Lu, Adrian Gomez, Gary C. Hon, Yanan Yue, Dali Han, Ye Fu, et al. 2014. 'N6-Methyladenosine-Dependent Regulation of Messenger RNA Stability.' *Nature* 505 (7481): 117–20. doi:10.1038/nature12730.

Wang, Yang, Yue Li, Julia I. Toth, Matthew D. Petroski, Zhaolei Zhang, and Jing Crystal Zhao. 2014. 'N6-Methyladenosine Modification Destabilizes Developmental Regulators in Embryonic Stem Cells.' *Nature Cell Biology* 16 (2): 191–98. doi:10.1038/ncb2902.

Weidensdorfer, Doreen, Nadine Stöhr, Anne Baude, Marcell Lederer, Marcel Köhn, Angelika Schierhorn, Sabine Buchmeier, Elmar Wahle, and Stefan Hüttelmaier. 2009. 'Control of c-Myc mRNA Stability by IGF2BP1-Associated Cytoplasmic RNPs.' *RNA (New York, N.Y.)* 15 (1): 104–15. doi:10.1261/rna.1175909.

Wellen, Kathryn E., and Gökhan S. Hotamisligil. 2005. 'Inflammation, Stress, and Diabetes.' *Journal of Clinical Investigation* 115 (5): 1111–19. doi:10.1172/JCI200525102.

Wellen, Kathryn E., and Craig B. Thompson. 2010. 'Cellular Metabolic Stress: Considering How Cells Respond to Nutrient Excess.' *Molecular Cell* 40 (2): 323–32. doi:10.1016/j.molcel.2010.10.004.

Wen, Wanqing, Yoon-Shin Cho, Wei Zheng, Rajkumar Dorajoo, Norihiro Kato, Lu Qi, Chien-Hsiun Chen, et al. 2012. 'Meta-Analysis Identifies Common Variants Associated with Body Mass Index in East Asians.' *Nature Genetics* 44 (3): 307–11. doi:10.1038/ng.1087.

Wen, Wanqing, Wei Zheng, Yukinori Okada, Fumihiko Takeuchi, Yasuharu Tabara, Joo-Yeon Hwang, Rajkumar Dorajoo, et al. 2014. 'Meta-Analysis of Genome-Wide Association Studies in East Asian-Ancestry Populations Identifies Four New Loci for Body Mass Index.' *Human Molecular Genetics* 23 (20): 5492–5504. doi:10.1093/hmg/ddu248.

Westbye, Marianne Pedersen, Emadoldin Feyzi, Per Arne Aas, Cathrine Broberg Vågbø, Vivi Anita Talstad, Bodil Kavli, Lars Hagen, et al. 2008. 'Human AlkB Homolog 1 Is a Mitochondrial Protein That Demethylates 3-Methylcytosine in DNA and RNA.' *Journal of Biological Chemistry* 283 (36): 25046–56. doi:10.1074/jbc.M803776200.

Wheeler, Eleanor, Ni Huang, Elena G. Bochukova, Julia M. Keogh, Sarah Lindsay, Sumedha Garg, Elana Henning, et al. 2013. 'Genome-Wide SNP and CNV Analysis Identifies Common and Low-Frequency Variants Associated with Severe Early-Onset Obesity.' *Nature Genetics* 45 (5): 513–17. doi:10.1038/ng.2607.

'WHO | Obesity.' 2015. *WHO*. Accessed January 5. http://www.who.int/topics/obesity/en/.

'WHO Europe Obesity.' 2015. Accessed January 7. http://www.euro.who.int/en/health-topics/noncommunicable-diseases/obesity.

'WHO Global Database on Child Growth and Malnutrition.' 2015. *WHO*. Accessed January 7. http://www.who.int/nutgrowthdb/en/.

Wilkinson, K. D. 1987. 'Protein Ubiquitination: A Regulatory Post-Translational Modification.' *Anti-Cancer Drug Design* 2 (2): 211–29.

Willer, Cristen J., Ellen M. Schmidt, Sebanti Sengupta, Gina M. Peloso, Stefan Gustafsson, Stavroula Kanoni, Andrea Ganna, et al. 2013. 'Discovery and Refinement of Loci

Associated with Lipid Levels.' *Nature Genetics* 45 (11): 1274–83. doi:10.1038/ng.2797.
Willer, Cristen J., Elizabeth K. Speliotes, Ruth J. F. Loos, Shengxu Li, Cecilia M. Lindgren, Iris M. Heid, Sonja I. Berndt, et al. 2009. 'Six New Loci Associated with Body Mass Index Highlight a Neuronal Influence on Body Weight Regulation.' *Nature Genetics* 41 (1): 25–34. doi:10.1038/ng.287.
Woelk, Tanja, Sara Sigismund, Lorenza Penengo, and Simona Polo. 2007. 'The Ubiquitination Code: A Signalling Problem.' *Cell Division* 2: 11. doi:10.1186/1747-1028-2-11.
'WoLF PSORT.' 2014. Accessed November 27. http://wolfpsort.org/.
'World Health Statistics 2014.' 2015. *WHO*. Accessed January 7. http://www.who.int/gho/publications/world_health_statistics/2014/en/.
Wu, Qiong, Rudel A Saunders, Maria Szkudlarek-Mikho, Ivana de la Serna, and Khew-Voon Chin. 2010. 'The Obesity-Associated Fto Gene Is a Transcriptional Coactivator.' *Biochemical and Biophysical Research Communications* 401 (3): 390–95. doi:10.1016/j.bbrc.2010.09.064.
Yamochi, Tadanori, Kei Ohnuma, Osamu Hosono, Hirotoshi Tanaka, Yoshiyuki Kanai, and Chikao Morimoto. 2008. 'SSA/Ro52 Autoantigen Interacts with Dcp2 to Enhance Its Decapping Activity.' *Biochemical and Biophysical Research Communications* 370 (1): 195–99. doi:10.1016/j.bbrc.2008.03.075.
Yang, Jian, Ruth J. F. Loos, Joseph E. Powell, Sarah E. Medland, Elizabeth K. Speliotes, Daniel I. Chasman, Lynda M. Rose, et al. 2012. 'FTO Genotype Is Associated with Phenotypic Variability of Body Mass Index.' *Nature* 490 (7419): 267–72. doi:10.1038/nature11401.
Yang, Y., T. Eversole, D. J. Lee, R. D. Sontheimer, and J. D. Capra. 1999. 'Protein-Protein Interactions between Native Ro52 and Immunoglobulin G Heavy Chain.' *Scandinavian Journal of Immunology* 49 (6): 620–28.
Yang, Y. S., M. C. Yang, B. Wang, and J. C. Weissler. 2000. 'Autoantigen Ro52 Directly Interacts with Human IgG Heavy Chain in Vivo in Mammalian Cells.' *Molecular Immunology* 37 (10): 591–602.
Yan, Qun, Jie Hong, Weiqiong Gu, Yifei Zhang, Qiaorui Liu, Yuxia Su, Yuwen Zhang, Xiaoying Li, Bin Cui, and Guang Ning. 2009. 'Association of the Common rs9939609 Variant of FTO Gene with Polycystic Ovary Syndrome in Chinese Women.' *Endocrine* 36 (3): 377–82. doi:10.1007/s12020-009-9257-0.
Yeo, Giles S. H., and Lora K. Heisler. 2012. 'Unraveling the Brain Regulation of Appetite: Lessons from Genetics.' *Nature Neuroscience* 15 (10): 1343–49. doi:10.1038/nn.3211.
Yuan, Hai-Xin, Yue Xiong, and Kun-Liang Guan. 2013. 'Nutrient Sensing, Metabolism, and Cell Growth Control.' *Molecular Cell* 49 (3): 379–87. doi:10.1016/j.molcel.2013.01.019.
Yu, Chin-Sheng, Yu-Ching Chen, Chih-Hao Lu, and Jenn-Kang Hwang. 2006. 'Prediction of Protein Subcellular Localization.' *Proteins* 64 (3): 643–51. doi:10.1002/prot.21018.
Yu, Chin-Sheng, Chih-Jen Lin, and Jenn-Kang Hwang. 2004. 'Predicting Subcellular Localization of Proteins for Gram-Negative Bacteria by Support Vector Machines Based on N-Peptide Compositions.' *Protein Science: A Publication of the Protein Society* 13 (5): 1402–6. doi:10.1110/ps.03479604.
Zeggini, Eleftheria, Laura J. Scott, Richa Saxena, Benjamin F. Voight, Jonathan L. Marchini, Tianle Hu, Paul I. W. de Bakker, et al. 2008. 'Meta-Analysis of Genome-Wide Association Data and Large-Scale Replication Identifies Additional Susceptibility Loci for Type 2 Diabetes.' *Nature Genetics* 40 (5): 638–45. doi:10.1038/ng.120.
Zeggini, Eleftheria, Michael N. Weedon, Cecilia M. Lindgren, Timothy M. Frayling, Katherine S. Elliott, Hana Lango, Nicholas J. Timpson, et al. 2007. 'Replication of Genome-Wide

Association Signals in UK Samples Reveals Risk Loci for Type 2 Diabetes.' *Science (New York, N.Y.)* 316 (5829): 1336–41. doi:10.1126/science.1142364.

Zhang, Ge, Rebekah Karns, Nina Smolej Narancic, Guangyun Sun, Hong Cheng, Sasa Missoni, Zijad Durakovic, Pavao Rudan, Ranajit Chakraborty, and Ranjan Deka. 2010. 'Common SNPs in FTO Gene Are Associated with Obesity Related Anthropometric Traits in an Island Population from the Eastern Adriatic Coast of Croatia.' *PloS One* 5 (4): e10375. doi:10.1371/journal.pone.0010375.

Zhang, Jing, Lei Fang, Xuguo Zhu, Yiting Qiao, Mei Yu, Lu Wang, Yuan Chen, Wu Yin, and Zi-Chun Hua. 2012. 'Ro52/SSA Sensitizes Cells to Death Receptor-Induced Apoptosis by down-Regulating c-FLIP(L).' *Cell Biology International* 36 (5): 463–68. doi:10.1042/CBI20110322.

Zhang, Y., R. Proenca, M. Maffei, M. Barone, L. Leopold, and J. M. Friedman. 1994. 'Positional Cloning of the Mouse Obese Gene and Its Human Homologue.' *Nature* 372 (6505): 425–32. doi:10.1038/372425a0.

Zhang, Zhiqiang, Musheng Bao, Ning Lu, Leiyun Weng, Bin Yuan, and Yong-Jun Liu. 2013. 'The E3 Ubiquitin Ligase TRIM21 Negatively Regulates the Innate Immune Response to Intracellular Double-Stranded DNA.' *Nature Immunology* 14 (2): 172–78. doi:10.1038/ni.2492.

Zhao, Xu, Ying Yang, Bao-Fa Sun, Yue Shi, Xin Yang, Wen Xiao, Ya-Juan Hao, et al. 2014. 'FTO-Dependent Demethylation of N6-Methyladenosine Regulates mRNA Splicing and Is Required for Adipogenesis.' *Cell Research* 24 (12): 1403–19. doi:10.1038/cr.2014.151.

Zheng, Guanqun, John Arne Dahl, Yamei Niu, Peter Fedorcsak, Chun-Min Huang, Charles J. Li, Cathrine B. Vågbø, et al. 2013. 'ALKBH5 Is a Mammalian RNA Demethylase That Impacts RNA Metabolism and Mouse Fertility.' *Molecular Cell* 49 (1): 18–29. doi:10.1016/j.molcel.2012.10.015.

Zimmermann, Esther, Sofia I. I. Kring, Tina L. Berentzen, Claus Holst, Tune H. Pers, Torben Hansen, Oluf Pedersen, Thorkild I. A. Sørensen, and Tine Jess. 2009. 'Fatness-Associated FTO Gene Variant Increases Mortality Independent of Fatness--in Cohorts of Danish Men.' *PloS One* 4 (2): e4428. doi:10.1371/journal.pone.0004428.

Appendix 3 Study of FTO Subcellular Localisation

Appendix 3.1 Results of the WoLF PSORT Analysis

GueryProtein WoLFPSORT prediction cyto: 15.5, cyto_nucl: 15, nucl: 13.5

test*k used for kNN is: 32*

PSORT features and traditional PSORTII prediction:

queryProtein (502 aa) queryProtein
PSG: a new signal peptide prediction method
N-region: length 11; pos.chg 3; neg.chg 3
H-region: length 0; peak value 0.00
PSG score: -4.40

GvH: von Heijne's method for signal seq. recognition
GvH score (threshold: -2.1): -8.85
possible cleavage site: between 56 and 57

>>> Seems to have no N-terminal signal peptide ALOM: Klein et al's method for TM region allocation
Init position for calculation: 1
Tentative number of TMS(s) for the threshold 0.5: 0
number of TMS(s) .. fixed
PERIPHERAL Likelihood = 5.83 (at 425)
ALOM score: 5.83 (number of TMSs: 0)

MITDISC: discrimination of mitochondrial targeting seq
R content: 1 Hyd Moment(75): 11.22
Hyd Moment(95): 3.87 G content: 0
D/E content: 2 S/T content: 1
Score: -5.39

Gavel: prediction of cleavage sites for mitochondrial preseq
R-2 motif at 13 KRV|QT

NUCDISC: discrimination of nuclear localisation signals
pat4: none
pat7: none
bipartite: KRVQTAEEREREAKKLR at 2
content of basic residues: 11.6%
NLS Score: 0.02

KDEL: ER retention motif in the C-terminus: none
ER Membrane Retention Signals:
XXRR-like motif in the N-terminus: KRVQ: none

SKL: peroxisomal targeting signal in the C-terminus: none

PTS2: 2nd peroxisomal targeting signal: none

VAC: possible vacuolar targeting motif: none

RNA-binding motif: none

Actinin-type actin-binding motif:
type 1: none
type 2: none

NMYR: N-myristoylation pattern : none

Farnesylation/Geranylgeranylation motif: none

memYQRL: transport motif from cell surface to Golgi: none

Tyrosines in the tail: none

Dileucine motif in the tail: none

checking 64 PROSITE DNA binding motifs: none

checking 1 PROSITE low specificity DNA binding motifs: none

checking 71 PROSITE ribosomal protein motifs: none

checking 33 PROSITE prokaryotic dna binding motifs: none

Table Appendix 1. Mouse FTO 32 Nearest Neighbours as analysed by WoLF PSORT.

ID	Site	Distance	Identity	Comments
NEMO_HUMAN	cyto_nucl	55.7781	14.741%	[Uniprot] SWISS-PROT45:Cytoplasmic and nuclear.
IRF4_MOUSE	nucl	61.9633	14.3141%	[Uniprot] SWISS-PROT45:Nuclear. GO:0005634; C:nucleus; Evidence:ISS.
GLNA_CRILO	cyto	62.8482	14.1434%	[Uniprot] SWISS-PROT45:Cytoplasmic.
IKBA_CHICK	cyto	71.4704	14.1434%	[Uniprot] SWISS-PROT45:Cytoplasmic.
NNP1_HUMAN	nucl	72.1256	12.8713%	[Uniprot] SWISS-PROT45:Nuclear; nucleolar. GO:0005634; C:nucleus; Evidence:TAS.
LDB1_XENLA	nucl	72.9321	13.745%	[Uniprot] SWISS-PROT45:Nuclear.
MTA2_MOUSE	nucl	72.9978	14.8204%	[Uniprot] SWISS-PROT45:Nuclear. GO:0005634; C:nucleus; Evidence:IDA.
GLNA_MOUSE	cyto	74.0591	12.9482%	[Uniprot] SWISS-PROT45:Cytoplasmic.
2A5B_HUMAN	cyto	75.147	13.1115%	[Uniprot] SWISS-PROT45:Cytoplasmic. GO:0005737; C:cytoplasm; Evidence:TAS.
CATA_DROME	pero	75.3592	10.7843%	[Uniprot] SWISS-PROT45:Peroxisomal.
IKKB_MOUSE	cyto	77.3657	13.4742%	[Uniprot] SWISS-PROT45:Cytoplasmic.
IKKB_RAT	cyto	78.046	14.2668%	[Uniprot] SWISS-PROT45:Cytoplasmic.
MBNL_HUMAN	nucl	78.7207	12.5498%	[Uniprot] SWISS-PROT45:Nuclear. GO:0005634; C:nucleus; Evidence:IDA.
GLNA_RAT	cyto	78.7424	13.5458%	[Uniprot] SWISS-PROT45:Cytoplasmic.
GLNA_HUMAN	cyto	79.0541	13.5189%	[Uniprot] SWISS-PROT45:Cytoplasmic.
LDB1_MOUSE	nucl	79.064	13.9442%	[Uniprot] SWISS-PROT45:Nuclear.
GLNA_PIG	cyto	79.1874	13.1213%	[Uniprot] SWISS-PROT45:Cytoplasmic.
SBP2_MOUSE	cyto	79.3372	11.1332%	[Uniprot] SWISS-PROT45:Cytoplasmic.
CAO2_RAT	pero	79.738	13.8032%	[Uniprot] SWISS-PROT45:Peroxisomal.
KARG_LIMPO	cyto	82.0846	14.9402%	[Uniprot] SWISS-PROT45:Cytoplasmic.
EG27_CAEEL	nucl	82.4729	11.1603%	[Uniprot] SWISS-PROT45:Nuclear. GO:0005634; C:nucleus; Evidence:IDA.
PPL2_HUMAN	nucl	82.8319	11.2595%	[Uniprot] SWISS-PROT45:Nuclear. GO:0005634; C:nucleus; Evidence:TAS.
DPOD_MESAU	nucl	83.3379	11.9674%	[Uniprot] SWISS-PROT45:Nuclear.
SR72_SCHMA	cyto	83.7308	13.1542%	[Uniprot] SWISS-PROT45:Cytoplasmic.
UNK_DROME	cyto	83.7397	12%	[Uniprot] SWISS-PROT45:Cytoplasmic. GO:0005737; C:cytoplasm; Evidence:IDA.
DPOD_RAT	nucl	84.3517	12.33%	[Uniprot] SWISS-PROT45:Nuclear.
PPCM_CHICK	mito	84.3543	16.4062%	[Uniprot] SWISS-PROT45:Mitochondrial.
DSRA_RAT	nucl	84.4467	10.7234%	[Uniprot] SWISS-PROT45:Nuclear.
SYI_MOUSE	cyto	85.2467	12.2029%	[Uniprot] SWISS-PROT45:Cytoplasmic.
GLYC_MOUSE	cyto	85.4113	10.9562%	[Uniprot] SWISS-PROT45:Cytoplasmic.
RU1C_XENLA	nucl	86.1542	7.76892%	[Uniprot] SWISS-PROT45:Nuclear.
MPI3_MESAU	nucl	86.1785	13.5189%	[Uniprot] SWISS-PROT45:Nuclear.

Table Appendix 2. Analysis report of human FTO sequence performed by CELLO v2.5.

Analysis	LOCALISATION	RELIABILITY
Amino Acid Composition	Cytoplasmic	0.635
N-peptide Composition	Nuclear	0.753
Partitioned sequence Composition	Cytoplasmic	0.744
Physico-chemical Composition	Cytoplasmic	0.733
Amino Acid Composition	Cytoplasmic	0.841
CELLO Prediction:	LOCALISATION	SCORE
1	Cytoplasmic	3.167
2	Nuclear	1.353
3	Mitochondrial	0.121
4	Extracellular	0.114
5	Peroxisomal	0.064
6	Golgi	0.055
7	Chloroplast	0.041
8	ER	0.039
9	PlasmaMembrane	0.016
10	Cytoskeletal	0.014
11	Lysosomal	0.009
12	Vacuole	0.006

```
FTOmouse        MKRVQTAEEREREAKKLRLLEELEDTWLPYLTPKDDEFYQQWQLKYPKLVFREAGSIPEE 60
FTOhuman        MKRTPTAEEREREAKKLRLLEELEDTWLPYLTPKDDEFYQQWQLKYPKLILREASSVSEE 60
                ***. ******************************************::***.*:.**

FTOmouse        LHKEVPEAFLTLHKHGCLFRDVVRIQGKDVLTPVSRILIGDPGCTYKYLNTRLFTVPWPV 120
FTOhuman        LHKEVQEAFLTLHKHGCLFRDLVRIQGKDLLTPVSRILIGNPGCTYKYLNTRLFTVPWPV 120
                ***** ***************:*******:**********:********************

FTOmouse        KGCTVKYTEAEIAAACQTFLKLNDYLQVETIQALEELAVREKANEDAVPLCM-AEFPRAG 179
FTOhuman        KGSNIKHTEAEIAAACETFLKLNDYLQIETIQALEELAAKEKANEDAVPLCMSADFPRVG 180
                **..:*:*********:**********:**********.:************ *:***.*

FTOmouse        VGPSCD--DEVDLKSRAAYNVTLLNFMDPQKMPYLKEEPYFGMGKMAVSWHHDENLVDRS 237
FTOhuman        MGSSYNGQDEVDIKSRAAYNVTLLNFMDPQKMPYLKEEPYFGMGKMAVSWHHDENLVDRS 240
                :*.* :  ****:**********************************************

FTOmouse        AVAVYSYSCEGSEDESEDESSFEGRDPDTWHVGFKISWDIETPGLTIPLHQGDCYFMLDD 297
FTOhuman        AVAVYSYSCEGPEEESEDDSHLEGRDPDIWHVGFKISWDIETPGLAIPLHQGDCYFMLDD 300
                ***********.*:****:* :****** ***************:***************
```

Figure Appendix 1. Sequence alignment of N-terminal domain of mouse and human FTO. Numbers represent amino acid location within the protein sequence. Starts represent residues identical in both sequences. Alignment was performed using ClustalW2 ('ClustalW2, Multiple Sequence Alignment, EMBL-EBI' 2015).

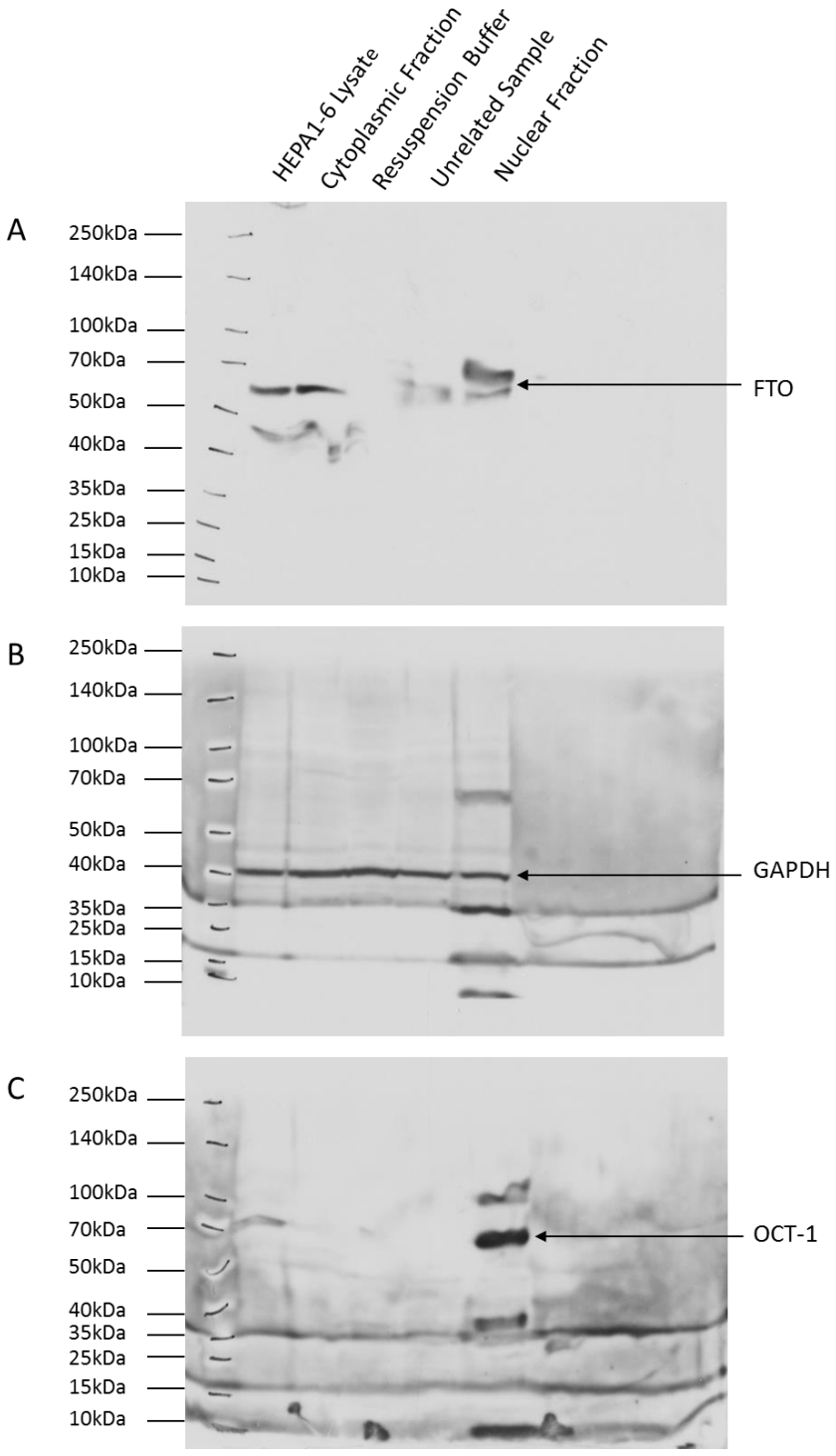

Figure Appendix 2. Immunoblotting analysis of subcellular fractions obtained by the nuclear extraction at the interface of two sucrose solutions. The protein concentration of each of the fractions was assessed by a colorimetric assay (2.4.3) and 50 µg of each samples was loaded in each well. Immunoblotting using specific antibody: **A**, in house raised rabbit anti-FTO; **B**, rabbit anti-GAPDH; **C**, rabbit anti-OCT1 (3.2.4).

Appendix 4 Identification of Proteins That Interact With FTO

Table Appendix 3. Proteins identified by MS in FTO pull-downs using increasing amounts of protein extract from HEPA1-6 cells.

A 250 µg of protein extract				B 500 µg of protein extract				C 5mg of protein extract			
Elution Beads		Elution Beads+αFTO		Elution Beads+αGFP		Elution Beads+αFTO		Elution Beads+αFTO		FTO control	
Score	Description	Score	Description	Score	Description	Score	Description	Score	Description	Score	Description
683	Trypsin	774	Trypsin	715	Ig gamma chain C region	150	Trypsin	351	Trypsin	429	Alpha-ketoglutarate-dependent dioxygenase FTO
444	Keratin, type II cytoskeletal 1	564	Keratin, type I cytoskeletal 10	599	Ig gamma chain C region	132	Keratin, type II cytoskeletal 1	226	60S ribosomal protein L7	338	Trypsin
189	Keratin, type II cytoskeletal 2 epidermal	513	Keratin, type II cytoskeletal 1	479	Ig gamma chain C region	62	Keratin, type I cytoskeletal 10	105	60 kDa heat shock protein, mitochondrial	21	Tetratricopeptide repeat protein 18
352	Keratin, type I cytoskeletal 10	315	Keratin, type II cytoskeletal 2 epidermal	423	Ig gamma chain C region	57	Keratin, type I cytoskeletal 9	65	Histone H1.2		
233	Anionic trypsin-1	161	Keratin, type II cytoskeletal 1	174	Ig kappa-b4 chain C region	24	Condensin complex subunit 1	44	Ig gamma chain C region		
213	Heat shock cognate 71 kDa protein	150	Keratin, type II cytoskeletal 6A	138	Ig kappa-b4 chain C region	22	Transcription factor HIVEP3	28	Adrenodoxin, mitochondrial		
128	Keratin, type I cytoskeletal 9	125	Keratin, type II cytoskeletal 1b	105	Keratin, type II cytoskeletal 1	21	Vacuolar protein sorting-associated protein 13B	25	Vimentin		
122	Keratin, type I cytoskeletal 17	58	Keratin, type II cytoskeletal 5	39	Trypsin	21	AT-rich interactive domain-containing protein 5B	23	Keratin, type II cytoskeletal 8		

A 250 µg of protein extract				B 500 µg of protein extract				C 5mg of protein extract			
Elution Beads		Elution Beads+αFTO		Elution Beads+αGFP		Elution Beads+αFTO		Elution Beads+αFTO		FTO control	
57	Alpha-S2-casein	231	Anionic trypsin-1	37	Ig kappa-b4 chain C region	302	Trypsin	19	Sperm equatorial segment protein 1		
55	Collagen alpha-1(I) chain	168	Ig gamma chain C region	35	Putative isochorismate synthase	48	Ig gamma chain C region	17	UDP-glucose:glycoprotein glucosyltransferase 1		
55	Alpha-S1-casein	155	Heat shock cognate 71 kDa protein	27	MIF4G domain-containing protein	25	Zinc finger protein 862	16	Suppressor of SWI4 1 homolog		
50	Trichohyalin	111	Keratin, type I cytoskeletal 9	26	Dedicator of cytokinesis protein 2	21	Keratin, type I cytoskeletal 9	563	Keratin, type II cytoskeletal 8		
42	Beta-lactoglobulin	61	Alpha-S1-casein	25	Kynureninase	19	6-phosphofructokinase type C	551	Vimentin		
33	Ribonuclease pancreatic	56	Alpha-S2-casein	25	Tyrosine-protein phosphatase non-receptor type 13	19	Abnormal spindle-like microcephaly-associated protein homolog	359	Trypsin		
30	Neutrophil cytosol factor 4	35	Ribonuclease pancreatic	24	Autophagy-related protein 2	151	Ig gamma chain C region	96	Heterogeneous nuclear ribonucleoprotein K		
28	Keratin, type II cytoskeletal 3	30	Ubiquitin-60S ribosomal protein L40	24	Thioredoxin	89	Trypsin	84	Anionic trypsin-1		
23	Neuroserpin	25	B-cell lymphoma/leukemia 11B	24	Cortactin-binding protein 2	86	Keratin, type II cytoskeletal 1	57	Pyruvate kinase isozymes M1/M2		
22	Coagulation factor XIII A chain	23	Solute carrier organic anion transporter family member 4A1	21	Guanylate-binding protein 3	72	Keratin, type I cytoskeletal 10	40	Keratin, type II cytoskeletal 1		

A 250 µg of protein extract				B 500 µg of protein extract				C 5mg of protein extract			
Elution Beads		Elution Beads+αFTO		Elution Beads+αGFP		Elution Beads+αFTO		Elution Beads+αFTO		FTO control	
19	Dual oxidase 1	17	RNA polymerase II subunit B1 CTD phosphatase Rpap2	21	T-box transcription factor TBX21	34	Keratin, type I cytoskeletal 17	32	Keratin, type II cytoskeletal 1b		
1029	Keratin, type II cytoskeletal 1	794	Keratin, type II cytoskeletal 1	20	Serine/threonine-protein kinase haspin	26	HEAT repeat-containing protein 5A	29	Serine/threonine-protein kinase LATS2		
493	Keratin, type II cytoskeletal 2 epidermal	230	Keratin, type II cytoskeletal 2 epidermal	19	Pyrophosphatase ppaX	24	V-set and transmembrane domain-containing protein 4	23	F-box only protein 24		
306	Keratin, type II cytoskeletal 1	765	Keratin, type I cytoskeletal 9	715	Ig gamma chain C region	23	Ig kappa-b4 chain C region	22	Histone H1t		
207	Keratin, type II cytoskeletal 1b	586	Trypsin	599	Ig gamma chain C region	20	Transcobalamin-2	22	tRNA pseudouridine synthase-like 1		
126	Keratin, type II cytoskeletal 75	237	Keratin, type I cytoskeletal 10	479	Ig gamma chain C region	20	Agrin	21	NF-kappa-B inhibitor zeta		
969	Keratin, type I cytoskeletal 10	123	Alpha-S1-casein	423	Ig gamma chain C region	18	A disintegrin and metalloproteinase with thrombospondin motifs 19	17	1-phosphatidylinositol 3-phosphate 5-kinase		
89	Keratin, type I cytoskeletal 14	120	Ig gamma chain C region	174	Ig kappa-b4 chain C region	199	Trypsin	551	ATP synthase subunit alpha, mitochondrial		
580	Keratin, type I cytoskeletal 9	68	Beta-lactoglobulin	138	Ig kappa-b4 chain C region	87	Keratin, type II cytoskeletal 1	394	Trypsin		
564	Trypsin	44	Alpha-S2-casein		Keratin, type II cytoskeletal 1	72	Keratin, type I cytoskeletal 10	199	60S ribosomal protein L14		
56	Alpha-S2-casein	37	Ribonuclease pancreatic		Trypsin	29	Ig gamma chain C region	193	60S ribosomal protein L14		

A 250 µg of protein extract				B 500 µg of protein extract				C 5mg of protein extract			
Elution Beads		Elution Beads+αFTO		Elution Beads+αGFP		Elution Beads+αFTO		Elution Beads+αFTO		FTO control	
54	Alpha-S1-casein	36	Serum albumin		Ig kappa-b4 chain C region	22	Disheveled-associated activator of morphogenesis 2	152	Heterogeneous nuclear ribonucleoprotein K		
41	Hepatocellular carcinoma-associated protein TD26 homolog	32	Ectopic P granules protein 5 homolog			21	Asparagine synthetase domain-containing protein 1	95	Ig gamma chain C region		
41	Protein kintoun	32	Hippocalcin-like protein 1					88	Vimentin		
30	Zinc transporter 9	29	Dermcidin					82	Elongation factor 1-alpha 1		
17	Actin-binding LIM protein 1	28	Solute carrier family 2, facilitated glucose transporter member 12					58	Keratin, type I cytoskeletal 18		
786	Keratin, type II cytoskeletal 1	26	Dual oxidase 1					57	D-3-phosphoglycerate dehydrogenase		
403	Keratin, type II cytoskeletal 2 epidermal	24	Trafficking protein particle complex subunit 9					41	Aldehyde dehydrogenase, mitochondrial		
203	Keratin, type II cytoskeletal 6A	17	Blood vessel epicardial substance					40	Keratin, type II cytoskeletal 8		
123	Keratin, type II cytoskeletal 75	669	Trypsin					31	Ankyrin repeat domain-containing protein SOWAHB		
77	Keratin, type II cytoskeletal 5	574	Keratin, type II cytoskeletal 1					22	Connector enhancer of kinase suppressor of ras 3		

A 250 µg of protein extract				B 500 µg of protein extract				C 5mg of protein extract			
Elution Beads		Elution Beads+αFTO		Elution Beads+αGFP		Elution Beads+αFTO		Elution Beads+αFTO		FTO control	
750	Keratin, type I cytoskeletal 10	258	Keratin, type II cytoskeletal 2 epidermal					20	UDP-glucose 6-dehydrogenase		
128	Keratin, type I cytoskeletal 14	135	Keratin, type II cytoskeletal 6C					16	Kelch-like protein 15		
102	Keratin, type I cytoskeletal 16	80	Keratin, type II cytoskeletal 5					268	Tubulin alpha-1B chain		
633	Trypsin	510	Keratin, type I cytoskeletal 10					233	Keratin, type I cytoskeletal 18		
316	Keratin, type I cytoskeletal 9	48	Keratin, type I cytoskeletal 14					92	Keratin, type I cytoskeletal 18		
153	Anionic trypsin-1	288	Keratin, type I cytoskeletal 9					222	Tubulin beta-5 chain		
110	Serum albumin	246	Ig gamma chain C region					210	Trypsin		
63	Dermcidin	183	Anionic trypsin-1					118	ATP synthase subunit beta, mitochondrial		
58	Alpha-S2-casein	135	Keratin, type I microfibrillar 48 kDa, component 8C-1					59	Elongation factor 1-alpha 1		
41	Alpha-S1-casein	89	Alpha-S1-casein					59	Heterogeneous nuclear ribonucleoprotein H		
34	Zinc transporter 9	67	Dermcidin					47	Heterogeneous nuclear ribonucleoprotein F		
23	Limbin	50	Serum albumin					45	40S ribosomal protein S6		

A 250 µg of protein extract				B 500 µg of protein extract				C 5mg of protein extract			
Elution Beads		Elution Beads+αFTO		Elution Beads+αGFP		Elution Beads+αFTO		Elution Beads+αFTO		FTO control	
		30	Pleckstrin homology domain-containing family A member 5					45	TAR DNA-binding protein 43		
		29	Nitric oxide synthase, brain					44	Obscurin		
		916	Keratin, type II cytoskeletal 1					38	Keratin, type I cytoskeletal 20		
		366	Keratin, type II cytoskeletal 6C					38	Heterogeneous nuclear ribonucleoprotein A3		
		154	Keratin, type II cytoskeletal 5					33	60S ribosomal protein L8		
		97	Keratin, type II cytoskeletal 2 epidermal					17	Sacsin		
		600	Keratin, type I cytoskeletal 9					285	Heterogeneous nuclear ribonucleoprotein A3		
		575	Trypsin					209	Trypsin		
		236	Anionic trypsin-1					207	Actin, cytoplasmic 1		
		408	Keratin, type I cytoskeletal 10					44	Keratin, type II cytoskeletal 1		
		393	Keratin, type I cytoskeletal 14					40	Keratin, type II cytoskeletal 1b		
		365	Keratin, type I cytoskeletal 16					39	Elongation factor Tu, mitochondrial		
		197	Keratin, type I cytoskeletal 17					30	Tripartite motif-containing protein 40		

A 250 µg of protein extract				B 500 µg of protein extract				C 5mg of protein extract			
Elution Beads		Elution Beads+αFTO		Elution Beads+αGFP		Elution Beads+αFTO		Elution Beads+αFTO		FTO control	
		231	Ig gamma chain C region					28	60S ribosomal protein L8		
		151	Alpha-S1-casein					27	60S ribosomal protein L14		
		51	Alpha-S2-casein					3021	Actin, cytoplasmic 2		
		38	Protein FAM35A					1453	Actin, alpha cardiac muscle 1		
		31	Pleckstrin homology domain-containing family A member 5					1141	Beta-actin-like protein 2		
		30	Ribonuclease pancreatic					183	Trypsin		
		28	Ribonuclease pancreatic					56	Keratin, type II cytoskeletal 1		
		26	Dermcidin					51	Poly(rC)-binding protein 1		
		26	Cytochrome P450 3A5					35	Calponin-3		
		21	Glucose-dependent insulinotropic receptor					30	Serine/threonine-protein kinase PLK1		
		20	Doublecortin domain-containing protein 5					25	Annexin A2		
								24	Heterogeneous nuclear ribonucleoprotein C		

Table Appendix 4. Unique FTO Proteins (without keratin) identified by MS in FTO pull downs using cryolysis and Dynabeads® M-270 Epoxy. PSC, protein score; SPM, significant protein matches; SPS, significant protein sequences.

Condition B					Condition C				
Accession	**Description**	**PSC**	**SPM**	**SPS**	**Accession**	**Description**	**PSC**	**SPM**	**SPS**
P60710	Actin, cytoplasmic 1	1048	40	8	P63260	Actin, cytoplasmic 2	445	24	6
Q8BGW1	Alpha-ketoglutarate-dependent dioxygenase FTO	500	26	18	Q62191	E3 ubiquitin-protein ligase TRIM21	246	10	1
Q62191	E3 ubiquitin-protein ligase TRIM21	305	12	8	Q64475	Histone H2B type 1-B	246	10	4
Q8CGP2	Histone H2B type 1-P	173	10	7	Q8BGW1	Alpha-ketoglutarate-dependent dioxygenase FTO	230	18	8
Q8R1M2	Histone H2A.J	159	10	3	Q8R1M2	Histone H2A.J	215	8	3
P14733	Lamin-B1	154	4	4	P62264	40S ribosomal protein S14	93	2	1
P17879	Heat shock 70 kDa protein 1B	147	8	2	P07724	Serum albumin	89	2	1
P02089	Hemoglobin subunit beta-2	114	5	4	Q60605	Myosin light polypeptide 6	79	3	3
Q64522	Histone H2A type 2-B	102	6	1	P62270	40S ribosomal protein S18	63	2	2
Q91VM5	RNA binding motif protein, X-linked-like-1	99	4	3	P67984	60S ribosomal protein L22	52	1	1
Q9Z204	Heterogeneous nuclear ribonucleoproteins C1/C2	92	2	2	Q61879	Myosin-10	49	2	1
P01942	Hemoglobin subunit alpha	91	3	3	P62317	Small nuclear ribonucleoprotein Sm D2	47	2	2
P10922	Histone H1.0	83	2	1	P84228	Histone H3.2	44	5	2
Q9WV02	RNA-binding motif protein, X chromosome	81	3	2	P61358	60S ribosomal protein L27	42	1	1
Q8C4J7	Transducin beta-like protein 3	66	1	1	Q9R0L6	Pericentriolar material 1 protein	41	1	1
P11276	Fibronectin	62	4	3	Q8CJ27	Abnormal spindle-like microcephaly-associated protein homolog	41	1	1
Q8VEK3	Heterogeneous nuclear ribonucleoprotein U	61	5	5	O35375	Neuropilin-2	39	3	1

P43274	Histone H1.4	60	1	1	P58774	Tropomyosin beta chain	38	1	1
Q8BL97	Serine/arginine-rich splicing factor 7	60	5	4	Q8BYW9	EGF domain-specific O-linked N-acetylglucosamine transferase	37	1	1
Q64012	RNA-binding protein Raly	59	1	1	P56480	ATP synthase subunit beta, mitochondrial	36	1	1
Q9Z2X1	Heterogeneous nuclear ribonucleoprotein F	57	2	2	Q99MY8	Histone-lysine N-methyltransferase ASH1L	35	1	1
P21619	Lamin-B2	53	1	1	Q3ZT31	Sorting nexin-25	35	2	2
P68433	Histone H3.1	53	2	1	Q9JK88	Serpin I2	35	1	1
P62307	Small nuclear ribonucleoprotein F	52	1	1	Q9QXV9	Protein sprouty homolog 1	34	1	1
Q9CYR0	Single-stranded DNA-binding protein, mitochondrial	51	2	2	Q9EQH3	Vacuolar protein sorting-associated protein 35	34	1	1
Q9D6Z1	Nucleolar protein 56	51	1	1	Q3UH60	Disco-interacting protein 2 homolog B	34	1	1
Q99KP6	Pre-mRNA-processing factor 19	49	2	2	Q91Z92	Beta-1,3-galactosyltransferase 6	34	1	1
P49312	Heterogeneous nuclear ribonucleoprotein A1	49	1	1	P22518	Dual specificity protein kinase CLK1	33	1	1
P32067	Lupus La protein homolog	49	1	1	Q5F201	WD repeat-containing protein 16	33	1	1
P62320	Small nuclear ribonucleoprotein Sm D3	48	1	1	P03995	Glial fibrillary acidic protein	32	1	1
P83917	Chromobox protein homolog 1	47	1	1	Q8C078	Calcium/calmodulin-dependent protein kinase kinase 2	32	1	1
P02104	Hemoglobin subunit epsilon-Y2	45	1	1	Q91W29	Cytochrome c oxidase subunit 4 isoform 2, mitochondrial	32	1	1
O35737	Heterogeneous nuclear ribonucleoprotein H	45	1	1	Q6A026	Sister chromatid cohesion protein PDS5 homolog A	31	1	1
Q62093	Serine/arginine-rich splicing factor 2	45	1	1	Q8BMI3	ADP-ribosylation factor-binding protein GGA3	31	1	1
Q9Z2W8	Glutamate receptor 4	45	1	1	Q91Y44	Bromodomain testis-specific protein	31	1	1
Q9R0E1	Procollagen-lysine,2-oxoglutarate 5-dioxygenase 3	45	1	1	Q7TQI3	Ubiquitin thioesterase OTUB1	30	1	1
P15331	Peripherin	44	2	1	Q6P5D8	Structural maintenance of chromosomes flexible hinge domain-containing protein 1	30	1	1

P61327	Protein mago nashi homolog	44	1	1	Q7SIG6	Arf-GAP with SH3 domain, ANK repeat and PH domain-containing protein 2	30	1	1
P46978	Dolichyl-diphosphooligosaccharide--protein glycosyltransferase subunit STT3A	44	1	1	Q80VC6	tRNA selenocysteine 1-associated protein 1	29	1	1
P27048	Small nuclear ribonucleoprotein-associated protein B	43	1	1	Q69Z37	Sterile alpha motif domain-containing protein 9-like	29	1	1
P84102	Small EDRK-rich factor 2	42	1	1	Q5KU39	Vacuolar protein sorting-associated protein 41 homolog	29	1	1
Q8CEC0	Nuclear pore complex protein Nup88	42	1	1	Q66PY1	Signal peptide, CUB and EGF-like domain-containing protein 3	28	1	1
Q61029	Lamina-associated polypeptide 2, isoforms beta/delta/epsilon/gamma	42	1	1	P70429	Ena/VASP-like protein	28	1	1
Q03265	ATP synthase subunit alpha, mitochondrial	41	1	1	Q9QY06	Unconventional myosin-IXb	28	1	1
Q8R4B8	NACHT, LRR and PYD domains-containing protein 3	41	1	1	Q9JI18	Low-density lipoprotein receptor-related protein 1B	27	1	1
Q9ERK4	Exportin-2	40	2	1	P04939	Major urinary protein 3	27	1	1
P38647	Stress-70 protein, mitochondrial	40	1	1	P43406	Integrin alpha-V	27	1	1
Q9D6L8	Peptidyl-prolyl cis-trans isomerase-like 3	40	1	1	Q3UPR9	Somatomedin-B and thrombospondin type-1 domain-containing protein	26	1	1
Q8R4P4	Transmembrane channel-like protein 2	40	1	1	Q9ER73	Elongator complex protein 4	25	1	1
Q9CZX8	40S ribosomal protein S19	40	1	1	Q68FL6	Methionine--tRNA ligase, cytoplasmic	25	1	1
Q80W93	Hydrocephalus-inducing protein	38	1	1	O54887	Testis-specific serine kinase substrate	25	1	1
Q62407	Striated muscle-specific serine/threonine-protein kinase	38	1	1	A2RTL5	Arginine/serine-rich coiled-coil protein 2	25	1	1
Q8K2W9	Uncharacterized protein C14orf93 homolog	37	1	1	Q9DBD0	Inhibitor of carbonic anhydrase	25	1	1
Q68FM6	Protein phosphatase 1 regulatory subunit 29	37	1	1	Q8K4L3	Supervillin	25	1	1
Q99N48	Synaptotagmin-like protein 3	37	1	1	Q8BY87	Ubiquitin carboxyl-terminal hydrolase 47	24	1	1
Q8C119	Protein NDNF	37	1	1	O35955	Proteasome subunit beta type-10	24	1	1
Q6NXJ0	Protein WWC2	37	1	1	P42859	Huntingtin	24	1	1

Q8C9X6	Enhancer of polycomb homolog 1	36	1	1	O54851	Gap junction delta-2 protein	24	1	1
A2A3V1	A-kinase anchor protein 17B	36	1	1	Q9QYZ6	Sperm motility kinase 2A	24	1	1
Q05816	Fatty acid-binding protein, epidermal	36	1	1	Q3UJB3	Leucine-rich repeat-containing protein 14B	24	1	1
P08249	Malate dehydrogenase, mitochondrial	36	1	1	Q8C0D0	Probable tRNA pseudouridine synthase 1	24	1	1
P43027	Growth/differentiation factor 5	35	1	1	Q3TYA6	M-phase phosphoprotein 8	23	1	1
Q9R160	Disintegrin and metalloproteinase domain-containing protein 24	35	1	1	Q65Z40	Wings apart-like protein homolog	23	1	1
Q9CQU1	Microfibrillar-associated protein 1	34	1	1	Q6PFD6	Kinesin-like protein KIF18B	23	1	1
Q08639	Transcription factor Dp-1	34	1	1	P97412	Lysosomal-trafficking regulator	23	1	1
Q924W5	Structural maintenance of chromosomes protein 6	33	1	1	P23607	Zinc finger autosomal protein	23	1	1
P12382	6-phosphofructokinase, liver type	33	1	1	Q9D7V2	LysM and putative peptidoglycan-binding domain-containing protein 2	23	1	1
O88286	Protein Wiz	33	1	1	Q8VE92	RNA-binding protein 4B	22	1	1
Q9WVC6	Serine/threonine-protein kinase Sgk1	33	1	1	Q99JX7	Nuclear RNA export factor 1	22	1	1
Q9JKX6	ADP-sugar pyrophosphatase	33	1	1	P51450	Nuclear receptor ROR-gamma	22	1	1
P62858	40S ribosomal protein S28	32	1	1	Q8BFX1	E3 ubiquitin-protein ligase RNF187	22	1	1
P62830	60S ribosomal protein L23	32	1	1	Q812A2	SLIT-ROBO Rho GTPase-activating protein 3	22	1	1
Q3TLH4	Protein PRRC2C	32	1	1	P26618	Platelet-derived growth factor receptor alpha	21	1	1
P50543	Protein S100-A11	31	1	1	A2AR50	Ras-specific guanine nucleotide-releasing factor RalGPS1	21	1	1
Q68FE6	Protein FAM65A	31	1	1	Q9JMC3	DnaJ homolog subfamily A member 4	21	1	1
P83510	Traf2 and NCK-interacting protein kinase	31	1	1	Q60770	Syntaxin-binding protein 3	21	1	1
P33267	Cytochrome P450 2F2	31	1	1	Q80V26	Inositol monophosphatase 3	21	1	1
A6H619	PHD and RING finger domain-containing protein 1	31	1	1	Q9QZ41	Protein DBF4 homolog A	21	1	1
Q9JLB2	MAGUK p55 subfamily member 5	31	1	1	Q8CG73	Protein fantom	21	1	1

Q52KG5	Kinesin-like protein KIF26A	31	1	1	Q80TZ3	Putative tyrosine-protein phosphatase auxilin	21	1	1
Q6PDQ2	Chromodomain-helicase-DNA-binding protein 4	30	1	1	Q80VM3	Tetratricopeptide repeat protein 29	21	1	1
P97820	Mitogen-activated protein kinase kinase kinase kinase 4	30	2	1	P97819	85 kDa calcium-independent phospholipase A2	21	1	1
P62264	40S ribosomal protein S14	30	1	1	Q61001	Laminin subunit alpha-5	20	1	1
Q8CBQ5	Phosphatidylinositol 4-kinase type 2-beta	30	1	1	P59096	StAR-related lipid transfer protein 6	20	1	1
Q8CI43	Myosin light chain 6B	30	1	1	Q80VL1	Tudor and KH domain-containing protein	20	1	1
P68254	14-3-3 protein theta	30	3	1	Q8BKX1	Brain-specific angiogenesis inhibitor 1-associated protein 2	20	1	1
Q8VCJ6	Mas-related G-protein coupled receptor member F	30	1	1	Q922U1	U4/U6 small nuclear ribonucleoprotein Prp3	20	1	1
Q9Z319	Atrial natriuretic peptide-converting enzyme	29	1	1	Q9DAU1	Protein canopy homolog 3	20	2	1
Q6PDH0	Pleckstrin homology-like domain family B member 1	29	1	1	Q8CHR6	Dihydropyrimidine dehydrogenase [NADP(+)]	20	1	1
Q8R480	Nuclear pore complex protein Nup85	29	1	1	Q7TPH6	Probable E3 ubiquitin-protein ligase MYCBP2	20	1	1
Q8BU00	Zinc finger protein Pegasus	29	1	1	Q6VYH9	Hematopoietic SH2 domain-containing protein	20	1	1
Q569L8	Centromere protein J	29	1	1	Q80YD1	ATP-dependent RNA helicase SUPV3L1, mitochondrial	19	1	1
Q61315	Adenomatous polyposis coli protein	29	1	1	Q6ZWQ0	Nesprin-2	19	1	1
Q3V125	Coiled-coil domain-containing protein 110	28	1	1	A2CG49	Kalirin	19	1	1
A2AWL7	MAX gene-associated protein	28	1	1	Q9Z2G1	Protein fem-1 homolog A-A	19	1	1
O70570	Polymeric immunoglobulin receptor	27	1	1	O08749	Dihydrolipoyl dehydrogenase, mitochondrial	19	1	1
P35330	Intercellular adhesion molecule 2	27	1	1	Q7TME0	Lipid phosphate phosphatase-related protein type 4	19	1	1
Q6ZPG2	WD repeat-containing protein 90	27	1	1	Q99NF8	Ran-binding protein 17	19	1	1

Q8BP00	IQ calmodulin-binding motif-containing protein 1	27	1	1	P08121	Collagen alpha-1(III) chain	19	1	1
Q9WVC8	Chloride anion exchanger	27	1	1	Q924C5	Alpha-protein kinase 3	18	1	1
Q9CU62	Structural maintenance of chromosomes protein 1A	26	1	1	Q80TY5	Vacuolar protein sorting-associated protein 13B	18	1	1
P35377	Nociceptin receptor	26	1	1	P43081	Guanylyl cyclase-activating protein 1	18	1	1
Q8BJQ2	Ubiquitin carboxyl-terminal hydrolase 1	26	1	1	Q9CXW3	Calcyclin-binding protein	18	2	2
P55066	Neurocan core protein	26	1	1	Q9D7Z6	Calcium-activated chloride channel regulator 1	18	1	1
P35601	Replication factor C subunit 1	26	1	1	P97927	Laminin subunit alpha-4	18	1	1
Q3TYG6	Protein FAM179A	26	1	1	Q61644	Protein kinase C and casein kinase substrate in neurons protein 1	18	1	1
P61358	60S ribosomal protein L27	26	1	1	O70306	T-box transcription factor TBX15	18	1	1
Q9QZ05	Eukaryotic translation initiation factor 2-alpha kinase 4	26	1	1	Q8BHM9	Transmembrane protease serine 11F	17	1	1
Q9Z1M0	P2X purinoceptor 7	26	1	1	P06801	NADP-dependent malic enzyme	17	1	1
Q02819	Nucleobindin-1	26	1	1	Q80Y39	Uncharacterized protein C10orf62 homolog	17	1	1
Q3UVR3	Tau-tubulin kinase 2	26	1	1	Q9CWP6	Motile sperm domain-containing protein 2	17	1	1
O35405	Phospholipase D3	25	1	1	Q04592	Proprotein convertase subtilisin/kexin type 5	17	1	1
Q8BKF1	DNA-directed RNA polymerase, mitochondrial	25	1	1	P58022	Lysyl oxidase homolog 2	17	2	2
Q7TSH3	Zinc finger protein 516	25	1	1	P47857	6-phosphofructokinase, muscle type	17	1	1
Q6PIX9	Uncharacterized protein C17orf80 homolog	25	1	1	Q3UHU5	Protein SOGA2	17	1	1
Q8VDF2	E3 ubiquitin-protein ligase UHRF1	24	1	1	Q149F3	Eukaryotic peptide chain release factor GTP-binding subunit ERF3B	17	1	1
Q99LQ1	MAP3K12-binding inhibitory protein 1	24	1	1	O08914	Fatty-acid amide hydrolase 1	17	1	1
Q6PFD7	Nuclear apoptosis-inducing factor 1	24	1	1	Q8C9E8	Protein FAM26F	17	1	1
P61407	Tudor domain-containing protein 6	24	1	1	Q62036	5-azacytidine-induced protein 1	17	1	1

P27773	Protein disulfide-isomerase A3	24	1	1	Q8BNJ2	A disintegrin and metalloproteinase with thrombospondin motifs 4	17	1	1
O55142	60S ribosomal protein L35a	24	1	1	Q5U430	E3 ubiquitin-protein ligase UBR3	17	1	1
Q9QXA6	B(0,+)-type amino acid transporter 1	23	1	1	Q99MQ5	Collagen alpha-1(XXV) chain	17	1	1
Q8BFX3	BTB/POZ domain-containing protein KCTD3	23	1	1	P62309	Small nuclear ribonucleoprotein G	16	1	1
Q6DFV6	Fibronectin type III domain containing protein 3C1	23	1	1	Q9QZL0	Receptor-interacting serine/threonine-protein kinase 3	16	1	1
Q3V3K7	Beta-1,3-galactosyl-O-glycosyl-glycoprotein beta-1,6-N-acetylglucosaminyltransferase 7	23	1	1	Q3UZ01	RNA-binding protein 40	16	1	1
O35638	Cohesin subunit SA-2	23	1	1	Q5XG71	Small subunit processome component 20 homolog	16	1	1
Q9Z1G3	V-type proton ATPase subunit C 1	22	1	1	Q3V079	Uncharacterized protein C14orf45 homolog	16	1	1
P62484	Abl interactor 2	22	1	1	Q07409	Contactin-3	16	1	1
D3YXK2	Scaffold attachment factor B1	22	1	1	Q8C0M8	Dynein intermediate chain 1, axonemal	16	1	1
Q8BJL1	F-box only protein 30	22	1	1	Q8CGM1	Brain-specific angiogenesis inhibitor 2	16	1	1
Q640L5	Coiled-coil domain-containing protein 18	22	1	1	A2AJB1	Uncharacterized coiled-coil domain-containing protein KIAA1984	15	1	1
Q66JV4	RNA-binding protein 12B-B	22	1	1	B2RX88	Centrosome and spindle pole associated protein 1	15	1	1
Q6VNB8	WD repeat and FYVE domain-containing protein 3	22	1	1	Q64739	Collagen alpha-2(XI) chain	15	1	1
Q62465	Synaptic vesicle membrane protein VAT-1 homolog	22	1	1	Q8K448	ATP-binding cassette sub-family A member 5	15	1	1
Q7TPH6	Probable E3 ubiquitin-protein ligase MYCBP2	22	1	1	P15208	Insulin receptor	15	1	1
P52482	Ubiquitin-conjugating enzyme E2 E1	22	1	1	Q68SA9	A disintegrin and metalloproteinase with thrombospondin motifs 7	15	1	1
Q9QZB0	Regulator of G-protein signaling 17	21	1	1	Q9EPU4	Cleavage and polyadenylation specificity factor subunit 1	15	1	1
Q9QZR9	Collagen alpha-4(IV) chain	21	1	1	Q8VI88	Outer dense fiber protein 4	15	1	1

Q6GQT6	Sterol regulatory element-binding protein cleavage-activating protein	21	1	1	Q811D0	Disks large homolog 1	15	1	1
Q9EQF6	Dihydropyrimidinase-related protein 5	21	1	1	Q8CCH2	NHL repeat-containing protein 3	14	1	1
Q6Q899	Probable ATP-dependent RNA helicase DDX58	21	1	1	O89023	Tripeptidyl-peptidase 1	14	1	1
Q9WTQ5	A-kinase anchor protein 12	21	1	1	P46096	Synaptotagmin-1	14	1	1
O35082	Klotho	20	1	1	D3YXK2	Scaffold attachment factor B1	14	1	1
Q7M742	Secretoglobin family 1C member 1	20	1	1	Q9D2G9	HHIP-like protein 2	14	1	1
O70133	ATP-dependent RNA helicase A	20	1	1	Q9DB15	39S ribosomal protein L12, mitochondrial	14	1	1
P50586	Tubby protein	19	1	1	Q9ET30	Transmembrane 9 superfamily member 3	14	1	1
Q03141	MAP/microtubule affinity-regulating kinase 3	19	1	1	Q9Z2U2	Zinc finger protein 292	13	1	1
P48356	Leptin receptor	19	1	1	Q8CIE6	Coatomer subunit alpha	13	1	1
Q5XF90	Probable cation-transporting ATPase 13A4	19	1	1	Q9Z1T6	1-phosphatidylinositol 3-phosphate 5-kinase	13	1	1
O35955	Proteasome subunit beta type-10	19	1	1	Q5SSM3	Rho GTPase-activating protein 44	13	1	1
Q8K2Z8	Ubiquitin-conjugating enzyme E2 Q2	19	1	1	Q00977	Gap junction beta-2 protein	13	1	1
Q8R4P9	Multidrug resistance-associated protein 7	18	1	1	O35368	Interferon-activable protein 203	13	1	1
Q3TB92	Allergin-1	18	1	1	Q8C4S8	DENN domain-containing protein 2A	13	1	1
Q6PCX9	E3 ubiquitin-protein ligase TRIM37	18	1	1	Q9WV34	MAGUK p55 subfamily member 2	13	1	1
Q99NE5	Regulating synaptic membrane exocytosis protein 1	18	1	1	Q9DAA6	Exosome complex component CSL4	13	1	1
B1AS29	Glutamate receptor, ionotropic kainate 3	17	1	1					
Q9EST1	Gasdermin-A	16	1	1					
Q921F2	TAR DNA-binding protein 43	16	1	1					
P21278	Guanine nucleotide-binding protein subunit alpha-11	15	1	1					
P32020	Non-specific lipid-transfer protein	15	1	1					
Q64318	Zinc finger E-box-binding homeobox 1	15	1	1					

Q9CWU0	Tudor domain-containing protein 12	14	1	1					
E9Q634	Unconventional myosin-Ie	13	1	1					
P62900	60S ribosomal protein L31	13	1	1					
Q99MR1	PERQ amino acid-rich with GYF domain-containing protein 1	13	1	1					

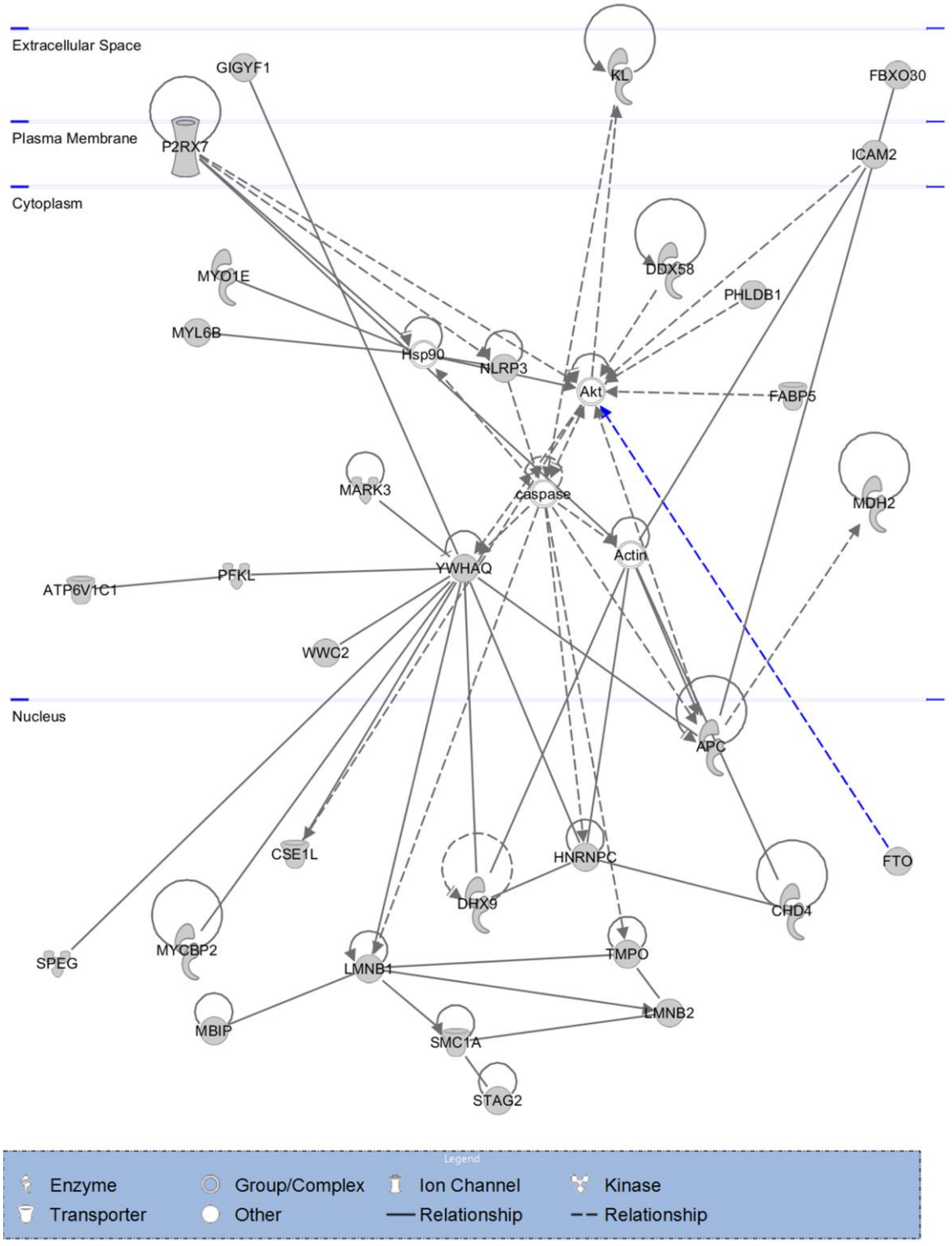

Figure Appendix 3. Graphical representation of the Network 1 identified by IPA. Proteins present in the FTO pull-down (Condition B) are filled in grey.

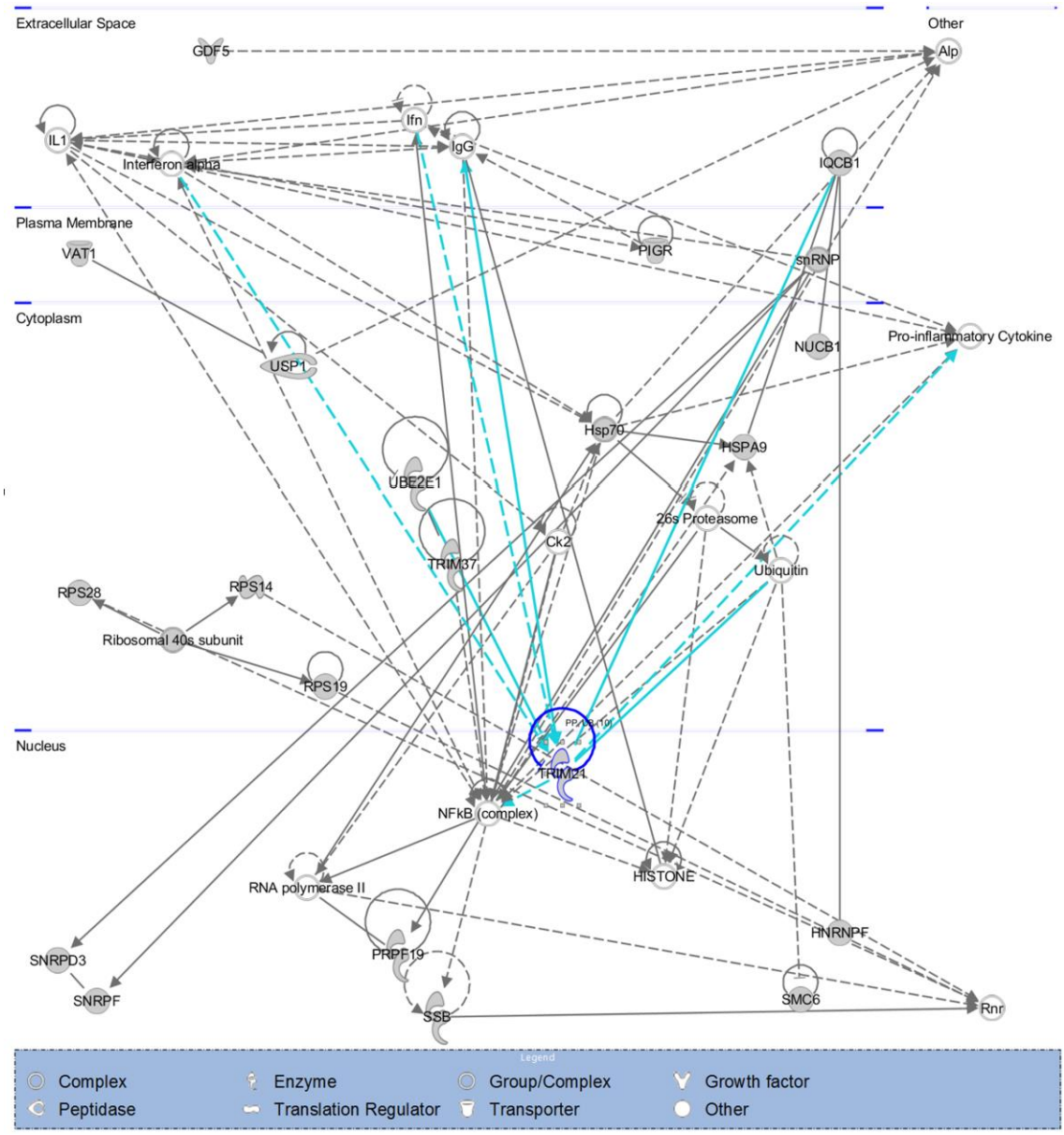

Figure Appendix 4. Graphical representation of the Network 3 identified by IPA. Proteins present in the FTO pull-down (Condition B) are filled in grey.

Appendix 5 Characterisation of TRIM21 and FTO Interaction

Appendix 5.1 In-Situ Cell Death Detection

Apoptotic cell death was studied using In-situ Cell Death Detection Kit (Roche, 11684795910) following the manufacturer's protocol for labelling adherent cells. The identification of apoptotic cells was based on the direct detection of DNA strand breaks by labelling them with fluorescein dUTP in the reaction catalysed by terminal transferase. Labelled with fluorescein DNA breaks were detected by the confocal laser microscopy using the green channel (2.3.4). The DNA fragmentation for the positive control was performed by incubating the cells with 3000 U/ml nuclease solution (Benzonase Nuclease E1014-25KU, Sigma-Aldrich) in 50 mM Tris-HCl, pH 7.5 for 10 minutes at 37 ^{o}C. Cells expressing MYC-TRIM21 and truncated variants were detected by the immunocytochemistry analysis according to the protocol described in 2.3.3 using the antibodies pair A2 and B2 as described in Chapter 5, 5.2.7.

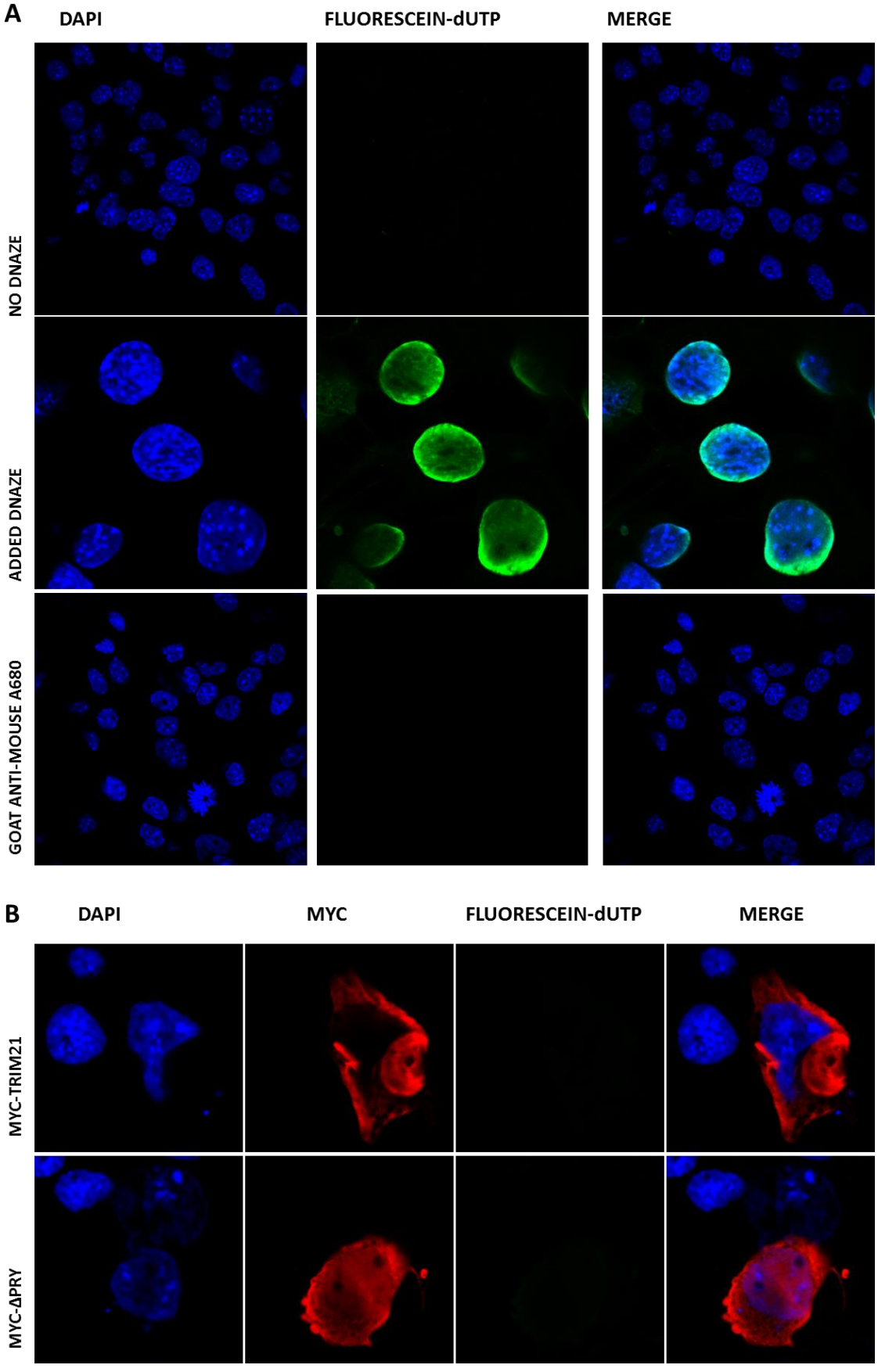
A
DAPI
FLUORESCEIN-dUTP
MERGE
NO DNAZE
ADDED DNAZE
GOAT ANTI-MOUSE A680
B
DAPI
MYC
FLUORESCEIN-dUTP
MERGE
MYC-TRIM21
MYC-ΔPRY

Figure Appendix 5. Analysis of HEPA1-6 cell death. Immunocytochemistry of HEPA1-6 cells subjected to In-situ Cell Death Detection. **A**, Confocal images of untreated cells, cells treated with DNase, and cells stained with Alexa 680 conjugated secondary antibody only. **B**, Confocal images of cells expressing full length MYC-TRIM21 and MYC-ΔPRY. The cell nucleus was visualised with DAPI (blue), DNA breaks were visualised by fluorescein-dUTP (green) and MYC-tagged TRIM21 variants were detected with mouse anti-MYC antibody and anti-mouse Alexa 680 secondary antibody (red).

Table Appendix 5. Proteins (without keratin, tubuline and myosine) identified by MS in FTO pull down from cell-based analysis of FTO ubiquitination experiment (5.3.5, Figure 36). Numbers in light grey cells represent gel pieces marked in the Figure 36. PSC, protein score.

FTO+TRIM21+UB			FTO+ΔRING+UB			FTO+UB+PR619		
Accession	**PSC**	**Description**	**Accession**	**PSC**	**Description**	**Accession**	**PSC**	**Description**
1			**1**			**1**		
Q62191	56	E3 ubiquitin-protein ligase TRIM21	Q62191	73	E3 ubiquitin-protein ligase TRIM21	Q8VDD5	45	Myosin-9
Q99PV0	40	Pre-mRNA-processing-splicing factor 8	Q8R081	36	Heterogeneous nuclear ribonucleoprotein L	Q8CGM2	41	Retinitis pigmentosa 1-like 1 protein
Q9QZM3	29	Cardiotrophin-like cytokine factor 1	Q9CQ10	29	Charged multivesicular body protein 3	Q80TV8	36	CLIP-associating protein 1
Q3UNZ8	21	Quinone oxidoreductase-like protein 2	Q7TPH6	24	Probable E3 ubiquitin-protein ligase MYCBP2	Q9JHU4	33	Cytoplasmic dynein 1 heavy chain 1
						P97868	28	E3 ubiquitin-protein ligase RBBP6
						Q9DCD2	24	Pre-mRNA-splicing factor SYF1
						Q8K093	23	Thyrotropin-releasing hormone-degrading ectoenzyme
						P61957	18	Small ubiquitin-related modifier 2
2			**2**			**2**		
Q01320	48	DNA topoisomerase 2-alpha	Q62191	185	E3 ubiquitin-protein ligase TRIM21	Q8BGW1	76	Alpha-ketoglutarate-dependent dioxygenase FTO
Q9EPW0	21	Type I inositol 3,4-bisphosphate 4-phosphatase	P62748	34	Hippocalcin-like protein 1	P62983	46	Ubiquitin-40S ribosomal protein S27a
Q9JJS0	14	Signal peptide, CUB and EGF-like domain-containing protein 2	Q64511	24	DNA topoisomerase 2-beta	P16546	33	Spectrin alpha chain, non-erythrocytic 1

			P82198	23	Transforming growth factor-beta-induced protein ig-h3	Q8CCM6	27	Mitochondrial import inner membrane translocase subunit Tim21
			Q91ZP3	23	Phosphatidate phosphatase LPIN1	Q6ZWR6	27	Nesprin-1
			O88286	17	Protein Wiz	Q3UTH8	25	Rho guanine nucleotide exchange factor 9
						Q9Z1K7	14	Adenomatous polyposis coli protein 2
3			**3**			**3**		
P11103	357	Poly [ADP-ribose] polymerase 1	Q62191	295	E3 ubiquitin-protein ligase TRIM21	P11103	81	Poly [ADP-ribose] polymerase 1
Q62191	201	E3 ubiquitin-protein ligase TRIM21	P11103	292	Poly [ADP-ribose] polymerase 1	Q8BGW1	53	Alpha-ketoglutarate-dependent dioxygenase FTO
Q920B9	126	FACT complex subunit SPT16	Q8BGW1	61	Alpha-ketoglutarate-dependent dioxygenase FTO	Q01320	39	DNA topoisomerase 2-alpha
O70133	53	ATP-dependent RNA helicase A	Q920B9	49	FACT complex subunit SPT16	Q8R4F0	28	Mucolipin-3
Q8VEK3	50	Heterogeneous nuclear ribonucleoprotein U	Q7TQI7	42	Ankyrin repeat and BTB/POZ domain-containing protein 2	Q9QYI7	27	DnaJ homolog subfamily B member 8
Q91ZW3	37	SWI/SNF-related matrix-associated actin-dependent regulator of chromatin subfamily A member 5	O70133	42	ATP-dependent RNA helicase A	P07901	23	Heat shock protein HSP 90-alpha
Q8R313	33	Exocyst complex component 6	Q91ZW3	40	SWI/SNF-related matrix-associated actin-dependent regulator of chromatin subfamily A member 5	Q8VHE6	23	Dynein heavy chain 5, axonemal
Q91WM1	33	Spermatid perinuclear RNA-binding protein	Q3URD3	38	Sarcolemmal membrane-associated protein	P30415	15	NK-tumor recognition protein

Q8BGW1	32	Alpha-ketoglutarate-dependent dioxygenase FTO	Q99PU8	36	Putative ATP-dependent RNA helicase DHX30			
Q80YR5	30	Scaffold attachment factor B2	Q4VAC9	34	Pleckstrin homology domain-containing family G member 3			
Q9Z0S4	26	Claudin-13	P97494	33	Glutamate--cysteine ligase catalytic subunit			
Q8K310	25	Matrin-3	Q91YX0	27	Protein THEMIS2			
Q9Z1A9	25	TBC1 domain family member 8	Q6GUQ1	25	Epidermal growth factor-like protein 8			
Q62074	23	Protein kinase C iota type	P97318	14	Disabled homolog 1			
P39688	20	Tyrosine-protein kinase Fyn						
4			**4**			**4**		
P11103	62	Poly [ADP-ribose] polymerase 1	Q62191	295	E3 ubiquitin-protein ligase TRIM21	P11499	178	Heat shock protein HSP 90-beta
Q08943	47	FACT complex subunit SSRP1	P11103	292	Poly [ADP-ribose] polymerase 1	P07901	143	Heat shock protein HSP 90-alpha
Q8BGW1	42	Alpha-ketoglutarate-dependent dioxygenase FTO	Q8BGW1	61	Alpha-ketoglutarate-dependent dioxygenase FTO	Q8BGW1	80	Alpha-ketoglutarate-dependent dioxygenase FTO
P62983	40	Ubiquitin-40S ribosomal protein S27a	Q920B9	49	FACT complex subunit SPT16	P20152	42	Vimentin
Q63ZV0	36	Insulinoma-associated protein 1	Q7TQI7	42	Ankyrin repeat and BTB/POZ domain-containing protein 2	P11103	41	Poly [ADP-ribose] polymerase 1
Q99KH8	32	Serine/threonine-protein kinase 24	O70133	42	ATP-dependent RNA helicase A	Q3URD3	34	Sarcolemmal membrane-associated protein
Q0P557	29	Mitochondria-eating protein	Q91ZW3	40	SWI/SNF-related matrix-associated actin-dependent regulator of chromatin subfamily A member 5	A1L314	20	Macrophage-expressed gene 1 protein
Q8BMA6	28	Signal recognition particle subunit SRP68	Q3URD3	38	Sarcolemmal membrane-associated protein			

O35286	26	Putative pre-mRNA-splicing factor ATP-dependent RNA helicase DHX15	Q99PU8	36	Putative ATP-dependent RNA helicase DHX30			
Q9D0E1	25	Heterogeneous nuclear ribonucleoprotein M	Q4VAC9	34	Pleckstrin homology domain-containing family G member 3			
Q61687	24	Transcriptional regulator ATRX	P97494	33	Glutamate--cysteine ligase catalytic subunit			
Q61001	23	Laminin subunit alpha-5	Q91YX0	27	Protein THEMIS2			
			Q6GUQ1	25	Epidermal growth factor-like protein 8			
			P97318	14	Disabled homolog 1			
			Q62191	258	E3 ubiquitin-protein ligase TRIM21			
			Q08943	70	FACT complex subunit SSRP1			
			Q8BGW1	51	Alpha-ketoglutarate-dependent dioxygenase FTO			
			Q9D0E1	47	Heterogeneous nuclear ribonucleoprotein M			
			Q7SIG6	43	Arf-GAP with SH3 domain, ANK repeat and PH domain-containing protein 2			
			Q640L5	40	Coiled-coil domain-containing protein 18			
			P51906	39	Excitatory amino acid transporter 3			
			Q505G8	29	Zinc finger protein 827			
			P15864	28	Histone H1.2			
			Q3UHQ6	28	Protein dopey-2			

			Q9JHC9	26	ETS-related transcription factor Elf-2			
			Q32KG4	24	Retrotransposon gag domain-containing protein 1			
			Q8R5K4	21	Nucleolar protein 6			
5			**5**			**5**		
Q8BGW1	506	Alpha-ketoglutarate-dependent dioxygenase FTO	Q8BGW1	600	Alpha-ketoglutarate-dependent dioxygenase FTO	P07901	113	Heat shock protein HSP 90-alpha
Q62191	475	E3 ubiquitin-protein ligase TRIM21	Q62191	529	E3 ubiquitin-protein ligase TRIM21	P11499	88	Heat shock protein HSP 90-beta
P14733	73	Lamin-B1	P20152	62	Vimentin	Q8BGW1	102	Alpha-ketoglutarate-dependent dioxygenase FTO
P62983	49	Ubiquitin-40S ribosomal protein S27a	P17879	48	Heat shock 70 kDa protein 1B	P14733	71	Lamin-B1
Q5ISE2	42	Zinc finger protein 36, C3H1 type-like 3	Q9Z148	34	Histone-lysine N-methyltransferase EHMT2	Q3URD3	40	Sarcolemmal membrane-associated protein
Q9DAL3	40	Coiled-coil domain-containing protein 54	Q62266	26	Cornifin-A	Q8R081	30	Heterogeneous nuclear ribonucleoprotein L
Q80W93	29	Hydrocephalus-inducing protein	Q8BGB7	25	Enolase-phosphatase E1	Q62191	30	E3 ubiquitin-protein ligase TRIM21
Q8BQP9	27	Regulator of G-protein signaling 7-binding protein				Q8K3X4	28	Interferon regulatory factor 2-binding protein-like
P26618	22	Platelet-derived growth factor receptor alpha				A2AUU0	26	Methyltransferase-like protein 8
Q8BYJ6	15	TBC1 domain family member 4				Q9WTS4	25	Teneurin-1
						Q91WF7	24	Polyphosphoinositide phosphatase
						Q8QZV7	15	Protein asunder homolog

6			6			6		
Q62191	1375	E3 ubiquitin-protein ligase TRIM21	Q62191	1577	E3 ubiquitin-protein ligase TRIM21	Q8BGW1	559	Alpha-ketoglutarate-dependent dioxygenase FTO
Q8BGW1	719	Alpha-ketoglutarate-dependent dioxygenase FTO	Q8BGW1	98	Alpha-ketoglutarate-dependent dioxygenase FTO	P20152	278	Vimentin
O35737	101	Heterogeneous nuclear ribonucleoprotein H	Q61457	38	G1/S-specific cyclin-E1	P10126	67	Elongation factor 1-alpha 1
Q9Z2X1	75	Heterogeneous nuclear ribonucleoprotein F	Q60668	36	Heterogeneous nuclear ribonucleoprotein D0	O70340	35	Neuronal pentraxin-2
P20152	45	Vimentin	P13504	29	Interleukin-1 receptor type 1	Q5SWU9	34	Acetyl-CoA carboxylase 1
P97499	43	Telomerase protein component 1	P21447	24	Multidrug resistance protein 1A	P70380	32	Interleukin-18
P36552	43	Coproporphyrinogen-III oxidase, mitochondrial				Q02357	28	Ankyrin-1
Q61457	41	G1/S-specific cyclin-E1				P60710	28	Actin, cytoplasmic 1
P42567	38	Epidermal growth factor receptor substrate 15				Q8BMN4	27	Leishmanolysin-like peptidase
Q7M6Y6	36	Maestro heat-like repeat-containing protein family member 2B				Q9EPL8	26	Importin-7
Q01338	14	Alpha-2A adrenergic receptor				Q9WU22	24	Tyrosine-protein phosphatase non-receptor type 4
						Q9CY62	24	E3 ubiquitin-protein ligase RNF181
						Q62191	23	E3 ubiquitin-protein ligase TRIM21
						Q8BRH0	19	Transmembrane and TPR repeat-containing protein 3

7			7			7		
Q62191	748	E3 ubiquitin-protein ligase TRIM21	Q62191	600	E3 ubiquitin-protein ligase TRIM21	Q6ZWX6	81	Eukaryotic translation initiation factor 2 subunit 1
Q8BGW1	295	Alpha-ketoglutarate-dependent dioxygenase FTO	P14206	121	40S ribosomal protein SA	P15864	74	Histone H1.2
Q9Z204	225	Heterogeneous nuclear ribonucleoproteins C1/C2	P15864	113	Histone H1.2	P20152	69	Vimentin
O88569	207	Heterogeneous nuclear ribonucleoproteins A2/B1	O88569	108	Heterogeneous nuclear ribonucleoproteins A2/B1	P07356	60	Annexin A2
P49312	177	Heterogeneous nuclear ribonucleoprotein A1	P51881	106	ADP/ATP translocase 2	P49312	60	Heterogeneous nuclear ribonucleoprotein A1
P51881	110	ADP/ATP translocase 2	Q8BGW1	103	Alpha-ketoglutarate-dependent dioxygenase FTO	Q9CXY6	60	Interleukin enhancer-binding factor 2
P15864	104	Histone H1.2	Q9Z204	101	Heterogeneous nuclear ribonucleoproteins C1/C2	P14869	56	60S acidic ribosomal protein P0
Q8BG05	102	Heterogeneous nuclear ribonucleoprotein A3	P49312	71	Heterogeneous nuclear ribonucleoprotein A1	O88569	52	Heterogeneous nuclear ribonucleoproteins A2/B1
Q60668	84	Heterogeneous nuclear ribonucleoprotein D0	P12970	66	60S ribosomal protein L7a	P47962	51	60S ribosomal protein L5
Q99020	79	Heterogeneous nuclear ribonucleoprotein A/B	P14869	64	60S acidic ribosomal protein P0	Q61937	51	Nucleophosmin
Q9CXY6	72	Interleukin enhancer-binding factor 2	P62918	52	60S ribosomal protein L8	P11499	50	Heat shock protein HSP 90-beta
P14869	54	60S acidic ribosomal protein P0	P25444	50	40S ribosomal protein S2	Q9JIF0	46	Protein arginine N-methyltransferase 1
Q3URD3	44	Sarcolemmal membrane-associated protein	P14148	46	60S ribosomal protein L7	P14206	42	40S ribosomal protein SA
Q9Z1W4	39	Growth/differentiation factor 11	Q9Z130	45	Heterogeneous nuclear ribonucleoprotein D-like	Q9CQE8	31	UPF0568 protein C14orf166 homolog

Q9CR35	38	Chymotrypsinogen B	P62702	42	40S ribosomal protein S4, X isoform	P51881	27	ADP/ATP translocase 2
Q61457	38	G1/S-specific cyclin-E1	P68040	42	Guanine nucleotide-binding protein subunit beta-2-like 1	Q9D379	26	Epoxide hydrolase 1
Q9WV02	37	RNA-binding motif protein, X chromosome	P47962	42	60S ribosomal protein L5	O89032	26	SH3 and PX domain-containing protein 2A
Q00519	36	Xanthine dehydrogenase/oxidase	Q99020	42	Heterogeneous nuclear ribonucleoprotein A/B	P28704	16	Retinoic acid receptor RXR-beta
P06151	35	L-lactate dehydrogenase A chain	P62754	41	40S ribosomal protein S6			
P97346	32	Nucleoredoxin	O35227	39	Disintegrin and metalloproteinase domain-containing protein 7			
Q91WN1	29	DnaJ homolog subfamily C member 9	P62908	31	40S ribosomal protein S3			
Q9Z247	28	Peptidyl-prolyl cis-trans isomerase FKBP9	P63040	31	Complexin-1			
P62196	28	26S protease regulatory subunit 8	Q62318	30	Transcription intermediary factor 1-beta			
P14206	27	40S ribosomal protein SA	P20152	27	Vimentin			
P70279	26	Surfeit locus protein 6	E9Q6X9	27	Rho GTPase-activating protein 40			
Q8VE97	26	Serine/arginine-rich splicing factor 4	P12388	27	Plasminogen activator inhibitor 2, macrophage			
Q5M8N0	19	CB1 cannabinoid receptor-interacting protein 1	Q9CR57	22	60S ribosomal protein L14			
Q9ERL7	19	Glia maturation factor gamma	Q80UN9	22	tRNA dimethylallyltransferase, mitochondrial			
8			**8**			**8**		
P51881	171	ADP/ATP translocase 2	Q62191	197	E3 ubiquitin-protein ligase TRIM21	Q8BGW1	267	Alpha-ketoglutarate-dependent dioxygenase FTO

Q62191	168	E3 ubiquitin-protein ligase TRIM21	P02535	99	Keratin, type I cytoskeletal 10	P62259	88	14-3-3 protein epsilon
Q8BGW1	95	Alpha-ketoglutarate-dependent dioxygenase FTO	Q8BGW1	84	Alpha-ketoglutarate-dependent dioxygenase FTO	P63101	71	14-3-3 protein zeta/delta
P43277	90	Histone H1.3	P62082	73	40S ribosomal protein S7	P15864	80	Histone H1.2
Q8VEM8	66	Phosphate carrier protein, mitochondrial	Q6ZWN5	65	40S ribosomal protein S9	Q8R1M2	68	Histone H2A.J
Q9CR57	59	60S ribosomal protein L14	Q9CR57	63	60S ribosomal protein L14	P62908	52	40S ribosomal protein S3
P23198	50	Chromobox protein homolog 3	P62242	62	40S ribosomal protein S8	P63163	48	Small nuclear ribonucleoprotein-associated protein N
P62908	46	40S ribosomal protein S3	Q6GSS7	57	Histone H2A type 2-A	P62702	41	40S ribosomal protein S4, X isoform
P49312	44	Heterogeneous nuclear ribonucleoprotein A1	Q8BP67	47	60S ribosomal protein L24	P62754	40	40S ribosomal protein S6
Q9CPR4	44	60S ribosomal protein L17	Q9CXW4	46	60S ribosomal protein L11	P58771	39	Tropomyosin alpha-1 chain
P62702	43	40S ribosomal protein S4, X isoform	Q9CZM2	42	60S ribosomal protein L15	P48962	39	ADP/ATP translocase 1
P62748	39	Hippocalcin-like protein 1	Q6P1I6	41	PH and SEC7 domain-containing protein 2	Q9CQE8	37	UPF0568 protein C14orf166 homolog
O88569	36	Heterogeneous nuclear ribonucleoproteins A2/B1	P84104	39	Serine/arginine-rich splicing factor 3	O08807	36	Peroxiredoxin-4
P62754	33	40S ribosomal protein S6	P51410	39	60S ribosomal protein L9	Q9CR57	34	60S ribosomal protein L14
Q9CQV7	31	Mitochondrial import inner membrane translocase subunit TIM14	P35980	33	60S ribosomal protein L18	Q6ZWN5	31	40S ribosomal protein S9
Q6PDM2	24	Serine/arginine-rich splicing factor 1	Q9CPR4	32	60S ribosomal protein L17	Q8BX90	27	Fibronectin type-III domain-containing protein 3A
Q8BNU0	20	Armadillo repeat-containing protein 6	Q3U1D0	32	Protein Lines homolog	P97447	25	Four and a half LIM domains protein 1

Q810A7	16	ATP-dependent RNA helicase DDX42	Q61220	31	Protein kinase C-binding protein NELL2	Q6PDF3	22	Putative transporter SVOPL
			Q9D417	30	F-box only protein 24	Q8C167	21	Prolyl endopeptidase-like
			P62751	30	60S ribosomal protein L23a	Q6PFG8	21	Oligodendrocyte transcription factor 3
			P48320	23	Glutamate decarboxylase 2	O88322	21	Nidogen-2
			Q9ES52	17	Phosphatidylinositol 3,4,5-trisphosphate 5-phosphatase 1			
9			**9**			**9**		
P10854	119	Histone H2B type 1-M	Q6GSS7	128	Histone H2A type 2-A	Q6GSS7	117	Histone H2A type 2-A
Q64524	111	Histone H2B type 2-E	Q8BGW1	72	Alpha-ketoglutarate-dependent dioxygenase FTO	P0C0S6	59	Histone H2A.Z
Q8BFU2	104	Histone H2A type 3	P62806	71	Histone H4	Q8BGW1	107	Alpha-ketoglutarate-dependent dioxygenase FTO
Q8BGW1	94	Alpha-ketoglutarate-dependent dioxygenase FTO	P47964	56	60S ribosomal protein L36	Q9D2U9	99	Histone H2B type 3-A
Q62191	93	E3 ubiquitin-protein ligase TRIM21	Q6LBE8	50	Histone H3.2	P62806	89	Histone H4
Q3URD3	55	Sarcolemmal membrane-associated protein	Q3URD3	45	Sarcolemmal membrane-associated protein	P62900	66	60S ribosomal protein L31
P62806	54	Histone H4	P63325	42	40S ribosomal protein S10	P62270	61	40S ribosomal protein S18
P63325	53	40S ribosomal protein S10	P62748	41	Hippocalcin-like protein 1	P17742	53	Peptidyl-prolyl cis-trans isomerase A
P62270	53	40S ribosomal protein S18	Q62188	40	Dihydropyrimidinase-related protein 3	Q6LBE8	49	Histone H3.2
P67984	52	60S ribosomal protein L22	P51906	37	Excitatory amino acid transporter 3	P62267	49	40S ribosomal protein S23
Q6LBE8	50	Histone H3.2	P61407	37	Tudor domain-containing protein 6	P18760	49	Cofilin-1

P84104	47	Serine/arginine-rich splicing factor 3	Q8BTM8	34	Filamin-A	P60867	47	40S ribosomal protein S20
Q3TTY5	46	Keratin, type II cytoskeletal 2 epidermal	Q3TXS7	34	26S proteasome non-ATPase regulatory subunit 1	Q3THE2	46	Myosin regulatory light chain 12B
Q8VED5	44	Keratin, type II cytoskeletal 79	P61358	33	60S ribosomal protein L27	P63325	44	40S ribosomal protein S10
Q9WUT3	43	Ribosomal protein S6 kinase alpha-2	Q62191	31	E3 ubiquitin-protein ligase TRIM21	P11499	39	Heat shock protein HSP 90-beta
P62267	38	40S ribosomal protein S23	D3YXK2	30	Scaffold attachment factor B1	P35700	37	Peroxiredoxin-1
P47964	37	60S ribosomal protein L36	P62267	28	40S ribosomal protein S23	P61358	37	60S ribosomal protein L27
P62082	28	40S ribosomal protein S7	Q8CDI7	28	Coiled-coil domain-containing protein 150	Q3URD3	36	Sarcolemmal membrane-associated protein
Q569Z5	28	Probable ATP-dependent RNA helicase DDX46	Q63ZV0	25	Insulinoma-associated protein 1	Q8VHP8	34	Ras-related protein Rab-40B
P48754	28	Breast cancer type 1 susceptibility protein homolog	Q9CY62	24	E3 ubiquitin-protein ligase RNF181	Q61001	30	Laminin subunit alpha-5
P30415	27	NK-tumor recognition protein	Q8BRH4	22	Histone-lysine N-methyltransferase 2C	P63276	29	40S ribosomal protein S17
			Q922J3	20	CAP-Gly domain-containing linker protein 1	E0CZ16	27	Kelch-like protein 3
			O35936	18	Arachidonate 8S-lipoxygenase			
10			**10**			**10**		
P62806	177	Histone H4	P62806	46	Histone H4	P62806	133	Histone H4
P62858	58	40S ribosomal protein S28	P62858	44	40S ribosomal protein S28	Q8BGW1	65	Alpha-ketoglutarate-dependent dioxygenase FTO
Q6GSS7	56	Histone H2A type 2-A	Q3URD3	38	Sarcolemmal membrane-associated protein	P07901	40	Heat shock protein HSP 90-alpha
Q8BGW1	41	Alpha-ketoglutarate-dependent dioxygenase FTO	Q8VE97	28	Serine/arginine-rich splicing factor 4	P51906	37	Excitatory amino acid transporter 3

Q80U44	30	Zinc finger FYVE domain-containing protein 16	P62858			Q8BWW9	28	Serine/threonine-protein kinase N2
Q60813	19	Disintegrin and metalloproteinase domain-containing protein 1a	Q3URD3			Q8BKS9	25	Pumilio domain-containing protein KIAA0020
			Q8VE97			O88322	23	Nidogen-2
						Q6PDK2	17	Histone-lysine N-methyltransferase 2D
						Q80ZA0	13	Intelectin-1b

Appendix 6 *Fto* Conditional Muscle Knock-Out

Table Appendix 6. Descriptive statistics of body length measurements of male and female mice at week 20.

Males				Females			
	N	Mean (cm)	Std. Error		N	Mean (cm)	Std. Error
WT WT	17	10.1647	0.08132	WT WT	21	9.6762	0.04776
WT CRE	20	10.19	0.05662	WT CRE	26	9.6154	0.0414
HOM WT	17	9.9765	0.03379	HOM WT	19	9.5368	0.04727
HOM CRE	23	10.0739	0.03987	HOM CRE	21	9.4857	0.05037

Table Appendix 7. Multiple Comparisons (post-hoc tests) of body length differences in males and females at week-20. Statistically significant values are highlighted in grey.

Males			Females		
Games-Howell post-hoc			Bonferroni post-hoc		
GENOTYPE	GENOTYPE	Sig.	GENOTYPE	GENOTYPE	Sig.
WT WT	WT CRE	0.994	WT WT	WT CRE	1.000
	HOM WT	0.173		HOM WT	0.273
	HOM CRE	0.749		HOM CRE	0.033
WT CRE	WT WT	0.994	WT CRE	WT WT	1.000
	HOM WT	0.015		HOM WT	1.000
	HOM CRE	0.351		HOM CRE	0.268
HOM WT	WT WT	0.173	HOM WT	WT WT	0.273
	WT CRE	0.015		WT CRE	1.000
	HOM CRE	0.260		HOM CRE	1.000
HOM CRE	WT WT	0.749	HOM CRE	WT WT	0.033
	WT CRE	0.351		WT CRE	0.268
	HOM WT	0.260		HOM WT	1.000

Table Appendix 8. Descriptive statistics and simple main effect of genotype analysis of body mass measurements of male mice within 4-20 weeks.

Week	WTWT		WTCRE		HOMWT		HOMCRE		ANOVA
	Mean (g)	Std. Error	Mean (g)	Std. Error	Mean (g)	Std. Error	Mean (g)	Std. Error	Sig.
4	14.187	0.633	17.011	0.554	17.609	0.610	16.379	0.524	0.002
5	20.742	0.517	21.747	0.452	21.271	0.498	20.773	0.428	0.370
6	23.158	0.552	23.976	0.483	22.581	0.532	23.341	0.457	0.287
7	25.190	0.542	25.860	0.474	24.476	0.523	24.565	0.449	0.160
8	22.691	0.469	23.125	0.410	22.156	0.452	21.845	0.388	0.132
9	27.579	0.554	28.005	0.485	26.859	0.534	26.741	0.459	0.221
10	28.082	0.573	29.040	0.501	28.289	0.552	28.031	0.474	0.469
11	29.383	0.531	29.778	0.464	29.189	0.512	28.908	0.439	0.591
12	26.205	0.514	27.056	0.450	26.230	0.496	25.889	0.425	0.296
13	30.443	0.512	30.745	0.448	30.198	0.493	30.054	0.423	0.707
14	31.089	0.569	31.361	0.497	31.341	0.548	30.894	0.470	0.894
15	31.523	0.590	31.719	0.516	31.547	0.568	31.514	0.488	0.991
16	28.449	0.545	28.705	0.476	28.631	0.525	28.612	0.451	0.998
17	32.172	0.580	32.533	0.507	32.177	0.559	32.420	0.480	0.952
18	32.156	0.612	32.792	0.535	32.894	0.589	33.174	0.506	0.644
19	33.078	0.637	33.565	0.557	33.469	0.614	33.996	0.527	0.736
20	32.852	0.629	33.528	0.550	33.167	0.606	33.598	0.520	0.792

Table Appendix 9. Descriptive statistics and ANOVA of food and water consumption, urine and faeces output in male mice measured over 24 hours at 14 weeks of age.

	WTWT		WTCRE		HOMWT		HOMCRE		ANOVA
	Mean (g)	Std. Error	Mean (g)	Std. Error	Mean (g)	Std. Error	Mean (g)	Std. Error	Sig.
Food intake	3.269	0.173	3.070	0.178	2.933	0.178	3.121	0.154	0.606
Water intake	3.755	0.175	3.470	0.168	3.616	0.167	3.570	0.201	0.742
Faeces	1.619	0.080	1.614	0.097	1.506	0.098	1.685	0.097	0.606
Urine	1.676	0.100	1.783	0.157	1.579	0.103	1.727	0.107	0.683

Table Appendix 10. Descriptive statistics and ANOVA of male mice BMD, BMC, brain, liver, heart, WAT and BAT mass measured at the 20 weeks of age.

	WTWT		WTCRE		HOMWT		HOMCRE		Method	Sig.
	Mean	Std. Error	Mean	Std. Error	Mean	Std. Error	Mean	Std. Error		
BMD (g/cm^2)	0.0564	0.0007	0.0561	0.0005	0.0544	0.0007	0.0541	0.0005	ANOVA	0.012
BMC (g)	0.5596	0.0139	0.5696	0.0109	0.5441	0.0132	0.5284	0.0087	ANOVA	0.053
Brain (g)	0.4912	0.0098	0.4872	0.0078	0.4726	0.0059	0.4857	0.0047	Welch	0.285
Liver (g)	1.3365	0.0463	1.4094	0.0415	1.3689	0.0477	1.3796	0.0491	ANOVA	0.772
Heart (g)	0.2024	0.0146	0.1867	0.0138	0.1474	0.0055	0.1748	0.0068	Welch	0.001
G. Muscle (g)	0.1580	0.0041	0.1468	0.0076	0.1592	0.0048	0.1617	0.0036	ANOVA	0.196
WAT (g)	0.5947	0.0601	0.6694	0.0521	0.7595	0.0773	0.9243	0.0677	ANOVA	0.004
BAT (g)	0.1000	0.0094	0.0831	0.0072	0.0726	0.0073	0.0878	0.0065	ANOVA	0.101

Table Appendix 11. Multiple Comparisons (post-hoc tests) of BMD, heart and WAT mass measured in male mice at the 20 weeks of age. Statistically significant values are highlighted in grey.

GENOTYPE	GENOTYPE	BMD Sig.	Heart Sig.	WAT Sig.
		Bonferroni	Games-Howell	Bonferroni
WT WT	WT CRE	1.000	0.863	1.000
	HOM WT	0.161	0.010	0.564
	HOM CRE	0.035	0.343	0.004
WT CRE	WT WT	1.000	0.863	1.000
	HOM WT	0.389	0.065	1.000
	HOM CRE	0.101	0.866	0.041
HOM WT	WT WT	0.161	0.010	0.564
	WT CRE	0.389	0.065	1.000
	HOM CRE	1.000	0.016	0.429
HOM CRE	WT WT	0.035	0.343	0.004
	WT CRE	0.101	0.866	0.041
	HOM WT	1.000	0.016	0.429

Table Appendix 12. Descriptive statistics and ANOVA of absolute fat mass and lean mass in male mice at various age. W- week.

	WTWT		WTCRE		HOMWT		HOMCRE		Method	Sig.
	Mean (g)	Std. Error	Mean (g)	Std. Error	Mean (g)	Std. Error	Mean (g)	Std. Error		
Fat Mass W5	2.053	0.081	2.129	0.085	2.284	0.070	2.172	0.070	ANOVA	0.226
Fat Mass W9	2.923	0.111	3.050	0.134	3.368	0.118	3.462	0.099	ANOVA	0.004
Fat Mass W13	3.550	0.137	3.680	0.199	4.061	0.197	4.236	0.142	ANOVA	0.017
Fat Mass W17	3.829	0.184	3.892	0.164	4.513	0.210	4.909	0.200	ANOVA	0.000
Fat Mass W20	4.122	0.252	4.278	0.224	4.753	0.382	5.490	0.309	ANOVA	0.005
Lean Mass W5	18.155	0.419	18.288	0.373	17.472	0.414	17.472	0.399	ANOVA	0.312
Lean Mass W9	22.302	0.555	22.904	0.352	21.712	0.491	20.968	0.445	ANOVA	0.017
Lean Mass W13	24.192	0.516	24.991	0.351	23.546	0.433	23.232	0.384	ANOVA	0.017
Lean Mass W17	25.188	0.506	25.895	0.332	24.751	0.471	24.240	0.471	ANOVA	0.062
Lean Mass W20	25.685	0.474	26.300	0.398	25.086	0.605	25.302	0.464	ANOVA	0.307

Table Appendix 13. Multiple Comparisons (post-hoc tests) of absolute fat mass and lean mass in male mice at various age. W- week. Statistically significant results are highlighted in grey.

GENOTYPE	GENOTYPE	Fat Mass W9	Fat Mass W13	Fat Mass W17	Fat Mass W20	Lean Mass W9	Lean Mass W13
WT WT	WT CRE	1.000	1.000	1.000	1.000	1.000	1.000
	HOM WT	0.082	0.266	0.107	0.801	1.000	1.000
	HOM CRE	0.011	0.032	0.001	0.007	0.253	0.642
WT CRE	WT WT	1.000	1.000	1.000	1.000	1.000	1.000
	HOM WT	0.371	0.739	0.176	1.000	0.421	0.111
	HOM CRE	0.064	0.117	0.001	0.022	0.013	0.018
HOM WT	WT WT	0.082	0.266	0.107	0.801	1.000	1.000
	WT CRE	0.371	0.739	0.176	1.000	0.421	0.111
	HOM CRE	1.000	1.000	0.863	0.529	1.000	1.000
HOM CRE	WT WT	0.011	0.032	0.001	0.007	0.253	0.642
	WT CRE	0.064	0.117	0.001	0.022	0.013	0.018
	HOM WT	1.000	1.000	0.863	0.529	1.000	1.000

Table Appendix 14. Descriptive statistics and ANOVA of relative fat mass and lean mass in male mice at various age. Rel. - Relative, W- week.

	WTWT		WTCRE		HOMWT		HOMCRE		Sig.
	Mean (%)	Std. Error	Mean (%)	Std. Error	Mean (%)	Std. Error	Mean (%)	Std. Error	
Fat Mass Rel. W5	9.894	0.384	9.991	0.341	10.957	0.269	10.575	0.310	0.082
Fat Mass Rel. W9	10.937	0.425	10.932	0.432	12.569	0.451	13.233	0.427	0.000
Fat Mass Rel. W13	11.946	0.465	11.952	0.633	13.576	0.514	14.308	0.492	0.003
Fat Mass Rel. W17	12.170	0.538	12.011	0.502	14.189	0.467	15.488	0.565	0.000
Fat Mass Rel. W20	12.642	0.688	12.758	0.624	14.469	0.879	16.334	0.793	0.002
Lean Mass Rel. W5	87.218	0.609	85.920	0.633	83.641	0.472	84.763	0.478	0.000
Lean Mass Rel. W9	82.947	0.663	82.337	0.590	80.602	0.646	79.598	0.437	0.000
Lean Mass Rel. W13	81.124	0.740	81.128	0.795	79.174	0.557	78.200	0.489	0.002
Lean Mass Rel. W17	80.129	0.624	79.859	0.628	78.319	0.506	76.421	0.610	0.000
Lean Mass Rel. W20	79.197	0.748	78.596	0.723	77.597	0.945	75.619	0.844	0.014

Table Appendix 15. Multiple Comparisons (post-hoc tests) of relative fat mass and lean mass in male mice at various age. Rel.- Relative, W- week. Statistically significant values are highlighted in grey.

GENOTYPE	GENOTYPE	Fat Mass Rel. W9	Fat Mass Rel. W13	Fat Mass Rel. W17	Fat Mass Rel. W20	Lean Mass Rel. W5	Lean Mass Rel. W9	Lean Mass Rel. W13	Lean Mass Rel. W17	Lean Mass Rel. W20
WT WT	WT CRE	1.000	1.000	1.000	1.000	0.666	1.000	1.000	1.000	1.000
	HOM WT	0.088	0.241	0.069	0.547	0.000	0.052	0.268	0.271	1.000
	HOM CRE	0.002	0.013	0.000	0.004	0.018	0.001	0.012	0.000	0.014
WT CRE	WT WT	1.000	1.000	1.000	1.000	0.666	1.000	1.000	1.000	1.000
	HOM WT	0.061	0.219	0.036	0.679	0.023	0.237	0.238	0.502	1.000
	HOM CRE	0.001	0.011	0.000	0.005	0.757	0.004	0.009	0.000	0.062
HOM WT	WT WT	0.088	0.241	0.069	0.547	0.000	0.052	0.268	0.271	1.000
	WT CRE	0.061	0.219	0.036	0.679	0.023	0.237	0.238	0.502	1.000
	HOM CRE	1.000	1.000	0.503	0.555	0.879	1.000	1.000	0.164	0.616
HOM CRE	WT WT	0.002	0.013	0.000	0.004	0.018	0.001	0.012	0.000	0.014
	WT CRE	0.001	0.011	0.000	0.005	0.757	0.004	0.009	0.000	0.062
	HOM WT	1.000	1.000	0.503	0.555	0.879	1.000	1.000	0.164	0.616

Table Appendix 16. Descriptive statistics and ANOVA/Welch of muscle strength in male mice at various age. W- Week.

Muscle Strength	WTWT		WTCRE		HOMWT		HOMCRE		Method	Sig.
	Mean (g)	Std. Error	Mean (g)	Std. Error	Mean (g)	Std. Error	Mean (g)	Std. Error		
W5	84.342	2.773	89.920	2.769	96.742	4.228	84.465	3.062	ANOVA	0.033
W9	121.055	5.069	130.813	5.036	142.300	5.136	134.054	4.114	ANOVA	0.038
W13	109.628	5.747	130.785	6.044	152.548	6.304	144.330	6.901	ANOVA	0.000
W17	120.607	3.058	138.968	5.149	163.321	5.696	152.200	5.322	Welch	0.000
W20	128.523	3.829	145.686	5.530	166.780	7.902	154.254	6.181	ANOVA	0.001

Table Appendix 17. Multiple Comparisons (post-hoc tests) of muscle strength in male mice at various age. M-muscle, W- week. Statistically significant values are highlighted in grey.

GENOTYPE	GENOTYPE	M. Strength W5	M. Strength W9	M. Strength W13	M. Strength W17	M. Strength W20
		Bonferroni	Bonferroni	Bonferroni	Games-Howell	Bonferroni
WT WT	WT CRE	1.000	0.935	0.134	0.022	0.169
	HOM WT	0.114	0.027	0.000	0.000	0.001
	HOM CRE	1.000	0.373	0.001	0.000	0.012
WT CRE	WT WT	1.000	0.935	0.134	0.022	0.169
	HOM WT	0.943	0.602	0.113	0.015	0.117
	HOM CRE	1.000	1.000	0.733	0.293	1.000
HOM WT	WT WT	0.114	0.027	0.000	0.000	0.001
	WT CRE	0.943	0.602	0.113	0.015	0.117
	HOM CRE	0.045	1.000	1.000	0.491	1.000
HOM CRE	WT WT	1.000	0.373	0.001	0.000	0.012
	WT CRE	1.000	1.000	0.733	0.293	1.000
	HOM WT	0.045	1.000	1.000	0.491	1.000

Table Appendix 18. Descriptive statistics and ANOVA of blood glucose and Area Under the Curve (AUC) of normalised blood glucose curves in male mice.

Time (min)	WTWT		WTCRE		HOMWT		HOMCRE		ANOVA
	Mean (mM)	Std. Error	Mean (mM)	Std. Error	Mean (mM)	Std. Error	Mean (mM)	Std. Error	Sig.
0	7.632	0.302	7.417	0.311	8.001	0.334	7.429	0.259	0.492
60	19.799	1.139	19.186	0.407	17.665	0.926	21.196	1.163	0.074
120	11.816	0.448	11.631	0.381	11.516	0.527	12.354	0.482	0.572
	Mean (mM×min)	Std. Error	Mean (mM×min)	Std. Error	Mean (mM×min)	Std. Error	Mean (mM×min)	Std. Error	Sig.
AUC	237.112	14.043	238.945	9.631	208.739	8.456	255.195	12.967	0.044

Table Appendix 19. Descriptive statistics of body mass repeated measurements of female mice (4-20 weeks).

Week	WTWT		WTCRE		HOMWT		HOMCRE	
	Mean (g)	Std. Error	Mean (g)	Std. Error	Mean (g)	Std. Error	Mean (g)	Std. Error
4	14.899	0.450	14.856	0.356	13.812	0.450	14.216	0.436
5	17.801	0.363	17.513	0.287	16.243	0.363	16.965	0.352
6	18.903	0.344	18.714	0.272	17.526	0.344	17.889	0.333
7	20.023	0.355	19.641	0.281	18.809	0.355	18.762	0.344
8	17.983	0.311	17.872	0.246	16.731	0.311	16.950	0.301
9	21.378	0.389	21.436	0.308	19.754	0.389	19.891	0.377
10	22.822	0.441	21.901	0.348	20.697	0.441	20.719	0.427
11	22.997	0.412	22.685	0.326	21.337	0.412	21.424	0.399
12	20.748	0.430	20.446	0.340	19.420	0.430	19.407	0.416
13	23.791	0.440	23.628	0.348	22.387	0.440	22.409	0.426
14	24.545	0.479	24.308	0.379	23.158	0.479	23.004	0.464
15	24.313	0.498	24.343	0.394	23.060	0.498	23.029	0.483
16	21.898	0.535	22.018	0.423	21.163	0.535	20.812	0.518
17	25.235	0.532	25.257	0.421	24.135	0.532	23.737	0.515
18	25.301	0.532	25.280	0.420	23.945	0.532	23.907	0.515
19	25.846	0.628	25.855	0.497	24.765	0.628	24.521	0.608
20	25.918	0.680	26.058	0.538	24.991	0.680	24.377	0.659

Table Appendix 20. Descriptive statistics and ANOVA of body weight of all females ever included in the phenotyping pipeline.

W	WTWT			WTCRE			HOMWT			HOMCRE			A
	Mean (g)	n	Std. Error	Mean (g)	n	Std. Error	Mean (g)	n	Std. Error	Mean (g)	n	Std. Error	Sig.
4	14.899	20	0.450	14.856	26	0.356	13.812	18	0.450	14.216	19	0.436	0.248
5	17.801	22	0.363	17.513	27	0.287	16.243	20	0.363	16.965	22	0.352	0.005
6	18.903	22	0.344	18.714	27	0.272	17.526	20	0.344	17.889	21	0.333	0.003
7	20.023	22	0.355	19.641	27	0.281	18.809	18	0.355	18.762	20	0.344	0.013
8	17.983	18	0.311	17.872	26	0.246	16.731	19	0.311	16.950	20	0.301	0.005
9	21.378	22	0.389	21.436	27	0.308	19.754	20	0.389	19.891	21	0.377	0.000
10	22.822	22	0.441	21.901	27	0.348	20.697	20	0.441	20.719	21	0.427	0.000
11	22.997	22	0.412	22.685	27	0.326	21.337	20	0.412	21.424	21	0.399	0.000
12	20.748	21	0.430	20.446	26	0.340	19.420	18	0.430	19.407	19	0.416	0.031
13	23.791	22	0.440	23.628	27	0.348	22.387	20	0.440	22.409	21	0.426	0.004
14	24.545	22	0.479	24.308	27	0.379	23.158	20	0.479	23.004	21	0.464	0.004
15	24.313	22	0.498	24.343	27	0.394	23.060	20	0.498	23.029	21	0.483	0.011
16	21.898	22	0.535	22.018	27	0.423	21.163	20	0.535	20.812	21	0.518	0.094
17	25.235	21	0.532	25.257	27	0.421	24.135	20	0.532	23.737	21	0.515	0.006
18	25.301	21	0.532	25.280	27	0.420	23.945	20	0.532	23.907	21	0.515	0.006
19	25.846	21	0.628	25.855	27	0.497	24.765	20	0.628	24.521	21	0.608	0.041
20	25.918	21	0.680	26.058	27	0.538	24.991	20	0.680	24.377	21	0.659	0.033

Table Appendix 21. Multiple Comparisons (post-hoc tests) of body weight of all females ever included in the phenotyping pipeline. Statistically significant values are highlighted in grey.

GENOTYPE	WT WT			WT CRE			HOM WT			HOM CRE		
GENOTYPE	WT CRE	HOM WT	HOM CRE	WT WT	HOM WT	HOM CRE	WT WT	WT CRE	HOM CRE	WT WT	WT CRE	HOM WT
Week 4	1.000	0.627	0.584	1.000	1.000	1.000	0.627	1.000	1.000	0.584	1.000	1.000
Week 5	1.000	0.003	0.250	1.000	0.061	1.000	0.003	0.061	0.744	0.250	1.000	0.744
Week 6	1.000	0.005	0.271	1.000	0.014	0.642	0.005	0.014	0.892	0.271	0.642	0.892
Week 7	1.000	0.029	0.076	1.000	0.242	0.559	0.029	0.242	1.000	0.076	0.559	1.000
Week 8	1.000	0.012	0.090	1.000	0.052	0.346	0.012	0.052	1.000	0.090	0.346	1.000
Week 9	1.000	0.002	0.010	1.000	0.003	0.019	0.002	0.003	1.000	0.010	0.019	1.000
Week 10	0.600	0.001	0.003	0.600	0.051	0.221	0.001	0.051	1.000	0.003	0.221	1.000
Week 11	1.000	0.001	0.004	1.000	0.012	0.038	0.001	0.012	1.000	0.004	0.038	1.000
Week 12	1.000	0.097	0.087	1.000	0.589	0.552	0.097	0.589	1.000	0.087	0.552	1.000
Week 13	1.000	0.011	0.069	1.000	0.046	0.242	0.011	0.046	1.000	0.069	0.242	1.000
Week 14	1.000	0.020	0.025	1.000	0.147	0.181	0.020	0.147	1.000	0.025	0.181	1.000
Week 15	1.000	0.032	0.108	1.000	0.113	0.352	0.032	0.113	1.000	0.108	0.352	1.000
Week 16	1.000	0.322	0.270	1.000	0.745	0.641	0.322	0.745	1.000	0.270	0.641	1.000
Week 17	1.000	0.041	0.027	1.000	0.176	0.123	0.041	0.176	1.000	0.027	0.123	1.000
Week 18	1.000	0.026	0.051	1.000	0.100	0.191	0.026	0.100	1.000	0.051	0.191	1.000
Week 19	1.000	0.123	0.197	1.000	0.328	0.511	0.123	0.328	1.000	0.197	0.511	1.000
Week 20	1.000	0.264	0.090	1.000	0.541	0.194	0.264	0.541	1.000	0.090	0.194	1.000

Table Appendix 22. Descriptive statistics and ANOVA of food and water consumption, urine and faeces output in female mice measured over 24 hours at the 14 weeks of age.

	WTWT		WTCRE		HOMWT		HOMCRE		Method	Sig.
	Mean (g)	Std. Error	Mean (g)	Std. Error	Mean (g)	Std. Error	Mean (g)	Std. Error		
Food intake	3.874	0.126	3.496	0.215	3.332	0.177	3.582	0.178	Welch	0.092
Water intake	4.336	0.179	3.963	0.230	3.239	0.286	3.988	0.215	ANOVA	0.015
Faeces	1.778	0.085	1.649	0.123	1.528	0.092	1.703	0.127	ANOVA	0.467
Urine	1.394	0.118	1.316	0.128	0.828	0.088	1.128	0.089	ANOVA	0.005

Table Appendix 23. Multiple Comparisons (post-hoc tests) of food and water consumption, urine and faeces output measured in female mice over 24 hours at the 14 weeks of age.

GENOTYPE	GENOTYPE	Water intake	Urine
WT WT	WT CRE	1.000	1.000
	HOM WT	0.010	0.006
	HOM CRE	1.000	0.643
WT CRE	WT WT	1.000	1.000
	HOM WT	0.162	0.017
	HOM CRE	1.000	1.000
HOM WT	WT WT	0.010	0.006
	WT CRE	0.162	0.017
	HOM CRE	0.184	0.487
HOM CRE	WT WT	1.000	0.643
	WT CRE	1.000	1.000
	HOM WT	0.184	0.487

Table Appendix 24. Descriptive statistics and ANOVA of BMD, BMC, brain, liver, heart, WAT and BAT mass in female mice measured at the 20 weeks of age.

	WTWT		WTCRE		HOMWT		HOMCRE		Method	Sig.
	Mean	Std. Error	Mean	Std. Error	Mean	Std. Error	Mean	Std. Error		
BMD (g/cm)	0.054	0.000	0.053	0.000	0.052	0.001	0.051	0.001	ANOVA	0.004
BMC (g)	0.506	0.007	0.497	0.009	0.457	0.009	0.474	0.008	ANOVA	0.001
Brain (g)	0.485	0.009	0.484	0.006	0.483	0.007	0.486	0.010	ANOVA	0.992
Liver (g)	1.082	0.038	1.035	0.024	1.025	0.019	1.036	0.039	ANOVA	0.583
G. Muscle (g)	0.127	0.006	0.116	0.005	0.122	0.003	0.118	0.005	Welch	0.559
Heart (g)	0.133	0.008	0.139	0.009	0.130	0.008	0.135	0.010	ANOVA	0.876
WAT (g)	0.808	0.131	0.754	0.138	0.778	0.112	0.686	0.083	ANOVA	0.253
BAT (g)	0.083	0.010	0.071	0.008	0.058	0.008	0.066	0.008	ANOVA	0.860

Table Appendix 25. Multiple Comparisons (post-hoc tests) of BMD and BMC measured in female mice at the 20 weeks of age.

GENOTYPE	GENOTYPE	BMD (g/cm)	BMC (g)
WT WT	WT CRE	1.000	1.000
	HOM WT	0.119	0.001
	HOM CRE	0.003	0.067
WT CRE	WT WT	1.000	1.000
	HOM WT	1.000	0.009
	HOM CRE	0.106	0.360
HOM WT	WT WT	0.119	0.001
	WT CRE	1.000	0.009
	HOM CRE	1.000	1.000
HOM CRE	WT WT	0.003	0.067
	WT CRE	0.106	0.360
	HOM WT	1.000	1.000

Table Appendix 26. Descriptive statistics and ANOVA of absolute fat mass and lean mass in female mice at various age. W- week.

	WTWT		WTCRE		HOMWT		HOMCRE		Method	Sig.
	Mean (g)	Std. Error	Mean (g)	Std. Error	Mean (g)	Std. Error	Mean (g)	Std. Error		
Lean Mass W5	14.991	0.218	14.605	0.255	13.518	0.342	14.148	0.300	ANOVA	0.004
Lean Mass W9	17.218	0.219	17.256	0.242	15.827	0.250	15.721	0.247	ANOVA	0.000
Lean Mass W13	18.556	0.202	18.439	0.235	16.971	0.313	16.938	0.244	ANOVA	0.000
Lean Mass W17	19.282	0.189	19.173	0.240	17.801	0.338	17.648	0.256	ANOVA	0.000
Lean Mass W20	19.594	0.201	19.380	0.249	18.189	0.307	18.025	0.255	ANOVA	0.000
Fat Mass W5	2.245	0.064	2.225	0.074	2.226	0.113	2.388	0.065	Welch	0.308
Fat Mass W9	2.896	0.183	2.931	0.193	2.907	0.146	3.018	0.142	ANOVA	0.963
Fat Mass W13	3.696	0.239	3.659	0.296	3.762	0.236	3.791	0.238	ANOVA	0.983
Fat Mass W17	4.531	0.326	4.335	0.382	4.304	0.308	4.390	0.262	ANOVA	0.967
Fat MassW20	4.781	0.497	4.905	0.607	4.812	0.511	4.598	0.316	ANOVA	0.979

Table Appendix 27. Multiple Comparisons (post-hoc tests) of absolute fat mass and lean mass in female mice at various age. W- week.

GENOTYPE	GENOTYPE	Lean Mass W5	Lean Mass W9	Lean Mass W13	Lean Mass W17	Lean Mass W20
WT WT	WT CRE	1.000	1.000	1.000	1.000	1.000
	HOM WT	0.003	0.001	0.000	0.001	0.002
	HOM CRE	0.229	0.000	0.000	0.000	0.000
WT CRE	WT WT	1.000	1.000	1.000	1.000	1.000
	HOM WT	0.042	0.000	0.000	0.001	0.008
	HOM CRE	1.000	0.000	0.000	0.000	0.001
HOM WT	WT WT	0.003	0.001	0.000	0.001	0.002
	WT CRE	0.042	0.000	0.000	0.001	0.008
	HOM CRE	0.744	1.000	1.000	1.000	1.000
HOM CRE	WT WT	0.229	0.000	0.000	0.000	0.000
	WT CRE	1.000	0.000	0.000	0.000	0.001
	HOM WT	0.744	1.000	1.000	1.000	1.000

Table Appendix 28. Descriptive statistics and ANOVA of relative fat mass and lean mass in female mice at various age. Rel. - Relative, W- week.

	WTWT		WTCRE		HOMWT		HOMCRE		Method	Sig.
	Mean (%)	Std. Error	Mean (%)	Std. Error	Mean (%)	Std. Error	Mean (%)	Std. Error		
Lean Mass Rel. W5	84.048	0.613	83.796	0.634	82.446	0.571	81.544	0.534	ANOVA	0.011
Lean Mass Rel. W9	80.183	0.926	80.947	0.818	80.647	0.812	78.950	0.750	ANOVA	0.355
Lean Mass Rel. W13	77.871	0.885	78.511	0.972	76.832	0.961	75.494	0.941	ANOVA	0.126
Lean Mass Rel. W17	75.696	1.009	76.794	1.079	75.311	0.960	74.761	0.893	ANOVA	0.508
Lean Mass Rel. W20	75.282	1.425	75.234	1.551	74.369	1.364	74.372	0.953	ANOVA	0.940
Fat Mass Rel. W5	12.561	0.270	12.760	0.365	13.524	0.553	13.813	0.361	Welch	0.043
Fat Mass Rel. W9	13.310	0.695	13.612	0.775	14.704	0.576	15.081	0.583	ANOVA	0.222
Fat Mass Rel. W13	15.328	0.844	15.282	0.999	16.834	0.844	16.732	0.887	ANOVA	0.464
Fat Mass Rel. W17	17.471	0.990	16.853	1.126	17.928	0.974	18.427	0.917	ANOVA	0.724
Fat Mass Rel. W20	17.749	1.347	17.970	1.660	18.950	1.475	18.754	1.080	ANOVA	0.927

Table Appendix 29. Multiple Comparisons (post-hoc tests) of relative fat mass and lean mass in female mice at various age. Rel.- Relative, W- week.

GENOTYPE	GENOTYPE	Lean Mass Rel.W5	Fat Mass Rel.W9
WT WT	WT CRE	1.000	0.972
	HOM WT	0.414	0.413
	HOM CRE	0.025	0.040
WT CRE	WT WT	1.000	0.972
	HOM WT	0.661	0.659
	HOM CRE	0.042	0.184
HOM WT	WT WT	0.414	0.413
	WT CRE	0.661	0.659
	HOM CRE	1.000	0.971
HOM CRE	WT WT	0.025	0.040
	WT CRE	0.042	0.184
	HOM WT	1.000	0.971

Table Appendix 30. Descriptive statistics and ANOVA of muscle strength in female mice at various age. W- Week.

Muscle strength	WTWT		WTCRE		HOMWT		HOMCRE		Method	Sig.
	Mean (g)	Std. Error	Mean (g)	Std. Error	Mean (g)	Std. Error	Mean (g)	Std. Error		
W5	73.708	3.088	79.230	3.148	80.770	3.916	82.512	3.099	ANOVA	0.288
W9	103.348	3.901	106.799	3.430	104.133	3.462	112.586	4.700	ANOVA	0.358
W13	119.686	3.261	115.716	4.439	121.473	4.571	118.700	5.967	Welch	0.834
W17	122.044	4.979	123.831	3.758	126.211	5.115	117.689	5.380	ANOVA	0.707
W20	129.123	23.519	130.126	16.742	120.800	24.496	114.319	16.458	ANOVA	0.050

Table Appendix 31. Descriptive statistics and ANOVA of blood glucose and Area Under the Curve (AUC) of normalised blood glucose curves in female mice. NA- not applicable.

Time (min)	WTWT		WTCRE		HOMWT		HOMCRE		ANOVA
	Mean (mM)	Std. Error	Mean (mM)	Std. Error	Mean (mM)	Std. Error	Mean (mM)	Std. Error	Sig.
0	7.490	0.236	6.666	0.225	7.071	0.248	6.744	0.236	NA
60	15.417	1.118	13.595	1.066	13.189	1.179	13.790	1.118	NA
120	10.066	0.771	9.216	0.735	9.724	0.813	9.564	0.771	NA
AUC	Mean (mM×min)	Std. Error	Mean (mM×min)	Std. Error	Mean (mM×min)	Std. Error	Mean (mM×min)	Std. Error	Sig.
	195.575	14.068	197.386	8.899	184.744	7.550	196.685	14.440	0.867

Table Appendix 32. Summary of all differences between the genotype groups identified in the analysis of the phenotyping data. A red arrow indicates statistically significant difference and a black arrow indicates nominal difference. (↑) indicates increase; (↓) indicates decrease. Yellow indicates differences identified in both HOMWT and HOMCRE.

Males		WTWT	WTCRE	HOMWT	HOMCRE
	Body length			↓	↓
	Body Mass	no differences			
	Food Consumption	no differences			
	Water consumption	no differences			
	Feaces	no differences			
	Urine	no differences			
	BMD			↓	↓
	BMC	no differences			
	Brain	no differences			
	Liver	no differences			
	GM	no differences			
	Heart			↓	
	WAT		↑	↑	↑
	BAT		↓	↓	
	Fat Mass Absotule ECHO			↑	↑
	Lean Mass Absolute ECHO				↓
	Fat Mass Relative ECHO			↑	↑
	Lean Mass Relative ECHO			↓	↓
	Muscle Strenght		↑	↑	↑
	IPGTT	no differences			
Females		WTWT	WTCRE	HOMWT	HOMCRE
	Body length		↓	↓	↓
	Body Mass			↓	↓
	Food Consumption	no differences			
	Water consumption			↓	
	Feaces	no differences			
	Urine			↓	
	BMD				↓
	BMC			↓	↓
	Brain	no differences			
	Liver	no differences			
	GM	no differences			
	Heart	no differences			
	WAT	no differences			
	BAT		↓	↓	↓
	Fat Mass Absotule ECHO	no differences			
	Lean Mass Absolute ECHO			↓	↓
	Fat Mass Relative ECHO	no differences			
	Lean Mass Relative ECHO	no differences			
	Muscle Strenght	no differences			
	IPGTT	no differences			